Origine de l'éclatement de grain sur des pièces forgées en Inconel 718

Andrea Agnoli

ParisTech
INSTITUT DES SCIENCES ET TECHNOLOGIES
PARIS INSTITUTE OF TECHNOLOGY

MINES ParisTech

Ecole doctorale n°364 : Sciences Fondamentales et Appliquées

Doctorat ParisTech

T H È S E

pour obtenir le grade de docteur délivré par

l'École nationale supérieure des mines de Paris

Spécialité "Sciences et Génie des Matériaux"

présentée et soutenue publiquement par

Andrea AGNOLI

le 19 décembre 2013

Origine de l'éclatement de grain sur des pièces forgées en Inconel 718

-

Origin of inhomogeneous grain growth in Inconel 718 forgings

Directeurs de thèse : **Nathalie BOZZOLO, Marc BERNACKI**

THESE CONFIDENTIELLE (date de fin : 20/12/18)

Jury

M. Patrick VILLECHAISE, Directeur de recherche CNRS, Institut P', ENSMA	Rapporteur
M. Bernard VIGUIER, Professeur, CIRIMAT, ENSIACET	Rapporteur
Mme Brigitte BACROIX, Directeur de recherche CNRS, Institut Galilée, Université Paris 13	Examinateur
M. Marc BERNACKI, Chargé de recherche, HDR, CEMEF, Mines ParisTech	Examinateur
Mme Nathalie BOZZOLO, Maître assistant, HDR, CEMEF, Mines ParisTech	Examinateur
Mme Johanne LAIGO, Docteur, Snecma-Villaroche	Invité

MINES ParisTech
Centre de Mise en Forme de Matériaux - CEMEF
1 rue Claude Daunesse – CS 10207
06904 Sophia Antipolis cedex, France

T H E S E

Acknowledgments

First and foremost, I want to thank my academic supervisors at Cemef Marc Bernacki and Nathalie Bozzolo. Indeed, without their support and guidance, I would have not been able to accomplish (not even begin!) this PhD work. My thanks to Nathalie for having encouraged me to work on this interesting project and for all the engaging discussions about microstructure evolution we had during the last three years. My thanks to Marc for sharing with me his passion for modeling and for his continuing support in this field so challenging for me. Overall, I want to thank my supervisors for all the time they spent advising me and reviewing in detail the work of this PhD.

I also would like to thank my industrial supervisors at Snecma Jean-Michel Franchet and Johanne Laigo for their involvement in this PhD work. My thanks for providing me all the material necessary to carry on smoothly the PhD activity and for bringing the necessary industrial perspective to guide the PhD research.

I want to thank as well Roland Logé for his support and involvement, especially at the beginning of this PhD. My thanks also to A. D. Rollet for sharing his remarks and advices on this work.

I also would like to express my gratitude to all the people of Cemef who helped me during the last years. In particular, my thanks to Gilbert and Suzanne who greatly helped me to carry out all the mechanical tests and characterizations presented in this work. Special thanks to Marie-Françoise, Geneviève and Patrick for all their administrative support.

On a more personal note, I would like to thank all the other students who I had the chance to meet at Cemef. Special thanks to my office colleagues, Michel and Steffen, for all the time we spent together supporting each other and having fun. My thanks also to Olivier, Ana-Laura, Yuan, Brian, Ugo, Ziad and Christophe for all the nice moments we shared together.

Last but not least, I want to thank Laura who has indefectibly supported me during all these years.

Contents

Introduction

Inhomogeneous grain growth

The aeronautic industry is always pushing higher the quality requirements of the materials used to manufacture aircrafts. Superalloys are commonly employed to produce critical parts of the aircraft engine where the thermomechanical conditions in service are very severe. Inconel 718 is a nickel based superalloy commonly used to manufacture the rotating disks of the engines. Such disks are generally produced by hot forging which involves a sequence of different deformation and annealing steps. For example, Figure 1 illustrates a common sequence to produce a ring from

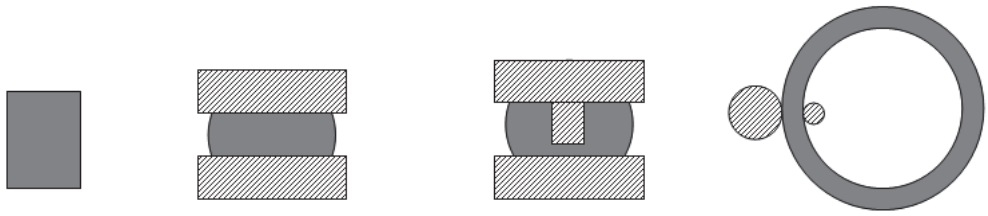

Figure 1: General scheme of forming steps to produce a ring. From left to right: initial billet, compression, hole punching, rolling [adapted from www.scotforge.com].

a cylindrical billet. It is to note that generally each forming step is executed on a different machine, so it is necessary to cool down the piece to room temperature and then to heat it again before the next step. The goal of hot forging is not only to shape the material but also to increase its mechanical properties by tailoring the features of its microstructure. In fact, during hot forging the microstructure evolves continuously via recovery, recrystallization and grain growth phenomena. A critical microstructural parameter that governs mechanical properties is grain size. Generally speaking, for turbine disk applications an homogeneous average grain size of about 10 μm is required in all the piece to comply with quality standards. It is to note that the homogeneity of the grain size in the piece is a critical microstructural parameter. Indeed, heterogeneous microstructures decrease the fatigue resistance of the material [1, 2, 3]. As an example, Figure 2 proves that the average fatigue resistance of a fine (15 μm) microstructure containing few bigger grains (160 μm) is almost the same as that of a conventional coarse (30 μm) microstructure. In particular, the percentage of samples that undergo failure at low cycles (that is the most important feature) is the same for the two microstructures. In other words, the possible increase in fatigue resistance due to a finer microstructure is lost due to heterogeneity of grain size.

During hot forging of Inconel 718 turbine disks, homogeneous microstructures of 10 μm average grain size can be obtained by means of dynamic recrystallization during deformation steps provided that the strain is high enough. However, during each an-

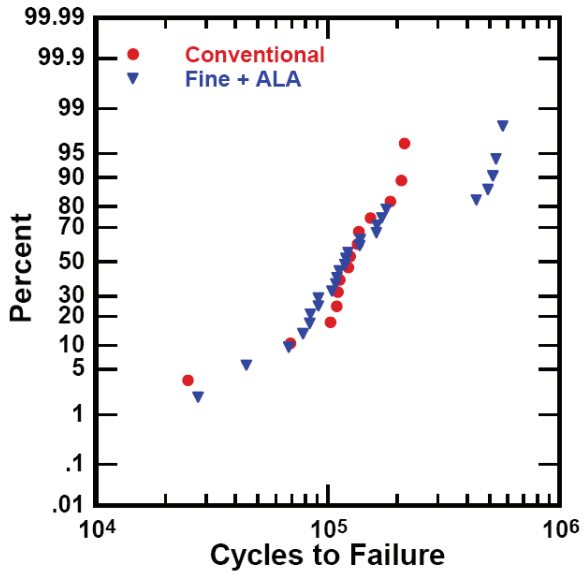

Figure 2: Effect of grain size distribution on fatigue life resistance in Waspaloy: percentage of sample failure as function of cycle number [1].

nealing step following deformation such fine microstructures can coarsen as a function of temperature and time. Hence, the choice of the annealing temperature is of great importance and it is directly linked to the solution temperature (T_δ=1000-1030°C) of the δ phase particles present in Inconel 718. During a δ super-solvus annealing, the temperature is higher than T_δ leading to the dissolution of the particles. As a result, grains can significantly grow driven by the capillarity force (i.e. the reduction of grain boundary energy) depending on the total time of the heat treatment or possibly by strain stored energy reduction depending on the initial metallurgical state. On the contrary, during a δ sub-solvus annealing the temperature is lower than T_δ, then δ phase particles are stable and they usually limit grain growth driven by capillarity forces via the Smith-Zener pinning phenomenon [4]. However, heterogeneity in terms of δ phase particles distribution, hardening or even texture may be present in the material and they can significantly influence the microstructure evolution during sub-solvus annealing, leading to inhomogeneous grain growth. In the worst scenario, this phenomenon can trigger the growth of grains ten times bigger than the initial ones, as illustrated in Figure 3. An interesting aspect linked to inhomogeneous grain growth concerns the microstructural features of the overgrown grains as revealed by optical microscopy observations. As it is shown in Figure 4, it is possible to detect three specific properties of overgrown grains:

- grain boundaries are missing (or they are poorly contrasted),
- twin density is high,
- intragranular δ phase are present.

The objective of this PhD work, funded by the Snecma company, is to understand

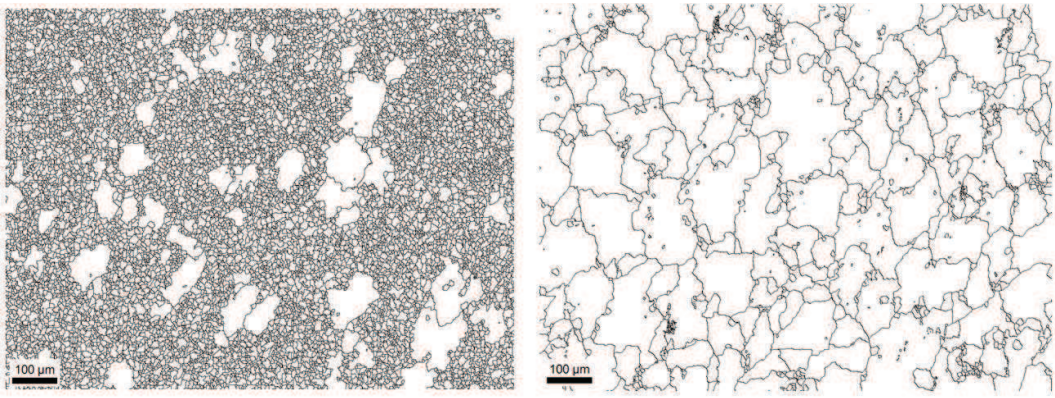

(a) (b)

Figure 3: Evolution of inhomogeneous grain structure after 1h (a) and 2h (b) of sub-solvus annealing in a Inconel 718 forged piece. EBSD maps showing only grain boundaries (twins excluded).

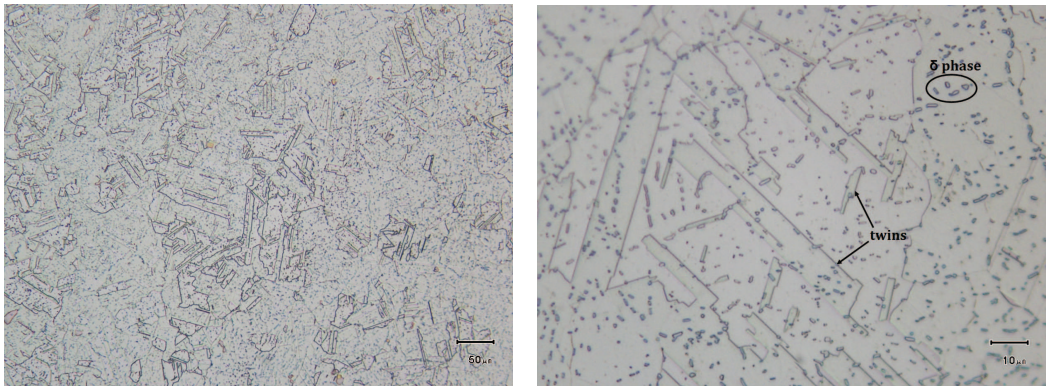

(a) (b)

Figure 4: Microstructural properties of overgrown grains (80 μm) detected by optical microscopy at low (a) and high (b) magnification.

and then model numerically the phenomenon of inhomogeneous grain growth which occurs during hot forging of Inconel 718 turbine disks. The physical mechanisms which may explain the occurrence of the phenomenon are investigated experimentally by performing scanning electron microscopy (SEM) and electron back-scattered diffraction (EBSD) analyses of Inconel 718 industrial pieces. Moreover, thermomechanical tests are carried out to study and reproduce the phenomenon. Then, the validity of the postulated mechanisms is assessed by modelling numerically the phenomenon. This requires the use of a mesoscopic model that may describe at the scale of a representative volume element (RVE) the abnormal grain growth phenomenon. Notably, the model must be able to take into account Smith-Zener pinning and the presence of a strain stored-energy distribution in the microstructure, as well as the capillarity effect.

Layout of the thesis

The work of this thesis is organized in five chapters. The first two chapters lay down the theoretical and experimental background that support this work. The last three chapters present and discuss the results of all the analyses and simulations performed to investigate the subject of this thesis.

Chapter 1 first introduces the phenomenon of Smith-Zener pinning by reviewing the analytical models that have been proposed in the literature during the last six decades. The numerical models of Smith-Zener pinning are presented focusing on the assumptions and limitations of each approach. Secondly, the phenomenon of abnormal grain growth is presented and its possible origins are discussed. The occurrence of abnormal grain growth in nickel base alloys is reviewed.

Chapter 2 begins with a concise description of the main microstructural properties of Inconel 178. Then, the experimental and analytical techniques employed in this work are presented: secondary electrons microscopy (SEM), energy dispersive spectroscopy (EDS), electron back-scattered diffraction (EBSD). The procedures for quantitative microstructure analysis and for evaluating the amplitude of the forces acting on grain boundaries are detailed.

In chapter 3, two industrial case studies of inhomogeneous grain growth are presented. The analysis of the microstructures of industrial pieces where the phenomenon occurs during δ sub-solvus annealing allows to tackle down the physical mechanisms that are involved. An explanation for the occurrence of inhomogeneous grain growth in the industrial pieces is proposed.

In chapter 4 the stability of several microstructures during δ sub-solvus annealing is investigated. Mechanical tests (hot torsion and compression) are exploited to generate microstructures with specific properties and to study the effect of thermomechanical parameters. The hypotheses raised for the postulated mechanism of inhomogeneous grain growth are tested. These results are compared with the ones obtained on the industrial pieces.

Chapter 5 begins describing the microstructure evolution model based on a level set description of interfaces. Then, 2D simulation results show the capability to take into account Smith-Zener pinning. The addition of strain stored energy in 2D Smith-Zener pinning simulations allows to study the occurrence of inhomogeneous grain growth in pinned systems.

Oral and written communications

The work of this thesis has contributed to the following written communications:

- Agnoli, A., Bernacki, M., Logé, R., Franchet, J.-M., Laigo, J. and Bozzolo, N. (2012) *Understanding and Modeling of Grain Boundary Pinning in Inconel 718*, in Proceedings of Superalloys 2012, John Wiley & Sons, Inc., Hoboken, NJ, USA.
- Bozzolo, N., Agnoli, A., Souaï, N., Bernacki, M., Logé, R. (2013) *Strain assisted abnormal grain growth in nickel base superalloys*, in Proceedings of ReX&GG V 2013, Materials Science Forum 753, 321-324.

And the following oral communications:

- Agnoli, A., Bozzolo, N., Bernacki, M., Logé, R. (2013) *A Zener pinning model based on a level set method*, in ReX&GG V 2013, 5-10 May 2013, Sydney.
- Bernacki, M., Agnoli, A., Bozzolo, N., Logé, R. (2012) *Modelling Zener pinning with a full field method based on a level set framework*, in ECCOMAS 2012, 10-14 September, Vienna.

1 Smith-Zener pinning models and abnormal grain growth

Contents

This chapter reviews the phenomena that may be involved in the case of inhomogeneous grain growth of this study. First of all, Smith-Zener pinning is introduced as it governs the stability during annealing of a microstructure containing second-phase particles (δ phase particles in the case of Inconel 718). It is shown that both analytical and numerical models still rely on several assumptions concerning the particle-grain boundary interaction that may influence inhomogeneous grain growth (i.e. particle morphology, anisotropic interfacial energies). Then, the main origins of abnormal grain growth are reviewed. If the capillarity force is the only driving force for boundary migration, then the phenomenon can be triggered when few grains enjoy a certain growing advantage over their neighbors (size, grain boundary mobility or energy). However, even critical strains can trigger the phenomenon. This last case seems to be the main cause of abnormal grain growth in superalloys.

1.1 Smith-Zener pinning analytical models

The Smith-Zener equation, commonly known as the Zener equation, is an analytical relation that links the average radius of grains $\overline{R}$ of a microstructure with the average radius $\overline{r}$ and volume fraction f of the secondary-phase particles. More precisely, the equation gives the stationary value of average grain size that is achieved when normal grain growth is completely inhibited by the pinning pressure exerted by particles. The most general form of the Smith-Zener equation is [5]:

$$\overline{R} = K\frac{\overline{r}}{f^m}, \tag{1.1}$$

where K and m are two parameters that fluctuate according to the assumptions that are made to obtain the equation. Table 1.1 summarizes different values of these coefficients determined by several authors who have considered different plausible hypotheses concerning the Smith-Zener pinning phenomenon.

References	K	m	Remarks
Zener-Smith (1948)	4/3	1	
Gladman (1996)	$\frac{\pi}{6}\left(\frac{3}{2}-\frac{2}{Z}\right)$	1	$\sqrt{2}\leq Z\leq 2$
Hellman-Hillert (1975)	4/9	1	
Anand-Gurland (1975)		1/2	most particles are located on grain-boundaries
Hellman-Hillert (1975)		1/3	most particles are located at grain corners

Table 1.1: Evaluation of coefficients m and K according to different authors: Z is a parameter relating to the initial grain size heterogeneity [6].

A comprehensive review of the original Smith-Zener model and of all its modifications during the following five decades is available here [5]. Historically, it first appeared in a work published by Smith [7], who acknowledged Zener for the main ideas behind the model. For this reason, Eq.(1.1) eventually became known as the Zener equation. In the original model, Smith considered the force balance for the interaction of a spherical particle with a grain boundary, as shown in Figure 1.1(a). The assumptions of the Smith-Zener model were:

1. particles are spherical (constant radius r) and incoherent with the matrix,
2. the surface tension between grains and particles is isotropic (γ_P^1 equals γ_P^2),
3. grain boundaries (GB) are not deformed macroscopically by particles,
4. each particle exerts the maximum restraining force (see Eq.(1.3)) at the same time,
5. the number density of particles on the boundary is that expected for a random distribution of particles (see Figure 1.1(b)).

Under the above assumptions and the notation of Figure 1.1, the pinning term exerted by a single particle on the grain boundary can be easily obtained. Indeed, this force can be expressed as the product of the total line of boundary in contact (equal to $2\pi r cos\theta$) by the vertical component of the surface tension (equal to $\gamma sin\theta$). Thus, the pinning force can be expressed as:

$$F = 2\pi r\gamma sin\theta cos\theta = \pi r\gamma sin2\theta, \tag{1.2}$$

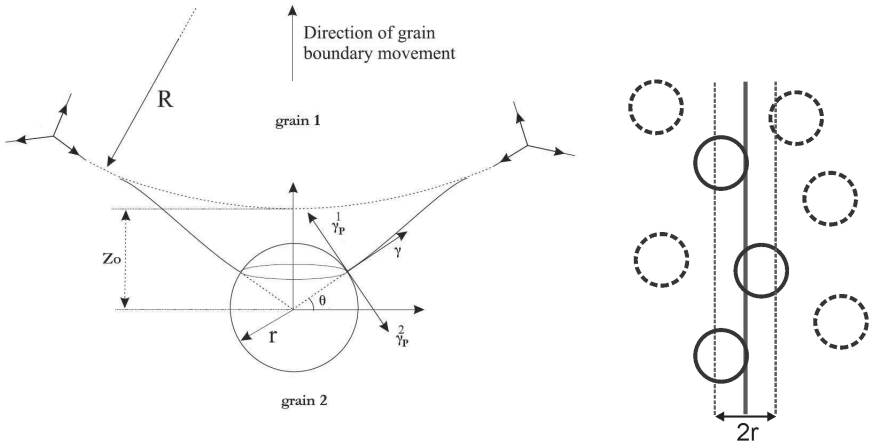

(a) (b)

Figure 1.1: Smith-Zener model geometry [8].

where γ is the surface tension at the grain boundary and θ is the bypass angle. It is to note that the force does not depend on γ_P^1 and γ_P^2 since these two components of the surface tension cancel each other as a consequence of hypothesis (2) in the Smith-Zener model. The maximum value of the force is attained when $\theta = 45°$, i.e.:

$$F_P = \pi r \gamma. \tag{1.3}$$

The number of particles per unit volume is given by $n = \frac{3f}{4\pi r^3}$, where f is the volume fraction of particles. The number of particles per unit area of GB is given by considering only a slice of thickness $2r$ centered on the GB (see Figure 1.1(b)):

$$n_{GB} = n \cdot 2r = \frac{3f}{2\pi r^2}. \tag{1.4}$$

Then, the resulting pinning pressure is equal to:

$$P_P = F_P \cdot n_{GB} = \frac{3\gamma f}{2r}. \tag{1.5}$$

The driving pressure for grain growth is $P_G = \gamma k$, where k is the mean curvature in the sense of fluid mechanics (i.e. equal to the sum of the two principal curvatures). For a spherical grain of radius R, $k = \frac{1}{R} + \frac{1}{R} = \frac{2}{R}$, then:

$$P_G = \frac{2\gamma}{R}. \tag{1.6}$$

At the steady state, the pinning pressure is equal to the driving pressure, so this gives:

$$P_P = P_G \rightarrow R = \frac{4r}{3f}, \tag{1.7}$$

which is the well-known Smith-Zener equation shown on the first line of Table 1.1.

It is interesting to extend the previous reasoning to the case of coherent particles, i.e. when assumption (2) of the Smith-Zener model is no longer considered. In this case, by considering the notation of Figure 1.2, a force balance allows to obtain the following equation:

$$\sin(\alpha) = \frac{\gamma_P^2 - \gamma_P^1}{\gamma}. \tag{1.8}$$

Moreover, following the same principle than for Eq.(1.2), in this case the pinning force is given by:

$$F = 2\pi r\gamma cos\theta sin(\theta + \alpha). \tag{1.9}$$

This force can be rewritten as $\pi r\gamma(sin(2\theta + \alpha) + sin(\alpha))$which leads, thanks to Eq.(1.8), to a maximum value of the force attained when $\theta = 45° - \frac{\alpha}{2}$ and equals to:

$$F_P = \pi r\gamma(1 + \frac{\gamma_P^2 - \gamma_P^1}{\gamma}). \tag{1.10}$$

Following the same steps leading from Eq.(1.4) to Eq.(1.7), in the context of coherent particles it results:

$$P_P = \frac{3\gamma f}{2r}(1 + \frac{\gamma_P^2 - \gamma_P^1}{\gamma}),\ R = \frac{4r\gamma}{3f(\gamma + \gamma_P^2 - \gamma_P^1)}. \tag{1.11}$$

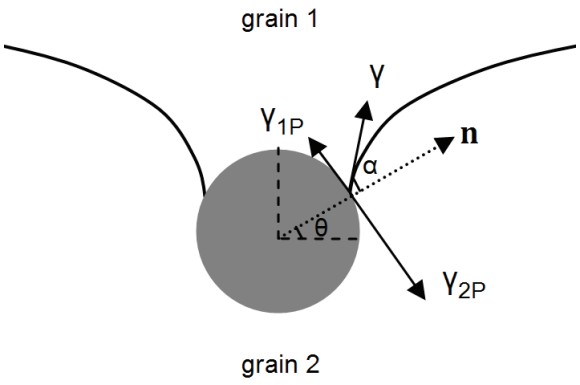

Figure 1.2: Smith-Zener model geometry in the case of coherent particles.

An interesting confrontation between the classical Smith-Zener pinning model and some experimental data was presented in [5] and summarized in Figure 1.3. The figure illustrates that, if the volume fraction of particles is less than roughly 5%, then experimental data can be fitted with the line for K=0.17 and m=1. However, values of K up to K=0.33 can also be found in literature [9]. This means that the original Smith-Zener equation (*K=1.33)* significantly overestimates the average value of grain size, but anyway it describes correctly the proportionality between R/r and f (m=1).

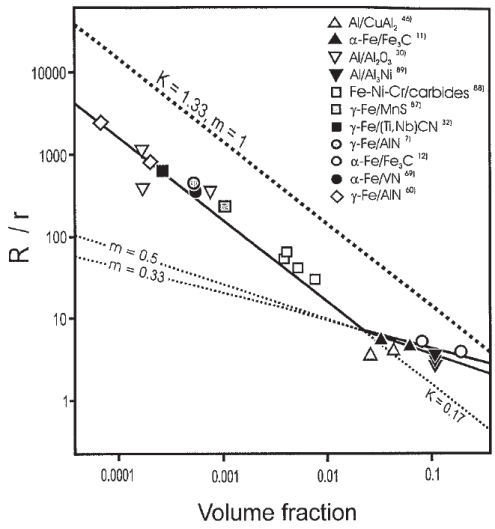

Figure 1.3: Relation between $\overline{R}/\overline{r}$ and f as defined in Eq.(1.1) from experimental data. [5]

There is global agreement [5] that the overestimation of grain size in the Smith-Zener model is a direct consequence of the overestimation of the driving pressure (Eq.(1.6)) and the underestimation of the pinning pressure (Eq.(1.5)), which is calculated for randomly distributed spherical particles. In fact, in real microstructures, particles have often plate- or needle-like shapes that can increase significantly the value of the maximum pinning force. Moreover, if particles are coherent with the matrix the pinning force can increase as well as shown in Eq.(1.10). If the fraction of particles is higher than 5%, then the deviation of the Smith-Zener equation from experimental data becomes more important (m=0.33) and can be explained by the fact that the random distribution of particles assumption is no longer verified. For example, particles are usually found mostly on grain boundaries as precipitation is easier. Indeed, the effect of prior deformation or the particular conditions under which particles have been formed can greatly affect the distribution of the particles in the microstructure.

1.2 Smith-Zener pinning numerical models

In literature, the most widely used numerical models to simulate the pinning effect of secondary-phase particles fall under three categories:

- Monte Carlo method,
- phase-field method,
- boundary-tracking approach.

Monte Carlo models, which were the first to be developed, and phase-field models, which have gained more attention in the last years, are able to simulate both the

2D and 3D Smith-Zener pinning phenomenon. On the contrary, boundary-tracking models are still limited to 2D simulations (vertex method) or 3D simulation of the interaction of a single grain boundary with particles (finite-element method). As it will be detailed in the following, each model has its own advantages and drawbacks as a consequence of its inherent assumptions.

1.2.1 Monte Carlo method

In Monte Carlo (Potts) simulations [10], which are based on probabilistic laws, the microstructure of a material is divided into a number of discrete cells (called pixels in 2D and voxel in 3D) which are arranged on a regular lattice; at each cell is associated an index corresponding to a grain orientation. Then, the model is run by selecting a cell at random and reorienting it to one of the adjacent grain orientations. The overall energy of the new system state is calculated and if the change of energy (ΔE) is negative, then the transition is accepted; otherwise, the reorientation may be accepted with a probability law. Different probability laws were proposed in the literature but the most famous one remains the formulation:

$$P(\triangle E) = \exp(\frac{-\Delta E}{kT}), \tag{1.12}$$

where the term kT has no direct physical meaning but it represents a thermal energy constant of the simulation, analogous to the physical thermal energy of the system.

The presence of particles can be introduced in the Monte Carlo simulation by assigning to several individual cells different indeces to any of the matrix cells and these sites are not allowed to switch orientation during the simulation [11]. Then, as the total energy of the configuration when a particle is on the grain boundary (Figure 1.4b) is lower compared to the situation when it is within a grain (Figure 1.4a), the resulting attraction between particles and grain boundaries hinder the movement of the boundaries.

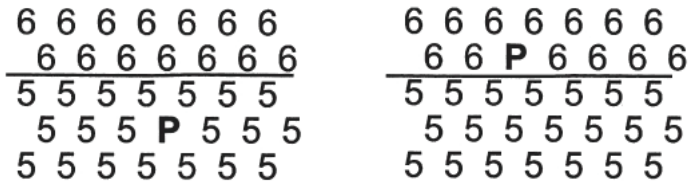

(a) (b)

Figure 1.4: Interaction of a grain boundary and a secondary-phase particle in the Monte Carlo model [9].

The first Monte Carlo 2D simulations of Smith-Zener pinning date from the eighties thanks to the work of Srolovitz [12]. The results of the simulations yielded values for the parameter m of Eq.(1.1) different from unity ($m < 0.5$): this was due to the fact that a particle in a 2D microstructure is equivalent to a fiber in a 3D microstructure

and so pinning forces are overestimated. Also successive 3D simulations yielded values of m different from unity. However, it was shown that this result is only the consequence of the artificial facetting of grain boundaries that is induced during the simulation [13]. Finally a large scale (about 10^7 voxels) 3D simulation where grain boundaries facetting could be inhibited [14] confirmed the value $m = 1$ as in the original Smith-Zener model, while $K = 0.73$ for a particle volume fraction lower than 10%.

Overall, Monte Carlo models allow to easily and successfully implement 3D simulations of Smith-Zener pinning, without making assumptions on the distribution of the particles or the shape of grains. However, up to now models still incorporate hypothesis (1) and (2) of the Smith-Zener model and only a small range of sizes and volume fractions of particles were considered. Other more general drawbacks of Monte Carlo models concern the questionable validity of the probabilistic laws employed to describe the phenomenon and the problematic introduction of the time scale, which is not transparent in the models.

1.2.2 Phase-field method

Recently, the phase-field model was developed for simulating microstructure evolution, like grain growth [15]. In this model a set of phase variables $\eta_{1,..,}\eta_P$ is used to represent the microstructure of a polycrystal: each variable is a continuous function of space and time. A grain G_i is identified by the variable $\eta_i = 1$ inside the grain while all other phase field variables equal zero; at the grain boundary between η_i and η_j, these two variables vary continuously between 1 and 0. The total free energy of the system at a given instant t is built as a function of all the phase variables: $F = f(\eta_{1,...,}\eta_P)$. It is to note that the specific form for F depends both on considerations of computational efficiency and the physics governing the phenomenon under study. The temporal evolution of each phase field variable is described by the time-dependent Ginzburg-Landau equation:

$$\frac{\partial \eta_i}{\partial t} = -L_i \frac{\partial F}{\partial \eta_i}, \ \forall i \epsilon \{1, ..., P\}, \tag{1.13}$$

where L_i is the kinetic coefficient related to the grain boundary mobility. The coupled set of Eq.(1.13) for $i = 1...P$ can then be discretized and solved numerically at each site of a grid or a finite element mesh spanning the simulation lattice.

The presence of secondary-phase particles can be implemented in the model by introducing an additional space-dependent energy term in the total free energy of the system [8]. This additional energy term is built so that the energy difference induced by a particle placed on a grain boundary is equal to the intersection area multiplied by the surface tension. For a spherical particle that is "cut" in half by a grain boundary, the energy difference is then $\pi r^2 \gamma$, where r is the particle radius and γ is the surface tension at the grain boundary. (see Figure 1.5).

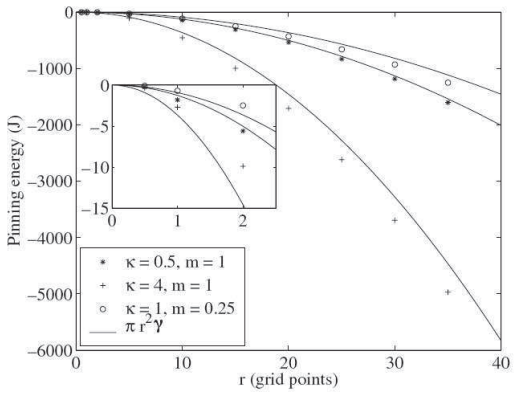

Figure 1.5: Pinning energy of a spherical particle as a function of particle radius (r) and numerical parameters (k,m) defined in the phase-field model [8].

Several 3D phase-field simulations of Smith-Zener pinning [16, 17] yielded values for m in Eq.(1.1) close to unity, in accordance both with the original Smith-Zener model and Monte Carlo simulations. On the contrary, the values for the coefficient K are more dispersed, even though the order of magnitude remains the same. Recently, the effect of spheroid secondary-phase particles characterized by different aspect ratios and sizes has been also studied [17, 18]. Results show that, for the same volume fraction of particles, smaller particles are more effective in pinning grain boundaries. Moreover, needle-shape particles have a stronger pinning effect than spherical ones, even though the difference remains quite limited. However, numerical results still differ from experimental data overestimating the final grain size.

The phase-field model has allowed to simulate in more details the Smith-Zener pinning phenomenon compared to Monte Carlo methods, allowing to study the influence of spheroid particles in the model. However both methods share common drawbacks. Notably, the model still assumes that particles are incoherent and the surface tension between grain and particles is isotropic (γ_P^1 equals γ_P^2). In addition to this, the construction of the energy functions is a delicate task, since it has to be built in such a manner that its minimization pathway yields physically plausible equations of motion for grain boundaries.

1.2.3 Boundary-tracking approaches

In Monte Carlo and phase-field models, local microstructural evolutions have to be calculated as a minimization of the free energy of the overall system. An alternative approach, that can be classified as "Boundary tracking", consists in solving numerically the local equations of motion for a set of points describing the network of grain boundaries in the microstructure. In the following, two different models that employ this approach for modelling Smith-Zener pinning will be presented.

Vertex In vertex models, grain boundaries are discretized into linear segments. Then, microstructure evolution is represented by the movement of the real (triple points) and virtual vertices which are needed for discretizing the grain boundaries. It is to note that there are several ways to derive vertex motion equations from the migration of the adjacent interfaces. In the model proposed by Weygand [19] vertex motion results from the balance between the reduction of the interfacial energy by boundary migration (V) and the dissipation potential due to the viscous force which opposes to the boundary motion (R). Then, the equations of motion for the vertices can be derived from the Lagrange equation:

$$\frac{\partial V}{\partial r_i} + \frac{\partial R}{\partial v_i} = 0, \tag{1.14}$$

where r_i and v_i are respectively the position and the velocity of the vertex i. Then, by using Eq.(1.14) for *i=1,...,N* (total number of vertices), a system of coupled equations is derived from which the velocity of each vertex is calculated.

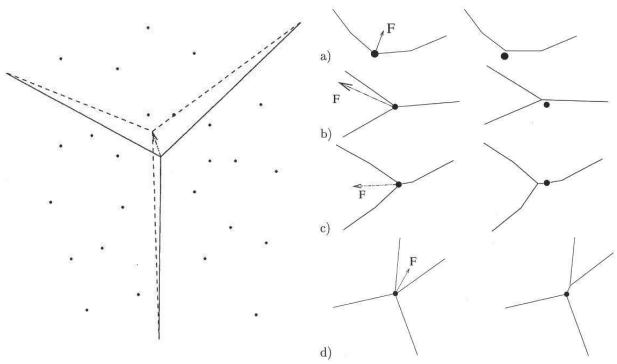

(a) (b)

Figure 1.6: Interaction of a grain boundary and secondary-phase particle in the vertex approach [20].

The presence of particles can be simulated by introducing in the model some "pinning centers", which are a new kind of vertex characterized by the maximum force (F_{MAX}) they can sustain*:* F_{MAX} is a function of a critical unpinning angle which is imposed arbitrarily [20]. When grain boundaries sweep an area which contains particles, the final position is chosen such that at most one particle is present in the triangular area swept (Figure 1.6a). Then, the conditions for unpinning are tested: in the simplest situation, if the force acting on the particle is higher than F_{MAX}, then grain boundary unpins. However, different rules are applied depending on the position of the particle on grain boundaries (Figure 1.6b). Simulations have shown that if the overall pinning force of particles (F_{MAX}) is increased, then the final grain size distribution shifts from a log-normal one to a normal one. Moreover, the number of particles effectively acting as pinning centers is inversely proportional to F_{MAX}.

Compared with other 2D simulations for Smith-Zener pinning, the Vertex model

is a very computational efficient and flexible method in which many new parameters can be easily introduced and varied. For example, the effect of different particles sizes or shapes can be studied by assigning to the pinning centers different values of F_{MAX}. Nonetheless, it remains questionable if the simulation of particles effects, simply introduced in the model as a new kind of vertex, can be really representative of real microstructures where the interaction between particles and grain boundaries can assume very complex configurations. Finally, another more general drawback of the vertex method is the difficulty to solve topological transformations in 3D, which are inherently handled in phase-field models, for example. As a result, up to now there are no 3D vertex simulations of Smith-Zener pinning.

Finite-element method Ten years ago, a finite-element method for modelling the interaction of a single moving planar grain boundary with several particles has been developed by Couturier et al. [21, 22]. The model, as in the case of Vertex simulations, is based on the principle that during boundary motion the excess of surface energy is entirely dissipated by viscous friction. Then, if a grain boundary is meshed with N nodes, the following variational formulation can be derived:

$$\sum_{i=1}^{N}(\frac{\partial V}{\partial r_i} + \frac{\partial R}{\partial v_i}) \cdot \delta v_i = 0, \tag{1.15}$$

where the notation is the same as in Eq.(1.14). The application of a finite-element approximation to Eq.(1.15) gives the instantaneous velocities of any node i. The interaction between the grain boundary and a particle is handled by applying kinematic conditions to the boundary nodes in contact with the particle so that their velocity remains tangential to a meridian of the particle.

Under certain assumptions on the grain geometry evolution during grain growth, it is possible to extend the results yielded from this single grain boundary model to obtain information on the behavior of a polycrystal. The evolution of the limiting grain size and the particle density is shown in Figure 1.7a. The plot shows that the value of m in Eq.(1.1) equals unity, in accordance with the results displayed in Figure 1.3. Moreover, the analysis of the configurations at steady state (see Figure 1.7b) has demonstrated that the effective pinning force of particles is almost 2 times smaller compared to the value proposed by Smith-Zener in Eq.(1.3). Then, the total pinning pressure of Eq.(1.5) underestimates the true dragging stress by a factor of about 2.

Compared to previous approaches, the finite-element model of Smith-Zener pinning allows to simulate the phenomenon in more details and on a more physically meaningful basis since the particle-grain boundary interaction is treated as a geometrical constraint to movement. Nonetheless, up to now simulations are limited to spherical particles and do not consider the surface tension between grains and

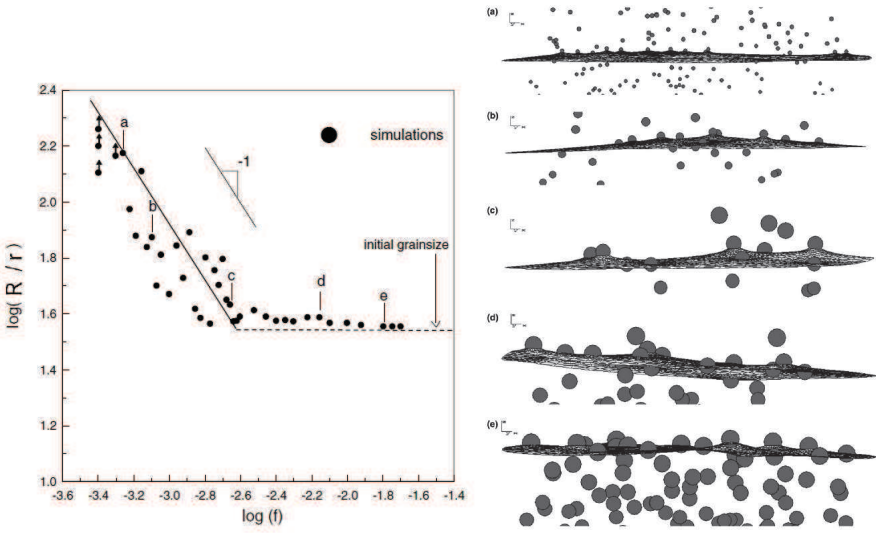

(a) (b)

Figure 1.7: Smith-Zener pinning in the finite-element model: (a) Evolution of limiting grain size (R) as a function of particle fraction (f) from simulation; (b) Steady state configurations corresponding to the points indicated by a letter in the plot on the left [22].

particles. Moreover, since the surface of grain boundaries is assumed to be planar with respect to particles, simulations are valid only if the ratio R/r (see Eq.(1.1)) is very important. Finally, as for Vertex models, the implementation of a full 3D simulations of a realistic polycrystal appears to be quite challenging due to the difficult treatment of topological transformations due to the explicit description of interfaces.

Overall, while all methods can effectively simulate Smith-Zener pinning in the simple case of spherical particles, there is not yet a model that can deal with particles with a more complex shape than a spheroid one. Moreover, particles were always considered to be incoherent with the matrix. These aspects can be regarded as the main limitations of all the methods reviewed above and could explain why, up to now, all numerical results concerning the limiting grain size differ from experimental data.

1.3 Abnormal grain growth

During normal grain growth the microstructure coarsens uniformly as a continuous process. In other words, while the average grain size increases, the grain size histogram remains monodispersed. On the contrary, during abnormal grain growth few grains grow much faster than the average grain, leading to a bimodal grain size and eventually to a single population of very coarse grains. Such process is discontinuous and its kinetics is similar to that of primary recrystallization. Hence, abnormal grain growth is also called secondary recrystallization [9].

If the only driving force of the phenomenon is the capillarity force, then the abnor-

mal grains must have some kind of growing advantage over their neighbors. If the phenomenon is triggered by critical stored energy distributions, then abnormal grains have usually lower stored energies compared to neighbors. In this case it remains questionable if the phenomenon should be described as a particular case of abnormal grain growth induced by strain energy or a particular case of recrystallization without nucleation of new grains. In this work, the former alternative is chosen.

1.3.1 Grain size, grain boundary mobility and energy advantages

Abnormal grain growth (driven only by capillarity) can occur when normal grain growth is inhibited (by the presence of particles) and/or certain grains enjoy some growing advantage over their neighbors, like:

1. bigger size,
2. higher boundary mobility,
3. lower boundary energy.

The effect of these grain parameters on the grain growth velocity can be discussed considering the following mean field model of grain growth developed by Humphreys [9]. The model is based on the energy variation ($\triangle E$) during grain growth of a 3D spherical grain of radius R and boundary energy γ in an assembly of grains of average radius $\overline{R}$ and energy $\overline{\gamma}$. If the grain grows by an amount $\triangle R$, then the energy variation is equal to the reduction of grain boundary energy per unit volume in the neighborhood ($E_v = \frac{3\bar{\gamma}}{2\bar{R}}$) and the increase of interfacial boundary energy of the growing grain:

$$\triangle E = 4\pi\beta R^2 E_v \triangle R - 8\pi\alpha\gamma R \triangle R, \tag{1.16}$$

where α and β are two positive geometrical parameters smaller than unity. The force on the boundary is simply $\triangle E/\triangle R$, then the driving pressure for boundary migration is:

$$P = \frac{1.5\beta\overline{\gamma}}{\overline{R}} - \frac{2\alpha\gamma}{R} \tag{1.17}$$

The presence of particles can be simply introduced by adding the Smith-Zener pressure of Eq.(1.5) in Eq.(1.17). Finally, the growth rate of a grain with boundary mobility M is given by:

$$\frac{dR}{dt} = MP = M(\frac{\bar{\gamma}}{\bar{R}} - \frac{\gamma}{R} - \Psi\frac{\bar{\gamma}}{\bar{R}}), \tag{1.18}$$

where $\alpha = 1/2$, $\beta = 2/3$ and $\Psi = \frac{3f\bar{R}}{2r}$ is a dimensionless parameter that takes into account Smith-Zener pinning, so it depends on the radius (r) and volume fraction (f) of secondary-phase particles. The values for parameters α and β were chosen so that Eq.(1.18) reduces (by removing the pinning term and by setting $\gamma = \overline{\gamma}$) to the same equation obtained by Hillert for the growth of a grain in a 3D assembly [23].

If all grain boundaries have the same mobility and energy, then the average growth rate can be described, based on the analysis made by Hillert [23], as:

$$\frac{d\overline{R}}{dt} = \frac{\overline{M}\overline{\gamma}}{\overline{R}}(\frac{1}{4} - \Psi), \tag{1.19}$$

It is worth noting that when Eq.(1.19) is used to evaluate the limiting grain size of a microstructure in equilibrium with a population of particles, it yields the same relation of Eq.1.1 with K=0.17 and m=1, which is very consistent with experimental data.

Now, if abnormal grain growth is triggered, then the growth rate of the large grain relative to that of the assembly must satisfy the following condition:

$$\frac{d}{dt}(\frac{R}{\bar{R}}) = \frac{1}{\bar{R}^2}(\bar{R}\frac{dR}{dt} - R\frac{d\bar{R}}{dt}) > 0. \tag{1.20}$$

The resolution of Eq.(1.20) yields the conditions, in terms of R, M and γ, under which abnormal grain growth can occur. In particular, for an assembly of grains with equal boundary energies and mobilities, it provides the minimum grain size ratio ($X = {}^{R}/_{\bar{R}}$) required to initiate abnormal grain growth, as shown in Figure 1.8. The plot illustrates that as the pinning term (Ψ) increases, the minimum ratio increases as well, so that for $\Psi > 1$ an infinite grain is required to trigger abnormal growth.

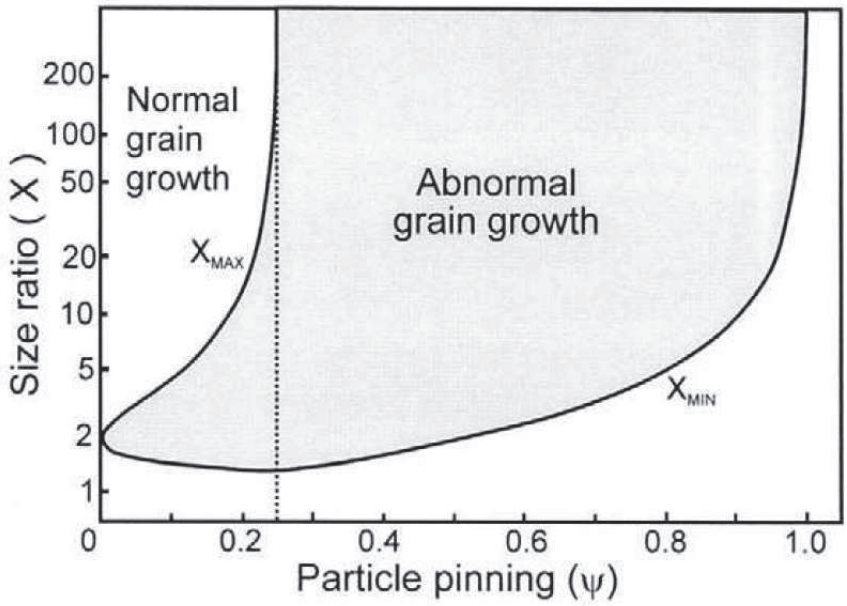

Figure 1.8: Plot of minimum grain size ratio ($X = {}^{R}/_{\bar{R}}$) to trigger abnormal grain growth as a function of the Smith-Zener pinning parameter ($\Psi = \frac{3f\bar{R}}{2r}$) [9].

A typical example of abnormal grain growth triggered by a grain size advantage is shown in Figure 1.9 for the case of steels [9]. Plain carbon steels do not contain pinning particles so annealing at any sufficient temperature just induces normal grain growth. If AlN particles are present, then grain growth is hindered at low temperatures, however between 1050°C and 1150°C particles coarsen and start to dissolve, decreasing the overall pinning force. As a result, certain grains can grow and gain a size advantage leading to abnormal grain growth. Above 1150°C all particles dissolve almost instantly, so all grains can grow.

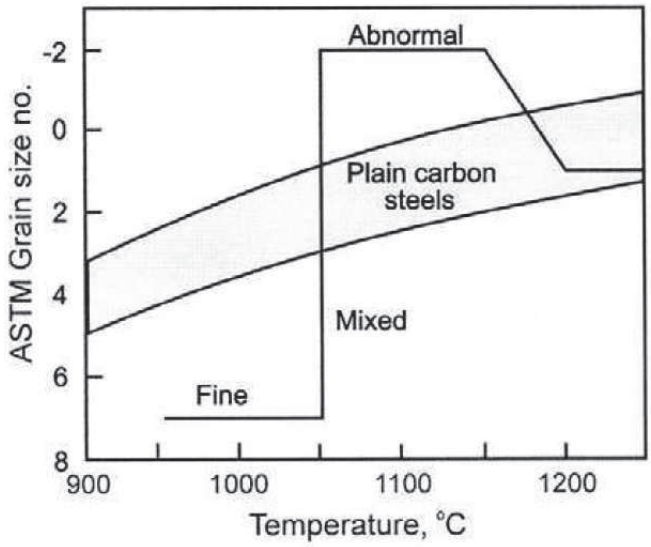

Figure 1.9: Abnormal grain growth occurring in steels at temperatures close to the dissolution of pinning particles [9].

Crystallographic texture may also trigger abnormal grain growth, by modifying the boundary mobility or energy of the grains (the values of M and γ in Eq.(1.18)). For example, the growth of the few grains whose crystallographic orientation is different from the main texture component can be promoted since there is a higher probability for these grains to have high angle grain boundaries, which exhibit higher mobility (M). This phenomenon can occur during annealing of highly textured materials as those obtained by extrusion or rolling processes [24]. Figure 1.10 shows the inverse pole figure of an extruded ODS superalloy where abnormal grain growth occurs during annealing. 90% of grains have an orientation so that a crystallographic direction between <001> and <111> is parallel to the extrusion axis, while only 10% of the grains have a <110> orientation parallel to the extrusion axis.

Texture may also induce the presence of grain boundaries with a particular misorientation leading to a low interfacial energy γ. Such boundaries migrate faster than normal boundaries, provided that they keep the same orientation relationship with respect to other random grains. Also the presence of "complexions" (which are particular configurations of the atomic structure of the interface at grain boundaries)

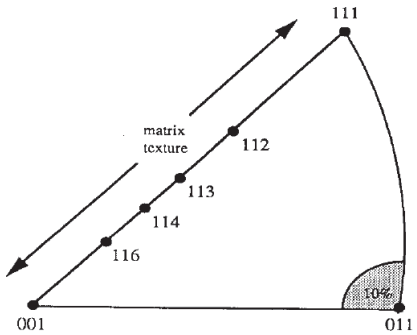

Figure 1.10: Abnormal grain growth occurring in ODS superalloy MA6000 due to texture [25].

can lower the energy of few grain boundaries, triggering abnormal grain growth [26]. As shown in Figure 1.11, 3D Monte Carlo numerical simulations have illustrated that if the energy of at least 20% of the boundaries of a grain is three times lower than the average grain boundary energy, then abnormal grain growth can be triggered [27].

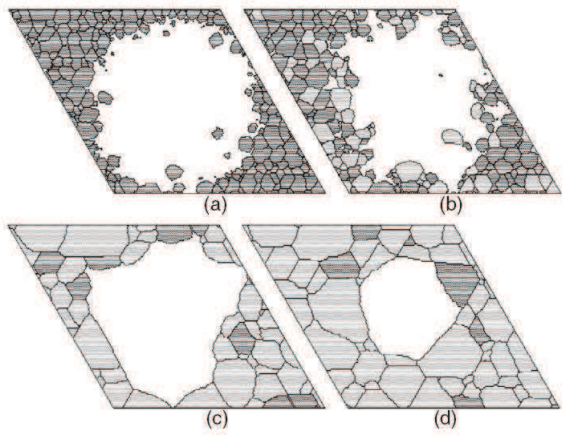

Figure 1.11: Monte Carlo simulation of abnormal grain growth as a function of the percentage of low energy boundaries of the white grain: (a) 100%, (b) 70%, (c) 20%, (d) 10% [27].

1.3.2 Strain-induced abnormal grain growth

Also low strains ($\varepsilon<0.1$) applied at room temperature can induce abnormal grain growth [28, 29, 30] in pure metals. Figure 1.12 describes the influence of small strains (ε=0.02-0.1) applied at room temperature on abnormal grain growth in pure iron. If strain is not applied before annealing, then normal grain growth occurs (bottom plot). However, if strain is applied, abnormal grain growth is triggered: higher strains shorten the time for the onset of the phenomenon and reduce the final grain size. However, it is not clear if the main driving force of the phenomenon is the reduction of strain energy (as in recrystallization) or the capillarity force (in this case

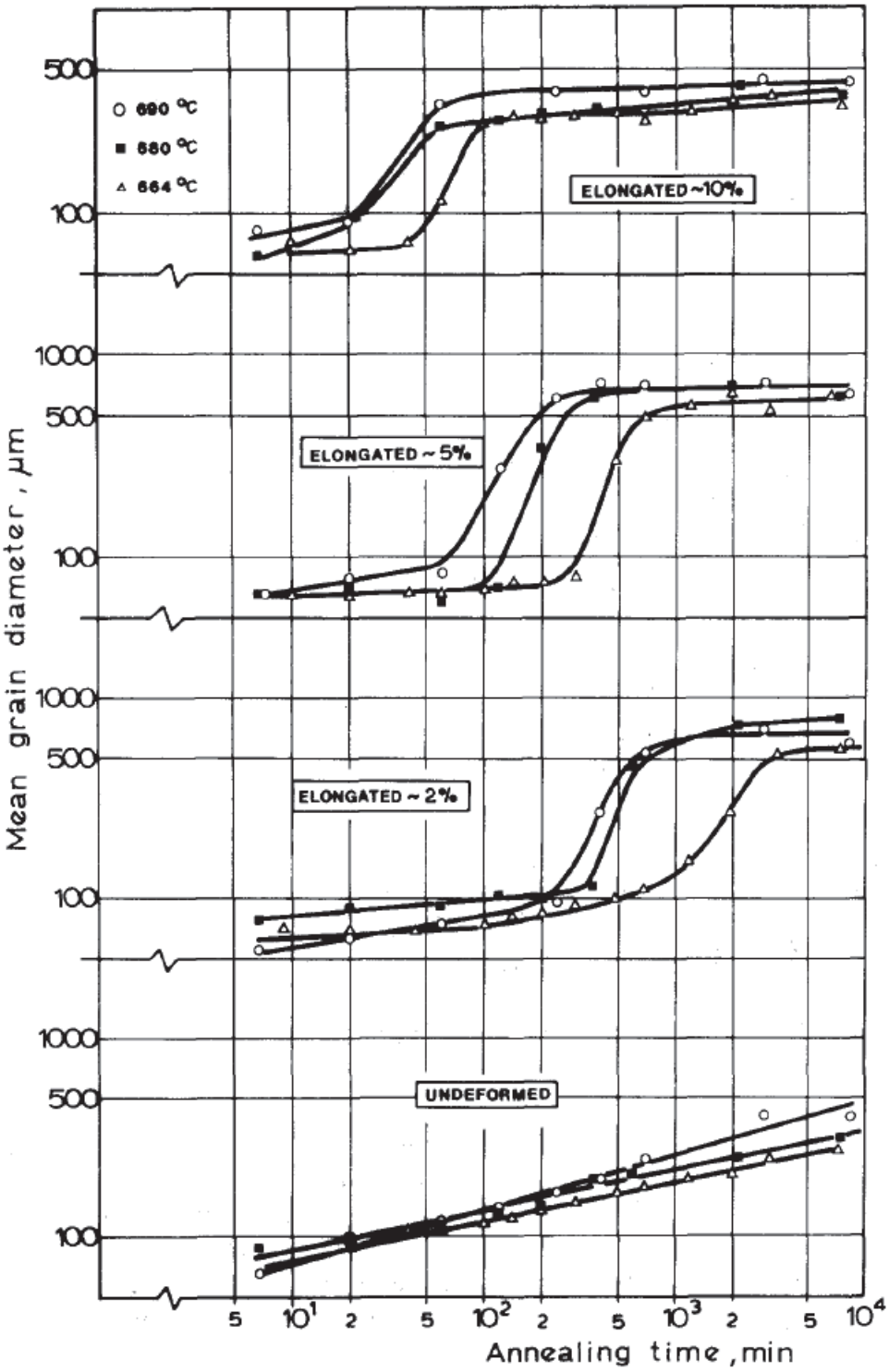

Figure 1.12: Abnormal grain growth in pure iron as a function of annealing temperature (664-690°C) and room temperature strain (ε=0.02-0.1) [30].

strain would modify grain boundary mobility via dislocation generation). The former possibility is supported in [31] where it is shown that abnormal grains in Fe1%Si alloy have lower intragranular misorientation (that is linked with strain stored-energy

as it will be shown in the following chapter) compared to neighboring grains during annealing. Then the effect of small strains is to introduce in microstructures critical distributions of stored energies that trigger the growth of few low energy grains. In [28] the effect of low strains on grain boundary mobility is discussed in a case of abnormal grain growth driven by capillarity in pure copper. In such material, abnormal grain growth is triggered as grain boundaries are faceted, so grain growth driven by capillarity is almost stopped. Only few bigger grains are able to grow, leading eventually to abnormal grain growth after very long annealing times (more than 24 hours). If very small strains ($\varepsilon<0.04$) are applied before annealing (Figure 1.13), then abnormal grain growth occurs after just 1h. If the strain is higher than $\varepsilon=0.04$ but less than $\varepsilon=0.08$ (critical strain for primary recrystallization), then normal grain growth occurs. The explanation, supported by TEM images, for such behavior is that very small strains induce the adsorption of lattice dislocations in grain boundaries ("extrinsic dislocations"), which can increase significantly the mobility of few grain boundaries. However, as strain increases up to $\varepsilon=0.08$ all grain boundaries are influenced by strain, so normal grain growth is triggered. If the strain is higher than $\varepsilon=0.08$, then static recrystallization, involving the nucleation of new grains, takes place.

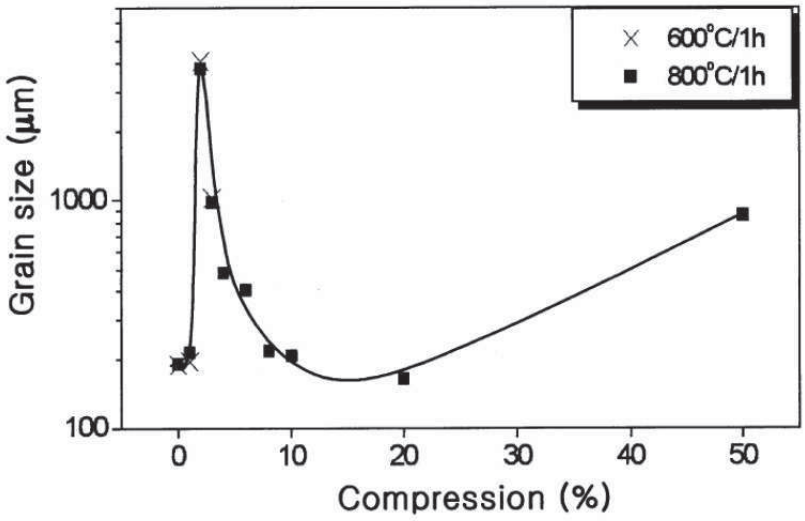

Figure 1.13: Abnormal grain growth in pure copper as a function of room temperature strain [28].

Two general remarks can be made concerning all these studies of strain induced abnormal grain growth. The first one is that the influence of small strains has been investigated only for deformations at room temperature. It would be interesting to know if the same phenomenon is triggered by small deformations at higher temperatures, where recovery can influence the dislocation structure. Secondly, none of the studied materials contains second phase particles. Then, it would be interesting to

investigate the influence of particles on the onset of abnormal grain growth.

Grain boundary engineering It is worth to note here that the microstructural phenomena responsible for strain-induced abnormal grain growth probably share many common points with those involved in "grain boundary engineering". It is recalled here that the idea behind the concept of "grain boundary engineering" is to design thermomechanical processing in order to control the type of grain boundaries present in the material. Generally, the objective is to increase the fraction of "special boundaries" like twin boundaries in face-centered cubic metals such as copper and nickel [32, 33]. Now, several processing routes are proposed in the literature to grain boundary engineer a material: they usually involve a single or iterative sequence of room temperature strain and short annealing steps [34]. One approach involves applying very low strains ($\varepsilon<0.1$) and annealing at high temperature for short times (few minutes), avoiding to trigger primary recrystallization. Microstructure evolution is then driven both by capillarity and stored-energy reduction: under such conditions, nucleation of annealing twins is enhanced [35]. Figure 1.14 shows that small room temperature strains ($\varepsilon<0.07$) increase the fraction of special boundaries in nickel after annealing. However, if primary recrystallization takes place ($\varepsilon=0.25$), then the fraction does not increase. Such results corroborate the idea that indeed there exists a regime of microstructure evolution that falls between simple grain growth (driven by capillarity) and simple recrystallization (driven by stored energy) and that is a function of annealing temperature and time. Such regime can be responsible for abnormal grain growth or it can be exploited to modify the type of grain boundaries present in the material.

1.3.3 Abnormal grain growth in nickel base superalloys

Several industrial patents published by General Electric address the problem of abnormal grain growth occurring during hot forging of nickel base superalloys. It is necessary to precise that all the patents concern the processing of γ' strengthened nickel-base alloys and that abnormal grain growth is termed "critical grain growth". Such phenomenon occurs during annealing above the γ' solvus temperature of "critically " strained materials: either small room temperature strains (Figure 1.15) or hot strain rates. One patent [37] stresses the importance of the control of the strain rate during superplastic forging which must not exceed a critical value ($\dot{\varepsilon} < 10^{-2}s^{-1}$). If the critical value is reached in some zones of the piece, during annealing abnormal grain growth will be triggered as a result of the growth of few recrystallized nuclei or pre-existing grains in the retained strain zones. Another patent [36] describes a hot forging process where the average strain rate is higher than $\dot{\varepsilon} = 10^{-2}s^{-1}$. In this case, in order to avoid abnormal grain growth during annealing, it is necessary to perform the forging by keeping a strain rate higher than a critical value all over the material: this is to ensure that every part of the piece will contain a critical value

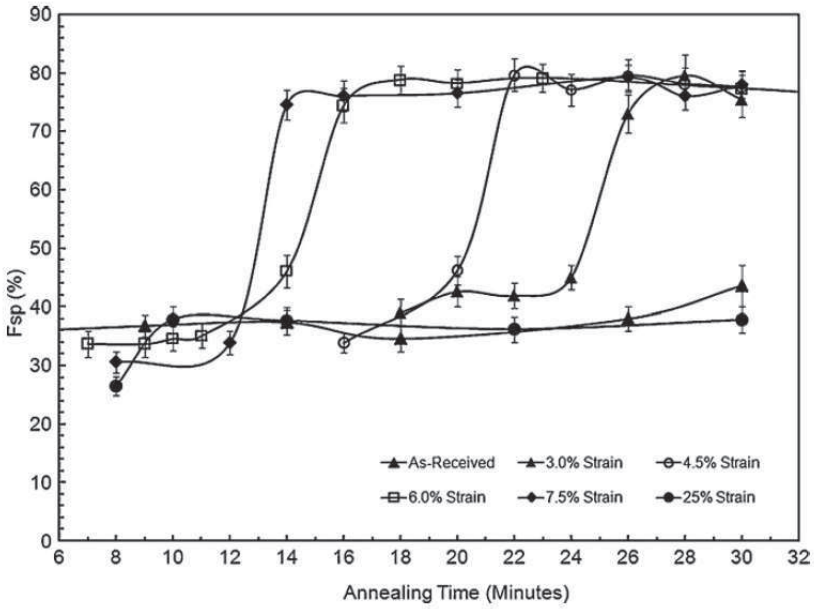

Figure 1.14: Evolution during annealing of the length fraction of "special grain boundaries" (Fsp) in nickel as a function of prior room temperature strain [33].

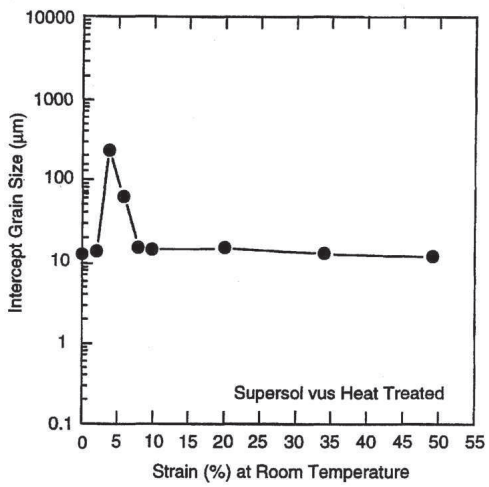

Figure 1.15: Abnormal grain growth occurring during super-solvus annealing of René88DT as a function of room temperature strain [36].

of deformation needed to trigger a uniform nucleation during recrystallization. Such results are consistent with those obtained by [38, 39] linking abnormal grain growth to the transition in behavior from stage 2 (superplastic regime) to stage 3 (normal regime) that occurs at about $\dot{\varepsilon} = 10^{-2}s^{-1}$ as indicated in Figure 1.16. Since the strict control of strain and strain rate inside the piece limits the complexity of the forged component, a different solution is found in [40] to avoid the abnormal grain growth that occurs during annealing above the γ' solvus temperature. In this case the carbon content of the alloy has been increased up to 0.03-0.1% (mass) in order

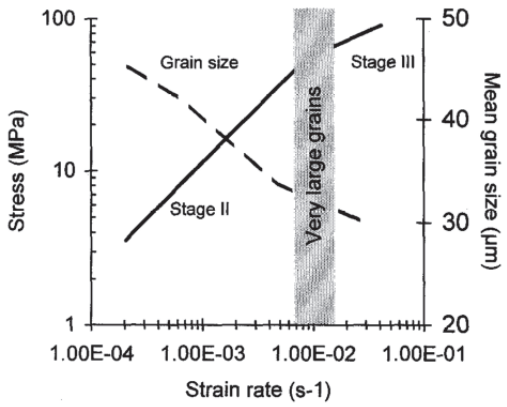

Figure 1.16: Abnormal grain growth occurring during super-solvus annealing of superalloy N18 as a function of strain rate [38].

to promote the precipitation of carbides capable of pinning the grain boundaries and limit grain growth.

An early work of 1956 [41] tried to tackle down the causes of abnormal grain growth during super-solvus annealing in three different nickel-based alloys. The results confirm the link between very small strains ($0.01<\varepsilon<0.05$) and abnormal grains. It is to note that the temperature at which small strains are applied has only a little influence on the phenomenon as seen in Figure 1.17. More precisely, the effect of strain temperature from 26°C up to 1090°C on grain size evolution is quite limited. On the contrary, when the temperature is 1150°C, the maximum grain size is reached at higher strains and it is smaller compared to all other deformation temperatures. Also in René88 superalloy, abnormal grain growth is induced during super-solvus annealing by small critical strains, however the underlying microstructural mechanism are not unanimously recognized. According to the work of Cho et al. [42], grain boundaries are mostly faceted and the effect of small strains is to generate extrinsic dislocations, which can increase significantly the mobility of few grain boundaries. However, according to the PhD work of DeMania [43], dislocations are not responsible for the occurrence of the phenomenon. Instead, dissolution of pinning particles (like carbides, oxides) or properties of the grain boundary network could be possible causes but no evidence is found.

Also dynamic abnormal grain growth, driven by strain-induced grain boundary motion, has been observed in PER®72 [44].

In oxide dispersion-strengthened superalloys, abnormal grain growth during super-solvus annealing is triggered by the grain size advantage of few grains thanks to texture [24], solute drag [45] or dissolution of pinning particles [46] effects.

Inconel 718 Few works investigated abnormal grain growth in Inconel 718. An early work of 1997 [3] studied abnormal grain growth occurring during δ sub-solvus

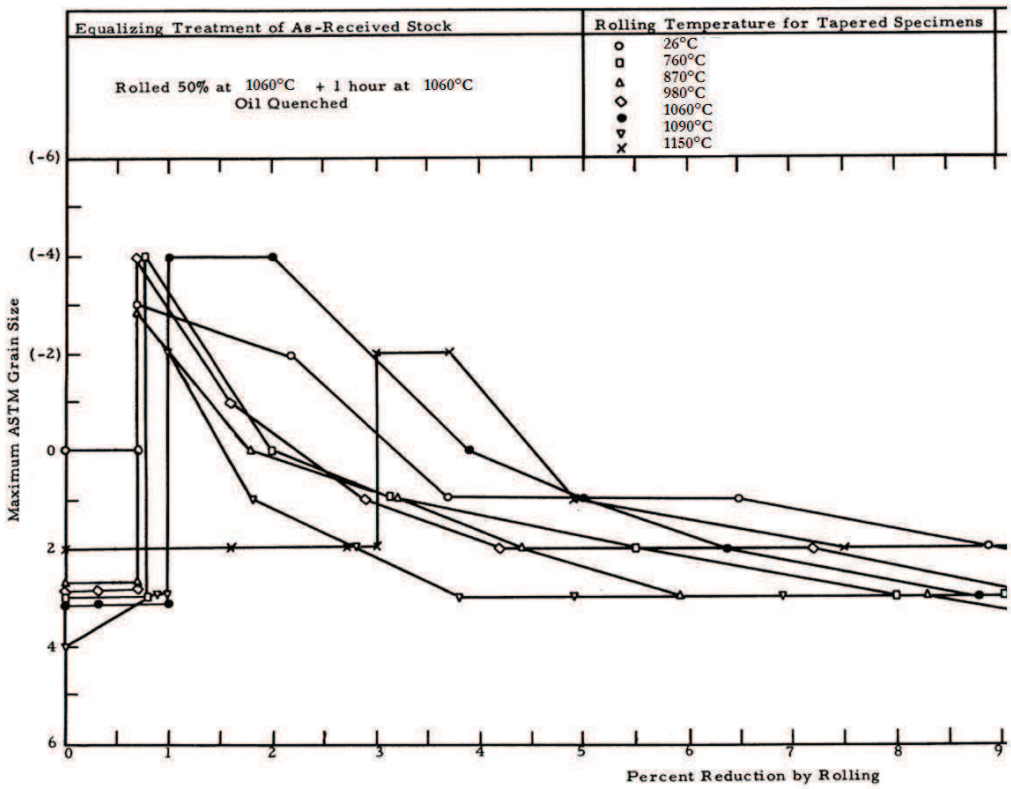

Figure 1.17: Abnormal grain growth occurring during super-solvus annealing of Waspaloy as a function of strain [41].

annealing after hot compression. Indeed, such conditions are very similar to those responsible for abnormal grain growth in this work. Results show that abnormal grains (40-60 μm) appear in a fine grain microstructure (15 μm) when the local deformation is less than ε=0.1, and so despite the high fraction of δ phase particles (about 8% surface fraction). However, the microstructural mechanism leading to abnormal grain growth is not discussed. In a more recent work [2], it is shown that neither texture nor δ phase particle heterogeneity can explain the occurrence of abnormal grains (about 70-100 μm) in industrial forged disks. It is interesting to note that in both works, abnormal grains (see Figure 1.18) share similar microstructural features: high twin density and intragranular δ phase particles.

Overall, abnormal grain growth occuring in Inconel 718 is not yet sufficiently understood. If low strains prior to annealing are likely to be involved in the phenomenon (as shown in the previous section for several superalloys), the mechanism of microstructure evolution remains unclear. Moreover, the thermomechanical conditions leading to abnormal grain growth due to small strains have not been investigated systematically. On the other hand, the role of δ phase particles concerning the occurence of the phenomenon remains ambiguous as it has never been discussed with respect to Smith-Zener pinning models taking into account also the strain stored energy. Finally, no attempts to simulate numerically the phenomenon are reported

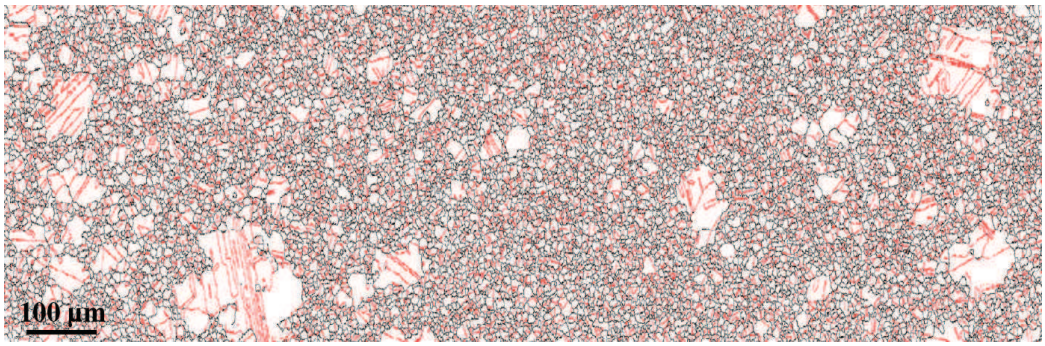

Figure 1.18: Abnormal grains in an industrial forged disk of Inconel 718. Grain boundaries are black and twins are red [2].

in the literature.

1.4 Summary

In this chapter, the two main phenomena that are supposedly involved in the case of inhomogeneous grain growth of this study are discussed.

First of all, the Smith-Zener pinning phenomenon is presented and the limits of its analytical description are discussed. Then, several numerical models of Smith-Zener pinning proposed in the literature are reviewed. Overall, while all numerical methods can simulate Smith-Zener pinning in the simple case of spherical particles, there is not yet a model that can deal with coherent particles or complex particles morphologies. These limits could explain why all numerical results concerning the limiting grain size differ from experimental data.

The main causes of abnormal grain growth reported in the literature (i.e. grain size, grain boundary mobility or energy advantages or small strains) are reviewed. Then, the focus is placed on the occurence of abnormal grain growth in superalloys where the principal origin of the phenomenon is attributed to critical thermomechanical conditions: low strains at room temperature or low strain rates at high temperature.

In Inconel 718 the origin of abnormal grain growth is not yet clear. Small strains at hot temperature were reported to trigger the phenomenon but the mechanism of microstructure evolution has not yet been investigated. Similarly, the critical thermomecanical conditions have not yet been investigated systematically. Moreover, the role of δ phase particles on the occurence of the phenomenon has never been discussed with respect to Smith-Zener pinning models taking into account strain stored energy.

Résumé

Dans ce chapitre, le deux principaux phénomènes supposés être à l'origine du phénomène de croissance de grains anormale qui fait l'objet de cette étude sont présentés. Premièrement, le phénomène d'ancrage de Smith-Zener est décrit et les limites

des modèles analytiques existants sont considérées. Ensuite, les différents modèles numériques basés sur une représentation explicite de la microstructure proposés dans la littérature sont présentés. En général, tous ces modèles (Monte Carlo, champ de phase, ...) peuvent simuler l'ancrage de Smith-Zener en présence d'une population de particules sphériques et incohérentes. En revanche, aucun modèle n'a été adapté pour prendre en compte la cohérence ou une morphologie complexe des particules. De plus l'interaction entre un joint de grain et une particule de seconde phase reste très souvent introduite de manière simplifiée dans les simulations. Ces limitations pourraient expliquer pourquoi la taille limite de grains prédite par les modèles numériques ne coïncident pas toujours avec les données expérimentales. Les principales causes de la croissance anormale proposées dans la littérature, reposant sur l'hétérogénéité de tailles de grains, ou sur des propriétés particulières (énergie, mobilité) de certains joints de grains, ou encore sur l'énergie stockée au cours de petites déformations, sont présentées. Ensuite, l'accent est mis sur l'apparition du phénomène dans les superalliages qui semble liée à des conditions thermomécaniques critiques : petites déformations à température ambiante ou faibles vitesses de déformation à haute température. Dans l'Inconel 718 l'origine de la croissance anormale n'est pas encore clairement identifiée. Une étude a montré que de petites déformations à haute température peuvent déclencher le phénomène, mais les mécanismes microstructuraux sous-jacents n'ont pas été analysés. De même, les conditions thermomécaniques critiques n'ont pas été établies. L'influence des particules de phase δ sur le déclenchement du phénomène n'a également jamais été discutée par rapport aux modèles d'ancrage de Smith-Zener en prenant en compte l'énergie de déformation.

2 Material and experimental methods

Contents

This chapter presents the material and experimental methods employed in this work. First of all, the most relevant metallurgical features of Inconel 718 for the present work are described. Notably, the role of δ phase particles during microstructure evolution is discussed. Then, the mechanical tests (hot torsion, compression) employed to generate different microstructures as a function of thermomechanical conditions are presented. The characterization techniques employed to study such microstructures, like scanning electron microscopy (SEM), energy dispersive spectroscopy (EDS) and electron backscattered diffraction (EBSD) are presented. Finally, the analysis methods used to evaluate microstructures properties and grain boundary driving pressures are discussed.

2.1 Inconel 718 metallurgy

Inconel 718 is a nickel-iron-base superalloy (the nominal composition is given in Table 2.1) that is strengthened predominantly by secondary phase precipitation and to a lower extent also by solid-solution elements. The matrix of this superalloy exhibits a face centered cubic structure made up mainly by atoms of nickel with the presence of several elements in solid solution: iron, chromium, molybdenum, niobium and, to a smaller extent, titanium, cobalt and aluminum. Several secondary phases can be found inside the matrix. The time-temperature-transformation diagram of Figure 2.1 shows that δ phase particles can be present up to about 1030°C, even though this solvus temperature varies mainly according to the chemical composition. In this work, super- or sub- solvus annealing is always defined with respect to the solvus temperature of δ phase particles. It is to note that γ' and γ'' particles are present

Ni	Cr	Fe	Nb+Ta	Mo	Ti	Al	Co	Mn	Si	Cu	C
50	17	bal.	4.75	2.80	0.65	0.20	-	-	-	-	-
55	21	bal.	5.50	3.30	1.15	0.80	1	0.35	0.35	0.30	0.08

Table 2.1: Limiting chemical composition (mass percent) of Inconel 718 alloy according to AMS specifications [47].

only up to 890°C: at higher temperatures it is reasonable to assume that all γ' and γ'' particles dissolve in the matrix after few minutes of annealing. It is to note that in all thermomechanical tests presented in this work, the lowest δ sub-solvus temperature that is employed is 920°C. Hence it is possible to assume that γ' and γ'' particles do not contribute to the microstructural mechanisms investigated in this work.

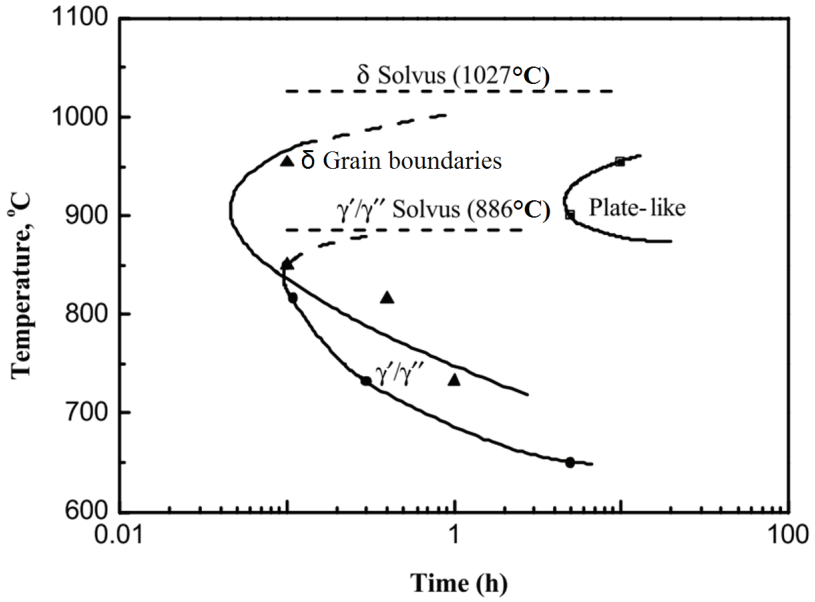

Figure 2.1: Time-Temperature-Transformation diagram of Inconel 718 alloy [48].

The γ' (Ni_3Al) phase is a simple cubic phase: precipitates are usually coherent with the matrix and they appear as spherical particles with dimensions of roughly 10-100nm [49]; even if the proportion of the γ' phase is low in Inconel 718 because of the low aluminum content, still it contributes to the strengthening of the alloy.

The γ'' (Ni_3Nb) phase is a metastable tetragonal phase: precipitates are coherent with the matrix and they form platelets with dimensions of about 10-100nm [49] (see Figure 2.2). The γ'' phase is the main phase contributing to the strength of the alloy (Orowan effect).

The δ phase is the stable form of the γ'' phase, it shares then the same chemical composition while it exhibits an orthorhombic structure. Particles are generally incoherent with the matrix (see the following section) and they can form both platelets or spheroids with dimensions in the range of 1-10 μm; the δ phase has a very signifi-

cant role in hindering grain growth during hot forging [4]. As marked in Figure 2.1, δ phase particles initially precipitate mostly on grain boundaries and only afterwards within grains, forming plate-like particles.

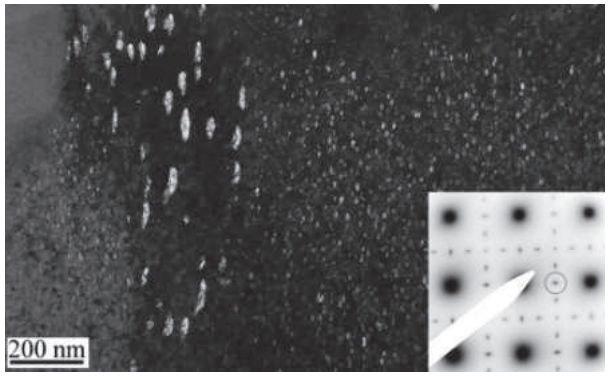

Figure 2.2: Morphology of γ'' particles measured by transmission electron microscopy [49].

Several types of carbides (M_xC_y) can be found with M=*Nb, Mo*; they appear on BSE graphs as coarse very bright irregular particles and, to some extent, they are also able to hinder grain growth even if their density is quite low [50]. Moreover, few carbonitrides (TiC_xN_y) can be detected [49]: they appear as dark blocky particles. Figure 2.3 shows an image of an Inconel 718 microstructure where all main phases appear.

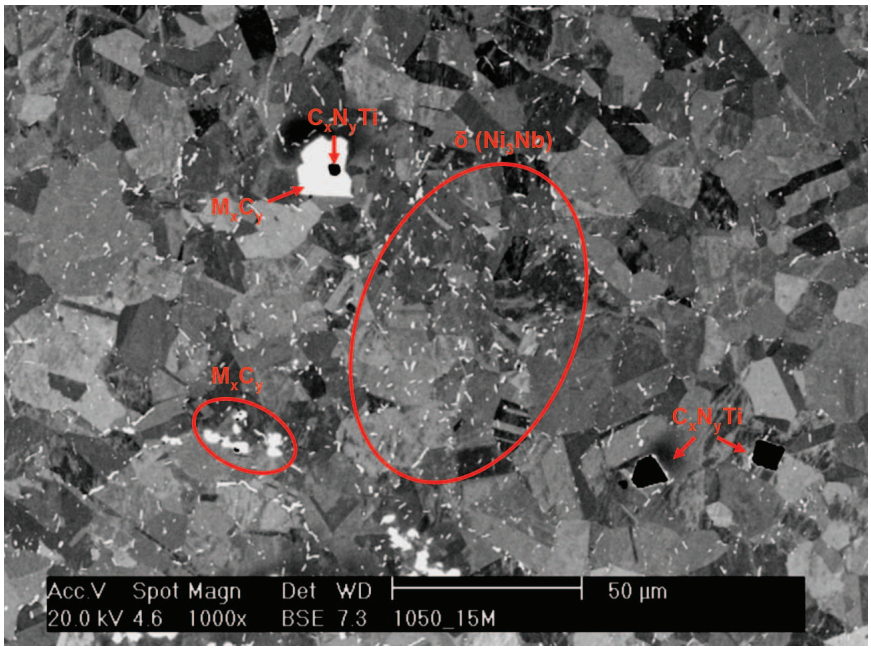

Figure 2.3: Backscattered electron image of an Inconel 718 microstructure.

2.1.1 The δ phase

A few more information will be given about the δ phase evolution during hot forging, because of the significant role played by this secondary phase on the microstructure evolution of Inconel 718. First of all, the solvus temperature range of the δ phase is about 1000-1030°C [50, 51]. The precise solvus temperature is mainly affected by the niobium content, even if the experimental values reported in the literature for a given niobium content are quite scattered [51]. Figure 2.4 shows that the volume fraction of δ phase starts to decrease significantly once the temperature of annealing is between 980-1025°C. Moreover, the equilibrium δ phase fraction at a given temperature increases if the niobium content is higher.

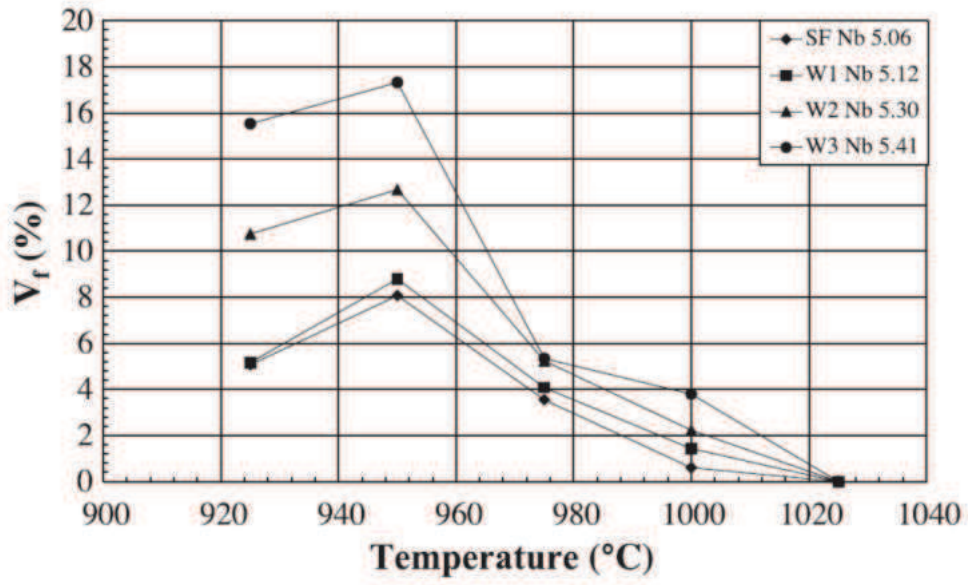

Figure 2.4: Evolution of δ phase particles as a function of Nb content and annealing temperature after 5h [50].

Another important feature regarding the δ phase concerns the evolution of the shape of the precipitates as a function of temperature [52] and deformation [53]. Indeed, when δ phase particles precipitate, they can form platelets semi-coherent with the γ phase of the matrix. The orientation relation is:

$$\begin{cases} (111)_\gamma // (010)_\delta \\ [\bar{1}10]_\gamma // [100]_\delta \end{cases}$$

However, high temperatures and local strains promote the dissolution and breakage of the platelets of δ phase, so that spherical shape mostly incoherent particles are then formed, as illustrated in Figure 2.5.

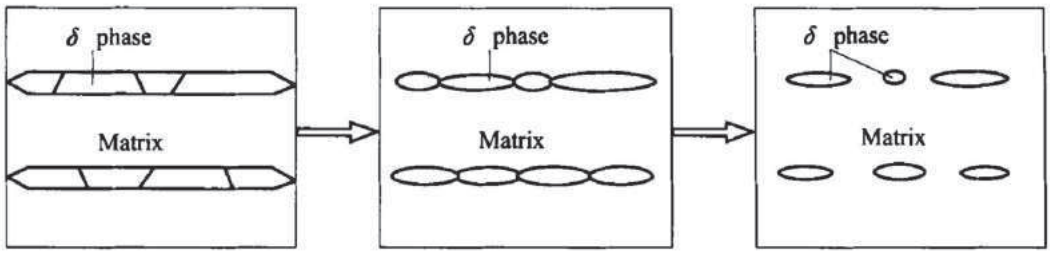

Figure 2.5: Morphology evolution of δ phase particles under typical hot forging conditions [52].

2.1.2 Dynamic recrystallization

Microstructure evolution of Inconel 718 alloy during hot forging often involves dynamic recrystallization. Several studies have investigated the microstructural mechanisms responsible for dynamic recrystallization in Inconel 718 [54, 55, 56]. Figure

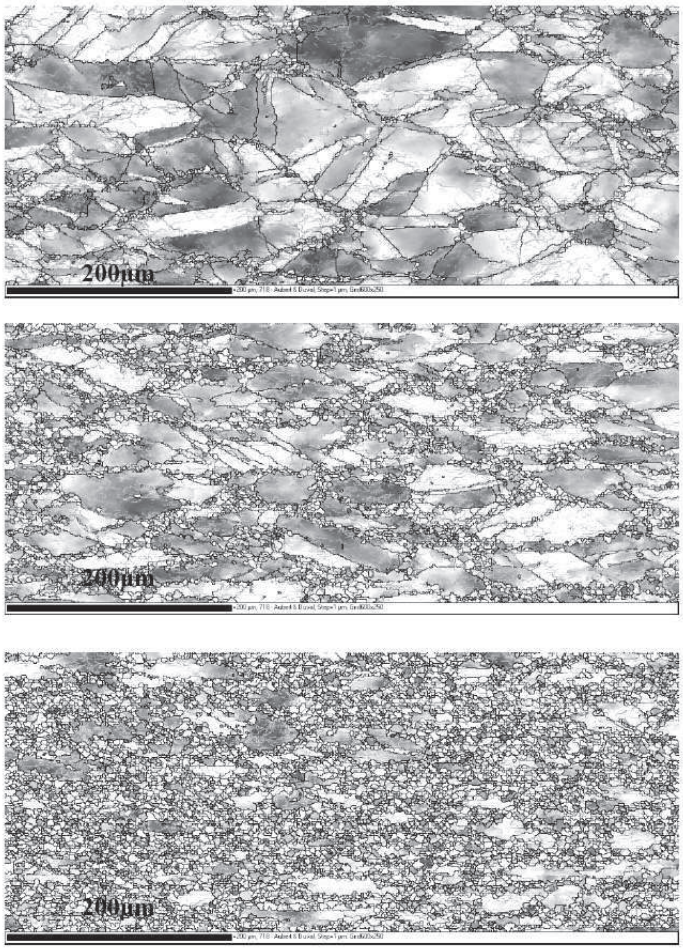

Figure 2.6: EBSD maps of dynamic recrystallization as a function of strain ($\dot{\varepsilon} = 0.1s^{-1}$) at temperature of 980°C: ε=0.4 (top), ε=0.7 (middle), ε=1 (bottom) [56].

2.6 illustrates the typical evolution of the deformed microstructure as a function of sub-solvus temperature strains at $\dot{\varepsilon} = 0.1s^{-1}$. The partially dynamically recrystallized microstructure exhibits a typical "necklace" topology: new recrystallized grains form at previous grain boundaries by bulging of grain boundaries driven by strain stored-energy differences. Such mechanism is discontinuous and it involves a clear nucleation and growth stage. New recrystallized grains can also form inside the hardened grains, at least if the deformation is applied at the sub-solvus temperature. In this case the formation of recrystallized grains is due the progressive subgrains rotation induced by strain, eventually leading to the formation of high angle mobile boundaries. However, this mechanism, which can be considered as a particular case of continuous dynamic recrystallization [9], is involved less frequently than grain boundary bulging as a nucleation mechanism in Inconel 718.

Indeed, dynamic recrystallization kinetics is strongly influenced both by deformation temperature and strain rate [57, 58]. Figure 2.7(a) shows the effect of temperature on stress-strain curves: as temperature increases, the stress peak decreases and shifts towards lower strain values. This is due to the fact that at higher temperatures dynamic recrystallization is triggered at lower strains and its kinetics is faster, producing a higher fraction of strain-free recrystallized grains (Figure 2.7(b)). It is to note that the stress peak of the curve obtained at 980°C (below the δ solvus) is reached at about $\varepsilon = 0.2$, while in the case of the curve obtained at 1060°C (above the δ solvus) the peak is reached at about $\varepsilon = 0.1$. In both cases, the critical strain triggering dynamic recrystallization is supposed to be slightly lower than the peak strain.

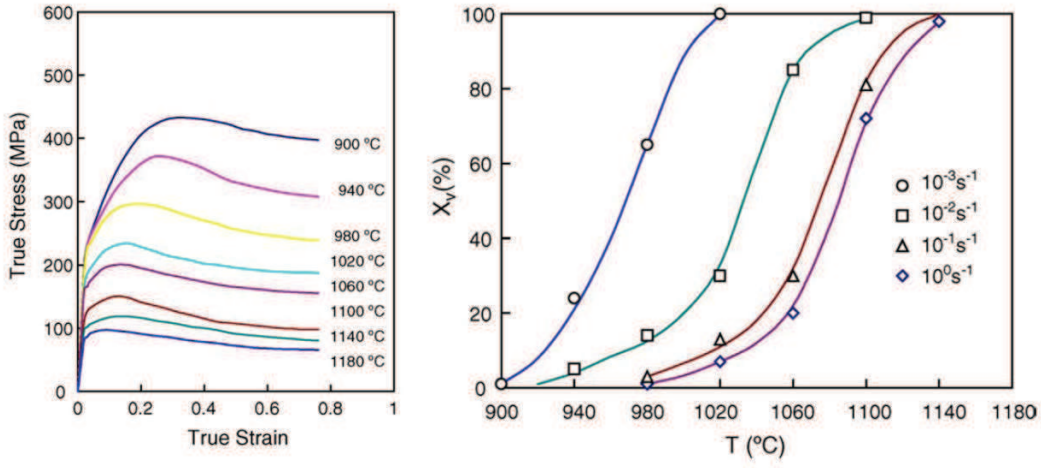

(a) (b)

Figure 2.7: Stress-strain curves for Inconel 718 deformed at $\dot{\varepsilon} = 0.1s^{-1}$ (a) and percentage of dynamic recrystallized grains (Xv) after $\varepsilon = 0.76$ as a function of deformation temperature and strain rate (b) [57].

2.2 Mechanical testing

In this work, hot mechanical tests are performed to generate several types of microstructures with different microstructural properties. Both hot torsion and compression tests are carried out to study the effect of thermomechanical parameters on the obtained microstructure.

2.2.1 Torsion test

The principle of torsion testing is to deform cylindrical samples by keeping fixed one side of the sample while the other is forced to turn at a certain speed. Such configuration induces shear stresses in the material. The geometry of torsion samples that were machined from a cylindrical Inconel 718 billet is illustrated in Figure 2.8. All samples were machined only along the mid-radius circumference of the billet in order to reduce chemical or microstructural heterogeneity: the longitudinal axis of the sample was parallel to the symmetrical axis of the cylindrical billet. It is to note that the gauge is thinner ($\Phi = 6mm$) in order to localize the strain only in this part. Both sides of the sample contain threads to fix it on the torsion machine. On the right side it is possible to see the drilled hole (dotted lines) that will contain the thermocouple. Such samples are deformed with the torsion test machine available

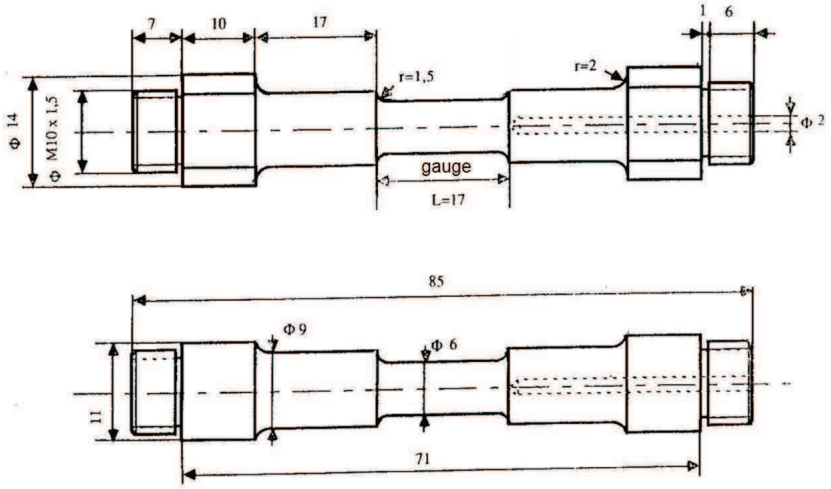

Figure 2.8: Geometry and dimensions in mm of torsion samples.

at Cemef. Figure 2.9 displays a sample mounted in the machine with the lamp furnace opened. Such machine allows both to heat and quench samples. Quenching is performed by forcing a water flow in the quartz tubes that completely surround the sample during testing: the operation requires less than 2 seconds. Heating is induced by a lamp heating system made by two shells containing the lamps: during testing, the shells are joined together, creating a sealed furnace chamber around the sample. Generally speaking, torsion testing has two main advantages. The first one is the possibility to apply high levels of strain before damaging the sample unlike in

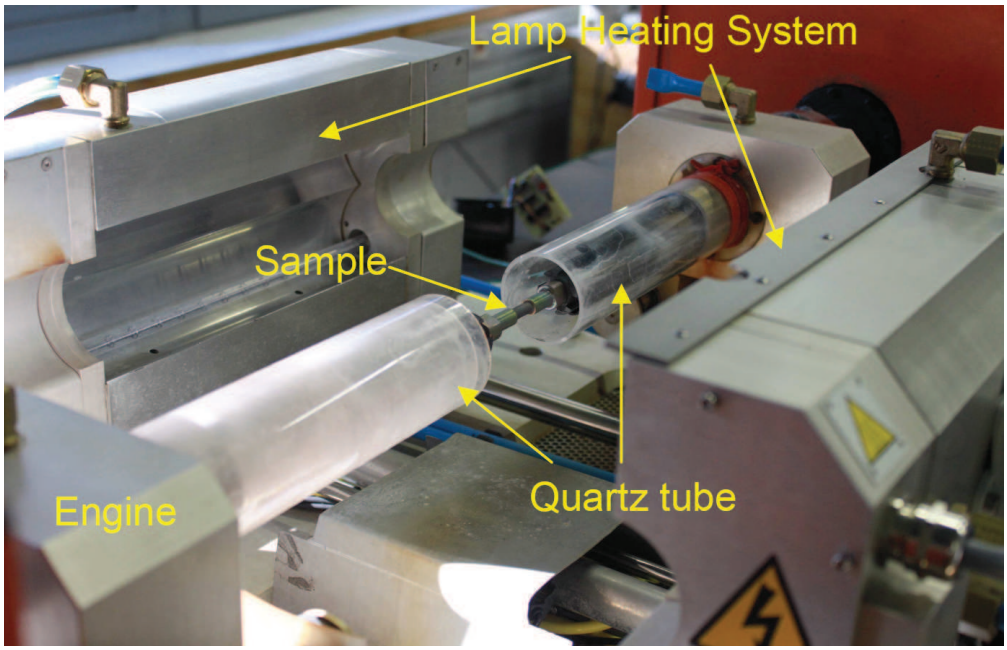

Figure 2.9: Experimental setup of the torsion machine at Cemef [59].

compression or tensile tests. The second advantage concerns the strain and strain rate distributions in the sample that are linear along the radius and can be calculated with analytical expressions. The equivalent strain and strain rate are respectively:

$$\bar{\varepsilon} = \frac{2\pi N R}{\sqrt{3}L}, \tag{2.1}$$

$$\dot{\bar{\varepsilon}} = \frac{2\pi \dot{N} R}{\sqrt{3}L}, \tag{2.2}$$

where R and L are respectively the radius and the length of the gauge and N is the number of turns. The drawback of torsion testing is linked to the calculation of stresses from torque data that is less direct and simple as compared to other mechanical tests. If the material is homogeneous and isotropic and the deformation is uniform in the gauge, then the analysis of Fields and Backofen can be used to evalute the equivalent stress acting on the surface of the sample [60]:

$$\bar{\sigma} = \frac{\sqrt{3}\Gamma}{2\pi R^3}(3 + \tilde{n} + \tilde{m}), \tag{2.3}$$

where Γ is the torque, $\tilde{n}$ and $\tilde{m}$ are two parameters defined as follows:

$$\tilde{m} = \left(\frac{\partial ln\Gamma}{\partial ln\dot{N}}\right)_N, \tag{2.4}$$

$$\tilde{n} = \left(\frac{\partial ln\Gamma}{\partial lnN}\right)_{\dot{N}}. \tag{2.5}$$

The strain-hardening parameter ($\tilde{n}$) can be easily estimated using the data from a single torsion test. On the contrary, the strain rate sensitivity ($\tilde{m}$) has to be calculated using at least two data sets obtained at different strain rates. However, in the case of cold torsion tests, the value of $\tilde{m}$ can often be neglected with respect to $\tilde{n}$. In hot torsion tests, the value of $\tilde{m}$ ranges from 0.1 to 0.3.

2.2.2 Compression test

In compression tests, cylindrical samples are put between two flat tools: generally one tool is fixed, while the other is pushed against the sample to reduce its height. Simple cylinders of diameter equal to 8 mm and height equal to 12 mm were machined from an Inconel 718 billet. Samples are tested with the compression test machine available at Cemef. Figure 2.10 displays the configuration of the machine: each tool is made by a body in superalloy that contains a low friction ceramic insert that is in contact with the sample. A thermocouple is welded under the surface of each tool. Hot tests can be performed thanks to a resistance furnace that surrounds both the tools and the sample. Quenching is not integrated in the machine, so it is performed manually by removing the sample from tools and dropping it in a water container: the operation requires less than 5 seconds. Unlike in torsion tests, the equivalent stress

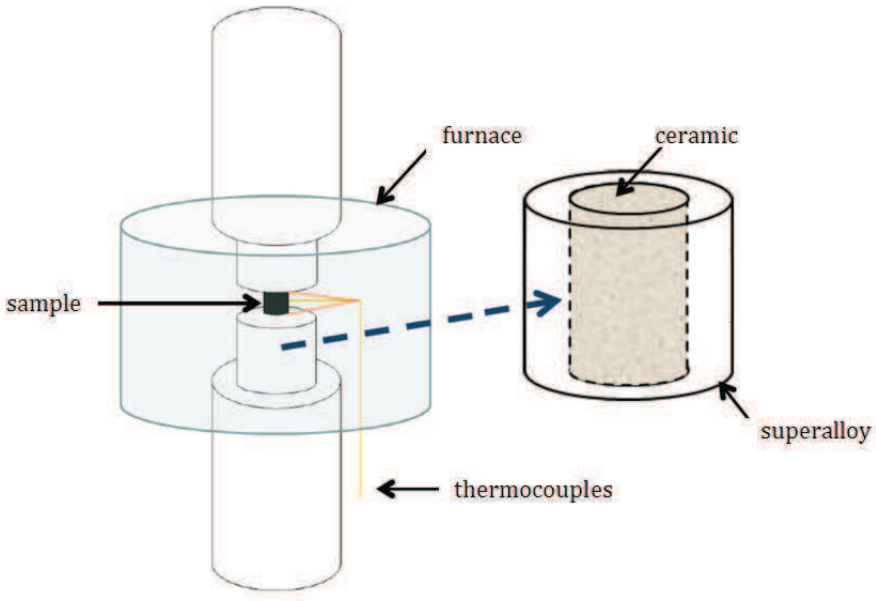

Figure 2.10: Experimental setup of the compression machine at Cemef [61].

is homogeneous in the whole piece and can be easily calculated from the measured force as:

$$\bar{\sigma} = \frac{F}{S}, \tag{2.6}$$

where F is the force applied by the tool and S is the surface of the sample. On the contrary the distribution of strain in the sample is a function of the friction between the sample and the tools. For the ideal case of perfect sliding (friction coefficient equal to zero), the equivalent strain and strain rate are homogeneous in the whole sample and they are calculated as follows:

$$\bar{\varepsilon} = ln(\frac{H_0}{H}), \tag{2.7}$$

$$\dot{\bar{\varepsilon}} = \frac{\dot{H}}{H}, \tag{2.8}$$

where H_0 and H are respectively the initial and the final height of sample. However, in real experimental conditions it is impossible to avoid friction. As a result, compared to the nominal (homogeneous) strain, in the zone of the sample close to the tools the strain is lower and at the core it can be up to 50% higher. For this reason, the numerical simulation of the compression test (for example using the software Forge ®) is necessary to evaluate the local distribution of strain in the sample.

Forge ® The finite element software Forge ® can be used to model several forming processes involving plastic deformation. In general, two types of objects are defined in a simulation: forming tools are non-deformable objects while the piece (for example a billet) is a deformable object. Each object is considered as a finite domain and an updated Lagrangian formalism is used to describe solid displacements. The behaviour of deformable objects is controlled by the fundamental principles of continuum mechanics which define the mechanical problem: conservation of the equilibrium and of the mass, associated with boundary conditions. For each deformable object a constitutive law linking stress, strain, strain rate tensors and the temperature must be defined. Then, the mechanical problem is solved using a velocity-pressure mixed formulation. A coupled thermic problem is also considered: it is solved by applying the heat equation associated with boundary conditions.

In this work, Forge ® simulation results are mainly exploited to assess the local values of strain in industrial pieces or in compression samples. Indeed, the most important simulation parameter that affects the strain distribution is the correct definition of the boundary conditions of the mechanical problem. As already pointed out, in the case of compression testing, the friction coefficient between the tools and the sample governs the strain heterogeneity.

2.3 Characterization techniques

The microstructures of Inconel 718 samples are mainly characterized by scanning electron microscopy. Scanning electron microscopy (SEM) images are used to investigate the distribution of δ phase particles (also with respect to grain boundaries).

Energy-dispersive X-ray spectroscopy (EDS) is used to analyse chemical composition. Electron backscatter diffraction (EBSD) is employed to investigate the grain size, the grain boundaries and the intragranular misorientation.

2.3.1 Scanning electron microscopy and EBSD

The principle of scanning electron microscopy is very well known: an electron beam is focused on the surface of a sample and it is swept across its surface. The interactions of the electron beam with the atoms of the sample cause the emission of several electrons and radiations (see Figure 2.11). The depth of the interaction volume can be estimated using the properties of the sample atoms and the accelerating voltage of the electron beam. In the case of nickel atoms and for a voltage of 20kV, the penetration depth is about 1.4 μm. Depending on the nature of the signal that is detected, different information about the sample can be collected.

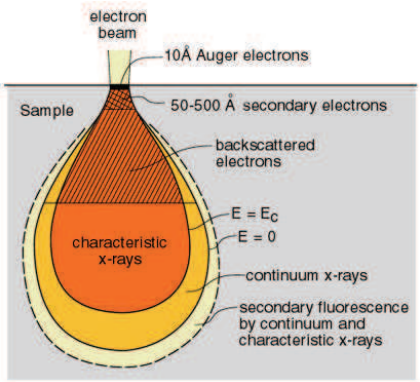

Figure 2.11: Interaction volume induced by an electron beam [http://www4.nau.edu].

Secondary electrons (SE) are produced by inelastic interactions and they have low energy: for this reason they come only from a very thin layer below the surface of the sample. The intensity of their signal is mainly linked to the topography of the surface. Backscattered electrons (BSE) are the result of quasi-elastic interactions, so they have high energy and because of that they can come from deeper regions of the sample, giving a lower spatial resolution. Their intensity is linked mainly to the chemical composition of the sample, but also to crystal orientation, because they can be channeled into the crystal. X-rays, resulting from the ionization processes of inner shell electrons of the atoms, provide information about the chemical composition of the material. X-rays can be analysed by using both energy-dispersive (EDS) or wavelength-dispersive (WDS) spectroscopy. In this work, semi-quantitative analyses (standardless) using an energy-dispersive detector installed on a SEM were performed.

Electron backscatter diffraction Electron backscatter diffraction (EBSD) is based on the analysis of the diffraction patterns produced by a fraction of the backscattered electrons that are subsequently diffracted by crystal planes. Such patterns, detected on a phoshor screen, contain the so-called Kikuchi bands that are the "finger print" of a specific diffracting crystallographic plane. Thus, it is possible to determine the crystal orientation of each point of a sample surface. A typical EBSD experimental setup is given in Figure 2.12. It is to note that the sample is tilted about 70° from the horizontal to optimize the pattern intensity. A camera and an image processing system are needed to acquire and filter diffraction patterns. Then, pattern bands are detected and transformed via a mathematical routine (Hough transform): every pixel in the Hough space denotes a unique line of the diffraction pattern. Then, it is possible to calculate the underlying crystal orientation, as angles between bands are gnomic projections of the angles between lattice planes. In this work, the EBSD system determines the crystal orientation by minimising the 'misfit' between the experimental pattern formed by at least 6 bands and the theoretical pattern of a candidate crystal orientation. If several phases are present in the material, in principle the EBSD system is able to correctly index the different phases. However, in this work only one phase, the nickel γ phase, was indexed (as explained in the following section).

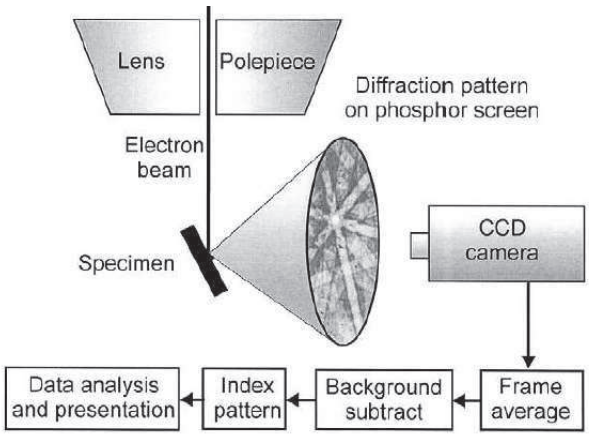

Figure 2.12: EBSD experimental setup [9].

Sample preparation Before polishing both torsion and compression samples are cut in half along the plane that intersects the symmetry axis, as shown in Figure 2.13. Unless otherwise stated all analyses on these samples are carried out in the zones marked by red rectangles, which correspond to the higher strain regions.

All samples for electron microscopy analysis are prepared following the same procedure:

- mechanical polishing with successive wet grinding papers and increasing polishing time from one to five minutes: 320 (1'), 600 (2'), 1200 (3'), 2400 (4'),

4000 (5') grit papers,

- mechanical polishing with a SiO_2 colloidal solution (OP-S) for ten minutes,
- vibration polishing with an anti-agglomerating SiO_2 colloidal solution for at least twelve hours.

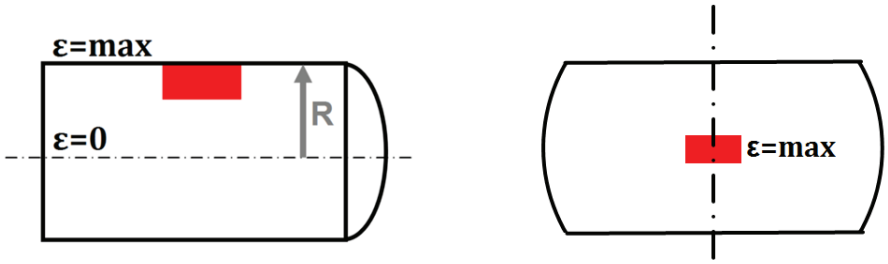

(a) (b)

Figure 2.13: Surface analysed in torsion (a) and (b) compression samples.

If samples were to be charaterized also by optical microscopy, then after surface polishing, they are etched with the Kalling solution for 2 minutes at room temperature (see Table 2.2).

$CuCl_2 - 2H_2O$	20g
C_2H_5OH	500ml
HCl (35%)	500ml

Table 2.2: Chemical composition of the Kalling solution.

2.3.2 Quantitative analysis of microstructures

EBSD measurements are performed using a Bruker Crystalign system. An appropriate step size is chosen ($0.2 - 1\mu m$) for each microstructure scale so that the pixel size is about ten times smaller than the average grain size of the smallest grains in case of bimodal distributions. The data set of an EBSD measurement stores the list of the pixels that compose the measured area. Each pixel has a crystallographic orientation that is determined by indexing only the nickel matrix phase. Then, non indexed pixels can be due either to second phase particles, sample surface pollution or grain boundaries. Such data sets are processed with the OIM software from TSL to determine microstructural parameters. First of all, *crystal* boundaries are defined between two pixels having a misorientation angle higher than 5°. If crystals made by only one pixel exist, their orientation is switched to the same orientation as that of the majority of the neighboring pixels. Then, all crystals made by a number of

pixels equivalent to a surface of less than $2\mu m^2$ are not taken into account for the estimation of microstructural parameters. Such crystals can correspond to second phase particles (like cubic carbides) that could be indexed as the nickel phase. *Twin* boundaries are those crystal boundaries having a misorientation (with a tolerance of 5°) equal to 60° along the axis $< 111 >$. *Grain* boundaries are defined as those crystal boundaries that do not satisfy the twin misorientation relation. Hence, a grain is composed by several twin-related crystals.

A grain size is calculated as the diameter of a circle having the same area as the considered grain. *Average* grain sizes are either number-weighted ($\bar{D}_N$) or area-weighted ($\bar{D}_A$). In this work, both $\bar{D}_N$ and $\bar{D}_A$ are used to describe all microstructures as they are generally heterogeneous, characterized by coarse grains and a small surface fraction (<10%) of fine grains. For example, Figure shows a typical heterogeneous microstructure where $\bar{D}_N$=13 µm and $\bar{D}_A$= 54 µm taking into account all grains. The surface fraction of grains smaller than 20 µm (highlighted in red) is 9% and $\bar{D}_N$=6 µm, while for grains bigger than 20 µm the average grain size is $\bar{D}_N$=45 µm.

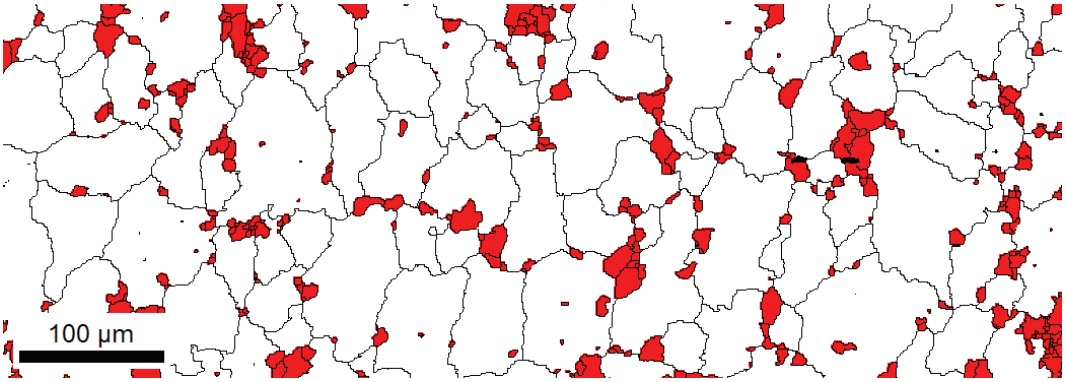

Figure 2.14: Example of an heterogeneous microstructure measured by EBSD. Grain boundaries are black, while twins are omitted. Red grains are smaller than 20 µm.

Twin densities are calculated using two different parameters. The number of twins per grain (T_G) is a dimensionless parameter calculated as follows:

$$T_G = \frac{n_C}{n_G} - 1, \tag{2.9}$$

where n_C and n_G are respectively the number of crystals and grains. The twin density ($T_A[mm^{-1}]$) is calculated as follows:

$$T_A = \frac{l_T}{A}, \tag{2.10}$$

where l_T is the length of twin boundaries measured within the area A.

Intragranular misorientation parameters In this work, three different parameters provided by the OIM software were used to describe the internal misorientation of crystals. It was decided to keep the same names of the software for these parameters (that are also used in the literature), even though in this work they all describe the internal misorientation at the crystal level. The kernel average misorientation (KAM)

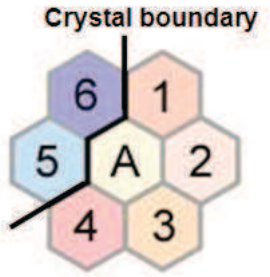

Figure 2.15: Definition of the kernel average misorientation (KAM). The KAM of pixel A is the average misorientation angle between pixel A and neighboring pixels belonging to the same crystal (i.e. 1,2,3,4). [62]

is calculated as the average misorientation angle of a pixel i with its neighbors in a crystal:

$$KAM = \frac{1}{m_i}\sum_{j=1}^{m_i}\theta_{ij}, \tag{2.11}$$

where θ_{ij} is the misorientation angle of pixel i with a neighbor pixel j and m_i is the number of neighbors of pixel i. Then, if a misorientation is higher than 5° (i.e. two pixels belong to different crystals as defined in this work) then it is not taken into account. An exemple is given in Figure 2.15. The KAM value for pixel "A" is the average of the misorientations with pixels 1 to 4, while misorientations with pixels 5 and 6 are excluded as they exceed 5°. The grain average misorientation (GAM) is the average of all KAM values inside a crystal:

$$GAM = \frac{1}{N}\sum_{i=1}^{N}\frac{1}{m_i}\sum_{j=1}^{m_i}\theta_{ij}, \tag{2.12}$$

where N is the total number of pixels in the crystal. Both the KAM and GAM parameters depend on the step size of the EBSD measurement and they provide information about short-range crystal orientation gradients. The GOS is the average misorientation angle between each pixel (in a crystal) and the average orientation of all pixels in the crystal:

$$GOS = \frac{1}{N}\sum_{i=1}^{N}\theta_i^{AVG}, \tag{2.13}$$

where θ_i^{AVG} is the misorientation angle between pixel i and the average crystal orientation. Thus, it does not depend on the step size (but it may be grain size

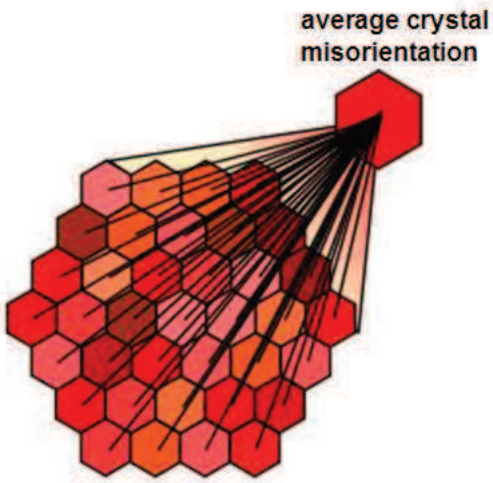

Figure 2.16: Definition of the grain orientation spread (GOS). The GOS is the average misorientation angle between each pixel in the crystal and the average orientation of all pixels in the crystal [62].

dependent) and it takes into account long-range crystal orientation gradients.

It is interesting comparing the KAM, GAM and GOS maps of a partially recrystallized Inconel 718 microstructure where both strain-free recrystallized crystals and hardened crystals are present (see Figure 2.17). The KAM map illustrates that in recrystallized crystals pixel to pixel misorientation is very low for all pixels. In Figure 2.18 the red curve shows that pixel to pixel misorientation is in the range 0.4°-0.7°, that is consistent with the angular precision of the EBSD system (about 0.5°). Interestingly, also the cumulative misorientation profile (blue curve) oscillates inside the same angular range, hence pixel to pixel misorientation values can be reasonably associated with the EBSD measurement noise.

On the contrary, in hardened crystals high KAM pixels are present, usually forming a network that divides a crystal in several sub-crystals. In the GAM map strain-free crystals have lower GAM values compared to hardened crystals, even if values remain quite close as only short-range orientation gradients are taken into account. Interestingly, in the GOS map the difference between strain-free and hardened crystals is enhanced as it takes into account long-range orientation gradients. Moreover, high or low GOS crystals correspond respectively to high or low GAM crystals.

Now, it is worth discussing the influence of neighbor pixel distance (i.e. EBSD measurement step size) on the GAM parameter, which will be used to estimated the density of geometrically necessary dislocations (GNDs) as described in the following section. In Figure 2.19, the value of GAM (normalized by the neighbor pixel distance) of three crystals is calculated using different neighboring pixel distances from 0.25 μm to 2 μm. The normalized value of GAM decreases very rapidly up to 0.5 μm and then it starts to stabilize for all three crystals. It follows that if the distance between

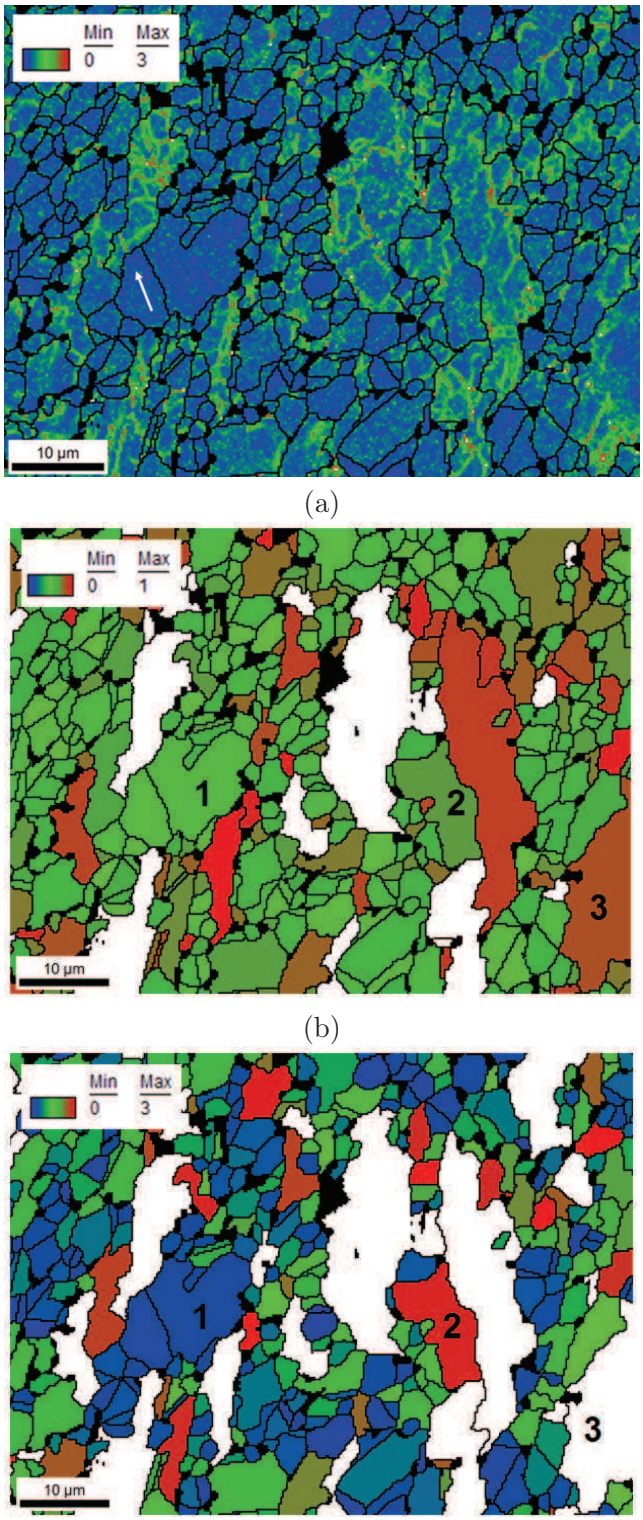

Figure 2.17: Comparison of KAM (a), GAM (b) and GOS (c) maps of a partially recrystallized Inconel 718 microstructure. Crystal boundaries are black. The EBSD measurement step size is 0.25 µm.

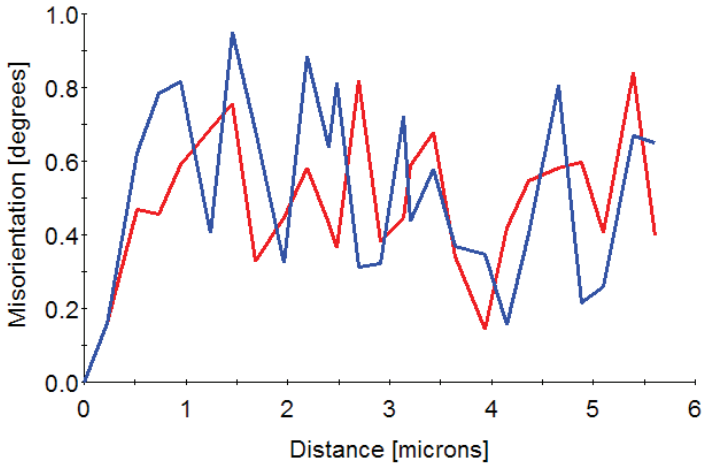

Figure 2.18: Pixel to pixel (red curve) and cumulative (blue curve) misorientation profile measured along the white arrow on grain 1 of Figure 2.17. The EBSD measurement step size is 0.25 μm.

pixels is too small, then GAM values are overestimated as EBSD measurement noise is added up. This effect is clear for crystal 1, that can be considered a strain-free crystal (see the KAM map of Figure 2.17), even though the normalized GAM value can reach a maximum of 2°/ μm.

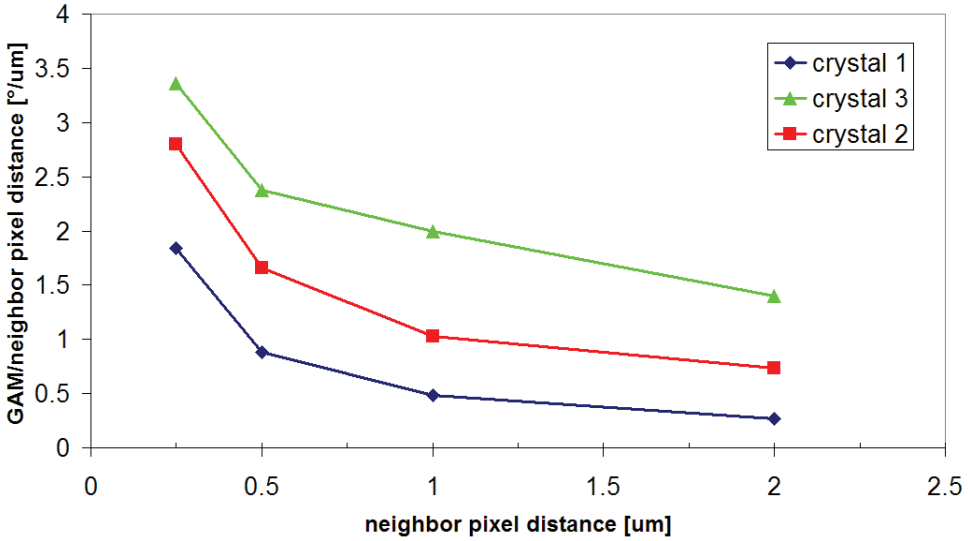

Figure 2.19: Influence of neighbor pixels distance on the intragranular misorientation gradient (measured as GAM/neighbor pixels distance) for three crystals of Figure 2.17.

Finally, in this work it seems reasonable to calculate GAM values using a neighbor pixel distance of about 1 μm: a bigger distance would not be compatible with the grain size of fine microstructures (about 6-10 μm). Hence, a strain-free crystal (like crystal 1) is characterized by a normalized GAM value of about 1°/ μm. It is to note

that the GOS value of crystal 1 is 0.4° and it does not change as a function of EBSD measurement size. In this work, the surface-weighted average GOS value ($\overline{GOS}_A$) will be used to characterize microstructures.

Distribution of the δ phase The surface fraction and size of δ phase particles are determined by image analysis using the UTHSCSA Image Tool software. At least five backscattered electrons (BSE) images per sample are analyzed: each image corresponds to an area of 100x150 μm. The δ average radius is the number-weighted radius of circles having the same area of the particles. Particles smaller than two pixels (i.e. radius$< 0.1\mu m$) are not taken into account.

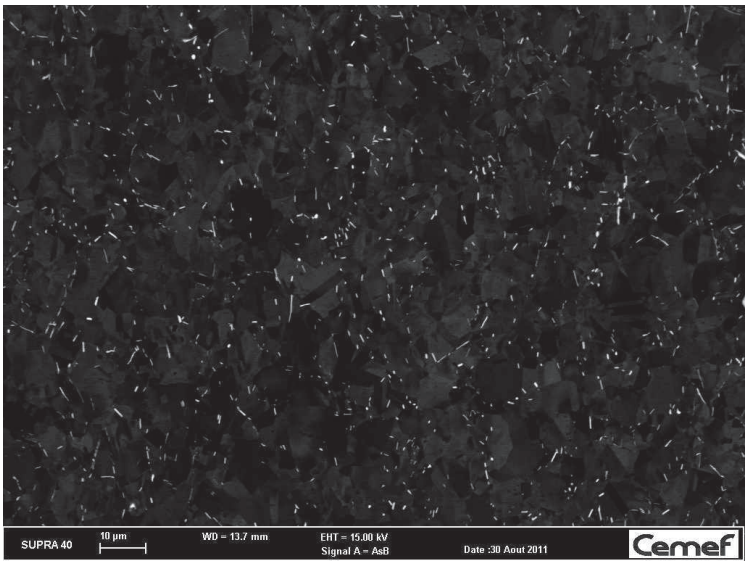

(a)

(b)

Figure 2.20: Example of δ phase quantification in a typical Inconel 718 microstructure: the backscattered electrons image (a) is filtered fixing a threshold on brightness intensity to reveal only particles (b).

An example of δ phase quantification is given in Figure 2.20. Backscattered electrons images are filtered fixing a threshold on brightness intensity to reveal only particles. Indeed, the filtering step is mainly affected by the threshold that is chosen manually in order to reveal at best all particles present in the experimental image without introducing artefacts. For example, if Figure 2.20 is filtered and measured ten times, then the particle surface fraction is found to be 2.35% with a standard deviation of 0.15% that is due to slight variations of the threshold from one filtering to the other. Hence, the absolute accuracy on the fraction measurement is not better than ±0.15% in this case. In general, the relative accuracy is then about ±6%.

2.3.3 Estimation of grain boundary driving forces

In this work, microstructural parameters are used to provide an estimation of the three driving forces that govern grain boundary migration associated to:

- capillarity,
- the stored energy difference across the grain boundary,
- Smith-Zener pinning.

If the boundary migrates driven by the capillarity effect, then the driving pressure for a spherical grain can be expressed as $P_G = \frac{2\gamma}{R}$ (see Eq.(1.6)). For pure nickel at 1000°C $\gamma \cong 0.6 J/m^2$ [63], however the presence of alloying elements is supposed to reduce this value in Inconel 718[64]. In real microstructures grains have different shapes and the effective driving force is found to be much lower as compared to the case of spherical particles. Stereological measurements on single phase materials revealed a correlation between the average mean curvature of the grain boundary network in three-dimensions ($\overline{k}$) and the average grain size ($\overline{R}$):

$$\overline{k} = \frac{1}{4\overline{R}}. \tag{2.14}$$

Then, using $P_G = \gamma \overline{k}$, the relation between the mean grain size radius and the effective driving force can be estimated as [5, 65]:

$$P_G = \frac{\gamma}{4\overline{R}}. \tag{2.15}$$

If a grain boundary separates two grains of different stored energy, then the driving pressure is equal to the difference of the energies per unit volume: $P_R = \triangle E$. The energy is linked to the dislocation density ρ by this equation [9]:

$$E = 0.5 \rho G b^2, \tag{2.16}$$

where G is the shear modulus (45GPa at 1000°C for Inconel 718 [47]) and b is the norm of Burgers vector (0.25nm). The density of geometrically necessary dislocations

(GNDs) in a grain is linked to intragranular misorientations. The local density (at the pixel scale) can be estimated as a first approximation from EBSD data as [66]:

$$\rho_{GND} = \frac{K}{b}\frac{\triangle\theta}{\triangle x}, \tag{2.17}$$

where $\triangle\theta$ is the mean misorientation angle between a pixel and its neighbors and $\triangle x$ is the measuring step size. The parameter K depends on the assumptions for the considered dislocation structure: it was found K=1 for tilt [67] and K=2 [68] for twist sub-boundaries. Since the present study deals mainly with torsion tests, K=2 was chosen. The average dislocation density in a grain is calculated by replacing $\triangle\theta$ in Eq.(2.17) with the GAM value (that is the average of $\triangle\theta$ in a grain).

It is to note that stress-strain curves (obtained for example by torsion tests) can be exploited to estimate both the density of GNDs and statistically stored dislocations (SSDs). In fact, in the literature the influence of dislocation density on flow stress is often described using the Taylor equation [69]:

$$\sigma = \sigma_0 + \alpha M G b\sqrt{\rho}, \tag{2.18}$$

where G is the shear modulus (77 GPa at room temperature for Inconel 718 [47]), b is the norm of the Burgers vector, α is a constant (in the range of 0.2-0.4 for metal alloys) and M is the Taylor factor that is equal to about 3.1 for a polycrystal. The parameter σ_0 should correspond to a "dislocation free" yield stress. In fact, assuming that σ_0 is equal to the yield stress of the material in the annealed state (lowest dislocation density), has allowed to verify the validity of Eq.(2.18) in steel [70] or several alloys [71]. In section 4.3.2, it will be shown that the density of GNDs measured from EBSD data and the total density of dislocations estimated using the Taylor equation have the same order of magnitude, the former being half of the latter.

The presence of secondary-phase particles hinders grain boundary migration with a pinning pressure $P_P = \frac{3\gamma f}{2r}$ (see Eq.(1.5)).

2.4 Summary

In this chapter, the most important metallurgical features of Inconel 718 are presented. It is shown that the solvus temperature of the δ phase is in the range 1000-1030°C, while the solvus temperature of the γ' or γ" phase is about 900°C. Thus, in the temperature range 900-1030°C only δ phase particles (except few other particles) are present in the microstructure of Inconel 718. The influence of hot forming parameters (temperature, strain, strain rate) on microstructure evolution are briefly presented.

Torsion and compression testing techniques are described. The main advantage of torsion testing with respect to compression testing is the possibility to easily control

the strain distribution in the sample, that can be calculated analytically.

The characterization techniques employed in this work are also presented. Scanning electron microscopy (SEM) is mainly used to measure the distribution of δ phase particles. Energy dispersive spectroscopy (EDS) is employed to perform semi-quantitative analyses of chemical composition. Electron backscattered diffraction (EBSD) is the main technique used in this work to measure grain size, twin fraction, grain boundary properties and intragranular misorientation.

Several intragranular misorientation parameters (KAM, GAM, GOS) are presented and compared to each other. Finally, it is shown how the three main forces governing grain boundary migration (capillarity, stored energy, Zener pinning) can be estimated from experimental data.

Résumé

Dans ce chapitre, les aspects métallurgiques les plus importants de l'alliage Inconel 718 sont présentés. La température de solvus de la phase δ est comprise entre 1000-1030°C et celle des phases γ' et γ'' est environ 900°C. Donc, pour des températures comprises entre 900-1030°C, seules des particules de phase δ (à l'exception d'autres particules issues de l'élaboration telles que des carbures, peu nombreuses) sont présentes dans la microstructure. L'influence des principaux paramètres de mise en forme à chaud (température, déformation, vitesse de déformation) sur l'évolution microstructurale est succinctement présentée. La mise en place des essais de torsion et compression est décrite. Le principal avantage de l'essai de torsion par rapport à l'essai de compression est la possibilité de maîtriser parfaitement l'hétérogénéité de la déformation dans l'éprouvette, qui varie linéairement avec la distance à la fibre neutre et peut ainsi être calculée analytiquement. Les techniques de caractérisation microstructurale qui seront employées dans ce travail sont ensuite décrites. La microscopie électronique à balayage (MEB) est utilisée principalement pour analyser la distribution des particules de phase δ. La spectrométrie des photons X caractéristiques par dispersion d'énergie (EDS) est utilisée pour réaliser des analyses semi-quantitatives de la composition chimique. La diffraction d'électrons rétrodiffusés (EBSD) produit des cartographies d'orientation dont sont déduits plusieurs paramètres microstructuraux : taille de grain, densité de macles, types de joints de grains et désorientation intragranulaire. La désorientation intergranulaire sera interprétée comme la signature de la présence de dislocations et donc d'énergie stockée. Plusieurs paramètres décrivant cette désorientation intragranulaire (KAM, GAM, GOS) sont décrits et comparés. Enfin, les méthodes employées pour évaluer les forces régissant la migration des joints de grains à partir des données expérimentales sont détaillées. Ces forces sont de trois types : force capillaire, différence d'énergie stockée et force d'ancrage de Smith-Zener.

3 Inhomogeneous grain growth in industrial forgings

Contents

This chapter begins with the analysis and discussion of the distinctive microstructural features of the overgrown grains. Then, microstructures taken from two industrial pieces where abnormal grain growth occurs during annealing are analysed. First of all, the initial microstructures are characterized, then their stability during annealing at different δ sub-solvus temperatures is investigated. The possible origins of abnormal grain growth are discussed.

3.1 Overgrown grain properties

As mentioned in the introduction, overgrown grains as characterized by optical microscopy feature three distinctive properties:

- grain boundaries are missing (or they are poorly contrasted),
- twin density is high,
- the fraction of intragranular δ phase is high.

The objective of this section is to confirm and discuss these properties, notably the first one. For this purpose, two samples of "normal" and "overgrown" grains having the same grain size ($\overline{D}_A$= 50 μm) are compared. Figure 3.1(a) illustrates the normal grain sample that was taken from an Inconel 718 billet, while Figure 3.1(b) displays the overgrown grain sample (corresponding to sample B'/985 that will be detailed in the next section).

Concerning the distribution of the δ phase, Figure 3.1(a) reveals that particles are mostly located on grain boundaries, even though it remains possible to see few of them inside the grains. In this case Smith-Zener pinning has probably governed the final grain size of the microstructure. On the contrary, in Figure 3.1(b) particles are spread all over the surface, notably within the grains. This feature is probably linked

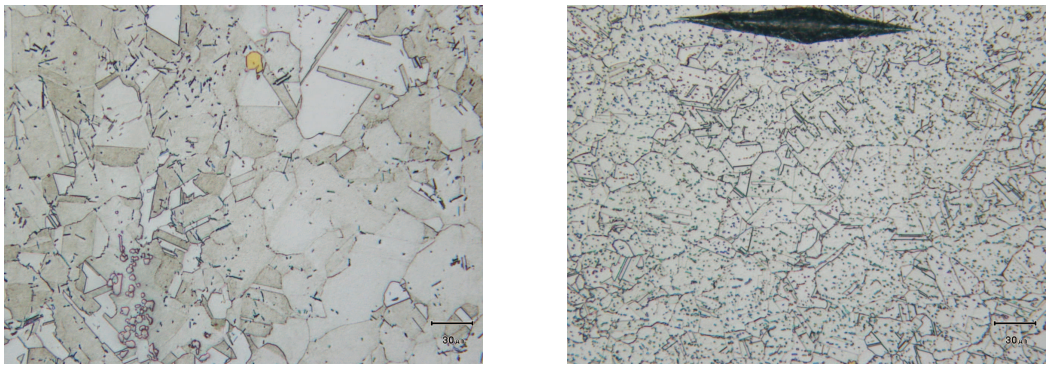

(a) (b)

Figure 3.1: Comparison of normal (a) and overgrown (b) grains having the same size ($\overline{D}_A$= 50 μm) by optical microscopy.

to the fact that Smith-Zener pinning was not sufficient to stop the growth of these grains, so particles are left behind as grain boundaries move. Otherwise, significant intragranular misorientation occurs only at low δ sub-solvus temperatures (close to 950°C) and particles would have mostly a rod-like shape [53], unlike those of Figure 3.1(b).

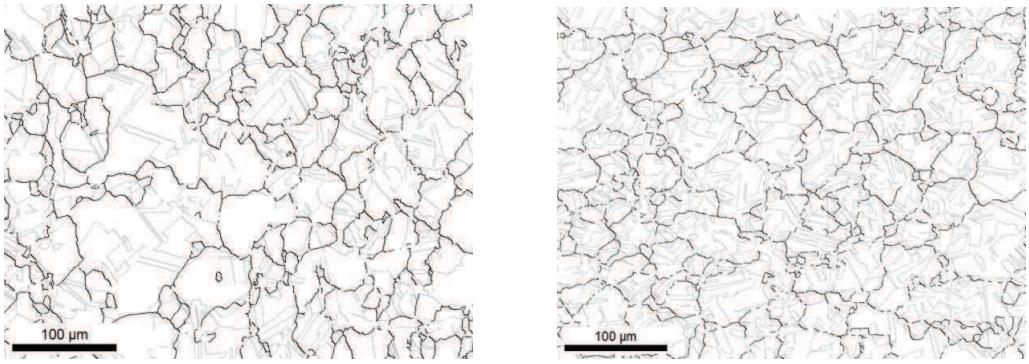

(a) (b)

Figure 3.2: Comparison of normal (a) and overgrown (b) grains having the same size ($\overline{D}_A$= 50 μm) by EBSD (black: grain boundaries, grey: twins).

Twins are shown as grey lines in the EBSD maps of Figure 3.2. The density of twins is obviously higher in Figure 3.2(b) where most of the twins appear as irregular lines (i.e. incoherent twins), while in Figure 3.2(a) there are less twins and they appear mostly as straight lines (coherent twins). This difference in morphology may suggest that twinning occured under different thermomechanical conditions in the two cases. Table 3.1 indicates that both the number of twins per grain and the length fraction of twins are roughly doubled in the case of overgrown grains with respect to normal grains. Now, as the definition of "normal" grains is somewhat arbitrary in this work, it was worth reporting also the twin densities measured in Inconel 718 after a well defined microstructural evolution, that is capillarity driven grain growth at different

δ super solvus temperatures [72]. Table 3.2 shows that twin densities are almost four times smaller compared to the value of overgrown grains.

	normal	overgrown
T_G [-]	3	7.7
T_A $[mm^{-1}]$	101	237

Table 3.1: Twin density of normal and overgrown grains of size ($\overline{D}_A$= 50 μm).

$\overline{D}_A$ [µm]	40	64	96
T_G [-]	1.6	1.6	1.3
T_A $[mm^{-1}]$	44	44	27

Table 3.2: Twin density of Inconel 718 microstructures after capillarity driven grain growth at different δ super solvus temperatures [72].

These data suggest that thermomechanical processing can greatly influence and promote the development of such microstructural properties, as twin boundaries. This concept is in fact at the basis of grain boundary engineering, whose goal is to improve the intergranular damage resistance properties of materials by promoting certain types of grain boundaries or twins through thermomechanical treatments. For this reason, understanding which phenomena have triggered the growth of overgrown grains (which contain many twins) could be also interesting with respect to grain boundary engineering. However, in this work twin density must be considered mainly as a "finger print" that helps indentifying overgrown grains that formed following the same microstructural mechanism.

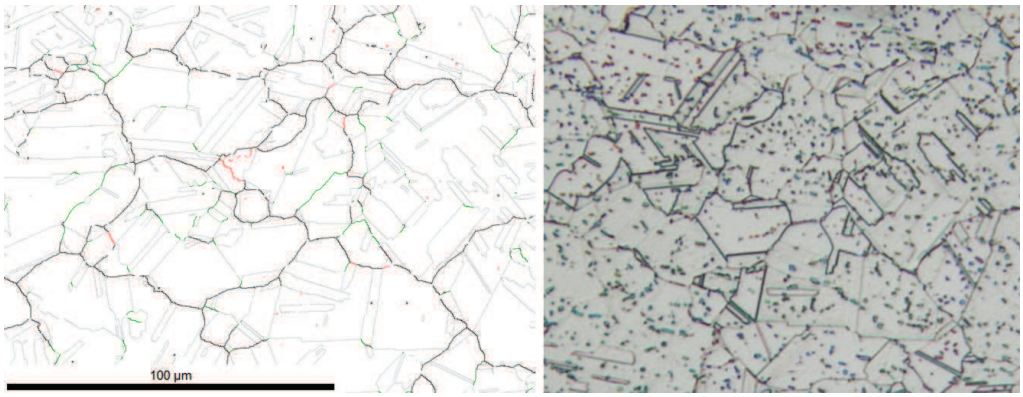

(a) (b)

Figure 3.3: Comparison of EBSD map (a) and optical microscope image (b) of the same overgrown grains (red: grain boundaries<15°, black: grain boundaries>15°, grey: twins, green: secondary twins).

Another particular feature of overgrown grains is the low contrast of grain boundaries on optical micrographs, as it can be seen in Figure 3.3(b). This feature can be investigated by comparing optical micrographs with EBSD maps to reveal the nature of grain boundaries. In overgrown grains twin boundaries are generally very well contrasted, but some of them are not revealed at all. On the contrary, grain boundaries can be detected but they are poorly contrasted even though all of them are characterized by high misorientation angles (>15°) as it can be seen on the EBSD map. Moreover, no coincidence site lattice (CSL) grain boundaries are significantly present in the microstructure (not shown), except for twins (Σ3) and secondary twins (Σ9). Similar remarks can be done by considering Figure 3.4 which displays images

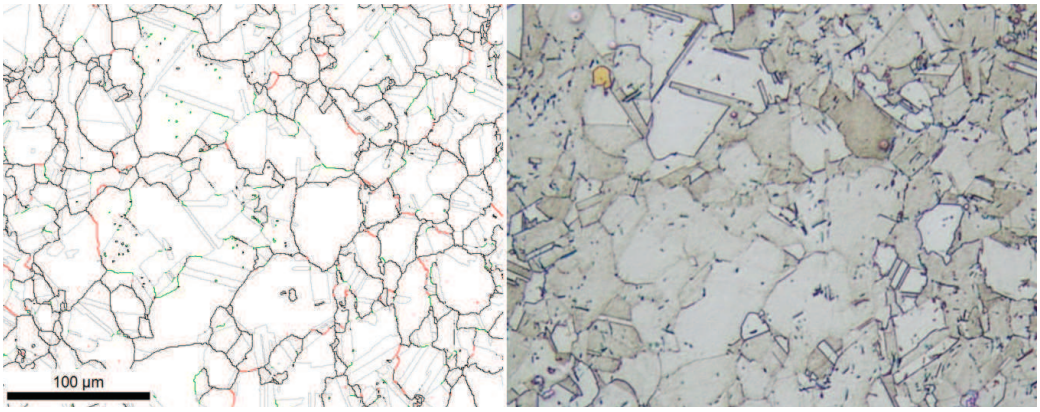

(a) (b)

Figure 3.4: Comparison of EBSD map (a) and optical microscope image (b) of the same normal grains (red: grain boundaries<15°, black: grain boundaries>15°, grey: twins, green: secondary twins).

of normal grains. However, since in this case both the density of twins and particles are lower, then it easier to distinguish grain boundaries on the optical microscope image. Then, the difficulty to detect overgrown grain boundaries in optical microscope images appears not to be linked to the "special" nature of the grain boundaries, since they are all random high angle boundaries. The difficulty probably arises from the high density of particles and twin boundaries that, being often better contrasted than other boundaries, hinder the detection of grain boundaries.

Such conclusion is corroborated by the analysis of the same zone of Figure 3.3 by optical profilometry, which allows to quantitatively measure the topography of the analysed surface. Figure 3.5 clearly shows that twin boundaries are highly contrasted in optical micrographs when they correspond to sharp transitions from valleys (dark areas) to peaks (bright areas) in the topography image.If the height profile along the black arrow is measured, then it is possible to quantify the distance from a valley to a peak which is about 250-300 *nm* (see Figure 3.6). On the contrary, twin boundaries are poorly contrasted if the transitions from valleys to peaks are smoother (as along the red arrow).

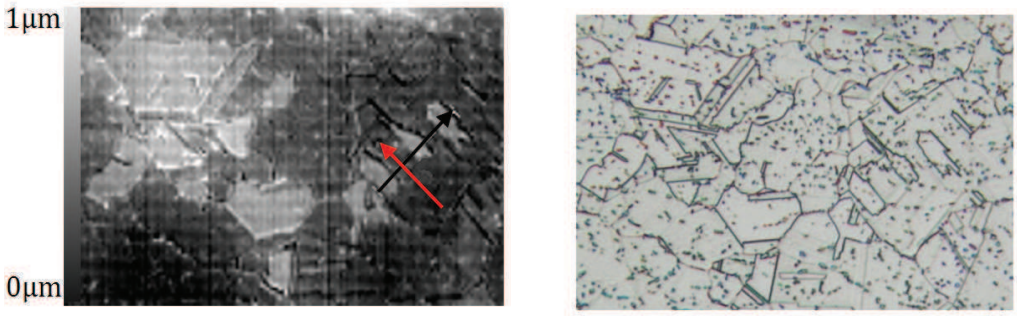

(a) (b)

Figure 3.5: Comparison of topography map (a) and optical microscope image (b) of overgrown grains.

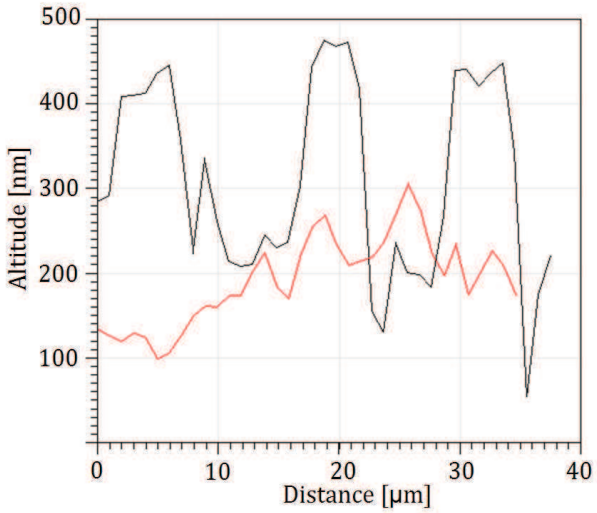

Figure 3.6: Height profile along the red and black arrows of Figure 3.5.

Indeed, such topography is the result of chemical etching whose intensity varies according to the crystallographic orientation of the grains at the surface. It is interesting to note that denser atomic planes should be more resistant to chemical etching compared to others. Now, as the matrix of Inconel 718 exhibits a face centered cubic structure, {111} dense planes should be less etched than other plane families. Figure 3.7 supports this statement as almost all plateau (bright areas) in the topography image correspond to planes {111} parallel to the sample surface.

In conclusion, the random intragranular distribution of δ phase particles and the high density of twins are definitely two significant aspects linked to the occurrence of overgrown grains. On the contrary, it seems that the boundaries of overgrown grains finally do not exhibit special features that distinguish them from normal grain boundaries.

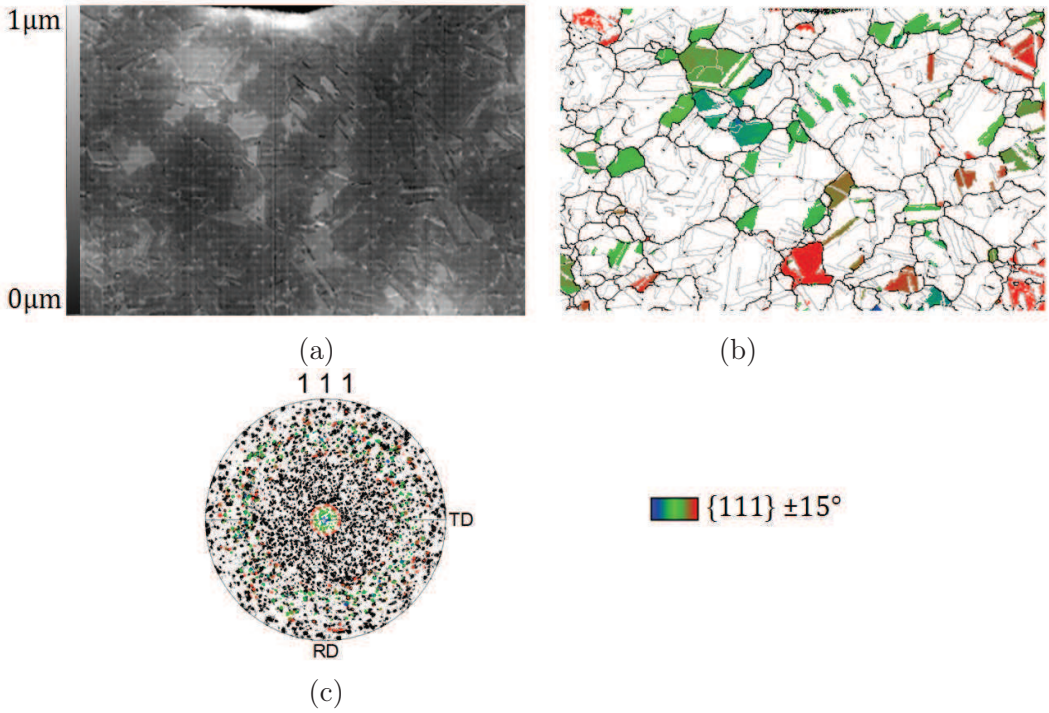

Figure 3.7: Comparison of topography map (a), EBSD map (b) and pole figure {111} of overgrown grains. Planes {111} parallel to the sample surface are highlighted with colors.

3.2 Industrial case studies

As mentioned in the introduction, industrial hot forging of a piece always involves a sequence of different deformation and annealing steps. Abnormal grain growth can occur during any annealing step following a deformation step. In this section, two different forged pieces where abnormal grain growth occured during industrial annealing are analysed. On each piece two zones which have followed a different thermomechanical path during the deformation step are investigated: zones A and B belong to the first piece, while C and D belong to the second one. Figure 3.8 illustrates the different thermomechanical paths for each analysed zone. As the area of zone B is quite large, an additional sample (B') is analysed in the same area.

	A	B	B'	C	D
$\bar{D}_N(\bar{D}_A)$ [µm]	12 (21)	6 (10.6)	5.4 (9.7)	9 (16)	6 (11.3)
δ fraction [%]	1.7	3.7	3.6	3.1	3
δ radius [µm]	0.25	0.3	0.3	0.4	0.35
$\overline{GOS}_A$ [°]	0.5	0.9	1.2	0.7	0.6

Table 3.3: Average microstructural properties of different zones analysed on industrial pieces after a deformation stage.

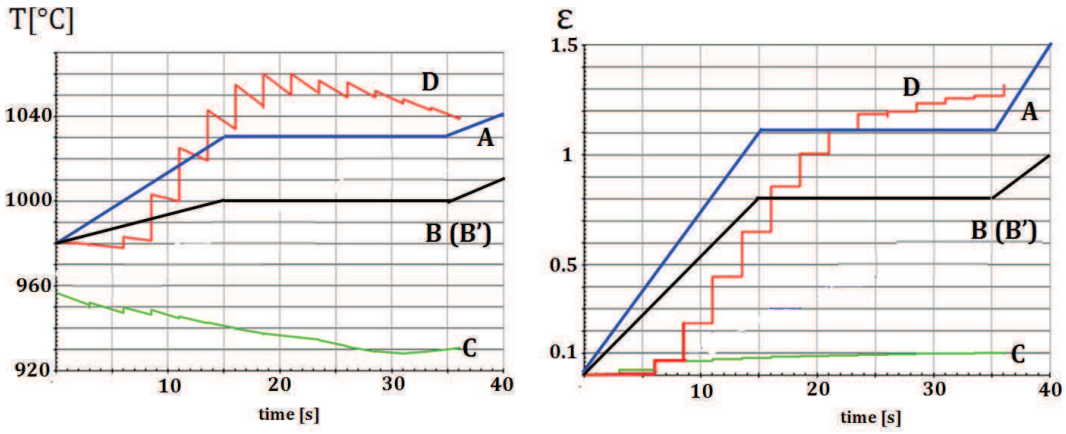

Figure 3.8: Different thermomechanical paths followed by zones A, B, C, D during the deformation step: (a) temperature and (b) strain evolution calculated by Forge® simulation.

It is to note that in all zones, except in the C zone, the final cumulative strain is higher than ε=1, so the final microstructure obtained after the deformation step should not be affected too much by the initial microstructure. In fact, dynamic recrystallization is supposed to be triggered in all samples (except in the C zone), leading to the formation of different microstructures as a function of thermomechanical conditions (temperature, strain, strain rate).

Table 3.3 and Figure 3.9 illustrate the average microstructural properties of the different zones after the deformation stage. Overall, all microstructures share similar properties which are probably the result of dynamic recrystallization that occured during the deformation stage. The average grain size is fine (in the range of 6-12 μm) and also intragranular misorientation is quite low (average GOS<1.2°). By comparison, in chapter 2 it was shown that a strain-free recrystallized grains has a GOS value of 0.3-0.4°, while unrecrystallized hardened grains have values higher than 3°. At least 2% surface fraction of δ phase is present in all microstructures and the average particle radius (0.2-0.4 μm) is similar.

Figure 3.9 shows in more details the differences between the microstructures. In samples A and B (or B') the morphology of δ phase particles is more heterogeneous: particles have both rounded and rod-like shapes. In samples C and D almost all particles are spheroids. Distributions of GOS values are similar, but they also show some differences. The GOS distribution of sample A is the narrowest and closest to small values, while the GOS distribution of sample B' is the broadest and shifted to higher values. Other distributions fall between these two extremes.

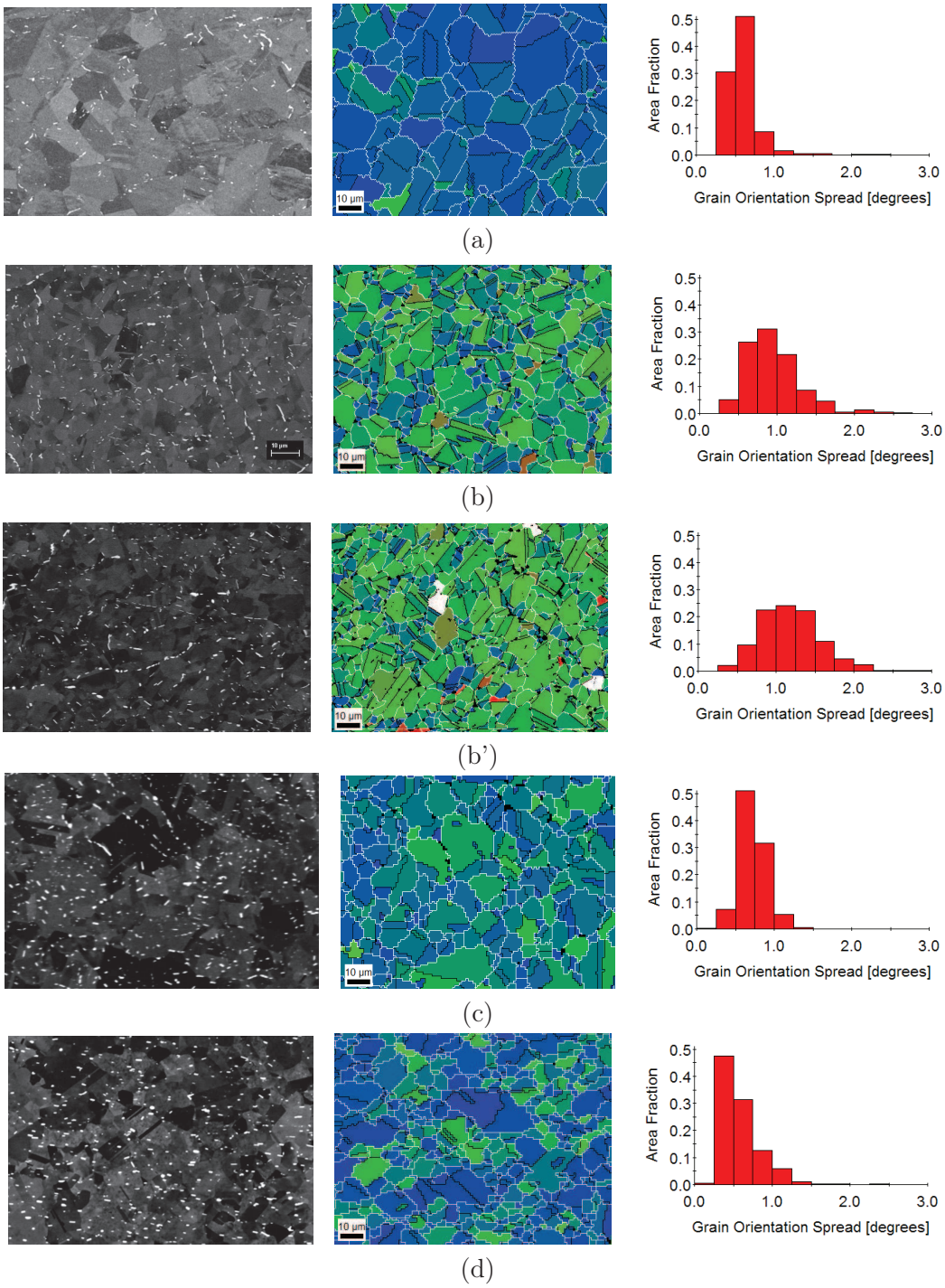

Figure 3.9: Microstructural properties of different zones analysed on industrial pieces after a deformation stage: (a) A, (b) B, (b') B', (c) C, (d) D. Left: BSE image. Center: EBSD map of GOS parameter (grain and twin boundaries are respectively white and black). Right: GOS distribution histogram.

3.3 Microstructure evolution during annealing

In the following, the microstructures of the two forged pieces are annealed at different δ sub-solvus temperatures to investigate the microstructure stability and the origin of

abnormal grain growth. The notation "X/T" will be used to label the microstructure of sample "X" after annealing at temperature "T" in degrees Celsius.

3.3.1 Annealing at 960°C

Samples B and B' were annealed at 960°C for 2 hours. Table 3.4 indicates that grain

	B/960	B'/960
$\bar{D}_N(\bar{D}_A)$ [μm]	6.2 (10.5)	10 (78)
δ fraction [%]	7	6
δ radius [μm]	0.5	0.5
$\overline{GOS}_A$ [°]	0.9	0.5

Table 3.4: Average microstructural properties of samples B and B' after annealing at 960°C for 2 hours.

growth did not occur at all in sample B/960 during annealing. Moreover, intragranular misorientation did not change either, suggesting that dislocation rearrangements (recovery) involving geometrically necessary dislocations did not occur. However, intragranular misorientation is not affected by statistically distributed dislocations, so it is not possible to completely exclude that recovery took place. On the contrary, in sample B'/960 grain growth occured and the GOS value decreases from 1.2° to 0.5°. The final microstructure is quite heterogeneous, as shown in Figure 3.10: coarse lower GOS grains and fine higher GOS grains are present. In both samples the δ phase particle fraction almost doubles and particles coarsen. As it will be shown in the next section, the different behaviour during annealing at 960°C of samples B and B' can be related to the initial different GOS distributions, which suggest different strain stored energy distributions.

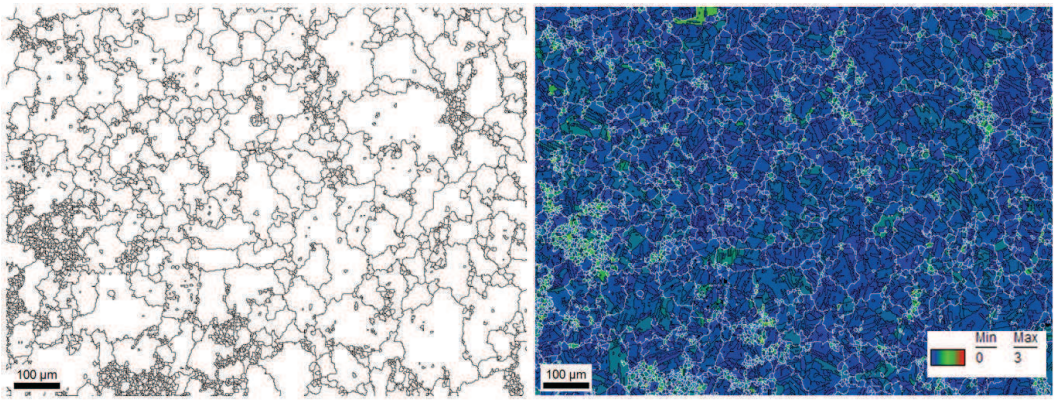

Figure 3.10: EBSD map of sample B'/960: (a) grain boundaries (b) GOS map where grain and twin boundaries are respectively white and black.

3.3.2 Annealing at 985°C

All samples from A to D and also sample B/960 were annealed at 985°C for 2 hours. The comparison of Table 3.3 and Table 3.5 indicates that in samples A/985 and C/985 almost no grain growth occured. Moreover, in these samples the average GOS value did not decrease after annealing. In all other samples the average GOS value decreases to similar values and the resulting GOS distribution is very narrow, like the one of Figure 3.9(a).

	A/985	B/985	B/960/985	B'/985	C/985	D/985
$\bar{D}_N$ ($\bar{D}_A$) [µm]	13 (22.5)	20 (97)	15 (101)	18 (50)	10 (20)	14 (31)
δ fraction [%]	2.4	3.7	4	3.8	4.5	4.5
δ radius [µm]	0.4	0.4	0.44	0.4	0.4	0.65
$\overline{GOS}_A$ [°]	0.6	0.6	0.5	0.5	0.7	0.5
T_G [-]	2.3	8	6.5	7.7	1.7	2.7
T_A [mm^{-1}]	165	200	186	237	143	159

Table 3.5: Average microstructural properties of different zones analysed on industrial pieces after annealing at 985°C for 2 hours.

It is to note that when dealing with possibly heterogeneous microstructures, average values can be misleading. Hence, heterogeneous microstructures will be described in more details. Figure 3.11 shows that grain growth does not occur in sample C/985: only few grains have grown and they have a lower GOS value compared to others. It is to note that even if sample C/985 is annealed for additional two hours at 985°C, such bigger low GOS grains do not grow at all. In all other samples generalized

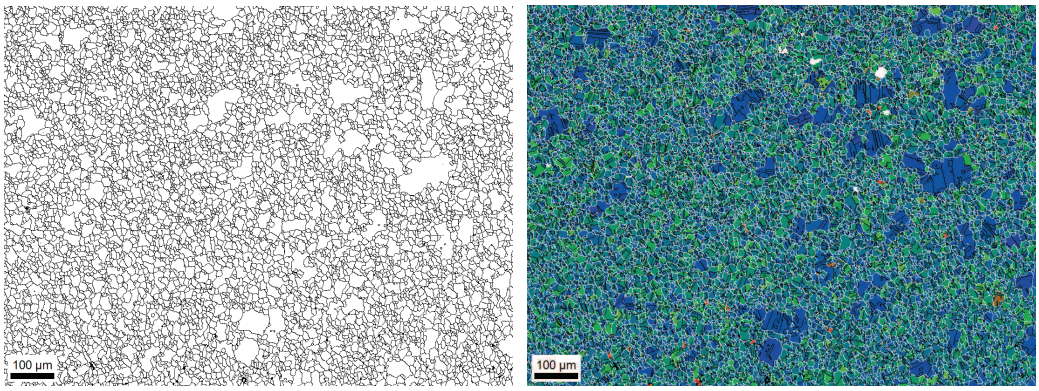

(a) (b)

Figure 3.11: EBSD map of sample C/985: (a) grain boundaries (b) GOS map where grain and twin boundaries are respectively white and black.

grain growth occured during annealing. The smallest final grain size is obtained in sample D/985, while the biggest final grain size is obtained in samples B/985 or B/960/985 where the final grain size is ten times bigger than the initial one. Figure

3.12 displays the microstructures of samples D/985 and B/960/985: they are both quite heterogeneous and contain many small initial grains that did not grow. This is clearer in sample B/960/985 where the final grain size is ten times bigger compared to the initial one. Moreover, in this sample the final twin density is also very high.

As already reported in Table 3.5, the grain size ($\bar{D}_A$) in sample B/985 or B/960/985 is almost the same: the size of overgrown grains is about 100 μm. This result reveals that pre-annealing at 960°C for two hours does not allow to prevent the occurrence of inhomogeneous coarsening during the subsequent annealing at 985°C for two hours. In fact, the higher δ phase fraction in sample B/960 seems to control only the fraction of small grains that remains in sample B/960/985, reducing the value of $\bar{D}_N$ with respect to sample B/985.

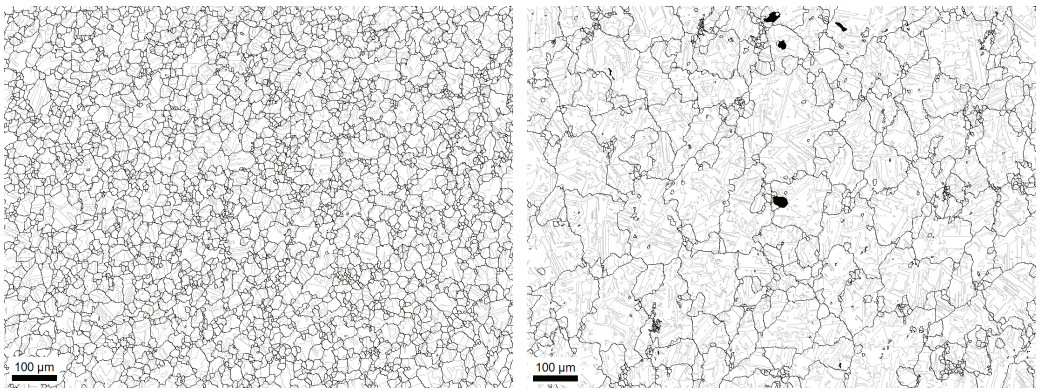

(a) (b)

Figure 3.12: EBSD maps of samples D/985 (a) and B/960/985 (b). Grain and twin boundaries are respectively black and grey.

The microstructure evolution of sample B/985 during annealing is illustrated in Figure 3.13. It reveals that grain growth occurs as a discontinuous process: isolated grains grow after 15 minutes, having almost the same size as the final grain size. Then, during time other overgrown grains appear at the expense of the fine initial grains that do not grow. Such behaviour is summarized in Figure 3.14 where the average grain size evolution during annealing is plotted. The evolution of the surface-weighted grain size follows the typical trend related to abnormal grain growth (see Figure 1.12). The number-weighted grain size curve shows that during annealing the fine initial grains do not grow at all. More precisely, even after one hour of annealing the number-weighted size of small grains is still equal to 6 μm. Moreover, even after 2 hours of annealing, there are several small grains, explaining why the number-weighted average is significantly lower than the surface-weighted average.

Experimental grain sizes can be compared to the limiting grain size predicted by the Smith-Zener equation (see Eq.(1.1)), as illustrated in Figure (3.15). It is to note that, as during annealing more δ phase particles precipitate, increasing the overall pinning force (except for sample B/960/985, where the δ phase fraction decreases,

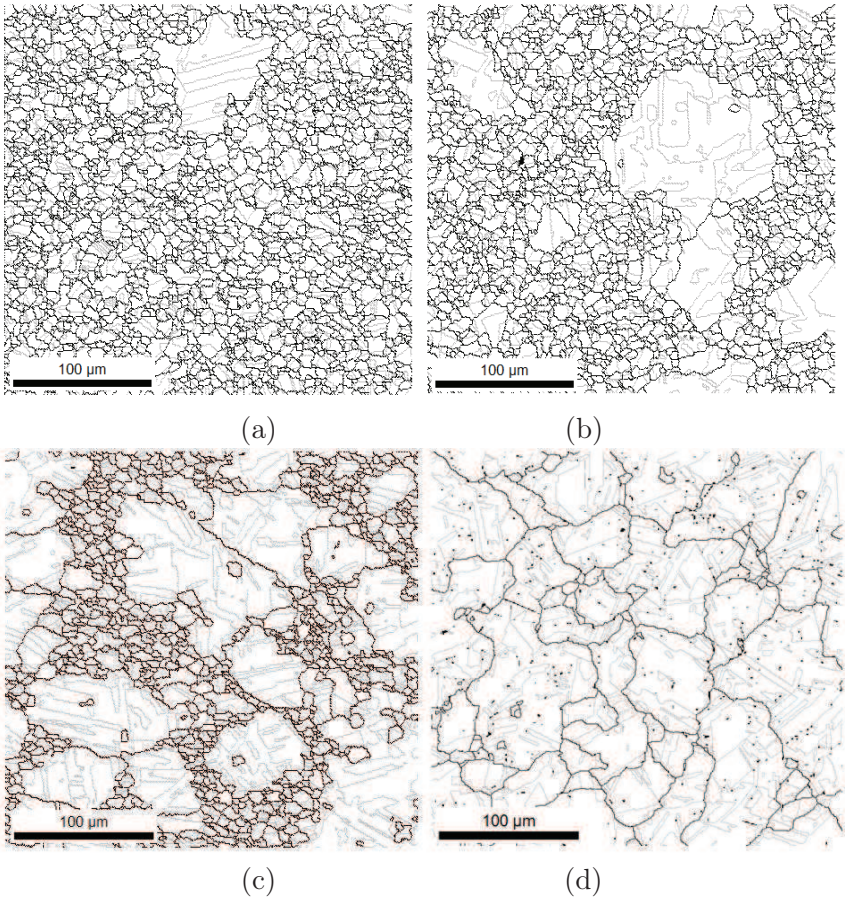

Figure 3.13: EBSD maps of samples B/985 during annealing after : (a) 15 minutes, (b) 30 minutes, (c) 60 minutes, (d) 120 minutes. Grain and twin boundaries are respectively black and grey.

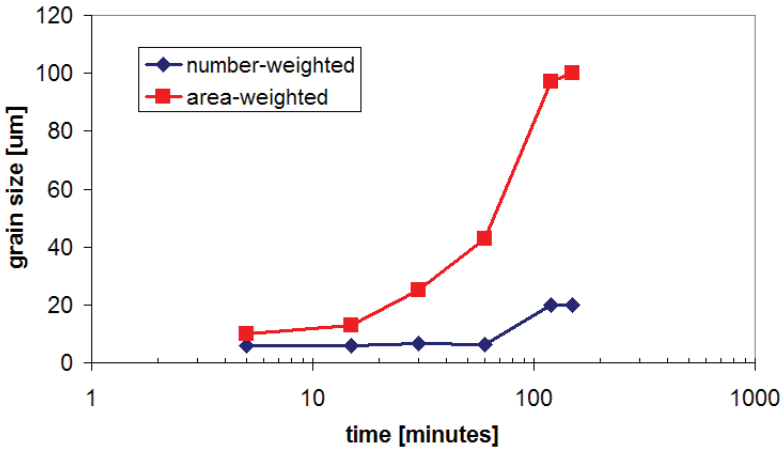

Figure 3.14: Average grain size evolution during annealing of sample B/985.

hence it is not treated here), the initial surface fraction of δ phase particles is taken into account, leading to an overestimation of the final grain size. Now, Figure (3.15) shows that $\bar{D}_N$ in samples A/985 and C/985 is well predicted by the Smith-Zener

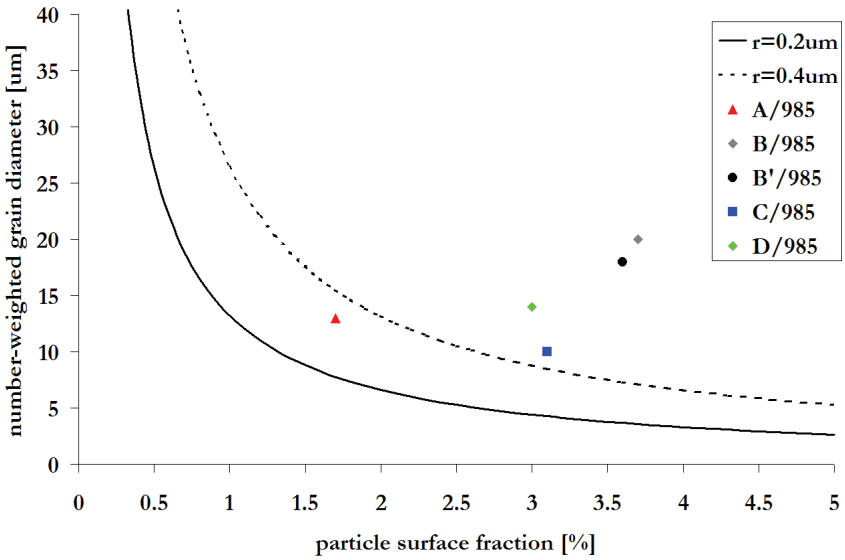

Figure 3.15: Comparison of Smith-Zener equation (Eq.(1.1) with K=0.33 and $\overline{r}$=0.2 μm or $\overline{r}$=0.4 μm) and microstructures obtained after annealing at 985°C for 2 hours.

equation with r=0.4 μm, meaning that particles do hinder grain growth. On the contrary, in all other samples the final grain size is higher than the prediction. Such deviation appears quite small but it reveals that, despite the presence of particles in all microstructures, grain coarsening eventually leading to abnormal grain growth occurs in some of the studied microstructures. For example, as already reported in Table 3.5, the value of $\bar{D}_A$ in sample B/985 or B/960/985 is five times bigger than in sample A/985. However, the microstructural feature triggering the phenomenon has to be investigated.

Origin of inhomogeneous grain growth In section 1.3 the main factors leading to abnormal grain growth were reviewed. Accordingly, in this section grain size, texture and strain induced effects are investigated to determine the triggering factor of the phenomenon.

In pinned microstructures few bigger grains can overgrow leading to abnormal grain growth simply because of a size advantage. Figure (3.16) shows the same plot of Figure (1.8) with the data points corresponding to microstructures of samples before annealing. The ratio of biggest grain over the average grain size ($X = \frac{D_{MAX}}{\bar{D}_N}$) is about 3-4 in all samples and the pinning parameter Ψ is in the range 0.4-0.6. Then, this analysis suggests that abnormal grain growth may occur in all samples during annealing. However, the phenomenon does not occur in samples A/985 and C/985. This could be due to the underestimation of the pinning pressure in the model that assumes a random distribution of spherical particles. Moreover, during annealing more δ phase particles precipitate, further increasing the pinning force, i.e. the value of Ψ.

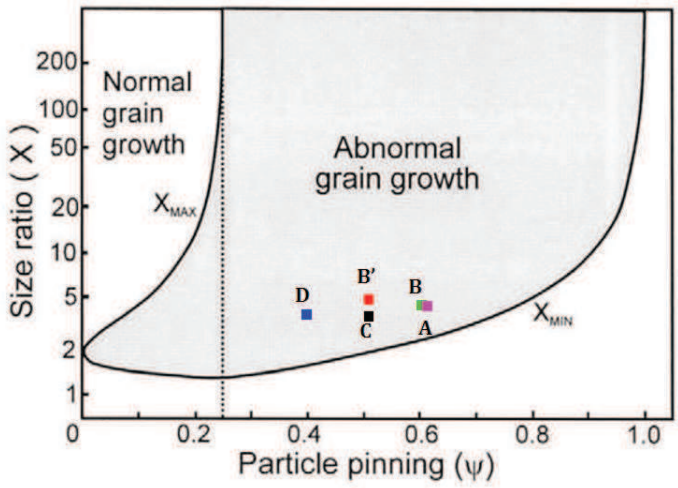

Figure 3.16: Plot of minimum grain size ratio to trigger abnormal grain growth as a function of Smith-Zener pinning [9] in samples A to D before annealing at 985°C.

Overall, the analysis of Figure 3.16 indicates that the initial distribution of grain size or δ phase is not sufficient to explain the occurence of abnormal grain only in certain samples. Indeed, such analysis is based only on the average pinning pressure and it does not take into account the local distribution of δ phase particles. For this reason, the local distribution of δ phase particles where overgrown grains appear was also investigated in sample B/985 after 15 minutes of annealing. Such short annealing time was chosen to limit the precipitation of new δ phase particles. The

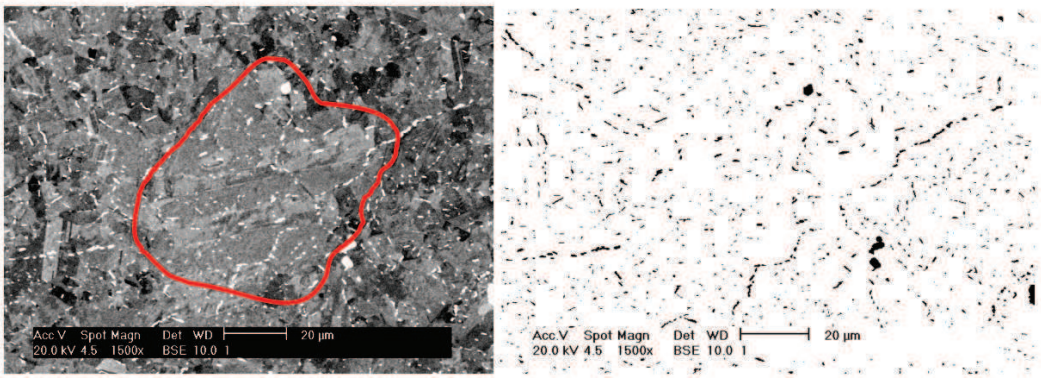

(a) (b)

Figure 3.17: Overgrown grain (surrounded by red line) appearing in sample B/985 after 15 minutes of annealing: (a) BSE image, (b) BSE image filtered to reveal only δ phase particles. Note: the 4 biggest black particles are carbides.

surface fraction of particles was measured both inside and outside overgrown grains as shown in Figure 3.17. Table 3.6 illustrates that the surface fraction measured inside or outside overgrown grains is not significantly different, while the average

particle size remains fairly constant (r=0.3 μm). Hence, the local heterogeneity of the particle distribution does not seem to be the key factor triggering abnormal grain growth.

overgrown grain	inside	outside
I	2.7	3
II	2.6	2.7
III	3.3	3

Table 3.6: Surface fraction of δ phase particles measured inside or outside three overgrown grains in sample B/985 after annealing fro 15 minutes.

If microstructures are strongly textured, then some grains can enjoy a mobility advantage leading to abnormal grain growth. That can not apply for any of the microstructures of the current study. In fact, the pole figures of Figure 3.18 indicate that only weak textures (close to random) are present in all samples.

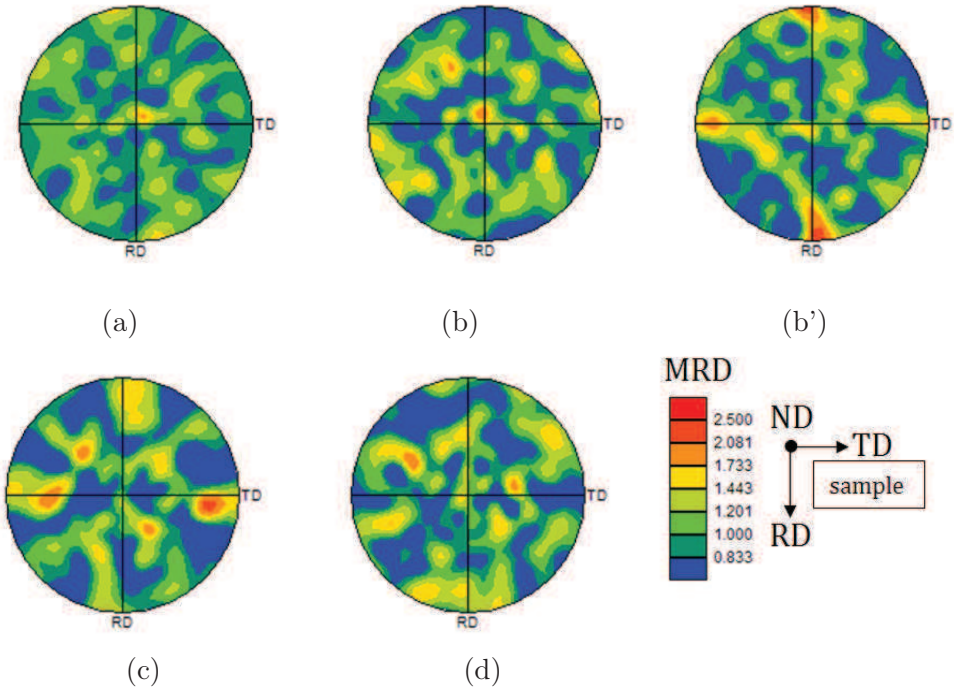

Figure 3.18: Pole figures of planes {100} in samples (a) A, (b) B, (b') B', (c) C, (d) D. Calculation method: harmonic series expansion (series rank=16, gaussian half-width=5°). The main deformation axis is along the RD direction.

The influence of strain on abnormal grain growth is not easy to be assessed. The reason is that the principal effect of strain on microstructures is to modify the dislocation structure (density and distribution) inside grains. Such dislocation structures can be investigated directly only by using very local characterization techniques: for

example transmission electron microscopy (TEM) for which statistical relevance is an issue or electron channelling contrast imaging (ECCI) in a SEM. However, dislocation structures can also be partially and indirectly assessed by EBSD through their effect on intragranular misorientation (see section 2.3).

Now, Figure 3.9 indicates that each microstructure before annealing is characterized by slightly different distribution of GOS, which describes the intragranular misorientation. In Figure 3.19 the average value and the standard deviation of each distribution before annealing are plotted in relation with the surface-weighted grain size after annealing. Such plot reveals that as the average GOS value (and its standard deviation) increases, the final grain size increases reaching a peak and then it falls down. Such evolution of the grain size is similar to that shown in Figure 1.15 if the level of strain is replaced by GOS values. Indeed, even if GOS values are not directly linked to the level of strain, it is reasonable to suppose that GOS values increase monotonically with strain, as long as dynamic recrystallization does not take place. Then, Figure 3.19 suggests that critical distributions of GOS, which imply critical distributions of dislocations, may trigger abnormal grain growth.

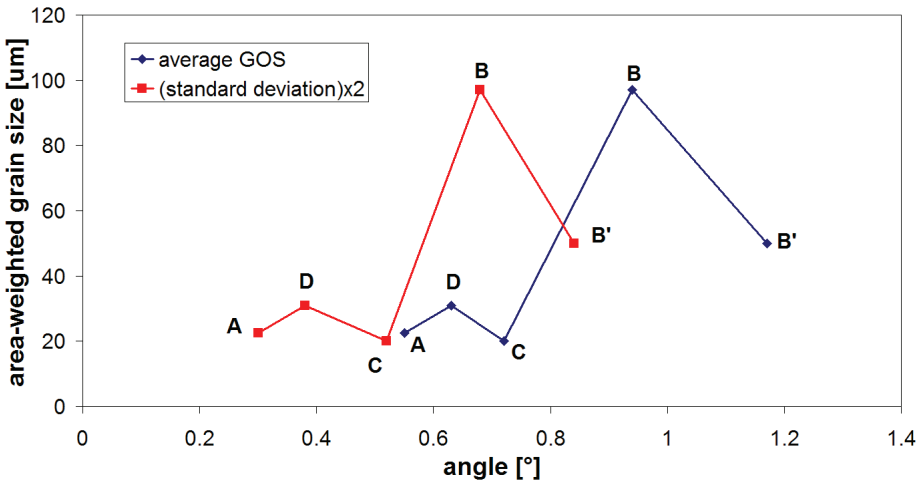

Figure 3.19: Influence of average and standard deviation of GOS histograms of microstructures from A to D before annealing on grain size after annealing at 985°C.

The estimation of driving pressures in samples B and B' provides a means to better understand the influence of strain on abnormal grain growth. In fact, in these two samples both the initial grain size and δ phase particle distribution are almost the same (see Table 3.3). However, average GOS values (respectively 0.9° and 1.2°) suggest that a small but significant difference may exist in terms of strain stored energy. In the following, Eq.(2.16) will be used to estimate the strain stored energy in these samples, considering only the contribution of GNDs. Indeed, this approach will lead to an underestimation of the total value of stored energy, however it will allow to semi-quantitatively estimate and compare the stored energy distributions in

the two samples.

	Pressure [kPa]
Pinning [Eq.(1.5), r=0.3 μm, f=3.6%]	-120
Capillarity [Eq.(2.15), 2R=6 μm]	50
Stored energy [Eq.(2.16), ΔGAM>0.5°/1.3 μm]	>70

Table 3.7: Comparison of the magnitude of driving and pinning pressures in samples B and B' before annealing.

Table 3.7 reports the estimated values of driving and pinning pressures for boundary migration in samples B and B'. It indicates that if stored energies differences are not present in microstructures, grain boundaries can not grow only by capillarity pressure due to pinning particles. In fact, the minimum stored energy difference across a grain boundary to trigger its migration is at least 70kPa. Using Eq.(2.16), 70kPa should correspond to a GAM difference between two grains of 0.5°/1.3 μm. Figure 3.20 shows that the GAM distribution of crystals spans from 0.4° to 1.8° in

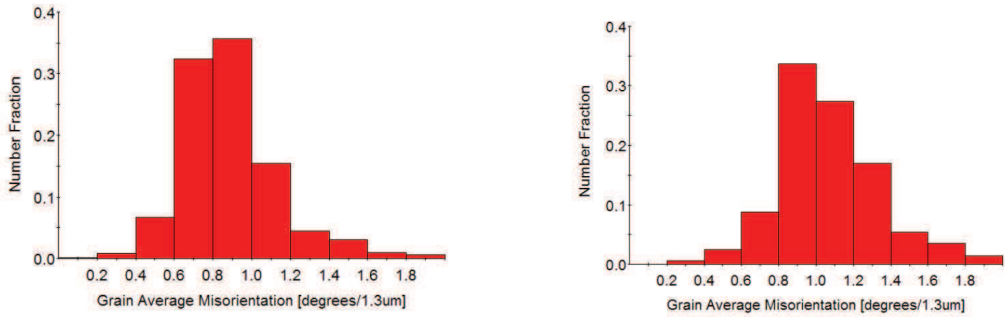

(a) (b)

Figure 3.20: Comparison between GAM histograms in samples (a) B and (b) B' before annealing.

both samples: it is also to note that in sample B' the distribution is shifted to higher GAM values. Then, from each GAM distribution it is possible to calculate the probability for a crystal boundary to separate two crystals with a given GAM difference. It is to note that such calculation is only statistically based, as it does not take into account the real topology of grain boundaries.

If f_i is the number fraction of crystals belonging to each class of the histogram of Figure 3.20 (where f_1 corresponds to the the furthest left and f_N to the further right class), then the probability (F_j) for a crystal boundary to separate two crystals belonging to two classes with a given GAM difference is:

$$F_j = 2\sum_{i=1}^{N-j} f_i \cdot f_{i+j}, \tag{3.1}$$

where N is the number of classes in the GAM histogram and j defines the GAM difference existing between the two crystals. For example, if $j = 0$, then the two crystals belong to the same class, if $j = 1$, they belong to adjacent classes, if $j = N - 1$, one belongs to the furthest left class and the other to the further right class of the histogram of Figure 3.20.

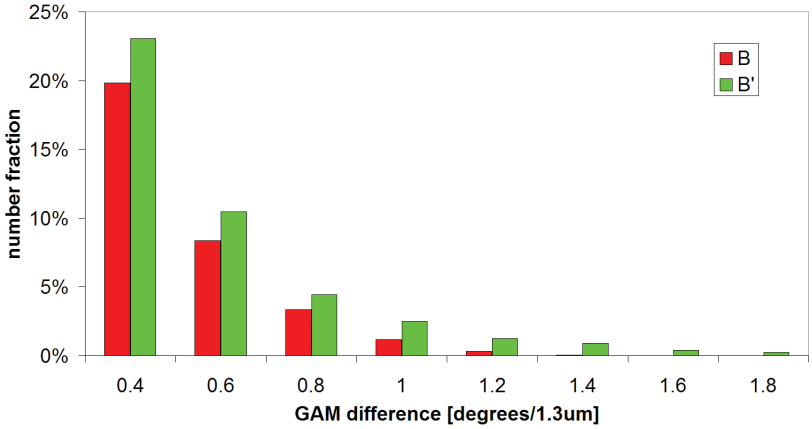

Figure 3.21: Histograms of the fraction of boundaries separating two crystals with a given GAM difference in samples B and B' before annealing. The fraction of boundaries corresponding to a GAM difference lower than 0.4°/1.3 μm is omitted.

Figure 3.21 indicates that indeed GAM differences higher than 0.5°/1.3 μm are found in both microstructures. Then, strain energy differences can trigger the growth of certain grains leading to abnormal grain growth. Moreover, in sample B' the total fraction of boundaries with a GAM difference higher than 0.5°/1.3 is higher compared to sample B. Then, the fraction of boundaries that can migrate driven by a stored energy difference would be higher in sample B', increasing the number of growing grains that will eventually impinge on each other hindering their growth. This would explain why after annealing the final grain size in sample B' is two times smaller than the one of sample B.

3.3.3 Annealing at 1010°C

Samples B, C/985 and D/985 were also annealed at 1010°C for 30 minutes. The average microstructural properties after annealing are reported in Table 3.8. Comparing the values with Table 3.3 and Table 3.5 shows that grain growth occurs in all samples. Moreover, unlike annealing at 985°C, in this case the δ phase fraction decreases in all samples as the temperature is closer to the higher δ solvus limit (1030°C). Average GOS values decrease in all samples to 0.5°, which is insignificant with regards to the accuracy of the EBSD measurements.

Microstructures of samples C/985/1010 and D/985/1010 are displayed in Figure 3.22. The average final grain size is very similar in both sample, however in sample

	B/1010	C/985/1010	D/985/1010
$\bar{D}_N$ ($\bar{D}_A$) [µm]	25 (62)	31 (120)	22 (120)
δ fraction [%]	2	3.3	2.5
δ radius [µm]	0.45	0.5	0.44
$\overline{GOS}_A$ [°]	0.5	0.5	0.5
T_G [-]	7	10.4	6
T_A [mm^{-1}]	160	142	130

Table 3.8: Average microstructural properties of different zones analysed on industrial pieces after annealing at 1010°C for 30 minutes.

D/985/1010 it is still possible to detect several small initial grains that did not grow. Moreover, both microstructures contain many twins.

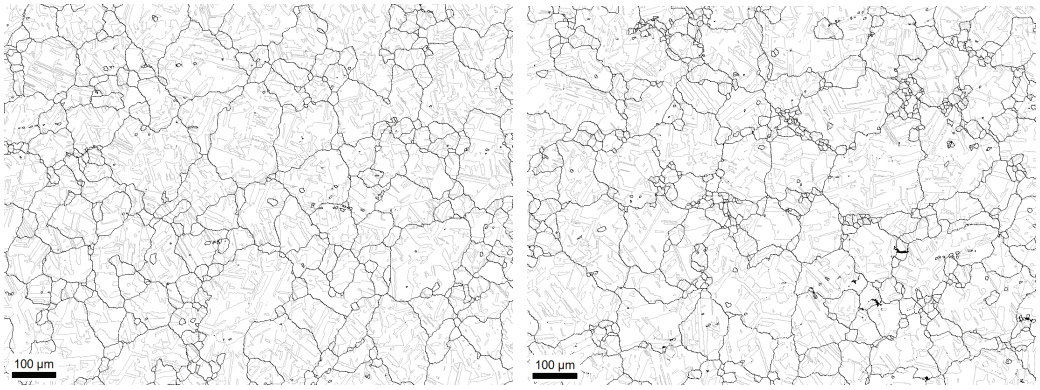

(a) (b)

Figure 3.22: EBSD maps of samples C/985/1010 (a) and D/985/1010 (b). Grain and twin boundaries are respectively black and grey.

Only sample B/1010 was also annealed at 1010°C for two hours: its evolution during annealing is shown in Figure 3.23. Grain size increases rapidly up to 30 minutes, then it slows down. It is to note that the average GOS decreases significantly during the first 15 minutes, then it remains constant at about 0.5° up to two hours. This suggests that strain stored energy driven grain growth occurs only during the first 15 minutes. Afterwards, grain growth is supposedly driven only by capillarity in a microstructure where δ phase particles continue to dissolve.

Once again, it is possible to compare the final grain sizes after annealing and the populations of δ phase particles with the Smith-Zener model. In this case, unlike annealing at 985°C, particles dissolve at 1010°C, then the final δ phase fraction after annealing is used in the Smith-Zener equation. Figure 3.24 shows that the final grain size ($\bar{D}_N$) is higher than the Smith-Zener limit for all samples. Such evolution can be explained by considering both the presence of strain energy and the dissolution of δ phase particles during annealing.

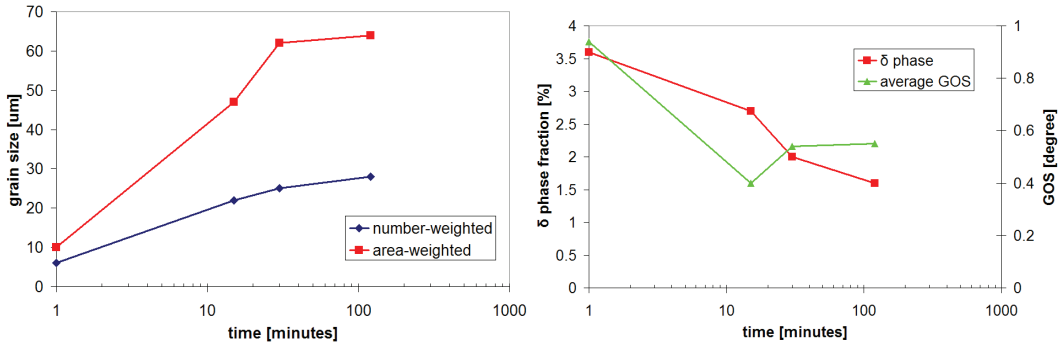

(a) (b)

Figure 3.23: Evolution of grain size (a), δ phase fraction and average GOS (b) in sample B/1010 during annealing at 1010°C for two hours.

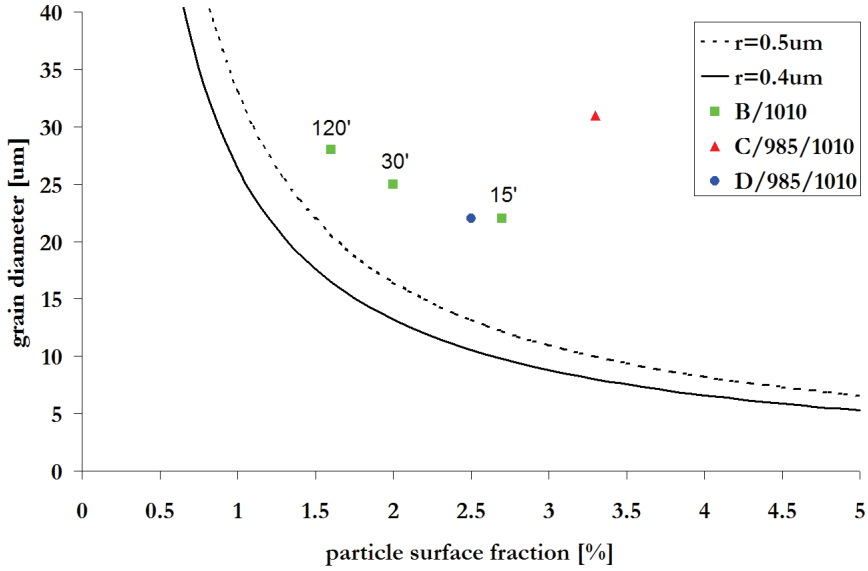

Figure 3.24: Comparison of Smith-Zener equation (Eq.(1.1) with K=0.33 and $\overline{r}$=0.4 μm or $\overline{r}$=0.5 μm) and microstructures obtained after annealing at 1010°C for 30 minutes.

Origin of inhomogeneous grain growth After annealing at 1010°C, final grain sizes overpass the Smith-Zener limit in samples B/1010 and C/985/1010 probably due to strain stored energy reduction. GOS histograms of both samples before annealing reveal that strain energies are indeed present in the microstructure (see Figure 3.9 and Figure 3.11). Then, during annealing differences of strain energies across boundaries trigger the coarsening of few grains. Such mechanism is the same as the one occuring at 985°C, however at 1010°C δ phase particles dissolve reducing the pinning pressure and thus the minimum stored energy difference to trigger the growth of grains. This would explain why in sample C/985/1010 the grain size ($\bar{D}_A$) increases up to 120 μm, while in sample C/985 almost no grain growth occured. Likewise, in sample B/1010 the final grain size after 15' (when all strain energy has been already consumed) or

even after two hours of annealing (64 μm) is smaller compared to the one of sample B/985 (97 μm), because in sample B/1010 the number of grains that overgrow and then impinge on each other is higher, thanks to the reduction of the Smith-Zener pinning forces.

However, it is not possible to exclude that the annealing temperature dependance of the final grain size in samples B and C/985 may be also due to the occurrence of nucleation, that is a thermally activated phenomenon. The nucleation of new strain-free grains at 1010°C would increase the number of growing grains, hence reducing the final grain size.

In the case of sample D/985/1010, the final grain size exceeding the Smith-Zener limit can not be explained by strain energy effects as after annealing the GOS value does not decrease with respect to the initial one (see Table 3.5). Moreover, sample D/985 is formed by grains that grew statically at 985°C, hence they should be strain-free. Then, the main driving force for boundary motion arises from grain boundary curvature that competes with Smith-Zener pinning. However, particles dissolution allows few grains to coarsen, gaining a size advantage with respect to pinned grains. Indeed, the final microstructure still contain many small initial grains. Such mechanism, triggered in pinned microstructure annealead at temperatures close to the dissolution temperature of particles, has already been discussed in section 1.3 for the case of steel (see Figure 1.9).

3.3.4 In situ annealing at δ super-solvus temperature

Sample B was in situ annealed at a δ super-solvus temperature in the chamber of the SEM. This technique allows to record the microstructure evolution of the same zone step by step, by performing EBSD scans after each annealing step. In the case under study, this technique appears very appealing, among other things, to analyse the properties of the initial grains that eventually will grow abnormally. The experimental set-up of this technique [73] requires the preparation of thin samples (less than 300 μm) that are welded on a tantalum sheet that heats the sample by the Joule effect. This technique allows to reach annealing or cooling rates of the order of 100°C/s. The sample area, that is analysed by EBSD at room temperature, is about 200x200 μm. Thermocouples are welded on the sample surface to measure and control its temperature. However, due to poor thermocouple welding conditions it was not possible to precisely record the temperature of the sample during the experiment. In fact, it is only possible to estimate that the temperature was higher than the δ super-solvus temperature (1025°C), as after only 5 minutes of annealing all δ phase particles are dissolved.

The evolution of the microstructure of sample B/>1025 is illustrated in Figure 3.25. The microstructure evolves discontinuously as low GOS grains grow at the expense of higher GOS grains until overgrown grains impinge on each other. Then,

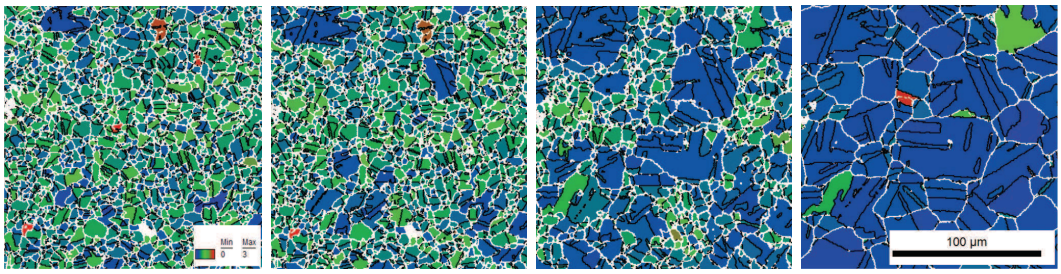

(a) (b) (c) (d)

Figure 3.25: GOS map evolution during super-solvus annealing of sample B/>1025: (a) 2', (b) 2'40, (c) 3'50, (d) 5'. Grain and twin boundaries are respectively white and black.

the final overgrown grain size is directly related to the number of grains that start to grow. The grain size evolution during annealing is reported in Figure 3.26. The first thing to notice is that even at a super-solvus temperature at least 2 minutes are necessary to trigger the growth of the first grains. Then, grain growth driven by strain energy advances rapidly as after 5 minutes all high GOS grains have disappeared. Interestingly, the final grain size of sample B/>1025 is almost the same as that of sample B/1010 after 15 minutes. This would suggest that the number of growing grains (which governs the final grain size) is not increased at δ super-solvus temperatures, while the growth kinetics is faster as expected.

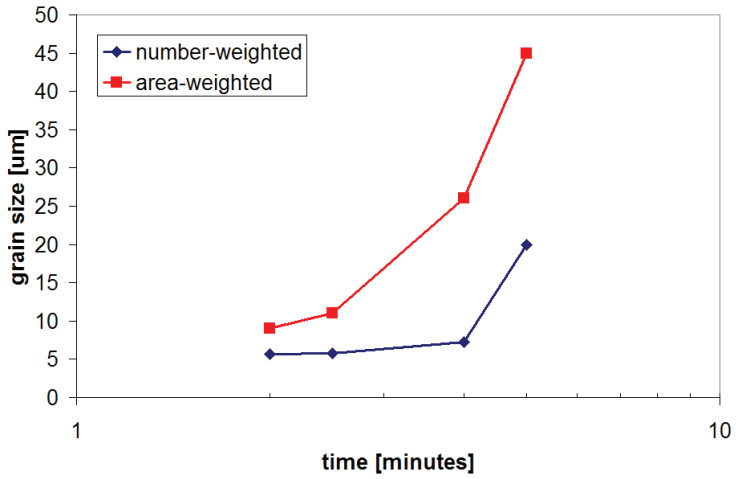

Figure 3.26: Average grain size evolution during annealing of sample B/>1025.

Concerning the origin of overgrown grains, none of them was already present in the mapped area of the initial microstructure. This can imply that a real nucleation process takes place, from which few new strain-free grains are formed and then overgrow. The nucleation process would be consistent with the observed existence of an incubation time during annealing at super-solvus temperatures or at 985°C (see Figure 3.13). The other possibility is that all overgrown grains originated from

grains which are just below the surface analyzed by EBSD and so they are not found in the scanned section. Moreover, the surface area analyzed by this technique is only 200x200 μm, so several tests should be performed to increase the statistical relevance of the results.

Overall, the annealing in situ analysis has confirmed qualitatively the current explanation of the phenomenon, as being driven by stored energies differences, but it has not cleared yet the precise origin of overgrown grains.

3.4 Summary

In this chapter, the distinctive microstructural properties of overgrown grains are compared with those of "normal" grains of equal size. Optical microscopy and EBSD analysis reveal that overgrown grains are characterized by a higher fraction of intragranular δ phase particles and twin density (T_A) is about two times higher compared to normal grains. It is also shown that overgrown grain boundaries are mostly general random high angle grain boundaries as those of normal grains. It is demonstrated that the poor contrast of overgrown grain boundaries analyzed by optical microscopy is mainly an artefact due to the high fraction of twin boundaries which are mostly better contrasted.

Several microstructures taken from two industrial pieces are analyzed before and after annealing at different δ sub-solvus temperatures. During annealing at 985°C, abnormal grain growth is triggered in those microstructures where a critical distribution of strain stored energy is present. It is shown that abnormal grain growth occurs when the stored energy driving pressure for boundary migration is of the same order of magnitude as the capillarity pressure, allowing to overcome the Smith-Zener pinning pressure (about 100kPa). The mechanism involves the selective growth of few low energy grains at the expanse of higher energy grains. Such mechanism assumes that low energy grains are already present before annealing, however it is not possible to exclude that low energy grains are generated by nucleation. Below a critical stored energy level, no grain growth occurs due to Smith-Zener pinning. It is shown that the average intragranular misorientation (via the GOS parameter) of a microstructure before annealing can be related to its grain size after annealing at 985°C.

During annealing at 1010°C, abnormal grain growth is also triggered by strain stored energy reduction, with the same mechanism occuring at 985°C. However, for a given initial microstructure, the number of growing grains is higher at 1010°C than at 985°C, suggesting the occurrence of a thermally activated mechanism like nucleation. In the absence of strain stored energy, abnormal grain growth can be also triggered by the dissolution of δ phase particles at 1010°C. In this case, few grains can gain a size advantage and grow faster than the others.

Overall, the analysis of microstructures of industrial pieces has allowed to identify

the most probable cause of inhomogeneous grain growth, that is strain stored energy. However, the critical thermomechanical conditions responsible for the formation of a critical distribution of strain stored energy have not yet been addressed. Figure 3.8, which reports the thermomechanical history of each microstructure, suggests that small strains ($\varepsilon < 0.3$) may be involved. This is clear for sample C, where the total cumulative strain is lower than $\varepsilon = 0.1$. In all other samples, even if the total cumulative strain is higher than $\varepsilon = 1$, it is to note that strain is applied non-uniformly: the highest amount of the total strain is applied during the first 10-20s, while a small strain ($\varepsilon < 0.3$) is applied during the last seconds of each cycle. Hence, small strains are indeed applied at the end of each cycle but their effect on microstructure hardening can not be directly investigated as only the final microstructure of each cycle could be characterized. Moreover, strains are applied at different temperatures, increasing the difficulty to discuss the effect of straining.

For this reason, it seems worth investigating the effect of small strains using hot torsion tests where the critical thermomechanical parameters can be identified and studied. Moreover, the focus will be placed on the occurrence of inhomogeneous grain growth during annealing at 985°C. In fact, it appears that at 1010°C (close to the δ solvus temperature), inhomogeneous grain growth can be triggered also by the dissolution of δ phase particles.

Résumé

Dans la première partie de ce chapitre, les caractéristiques des grains anormaux sont comparées avec celles de grains « normaux » de même taille. La microscopie optique et l'analyse EBSD ont révélé que pour les grains anormaux la fraction de particules de phase δ intragranulaire est plus élevée et que la densité de macles (T_A, longueur de joints de macle par unité d'aire) est environ deux fois plus importante que celle des grains normaux. De plus, la plupart des joints délimitant les grains anormaux sont des joints généraux de forte désorientation, comme les joints des grains normaux. Il a également été démontré que le faible contraste des grains anormaux qui apparaît dans les micrographies optiques est un artefact causé principalement par l'importante densité de macles dont certaines apparaissent plus contrastées que les autres joints de grains. Plusieurs microstructures prélevées sur des pièces industrielles ont ensuite été analysées avant et après un recuit à différentes températures, mais toujours en dessous de la température de solvus de la phase δ. Après un recuit à 985°C, la croissance anormale des grains est déclenchée dans les microstructures où était stockée une distribution critique d'énergie de déformation. La croissance anormale apparaît lorsque la force motrice des joints de grains liée aux différences d'énergie stockée est du même ordre de grandeur que la force capillaire et s'ajoute à celle-ci pour dépasser la force de freinage de Smith-Zener (100kPa). Ce mécanisme prévoit donc la croissance préférentielle d'un nombre limité de grains de faible

énergie par rapport aux grains voisins. A ce stade, on suppose que les grains de faible énergie se trouvent initialement dans la microstructure avant recuit, mais on ne peut pas exclure la possibilité que ces grains soient issus d'un processus de germination. On remarque également qu'en dessous d'un niveau critique d'énergie stockée, la croissance des grains est en revanche complètement bloquée grâce à l'ancrage de Smith-Zener. De plus, la désorientation intragranulaire moyenne (définie ici comme le paramètre GOS, grain orientation spread) d'une microstructure avant recuit peut être reliée à la taille de grain finale après recuit à 985°C. Après un recuit à 1010°C, la croissance anormale des grains est aussi déclenchée par la réduction de l'énergie stockée, suivant le même mécanisme qui se produit à 985°C. Cependant, pour une microstructure donnée, le nombre de grains anormaux qui grossissent pendant un recuit à 1010°C est plus important que celui à 985°C : ce résultat suggère l'intervention d'un processus thermiquement activé, qui pourrait être la germination. Il est à noter que la croissance anormale peut être déclenchée aussi en absence d'énergie stockée. Dans ce cas, le mécanisme est différent et repose sur la dissolution de particules de phase δ permettant à certains grains d'acquérir un avantage de taille suffisant pour grossir beaucoup plus rapidement que les autres grains. Globalement, l'analyse des microstructures des pièces industrielles a donc permis d'identifier la cause la plus probable de la croissance anormale, c'est-à-dire l'énergie de déformation. Cependant, les conditions thermomécaniques qui provoquent la formation d'une distribution critique d'énergie restent à étudier. Les courbes de la Figure 3.8, décrivant l'histoire thermomécanique de chacune des microstructures prélevées dans les pièces industrielles, suggèrent que de petites déformations ($\varepsilon<0.3$) pourraient être responsables de la formation de microstructures critiques. Cela apparaît évident pour l'échantillon C où la déformation totale cumulée ne dépasse pas $\varepsilon=0.1$. Dans les autres échantillons, même si la déformation totale cumulée dépasse $\varepsilon=1$, on remarque qu'une petite déformation est systématiquement appliquée à la fin de chaque cycle tandis que la déformation est appliquée de façon progressive: la plus grosse partie de la déformation totale est appliquée pendant les premières 10 à 20s. Cependant, l'effet de ces petites déformations sur l'écrouissage n'a pas pu être isolé car il n'a pas été possible de prélever des échantillons juste avant leur application. Seule la microstructure résultante de la gamme complète a été caractérisée. De plus, les déformations sont appliquées en conditions industrielles à des températures différentes, ce qui augmente la complexité de l'analyse. Par conséquent, il sera intéressant d'étudier l'effet de petites déformations en mettant en place des essais de torsion à chaud pour étudier et quantifier les paramètres thermomécaniques critiques. Dans la suite, l'étude portera uniquement sur l'apparition de la croissance anormale des grains à 985°C. A cette température, le phénomène semble être principalement contrôlé par l'écrouissage, qui fournit une force motrice supplémentaire et permet de dépasser la force d'ancrage de Smith-Zener. On retiendra toutefois que, comme mentionné plus haut, lorsque le recuit est appliqué à une température proche du solvus de la phase δ (1010°C)

le phénomène peut également être déclenché aussi par la dissolution des particules. Le couplage de ces deux mécanismes est complexe et nécessitera ultérieurement une étude dédiée, intégrant l'évolution des particules de phase δ.

4 Study of abnormal grain growth with mechanical testing

Contents

In this chapter torsion tests are exploited to investigate the influence of small prior strains on the occurence of abnormal grain growth during δ sub-solvus annealing at 985°C for two hours. First of all, a reference microstructure is generated such that it is free of strain stored energy and grain size is fine (10 μm) and homogeneous. The effect of δ sub-solvus small strains on microstructure stability during subsequent annealing is investigated. Then, it is shown that critical conditions leading to abnormal grain growth are similar even if super-solvus or room temperature small strains are applied.

4.1 Sub-solvus straining

In this torsion series a reference microstructure is subjected to small strains ($\varepsilon<0.3$) applied at 985°C (see Figure 4.1). Then, the influence of such small strains on the stability of the reference microstructure during δ sub-solvus annealing at 985°C for two hours is investigated. It is recalled that all EBSD measurements are performed as described in Figure 2.13, so the top of each EBSD map always corresponds to the surface of the torsion sample where the maximum strain is reached.

4.1.1 Reference microstructure stability

The reference microstructure is obtained as described in Figure 4.1 where the dotted line marks when such microstructure is cooled down to room temperature to be

characterized. Three stages are necessary to produce the reference microstructure.

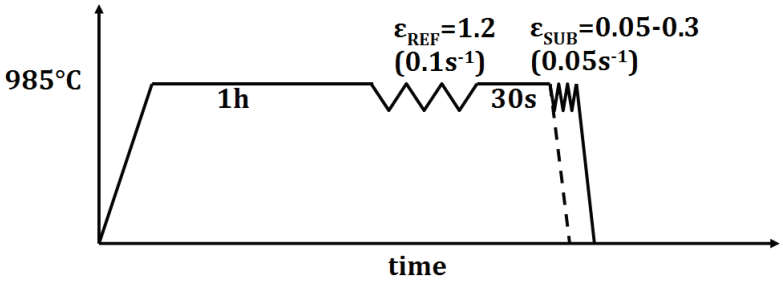

Figure 4.1: Thermomechanical scheme of the sub-solvus torsion series. The dotted line marks the cooling of the reference microstructure.

First of all, the torsion sample (that is machined from an Inconel 718 billet) is annealed at 985°C for one hour to dissolve hardening particles (γ'' and γ') and to precipitate δ phase particles. Then, the sample is strained up to ε=1.2 ($0.1s^{-1}$) to trigger dynamic recrystallization. Finally, it is maintained for 30 seconds at 985°C allowing post-dynamic recrystallization to take place. The influence of post-dynamic recrystallization on microstructure evolution can be seen in Figure 4.2. Just after deformation up to ε=1.2 the microstructure is partially recrystallized: big hardened grains coexist with fine recrystallized grains which are partially hardened as well. Such microstructure is similar to that of Figure 2.6(c) which was obtained with ε=1 ($0.1s^{-1}$). After holding at 985°C for 30 seconds strain-free recrystallized grains have grown and fill the microstructure: only few hardened grains remain. Then, an almost strain-free microstructure is formed. Such microstructure (displayed in Figure 4.2(b)) will be further referred to as the reference microstructure (REF_{SUB}).

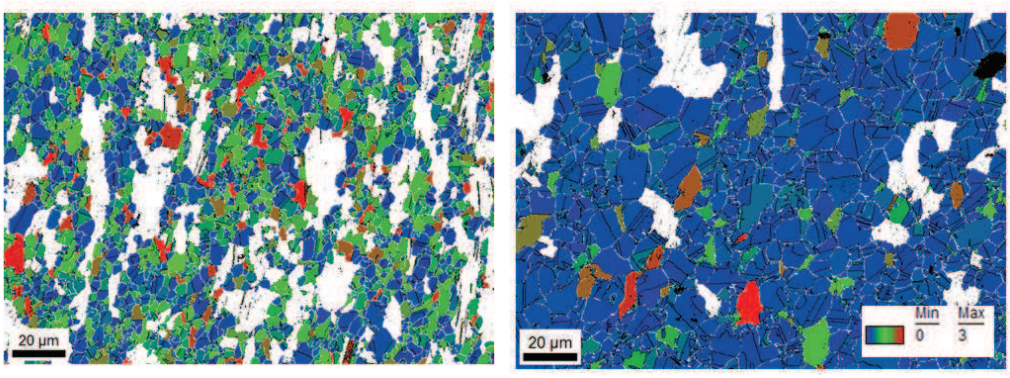

(a) (b)

Figure 4.2: GOS maps (grain and twin boundaries are respectively white and black) of reference microstructure just after deformation up to ε=1.2 (a) and after 30 seconds of annealing at 985°C (b). White grains have GOS values higher than 3°.

The properties of the reference microstructure are summarized in Table 4.1. The average grain size is quite fine and comparable to those measured in the industrial pieces of chapter 3. The average GOS parameter is low because almost all grains are recrystallized.

	REF_{SUB}	REF_{SUB}/985
$\bar{D}_N(\bar{D}_A)$ [µm]	5.8 (11)	7.2 (12)
δ fraction [%]	1.7	4
δ radius [µm]	0.25	0.4
$\overline{GOS}_A$ [°]	0.6	0.5

Table 4.1: Average microstructural properties of reference microstructure (REF_{SUB}) before and after annealing at 985°C for two hours.

Annealing If the reference microstructure (REF_{SUB}) is further annealead at 985°C almost no grain growth occurs as shown in Table 4.1. Only a slight increase in grain size and a decrease of the GOS parameter can indeed be detected. The GOS reduction is probably due to the disappearance of the few hardened grains still present in the microstructure before annealing. In any case, the microstructure can be considered to be stable during annealing as abnormal grain growth does not occur (see Figure 4.3).

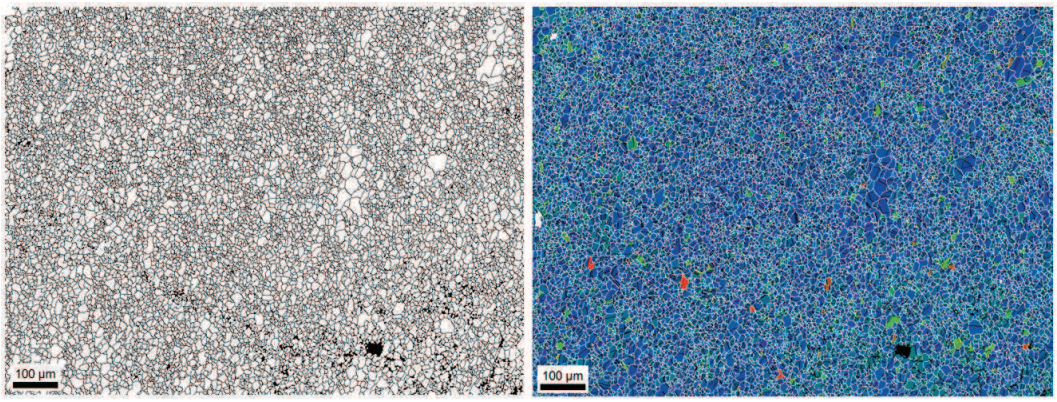

(a) (b)

Figure 4.3: Microstructure evolution of the reference microstructure after annealing at 985°C for 2 hours: grain boundaries (a) and GOS map (b) where grain boundaries are white, twins are black and white grains have GOS values higher than 3°.

As expected, the δ phase fraction increases during annealing at 985°C. Particles pin grain boundaries, so grain growth driven by capillarity is hindered. The microstructure after annealing nevertheless exhibits few grains somewhat bigger than the average grain size (see Figure 4.4). Such grains are indeed correlated with lower

local fractions of δ phase. However, it remains questionable if the heterogeneity of the δ phase distribution after annealing should be considered as the origin or the consequence of such grain size heterogeneity. In fact, as δ phase particles precipitate preferentially on grain boundaries, the local fraction of particles around bigger grains is lower. As it will shown in the next section (see sample $\varepsilon_{SUB} = 0.05/985$), such bigger grains do not grow further even after two additional hours at 985°C.

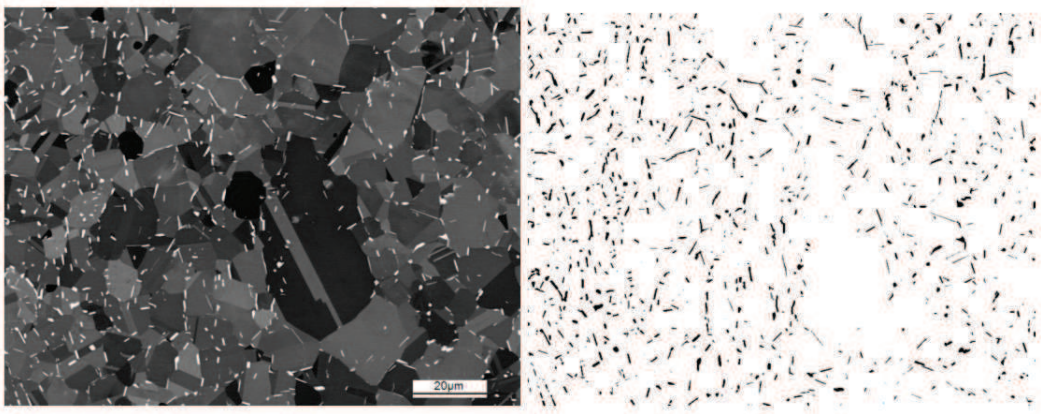

(a) (b)

Figure 4.4: Correlation of grain size with δ phase fraction in sample $REF_{SUB}/985$: BSE image (a) and BSE image filtered to show only δ phase particles (b).

4.1.2 Influence of hardening on microstructure stability

In the previous section it was shown that a reference microstructure, that is strain-free and with fine grains, is stable during annealing at 985°C for 2 hours. In this section the influence of hardening on the stability of the reference microstructure is investigated. Different levels of strain are applied to the reference microstructure (see Figure 4.1): $\varepsilon_{SUB} = 0.05 - 0.1 - 0.3$. As expected, Table 4.2 indicates that the

ε_{SUB}	0.05	0.1	0.3
$\bar{D}_N(\bar{D}_A)$ [µm]	5.2 (8.4)	4.6 (8.5)	4 (9.2)
δ fraction [%]	1	2.2	1.4
δ radius [µm]	0.25	0.25	0.25
$\overline{GOS}_A$ [°]	0.8	1.2	2.4

Table 4.2: Average microstructural properties of reference microstructure after application of low strains.

microstructures of strained samples do not differ much from the reference microstructure in terms of grain size and δ phase distribution. The average grain size ($\bar{D}_N$) is 4-5 µm and the δ phase surface fraction is in the range 1-2%. Only GOS values

are significantly higher due to straining. Figure 4.5 reveals how GOS distributions

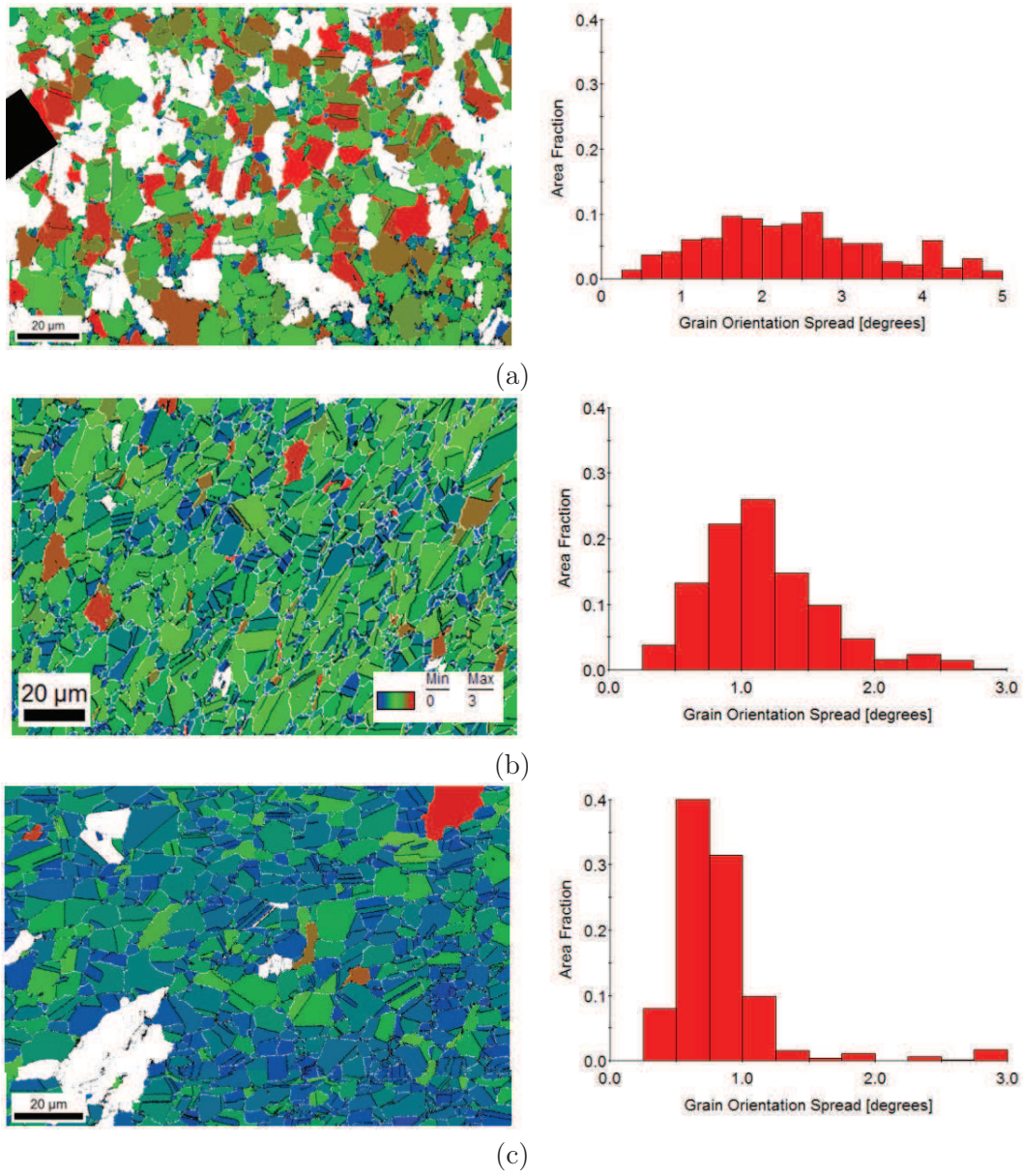

Figure 4.5: Grain orientation spread (GOS) distribution in samples $\varepsilon_{SUB} = 0.3$ (a), $\varepsilon_{SUB} = 0.1$ (b), $\varepsilon_{SUB} = 0.05$ (c). In GOS maps grain boundaries are white, twins are black and white grains have GOS values higher than 3°.

widen and shift towards higher values as strain increases. It is interesting to note that GOS histograms can reveal differences in hardened microstructures induced by differences in strain as small as $\varepsilon = 0.05$.Moreover, GOS values can be well correlated to the local values of strain (see Figure 4.6). In fact, in the range $\varepsilon = 0.05 - 0.3$ GOS values increase almost linearly with respect to strain. Similar considerations can be made about the evolution of the standard deviation (i.e. the width of the GOS distribution).

At this point, it seems interesting to investigate the relation between the stress-

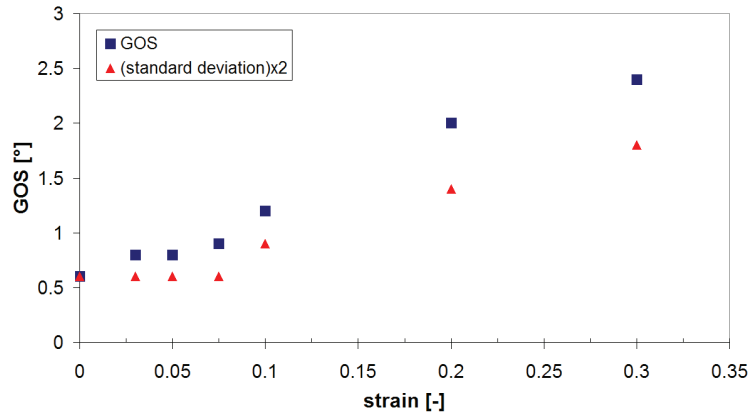

Figure 4.6: Correlation between strain and average or standard deviation of GOS histograms.

strain curves of the two hot torsion tests of the cycle of Figure 4.1 and the hardened microstructures presented in Figure 4.5.

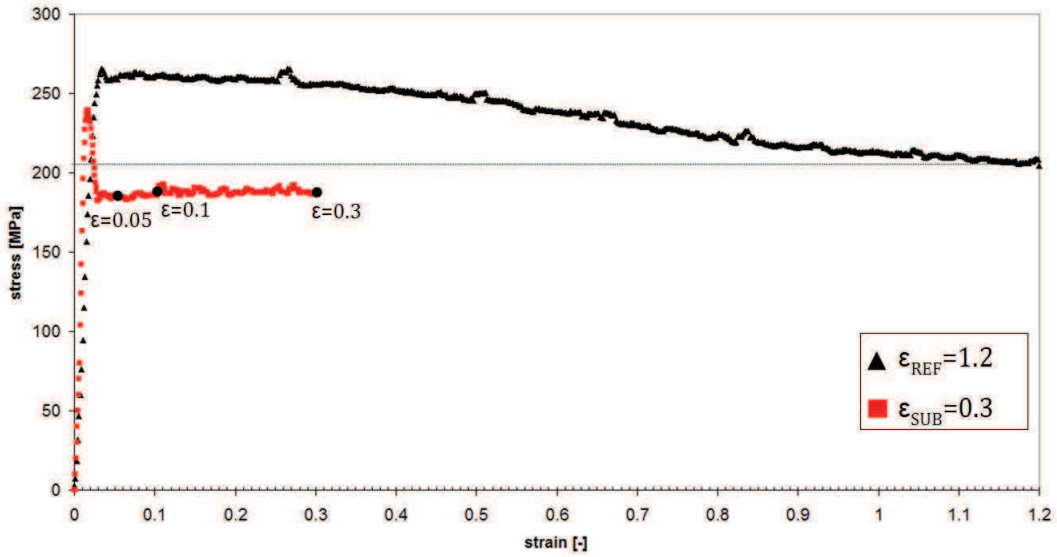

Figure 4.7: Stress-strain curves of the two hot torsion tests of the cycle described in Figure 4.1.

In Figure 4.7, the evolution of the stress-strain curve related to the generation of the reference microstructure (ε_{REF}) is governed by the occurrence of dynamic recrystallization. In fact, the stress reaches a broad peak at about $\varepsilon = 0.07$, then it decreases due to the formation of new recrystallized grains, eventually reaching the steady stress at about 200MPa. The microstructure at $\varepsilon = 1.2$ and its post-dynamic evolution during 30s were already shown in Figure 4.2. The stress-strain curve of the second torsion test exhibits a very sharp peak at about $\varepsilon = 0.02$, then the stress slighly increases reaching a steady stress at about $\varepsilon = 0.2$ that is lower than the one of the first torsion test. The first sharp peak is attributed to the

blocking of dislocations due to solute atoms, as already observed in the literature [74]. It is to note that, as previously shown (see Figure 4.5), grain structure does not evolve significantly increasing strain up to $\varepsilon = 0.3$, while intragranular misorientation (GOS) does increase.

These results clearly reveal that the initial microstructure greatly affects the stress-strain behaviour. In particular, if the initial microstructure is fine and strain-free, the typical broad stress peak associated with the nucleation of new grains does not appear. Instead, the stress slightly increases, due to hardening, before entering the steady stress regime where nucleation of new grains or other softening mechanisms may come into play.

Annealing Microstructure evolution of strained samples after annealing at 985°C for 2 hours is illustrated in Figure 4.8. Microstructures suggest a clear relation between the final grain size and the strain level applied before annealing. In sample $\varepsilon_{SUB} = 0.05$ only few grains have grown during annealing: these grains are characterized by low GOS values. However, the overall microstructure does not coarsen and the strain energy introduced by deformation is still stored in grains as shown by the GOS map. In sample $\varepsilon_{SUB} = 0.1$, a dramatic increase of grain size has occured during annealing. In the upper part of the sample where $\varepsilon = 0.1$, the microstructure is almost homogeneous, composed by one population of strain-free overgrown grains. In the lower part of the sample where $\varepsilon = 0.07$ there are clearly two populations of hardened fine grains and strain-free overgrown grains. If the two populations are analyzed separately, the number-weighted grain size of the two populations are respectively equal to 6.2 μm and 52 μm. So, fine grains coarsened a bit with respect to the initial grain size before annealing (4.6 μm). Such heterogeneous microstructure is the result of the discontinuous growth of selected grains, a phenomenon that can be referred to as abnormal grain growth with regards to the resulting grain size distribution. In sample $\varepsilon_{SUB} = 0.3$ the overall microstructure is quite homogeneous: it is composed by strain-free grains 3-4 times bigger than the initial ones. It is also to remark that grain size increases from the top ($\varepsilon = 0.3$) to the bottom ($\varepsilon = 0.2$) of the map.

Table 4.3 summarizes the properties of strained samples after annealing. The grain size and GOS values in sample $\varepsilon_{SUB} = 0.05$ are very close to those before annealing. On the contrary, in other samples GOS values decreased, as a result of hardened grains being consumed. The most significant microstructure evolution occured in sample $\varepsilon_{SUB} = 0.1$. The final grain size is 6 times bigger than the initial one and twin density (T_A) is very high, reaching almost the same value as the one of sample B'/985 from the industrial piece (see Table 3.5). Indeed, microstructure evolution in sample $\varepsilon_{SUB} = 0.1$ closely resembles the phenomenon occuring in sample B'/985.

Figure 4.9 compares the prediction of the Smith-Zener equation with the effective grain sizes of strained samples after annealing. As for Figure 3.15, δ phase fractions

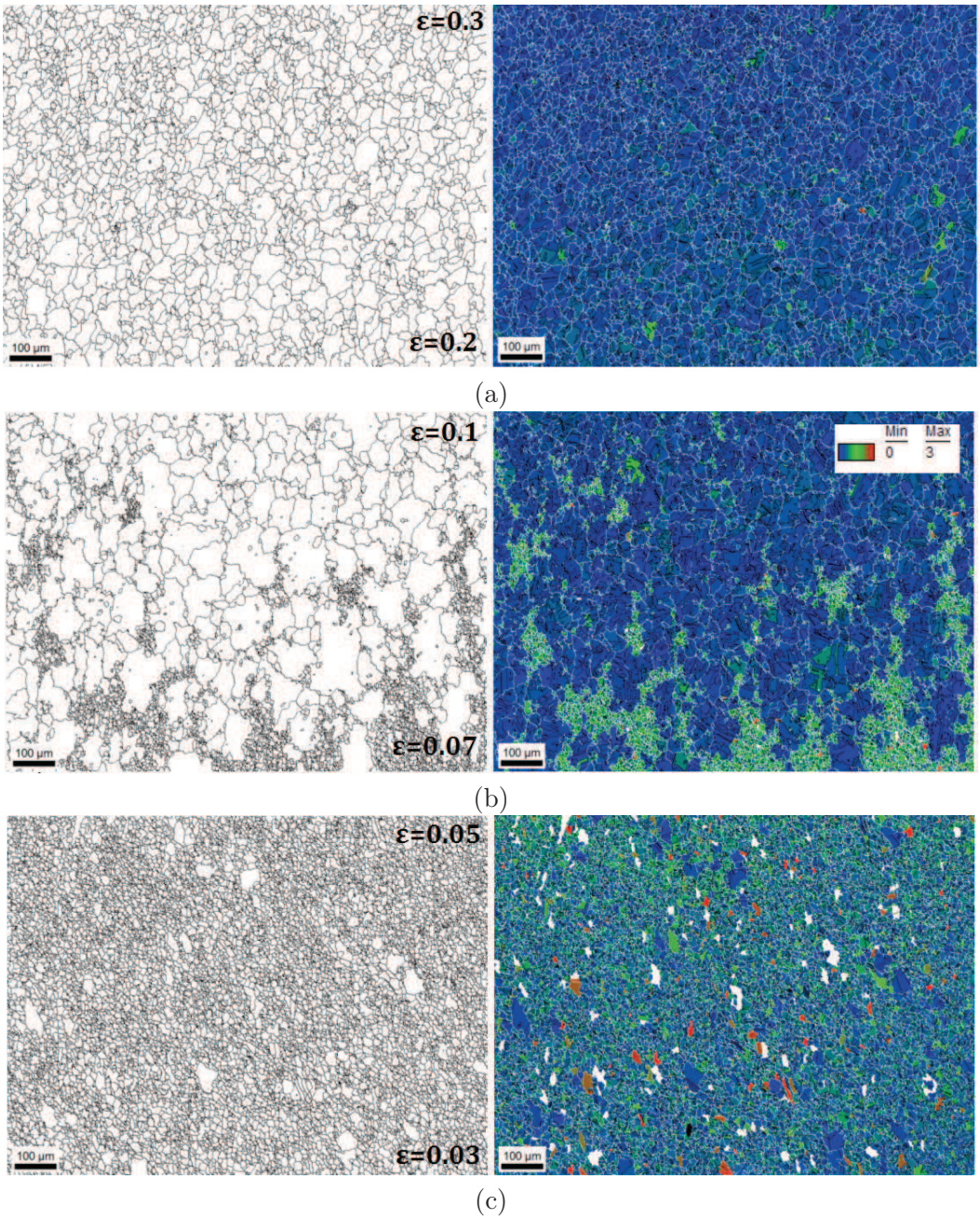

Figure 4.8: Microstructure evolution of reference microstructure after application of low strains and annealing at 985°C for 2 hours in samples $\varepsilon_{SUB} = 0.3$ (a), $\varepsilon_{SUB} = 0.1$ (b), $\varepsilon_{SUB} = 0.05$ (c). Left: grain boundaries. Right: GOS maps (grain boundaries are white, twins are black and white grains have GOS values higher than 3°).

measured before annealing were considered even though particles precipitate during annealing. The plot shows that the average grain size ($\bar{D}_N$) of all samples does fall under the curve assuming that the average particle radius is equal tp 0.3 µm, then on average particles pin grain boundaries as expected. However, as already reported in Table 4.3, the surface-weighted average grain size ($\bar{D}_A$) reveals significant differences

ε_{SUB}/985	0.05	0.1	0.3
$\bar{D}_N(\bar{D}_A)$ [μm]	7 (13)	10 (57)	13 (29)
$\overline{GOS}_A$ [°]	0.7	0.4	0.5
T_G [-]	1.3	4.2	3.7
T_A $[mm^{-1}]$	160	223	202

Table 4.3: Average microstructural properties of reference microstructure after application of low strains and annealing at 985°C for 2 hours.

among samples: in particular, in sample $\varepsilon_{SUB} = 0.1$ the average grain size ($\bar{D}_A$=57 μm) is almost 5 times bigger than that of samples $\varepsilon_{SUB} = 0$ or $\varepsilon_{SUB} = 0.05$. Such result indicates that, despite Smith-Zener pinning, inhomogeneous grain growth can be triggered provided that sufficient strain stored energy is present.

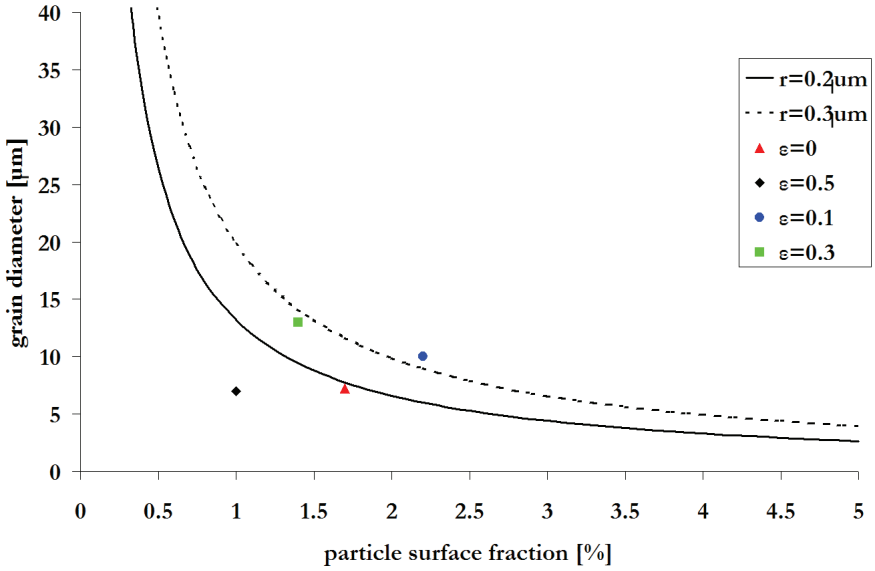

Figure 4.9: Comparison of Smith-Zener equation (Eq.(1.1) with K=0.33 and $\overline{r}$=0.2 μm or $\overline{r}$=0.3 μm) and microstructures of strained samples $0 < \varepsilon_{SUB} < 0.3$ obtained after annealing at 985°C for 2 hours.

Mechanism of microstructure evolution Indeed, grain coarsening during annealing in strained samples is due to the effect of strain energy. The influence of local strain on final grain size in strained samples is plotted in Figure 4.10. The evolution of the area-weighted grain size is similar to that of Figure 1.15: grain size after annealing reaches a peak at low strains ($0.05 < \varepsilon_{SUB} < 0.1$), then it decreases as strain increases. However, in Figure 4.10 the peak is not very sharp as after its maximum grain size decreases slowly as a function of strain. Even after $\varepsilon_{SUB} = 0.3$, grain size is still bigger than the initial one. If in Figure 4.10 the strain is replaced by the corresponding GOS value, then Figure 4.12 is obtained. By comparing this plot

with the equivalent plot of Figure 3.19, it is possible to remark that in both cases the grain size peak is reached for similar GOS distributions: average GOS around 1° and standard deviation around 0.3°.

The decrease in grain size after the peak is probably best interpreted as a case of static recrystallization involving nucleation of new grains. As strain increases, the number of nuclei increases and so the final grain size reduces. Indeed, in the sample $\varepsilon_{SUB} = 0.3$ the strain seems high enough to trigger the static nucleation of new strain-free nuclei during annealing. It would be consistent with Figure 2.6(a) showing that recrystallized grains do form dynamically in Inconel 718 after a deformation of $\varepsilon = 0.4$ (at 980°C and $\dot{\varepsilon} = 0.1s^{-1}$). Hence, it seems reasonable that they could nucleate statically after a deformation of $\varepsilon = 0.3$ and annealing at 985°C. If the critical strain to trigger nucleation of new grains during annealing is in the range $0.05 < \varepsilon_{SUB} < 0.1$, then it would explain why the grain size peak is reached in this range. In fact, the critical strain is the one that triggers the nucleation of the smallest number of new grains.

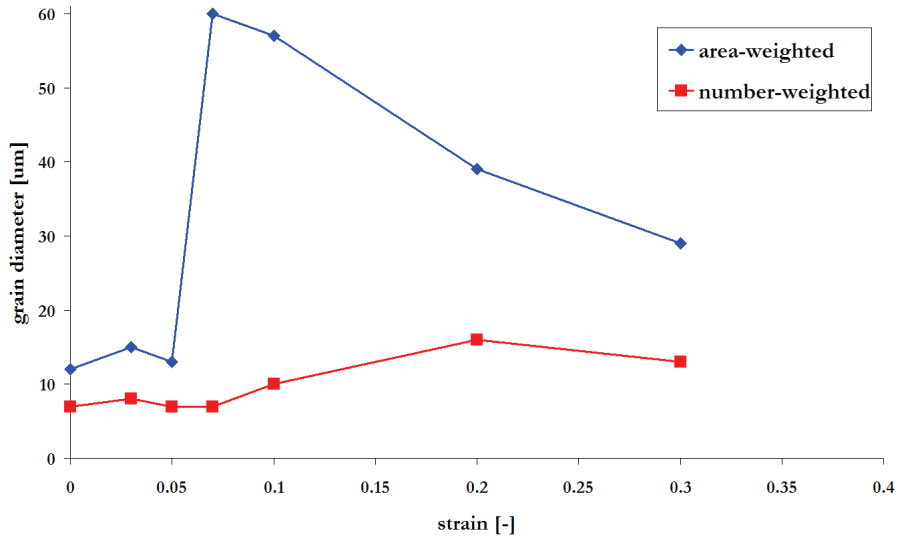

Figure 4.10: Evolution of grain size in strained samples $0 < \varepsilon_{SUB} < 0.3$ after annealing at 985°C for 2 hours as a function of local strains before annealing. For each microstructure both the number-weighted and the surface-weighted averages are given.

Supposing that nucleation takes place in sample $\varepsilon_{SUB} = 0.1$, then its worth considering the balance of driving forces for boundary migration for a strain-free nucleus of size 1 μm (that is the supposed size for a nucleus [9]). It is to note that Zener pinning was not considered as the size of a nucleus is smaller than the average distance between δ phase particles and only GNDs are taken into account to estimate the strain energy. Table 4.4 indicates that a nucleus may grow only by bulging into a grain having a GAM of 1.2°/0.8 μm. Now, Figure shows that grains having a GAM value higher than 1.2°/0.8 μm are indeed present both in samples $\varepsilon_{SUB} = 0.1$

	Pressure [kPa]
Capillarity [Eq.(2.15), 2R=1 μm]	-300
Stored energy [Eq.(2.16), ΔGAM>1.2°/0.8 μm]	>300

Table 4.4: Comparison of grain boundary migration driving pressures in sample $\varepsilon_{SUB} = 0.1$ for the growth of a nucleus.

and $\varepsilon_{SUB} = 0.05$. Then, it is not possible to exclude that nuclei may form, coarsen and eventually grow abnormally. Moreover, in Table 4.4 the minimum GAM value necessary to counterbalance the capillarity force of a nucleus is calculated taking into account only the contribution of GNDs to strain energy, so even grains having a GAM value lower than 1.2°/0.8 μm may be consumed by a nucleus.

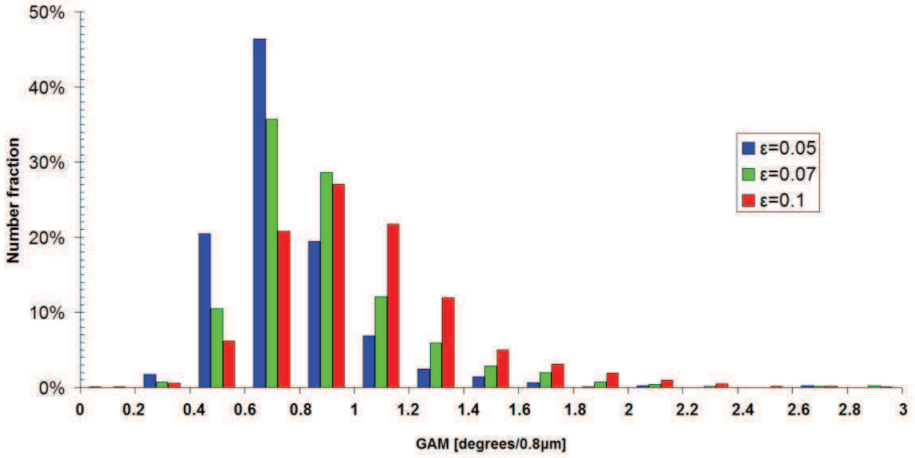

Figure 4.11: GAM histograms of crystals in samples $\varepsilon_{SUB} = 0.1$ and $\varepsilon_{SUB} = 0.05$.

Another possible mechanism, which would not involve the nucleation on new strain-free grains, is the growth of few existing low stored energy grains the expense of higher energy grains. Table 4.5 reports the estimation of driving forces for grain boundary

	Pressure [kPa]
Pinning [Eq.(1.5), r=0.25 μm, f=2.2%]	-90
Capillarity [Eq.(2.15), 2R=4.6 μm]	70
Stored energy [Eq.(2.16), ΔGAM>0.1°/0.8 μm]	>20

Table 4.5: Comparison of driving and pinning pressures in sample $\varepsilon_{SUB} = 0.1$ for the growth of existing grains before annealing.

migration in sample $\varepsilon_{SUB} = 0.1$. If strain energy is not taken into account, then the microstructure does not coarsen due to particle pinning. However, if a stored energy difference of at least 20kPa exists across a grain boundary, then grain boundary motion can be triggered. Now, a driving pressure of 20kPa corresponds to a difference

of GAM between neighbour grains of only 0.1°/0.8 μm. Such a small GAM difference is beyond the angular resolution of the EBSD sytem, however it is still worth looking at the fraction of boundaries separating two crystals with a GAM difference of at least 0.4°/0.8 μm (0.4° being considered as the minimum misorientation angle that can be measured with confidence by the EBSD system). Figure 4.13 displays the

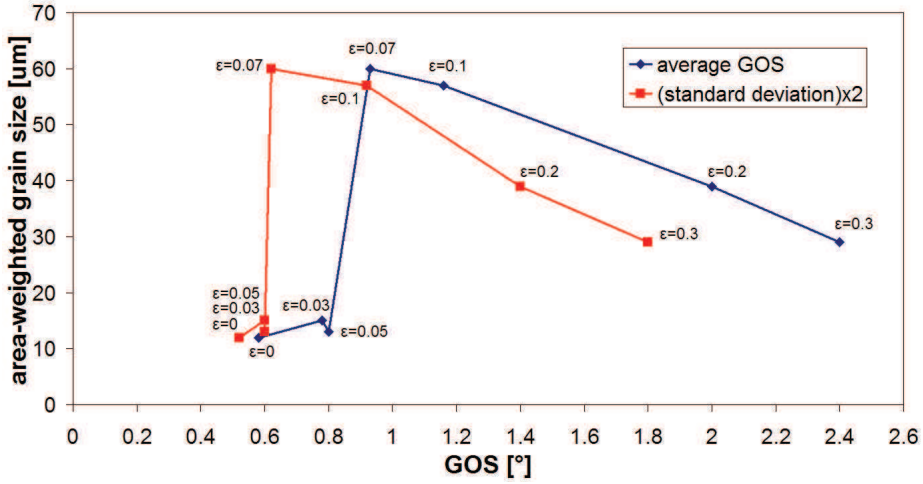

Figure 4.12: Evolution of grain size in strained samples $0 < \varepsilon_{SUB} < 0.3$ after annealing at 985°C for 2 hours as a function of local values of GOS before annealing.

histogram of the fraction of boundaries separating two crystals with a fixed GAM difference. It is to note that such histrogram, unlike that of Figure 3.21, is calculated taking into account the topology of the microstructure. In practice, the histogram is calculated using a table (provided by the OIM software) which reports for each crystal the value of GAM and the list of neighbor grains. Hence, it is possible to calculate the real fraction of boundaries separating two crystals with a given GAM difference.

Now, Figure 4.13 shows that the fraction of boundaries separating two crystals with a GAM difference of at least 0.4°/0.8 μm in sample $\varepsilon_{SUB} = 0.1$ is about 30%; by comparison, in the sample deformed up to $\varepsilon_{SUB} = 0.05$ the fraction is only about 15%. These results suggest that small stored energy differences, which can trigger the growth of some grains overpassing the Smith-Zener limit, are indeed present in the microstructure before annealing. Moreover, the probability to trigger the growth of a grain increases with strain, as the fraction of boundaries separating two crystals with a GAM difference of at least 0.4°/0.8 μm is higher.

Finally, the grain size evolution in Figure 4.12 is governed by the number of growing grains driven by stored energy differences. The number of growing grains increases (hence grain size reduces) either if the width of the strain energy distribution increases (growth of existing grains) or if the fraction of high stored energy grains increases (nucleation and growth of nuclei).

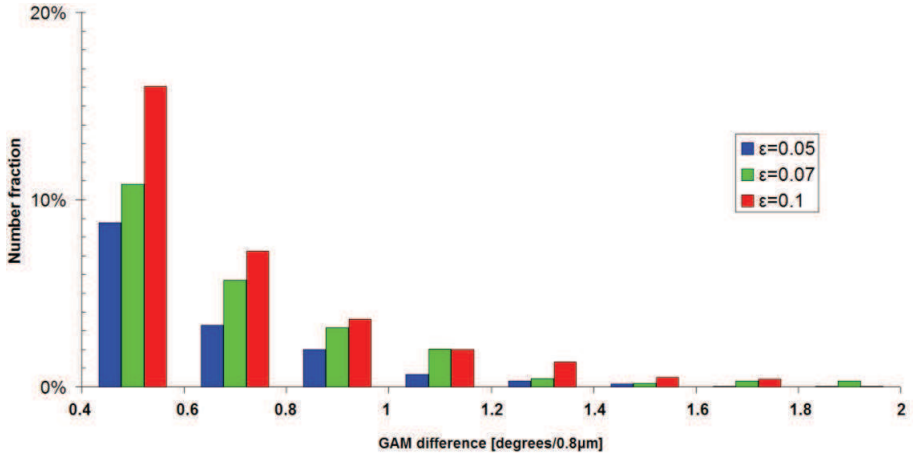

Figure 4.13: Histogram of the fraction of boundaries separating two crystals with a fixed GAM difference in samples $\varepsilon_{SUB} = 0.1$ and $\varepsilon_{SUB} = 0.05$. The fraction of boundaries corresponding to a GAM difference lower than 0.4°/0.8 μm is not displayed.

4.1.3 Influence of reference microstructure

In the previous section it was shown that the evolution during annealing of the reference microstructure is strictly dependant on the hardening that is introduced via the last deformation (ε_{SUB}) of Figure 4.1. The critical strain range leading to a dramatic increase of grain size during annealing is $0.05 < \varepsilon_{SUB} < 0.1$. In this section, the reference microstructure is replaced by different microstructures before applying $\varepsilon_{SUB} = 0.1$ in order to investigate the influence of different parameters on microstructure evolution during annealing.

Inconel 718 billet The same thermomechanical cycle of Figure 4.1 is performed using a torsion sample that is machined from a billet produced by an alternative supplier of Inconel 718 alloy. Moreover, two torsion tests are performed in order to assess the reproducibility of the torsion test. Then samples are annealead at 985°C for two hours. Figure 4.14 indicates that after annealing microstructure evolution is similar to that of Figure 4.8(b), that is, the microstructure is heterogeneous with fine initial grains and coarse overgrown grains. However, in Figure 4.14 the relation between local grain size and level of strain is weaker or absent as the top and bottom of microstructures are quite similar. Notably, where the level of strain is $\varepsilon = 0.1$ there are still many fine grains that did not grow during annealing, despite the presence of a stored energy distribution before annealing (see Figure 4.15, where the average GOS value is 1.1°) that is almost the same as that of Figure 4.5(b). A high δ phase fraction may explain the stability of small grains, however the fraction of particles before annealing is only 1.1% for the microstructure of Figure 4.14(a). Indeed, there must be another factor which hinders grain growth in the samples machined from the alternative supplier. Chemical composition heterogeneity could be involved via its

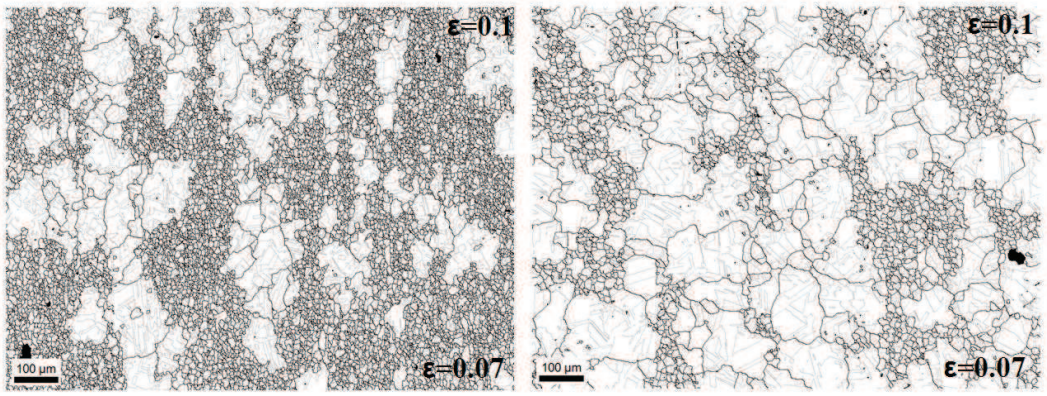

(a) (b)

Figure 4.14: EBSD maps of two samples obtained after application of the cycle of Figure 4.1 with $\varepsilon_{SUB} = 0.1$ and annealing at 985°C for two hours. The two torsion samples are machined from the same billet produced by an alternative supplier. Grain and twin boundaries are respectively black and grey.

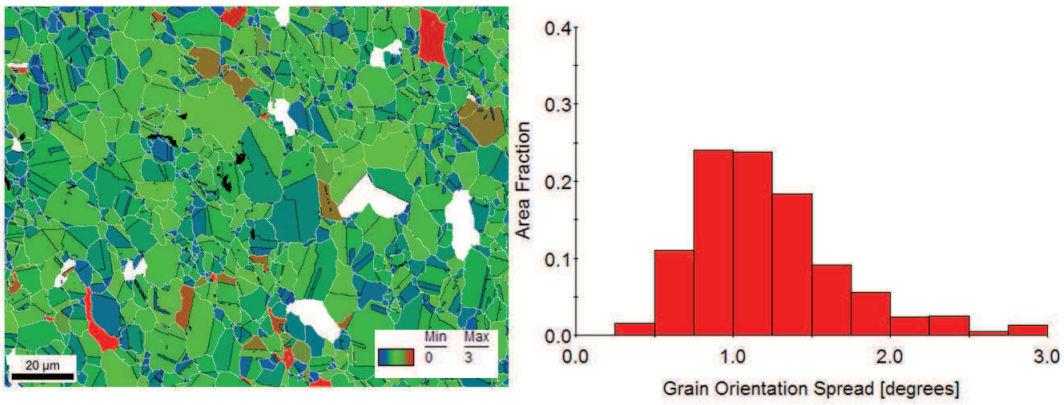

Figure 4.15: Grain orientation spread (GOS) distribution before annealing of microstructure shown in Figure 4.14(a) where $\varepsilon = 0.1$. In GOS map grain boundaries are white, twins are black and white grains have GOS values higher than 3°.

effect on grain boundary mobility. Alloying elements, which are concentrated mostly at grain boundaries, can greatly slow down grain boundary migration via the "solute drag" effect. However, this phenomenon is very effective only in pure metals [9].

Chemical heterogeneity also affects the distribution of δ phase particles. In Inconel 718 the most important alloying element is niobium which controls both the kinetics and fraction of δ phase particles. For this reason, the niobium content was measured by energy-dispersive spectroscopy (EDS) in an heterogeneous microstructure as that of Figure 4.14(a). Figure 4.16 reveals that coarse grains regions (red boxes) are characterized by lower Niobium content compared to fine grains regions (white boxes). Moreover, it is to note that the δ phase fraction in the coarse grain region (2.2%) is

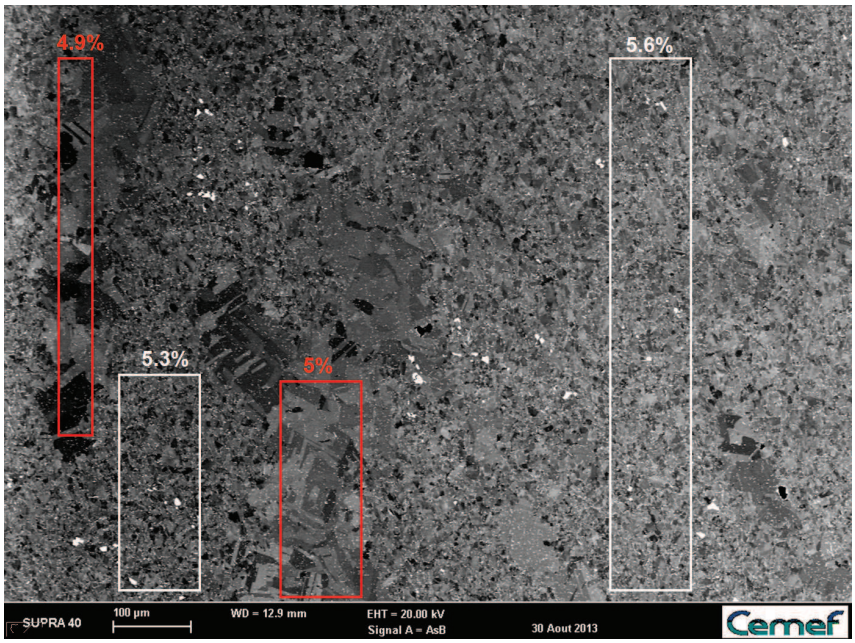

Figure 4.16: Energy-dispersive spectroscopy (EDS) analysis to determine the niobium content in an heterogeneous microstructure as that of Figure 4.14(a). Values are given as percent by weight.

almost half of the fraction in the fine grain region (4.8%). Then, this difference could explain why grain coarsening does not occur everywhere, as chemical heterogeneity affects particle precipitation and so the pinning pressure.

If the two microstructures of Figure 4.14 are compared, it is possible to note that in one sample both fine and coarse grains are slightly bigger than those in the other sample even if the same thermomechanical cycle was applied. This difference can be the result of chemical or microstructural differences that always exist inside Inconel 718 billets from which torsion samples are machined.

δ phase fraction In sample $\varepsilon_{SUB} = 0.1$ the δ phase fraction (2.2%) introduces a pinning pressure of the same order of magnitude as the driving pressure for boundary migration associated with capillarity and stored energy (see Table 4.5). Then, it would be interesting to investigate what is the influence of lower or higher δ phase fractions on microstructure stability during annealing, by keeping the same amount of hardening that is introduced by a small deformation $\varepsilon = 0.1$ on a strain-free microstructure.

If the thermomechanical cycle of Figure 4.1 is modified as illustrated in Figure 4.17(a), then it is possible to increase the amount of δ phase (that will precipitate mostly on grain boundaries), while keeping the same hardening of the sample $\varepsilon_{SUB} = 0.1$. On the contrary, in order to generate a strain-free and δ phase-free fine microstructure, it is possible to perform torsion at δ super-solvus temperatures. At such high temperatures, δ phase particles are dissolved and grain boundary mo-

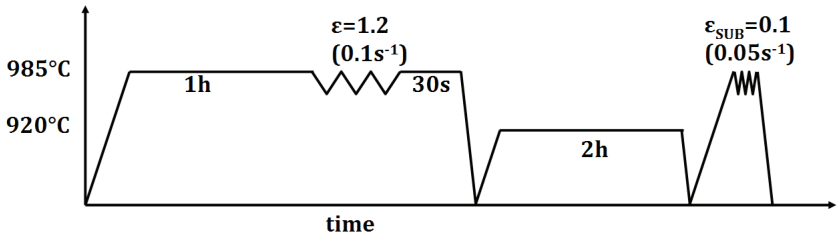

(a)

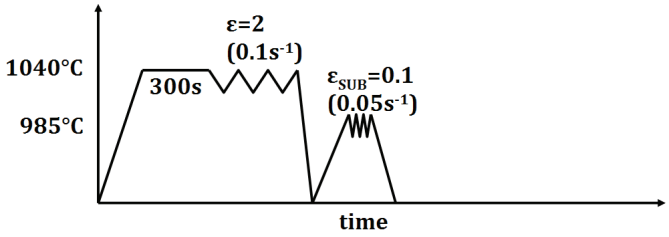

(b)

Figure 4.17: Thermomechanical schemes to obtain a microstructure with the same hardening as that of sample $\varepsilon_{SUB} = 0.1$ but with higher (a) or lower (b) δ phase fraction.

bility is enhanced, so post-dynamic evolution is very fast, leading to a strain-free microstructure during the few seconds between the end of straining and the start of cooling. Then, hardening is introduced by applying a small final deformation as shown in Figure 4.17(b). Figure 4.18 confirms that just after δ super-solvus torsion and quenching the obtained microstructure is almost strain-free.

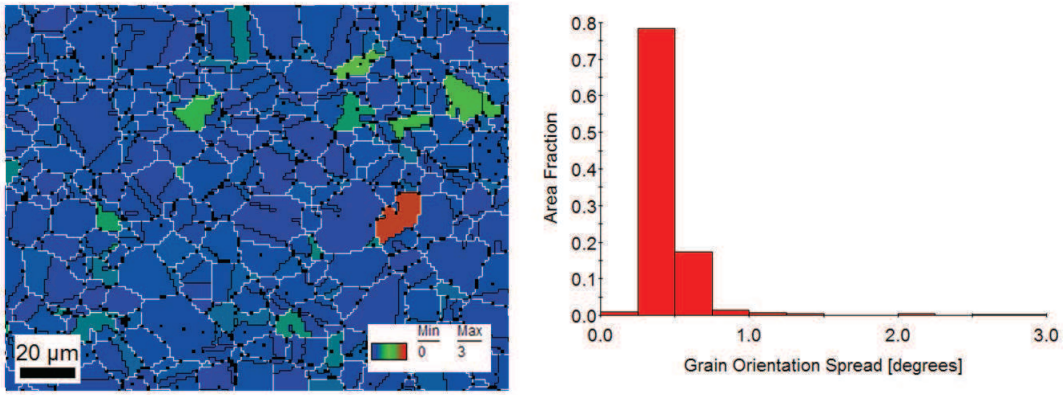

Figure 4.18: Grain orientation spread (GOS) distribution after δ super-solvus torsion at 1040°C up to $\varepsilon = 2$ and quenching. In GOS map grain boundaries are white, twins are black and white grains have GOS values higher than 3°.

Microstructural properties of samples obtained after the cycles of Figure 4.17 and annealing at 985°C are shown in Table 4.6. Before annealing, the average GOS value of both samples is the same as the one of sample $\varepsilon_{SUB} = 0.1$ (see Table

	HIGH	LOW	HIGH/985	LOW/985
$\bar{D}_N(\bar{D}_A)$ [μm]	7(14)	10(17)	18(59)	25(71)
δ fraction [%]	5±0.7	0.3	-	-
δ radius [μm]	0.3	0.2	-	-
$\overline{GOS}_A$ [°]	1.2	1.2	0.4	0.4
T_G [-]	-	-	6.3	7.2
T_A $[mm^{-1}]$	-	-	181	143

Table 4.6: Average microstructural properties of samples with the same hardening of sample $\varepsilon_{SUB} = 0.1$ but higher (HIGH) or lower (LOW) δ phase fraction. Also the evolution after annealing at 985°C for two hours is reported.

4.2), as expected. On the contrary, the δ phase fraction is significantly different and grain size is sligthly coarser, even in the sample with the higher fraction of particles. Once again, microstructural heterogeneity of the initial billet may explain such results. Abnormal grain growth occured in both samples leading to almost the same final grain size as that of sample $\varepsilon_{SUB} = 0.1/985$ ($\bar{D}_N$=10 μm, $\bar{D}_A$=57 μm). Such results reveal that δ phase particles, despite their pinning effect with respect to grain boundaries, do not influence significantly the final grain size that is thus governed mainly by the level of hardening.

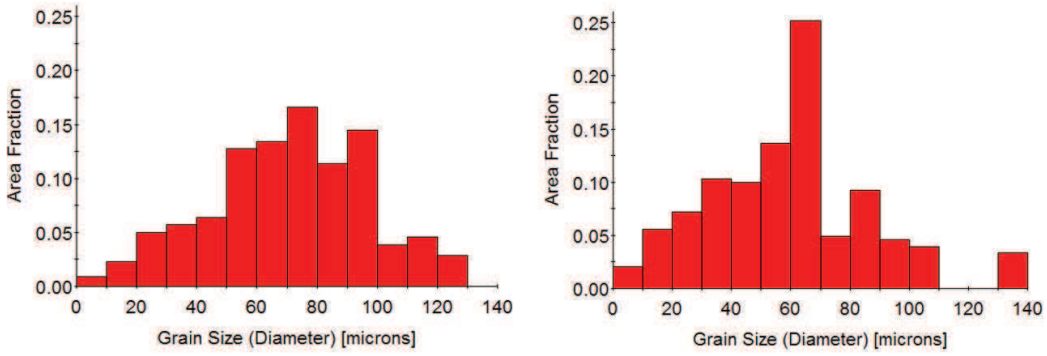

(a) (b)

Figure 4.19: Surface-weighted grain size distributions in samples LOW/985 (a) and HIGH/985 (b).

Indeed, by comparing the number-averaged grain sizes of the two samples it is possible to remark that more particles leads to a higher number of small grains after annealing, but this does not prevent abnormal grain growth to occur. Grain size histograms (see Figure 4.19) reveal that in sample HIGH/985 the surface fraction of grains smaller than 20 μm is about 7%, while in sample LOW/985 the fraction is only 3%. Twin density values (T_A) in both samples are lower than in sample $\varepsilon_{SUB}/985 = 0.1$: the minimum value is found in the sample with the initial lower

particle fraction and initial higher grain size.

It is interesting to look at the microstructure evolution of the sample with higher δ phase fraction, which is shown in Figure 4.20. After only 15 minutes of annealing microstructure evolution is clearly governed by the level of local strain. At the top of the image where the strain is $\varepsilon = 0.1$ coarse grains almost fill the microstructure, while at the bottom almost no grain growth has occured yet. After two hours of annealing the whole surface is covered by coarse grains. This confirms that in the bottom region where $\varepsilon = 0.07$, abnormal grains appear only after a certain incubation time (10-15 minutes), as already observed in the industrial pieces (see Figure 3.13). This would support that a nucleation process does take place

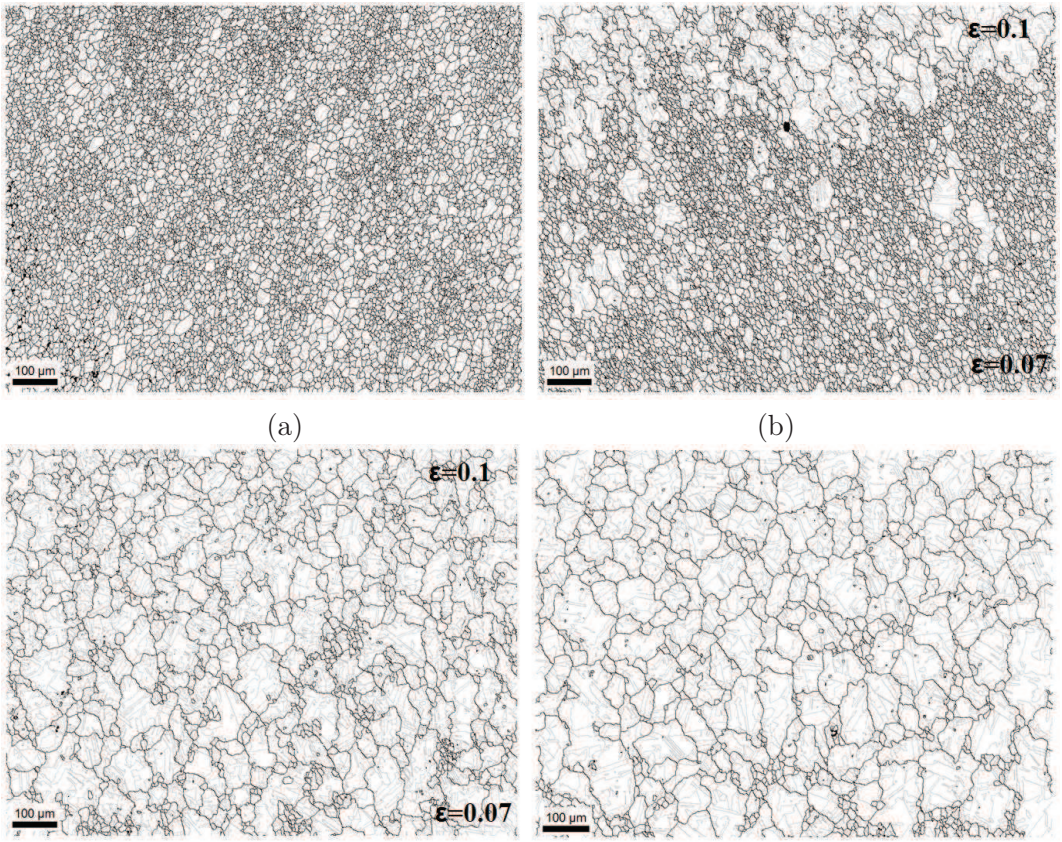

Figure 4.20: Microstructure evolution during annealing at 985°C of the sample with higher δ phase fraction (HIGH): before annealing (a), after 15 minutes (b) and after two hours (c). Also the microstructure of the sample with the lower δ phase fraction (LOW) after two hours is reported (d).

Hardening In previous tests, the reference microstructure is always generated following the cycle of Figure 4.1, leading to a strain-free microstructure that is ideal to assess the effect of successive small strains. Results have shown that abnormal grain growth is triggered in the strain range $0.05 < \varepsilon_{SUB} < 0.1$. Now, it seems interesting

to investigate if the same result is obtained when the reference microstructure is no longer free of strain energy. For this purpose, three torsion tests are performed using the same cycle of Figure 4.1 (with $\varepsilon_{SUB} = 0.1$) but introducing the following modifications:

- the time between ε_{REF} and ε_{SUB} is reduced to 10 seconds (sample "TIME"),
- the temperature of the whole cycle is decreased to 945°C (sample "TEMP"),
- the first strain level is increased to $\varepsilon_{REF} = 2.4$ with $\dot{\varepsilon}_{REF} = 0.2s^{-1}$ (sample "STRAIN").

The properties of microstructures just after thermomechanical cycles are reported in Table 4.7. Overall, the properties of the three samples are close to those of sample $\varepsilon_{SUB} = 0.1$ (see Table 4.2), notably in terms of average GOS values. However, a more

	TIME	STRAIN	TEMP
$\bar{D}_N(\bar{D}_A)$ [μm]	4 (7.4)	5.7 (10)	3.6 (7.7)
δ fraction [%]	1	1.4	2.3
δ radius [μm]	0.25	0.25	0.25
$\overline{GOS}_A$ [°]	1.5	1.2	1.5

Table 4.7: Average microstructural properties of three samples obtained by modifying the cycle of Figure 4.1

detailed analysis of microstructures (see Figure 4.21) reveals small but significant differences between the three samples. In sample STRAIN the grain size distribution is quite homogeneous and GOS values do not exceed 3° (as in sample $\varepsilon_{SUB} = 0.1$, see Figure 4.5). On the contrary, in the other two samples the grain size distribution is more heterogeneous and the fraction of grains with GOS higher than than 3° is not neglectable. Indeed, this is the result of reducing the temperature or the time between ε_{REF} and ε_{SUB} in the thermomechanical cycle. In fact, both modifications are supposed to slow down or limit the post-dynamic process that leads to the formation of a strain-free microstructure (see Figure 4.2).

Table 4.8 reports the properties of the three microstructures after annealing at 985°C for two hours. GOS values decrease in all samples, suggesting that stored energy reduction has driven microstructure evolution. All final grain sizes are smaller than the one reached in sample $\varepsilon_{SUB} = 0.1/985$ (about $\bar{D}_A = 60\mu m$). In particular, in sample TEMP/985 the final grain size remains quite fine ($\bar{D}_A = 15\mu m$). In other samples, grains coarsen up to about $\bar{D}_A = 30\mu m$, but grain distributions are quite different as revealed by $\bar{D}_N$ values. In fact, Figure 4.22 shows that while in sample STRAIN/985 grain size is quite homogeneous, in sample TIME there is a significant fraction of fine grains. These fine grains have the highest GOS values in the microstructure, suggesting that they were already present before annealing. Indeed, GOS values of fine grains are similar to those of grains in Figure 4.21(a).

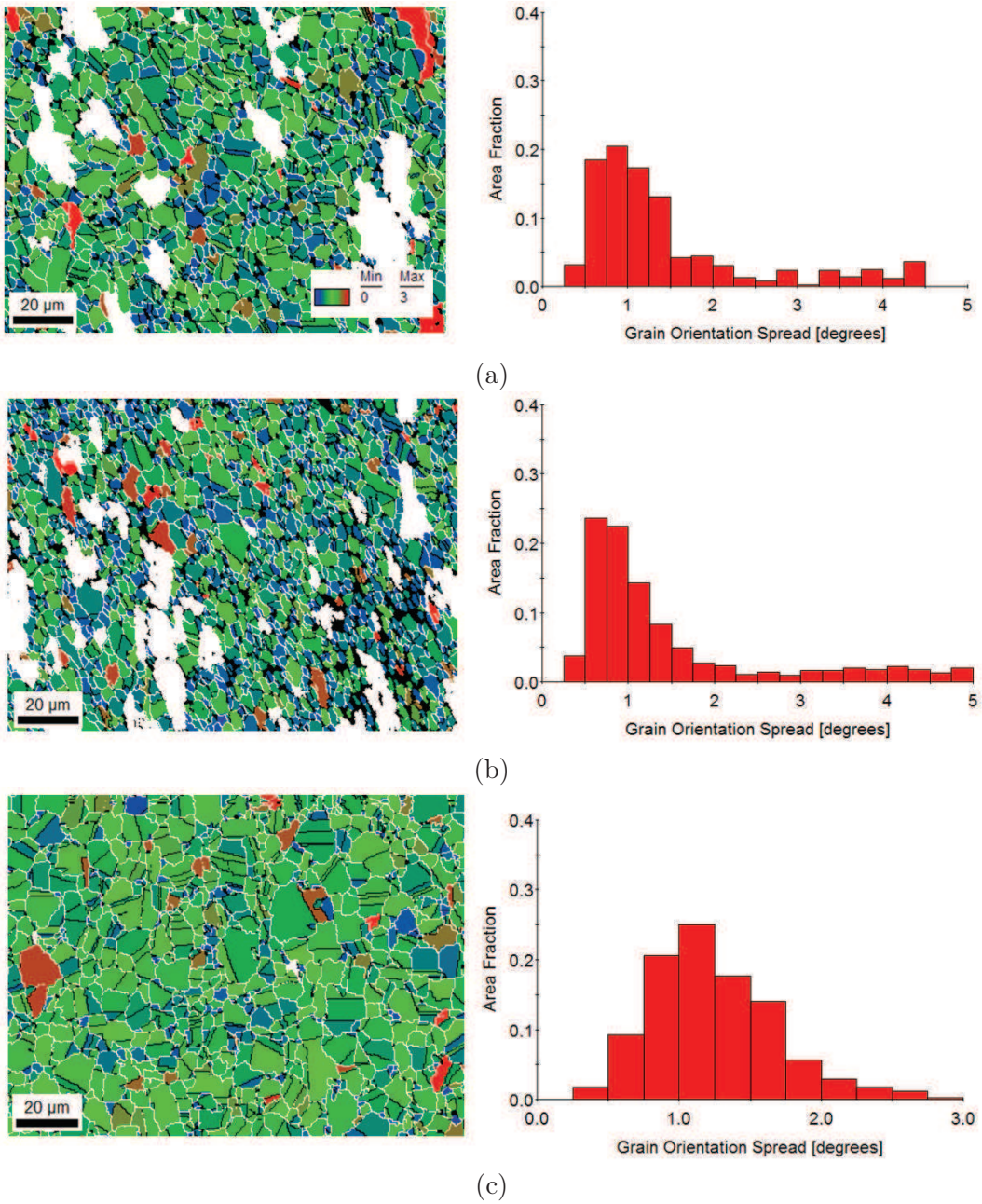

Figure 4.21: Grain orientation spread (GOS) distribution in samples TIME (a), TEMP (b) and STRAIN (c). In GOS maps grain boundaries are white, twins are black and white grains have GOS values higher than 3°.

Overall, these results reveal two important aspects concerning the occurence of inhomogeneous grain growth induced by strain. First of all, sample TEMP/985 demonstrates that the critical strain $\varepsilon = 0.1$ does not trigger necessarily inhomogeneous grain growth (as it occurs in sample $\varepsilon_{SUB} = 0.1/985$) if it is applied on a microstructure that is not strain-free. In this case, the small strain is supposed to just increase the hardening of a partially recrystallized microstructure that will statically and post-dynamically recrystallize during annealing. If the total hardening

	TIME/985	STRAIN/985	TEMP/985
$\bar{D}_N(\bar{D}_A)$ [µm]	8.7(32)	17(36)	8.5(15)
$\overline{GOS}_A$ [°]	0.5	0.4	0.4
T_G [-]	2.5	4	1.8
T_A $[mm^{-1}]$	214	160	208

Table 4.8: Average microstructural properties of three samples obtained by modifying the cycle of Figure 4.1 and annealing at 985°C for 2 hours.

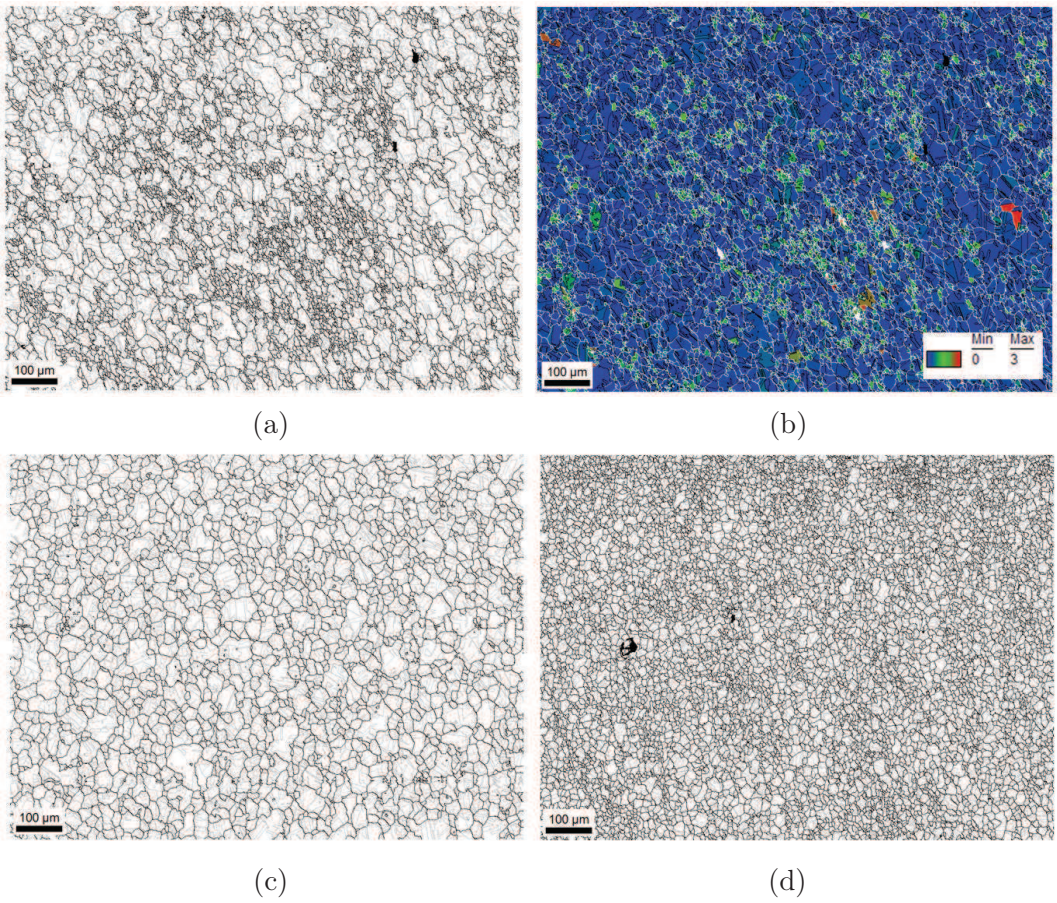

(a) (b)

(c) (d)

Figure 4.22: Microstructure after annealing at 985°C for two hours of samples TIME (a), STRAIN (c) and TEMP (d). The GOS map of sample TIME is also shown (b): grain boundaries are white, twins are black and white grains have GOS values higher than 3°.

is high enough, then many nuclei will appear during, thus forming a fine grain size. A similar mechanism may occur in sample TIME/985, but in this case the number of nuclei is maller, thus forming a coarser and heterogeneous microstructure.

Secondly, sample STRAIN/985 reveals the limit of the average GOS parameter as a means to predict the final grain size after annealing. In fact, according to the plot of Figure 4.12, the final grain size of sample STRAIN/985 should be around

$\bar{D}_A = 60\mu m$, while it reaches only 30 μm. Once again, this is due to the fact that the plot of Figure 4.12 was determined by applying strains on an ideal strain-free reference microstructure obtained by post-dynamic evolution of a partially recrystallized microstructure. This may not be the case for the sample STRAIN, where the initial microstructure is generated by applying a very high strain ($\varepsilon_{REF} = 2.4$) that is supposed to completely recrystallize the microstructure. Hence, the following post-dynamic evolution will be different from that of the reference microstructure (see Figure 4.2), leading to the formation of a similar microstructure in terms of GOS distribution, but not necessarily the same stored energy distribution or grain boundary properties. Overall, additional analyses should be carried out on the microstructures of samples STRAIN, TEMP and TIME before the application of the small strain ($\varepsilon = 0.1$) in order to better understand the differences with the reference microstructure.

4.1.4 Influence of compressive stress

In all previous torsion tests, the sample was strained as a result of shear stresses in the material. Now, it would be interesting to investigate if straining by compressive stresses also leads to the same critical microstructures previously obtained. Then, in this section compression testing is performed on a cylindrical sample following the same thermomechanical cycle described in Figure 4.1, but reducing nominal strains to $\varepsilon = 0.8$ and $\varepsilon_{SUB} = 0.07$. In fact, at the core of the compression sample the strain is higher than the nominal strain due to friction. In Figure 4.23 the strain distribution induced by $\varepsilon = 0.8$ and $\varepsilon_{SUB} = 0.07$ in the cylindrical sample are calculated using the software Forge® where the friction coefficient is calibrated to fit the barreling measured on the experimental sample. Two different zones of the compression sample (CORE and EDGE) are analyzed corresponding to different local strain values.

Microstructural properties of these two zones of the compression sample before and after annealing at 985°C for two hours are reported in Table 4.9. Before annealing, both microstructures are composed by fine grains which were formed by dynamic recrystallization during the first compression step of nominal strain equal to $\varepsilon = 0.8$. The GOS value of the zone at the core of the sample is slightly higher than the value measured close to the sample edge. This can be considered as a consequence of the heterogeneous hardening applied by the second compression step of nominal strain equal to $\varepsilon = 0.07$, assuming that a strain-free microstructure was formed by post-dynamic evolution (as in torsion samples). As shown in Figure 4.23, strain is higher at the sample core than it is close to the sample edge. Moreover, it is interesting to note that the GOS value measured at the sample core (where $\varepsilon = 0.08$) is almost the same as the one measured by torsion at $\varepsilon = 0.1$ (see Table 4.2). After annealing, grain size increases significantly in both microstructures and GOS values fall below the detection limit of the EBSD technique. As already observed in

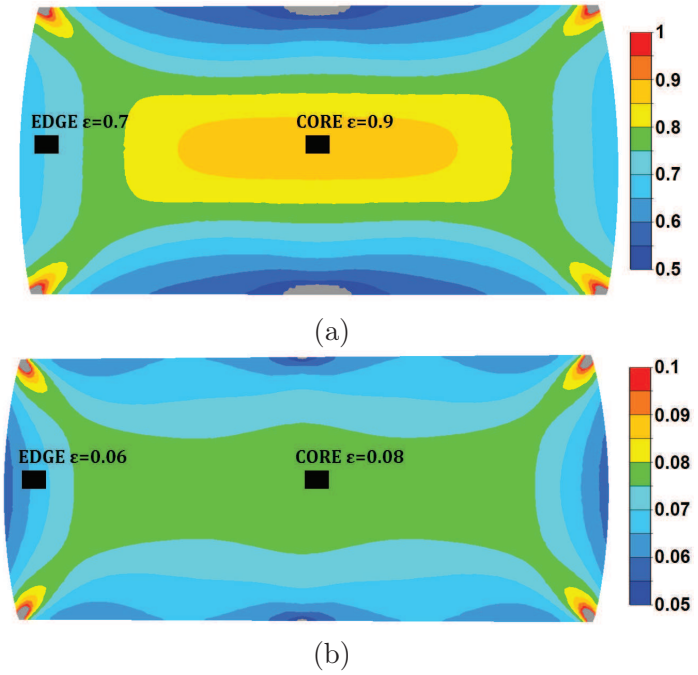

Figure 4.23: strain maps obtained by Forge® simulation of two succesive compression steps applied on a cylindric sample: nominal strain of each step is $\varepsilon = 0.8$ (a) and $\varepsilon = 0.07$ (b).

	CORE	EDGE	CORE/985	EDGE/985
$\bar{D}_N(\bar{D}_A)$ [µm]	5.7(11)	5.6(12)	25(64)	18(87)
δ fraction [%]	2.2	2	4	4.3
δ radius [µm]	0.35	0.35	0.4	0.4
$\overline{GOS}_A$ [°]	1.1	0.9	0.4	0.4
T_G [-]	-	-	8	6.6
T_A $[mm^{-1}]$	-	-	161	165

Table 4.9: Average microstructural properties of compression sample measured in the two zones marked in Figure 4.23. Also the evolution after annealing at 985°C for two hours is reported.

torsion samples, few small grains (less than 5% in surface fraction) remain in the microstructure, explaining why number-weighted averages are much lower compared to surface-weighted averages. Indeed, microstructure evolution is triggered by the same strain stored-energy reduction mechanism occuring in torsion samples. It is interesting to note that also in the compression sample it is possible to reveal a microstructure gradient linked to the strain gradient, as already shown in Figure 4.8 for torsion samples. Figure 4.24 illustrates the microstructure evolution from the EDGE zone (right-hand side) to the surface of the sample (left-hand side) where the local strain is lower and so fine hardened grains do not grow during annealing. Moreover,

the average number-weighted grain size of the fine grains is 7.3 μm, revealing that they did not coarsen much during annealing due to Smith-Zener pinning.

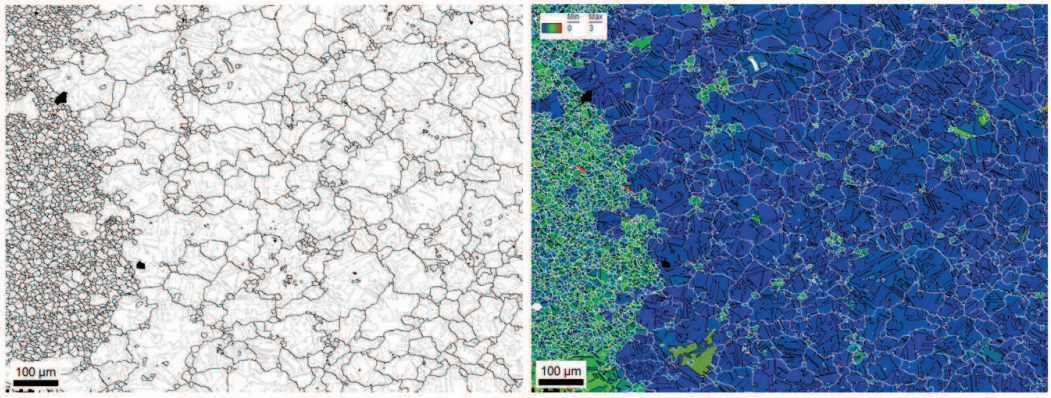

(a) (b)

Figure 4.24: Microstructure evolution in the compression sample from the EDGE zone (right-hand side) to the surface of the sample (left-hand side):grain boundaries (a) and GOS map (b). Grain boundaries are white, twins are black and white grains have GOS values higher than 3°.

Concerning the relation between average GOS values before annealing and final grain sizes, Figure 4.25 reveals that compression results fall very close to the curve obtained from the microstructures of industrial forgings (see Figure 3.19).

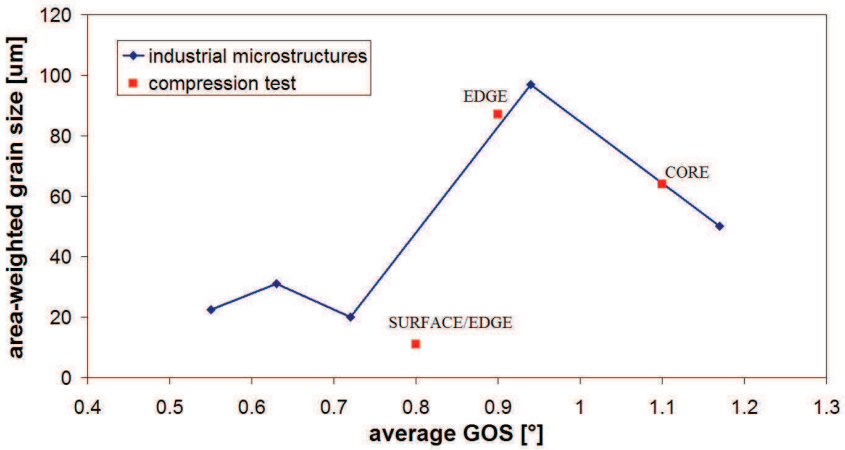

Figure 4.25: Correlation between average GOS values before annealing and final grain sizes in industrial microstructures and in the compression sample.

4.2 Anisothermal super-solvus hardening

In section 4.1 it was shown that small strains applied at δ sub-solvus temperature (985°C) can introduce critical stored energy distributions that eventually lead to abnormal grain growth during annealing. Then, it is worth investigating if similar results can be obtained also by small strains applied at anisothermal δ super-solvus

temperatures, imposing a more complex thermomechanical cycle closer to real industrial conditions.

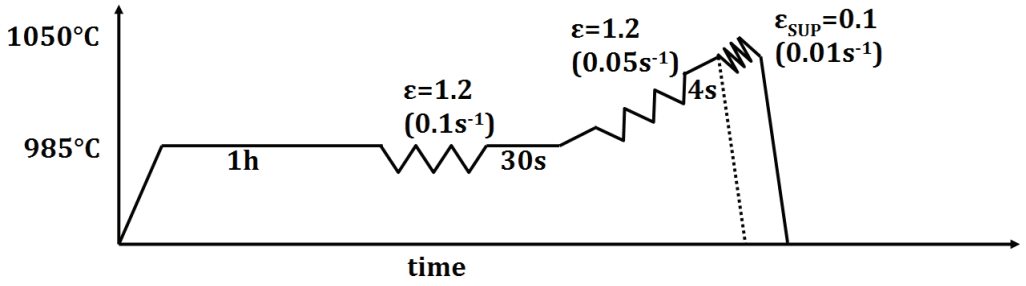

Figure 4.26: Thermomechanical scheme employed to produce microstructures hardened at δ super-solvus temperatures.

4.2.1 Hardened microstructures

The thermomechanical cycle of Figure 4.26 is applied to two torsion samples to obtain microstructures hardened at δ super-solvus temperatures. The cycle is made by three parts simulating the thermomechanical conditions that can occur in real industrial cycles. First of all, δ sub-solvus torsion at 985°C followed by a short annealing (30s) is applied to obtain a fine strain-free microstructure. Then, δ super-solvus torsion at non constant temperature followed by a very short annealing (4s) is applied to dynamically and post-dynamically recrystallize the microstructure. Finally, a small strain $\varepsilon_{SUP} = 0.1$ is applied at a low strain rate ($\dot{\varepsilon} = 0.1s^{-1}$) to indroduce hardening.

The strain during the intermediate and final torsion tests of Figure 4.26 is applied differently to the two samples. As shown in Figure 4.27, one sample is strained continuously up to $\varepsilon = 1.2$ ($\dot{\varepsilon} = 0.05s^{-1}$) and the temperature is in the range 1040-1050°C. The other sample is strained discontinuously: a small deformation of $\varepsilon = 0.2$ at high strain rate ($\dot{\varepsilon} = 5s^{-1}$) is applied six times to obtain a cumulative strain of $\varepsilon = 1.2$ while temperature increases from 985°C to 1035°C: the small peaks visible on the temperature curve are due to the self-heating induced by the high strain rate.

$\varepsilon_{SUP} = 0.1$	continuous	discontinuous
$\bar{D}_N(\bar{D}_A)$ [μm]	9 (17)	9 (14)
δ fraction [%]	0.25	1.3
δ radius [μm]	0.2	0.25
$\overline{GOS}_A$ [°]	0.8	0.9

Table 4.10: Average microstructural properties of two microstructures hardened at δ super-solvus temperatures

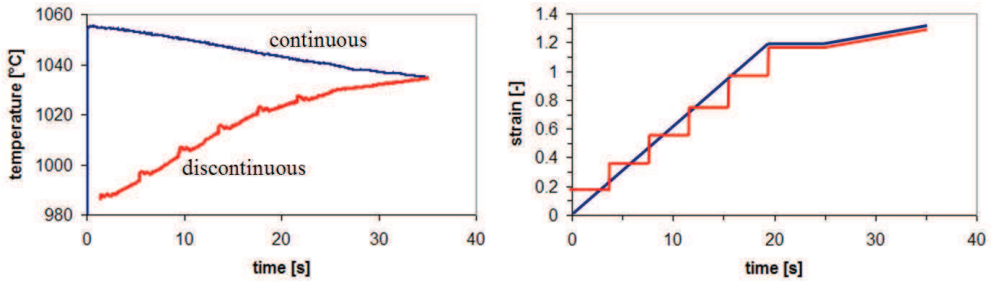

(a) (b)

Figure 4.27: During the intermediate and final torsion tests of Figure 4.26, strain is applied continuously in one sample and discontinuously in the other: (a) temperature and (b) strain evolution.

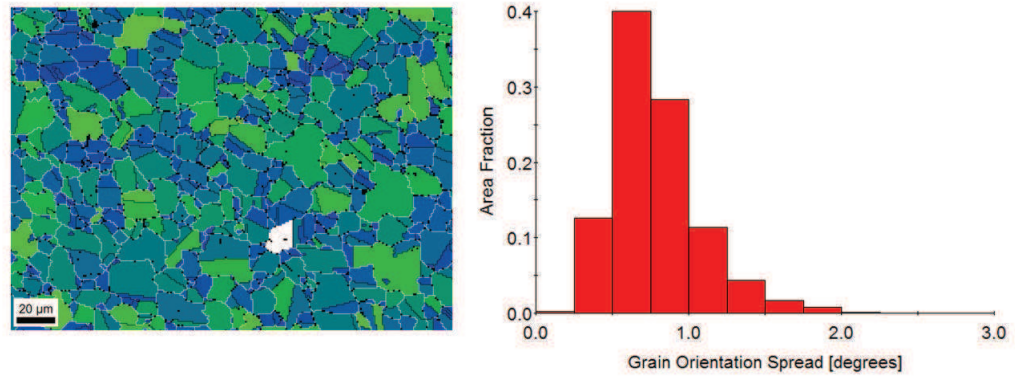

(a)

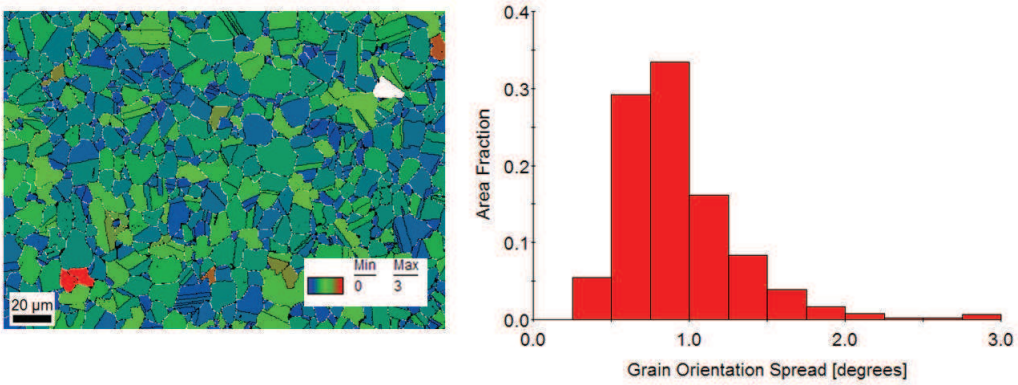

(b)

Figure 4.28: Grain orientation spread (GOS) distribution in samples hardened at super-solvus temperature after continuous (a) or discontinuous (b) torsion. In GOS maps grain boundaries are white, twins are black and white grains have GOS values higher than 3°.

The microstructural properties of the two samples after application of the cycle of Figure 4.26 are shown in Table 4.10. Both microstructures have similar values of grain size, which is mainly due to the fact that the same cumulative strain was applied during torsion. Also average GOS values are both lower than 1° and they are quite

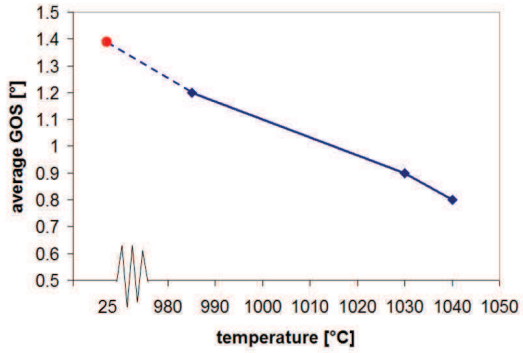

Figure 4.29: Influence of straining temperature on average GOS values of microstructures after application of a small strain (ε=0.1). The red point corresponds to room temperature (25°C) straining (see section 4.3).

close, which would suggests that in this case geometrically necessary dislocations are stored mostly during the last small deformation. On the contrary, there is a significant difference in the δ phase fraction that can be linked to the temperature during the intermediate and the last torsion tests (see Figure 4.10).

GOS distributions are shown in Figure 4.28. Even if it is hard to distinguish the two GOS distributions, it is possible to remark that the GOS distribution of the sample subjected to discontinuous torsion is slightly shifted towards higher values. This is probably due to the lower average temperature during discontinuous torsion (1030°C) with respect to continuous torsion (1040°C), because it should slow down recovery or recrystallization phenomena. It is interesting to note that GOS distributions of Figure 4.28 are very similar to those of Figure 4.5 obtained by sub-solvus hardening with $0.05 < \varepsilon_{SUB} < 0.1$. More precisely, Figure 4.29 shows that higher straining temperatures reduce the average GOS value after a deformation of ε=0.1. However, it is to note that during anisothermal super-solvus straning the strain rate is lower ($\dot{\varepsilon} = 0.01s^{-1}$) compared to that of sub-solvus straining ($\dot{\varepsilon} = 0.05s^{-1}$), hence it is not possible to exclude its contribution to the reduction of GOS values.

4.2.2 Microstructure stability during annealing

If samples hardened at super-solvus temperatures are annealed at 985°C for two hours, microstructures evolve as shown in Figure 4.30 and Table 4.11. They show that in the sample deformed by continuous torsion most of the microstructure is still made by small grains and only few coarse grains appear. On the contrary, the other sample is made mostly by big coarse grains and few clusters of small grains.

Grain coarsening is probably driven by the reduction of stored energy in both samples, as shown by the reduction of average GOS values after annealing. Now, if average GOS values before annealing (see Table 4.10) were plotted in Figure 4.12, they would fall on the left side of the grain size peak where as average GOS increases, microstructure starts to coarsen leading eventually to abnormal grain growth. Indeed,

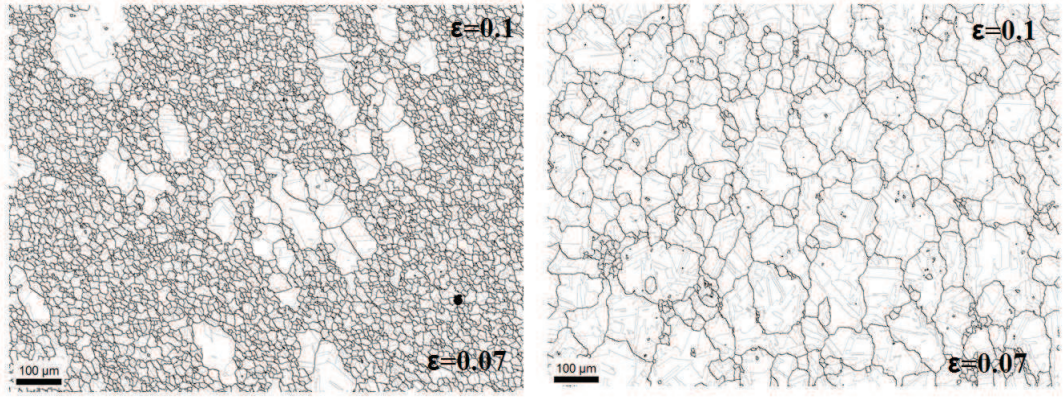

(a) (b)

Figure 4.30: EBSD maps of two microstructures hardened at δ super-solvus temperatures following continuous (a) or discontinuous (b) torsion and after annealing at 985°C for two hours. Grain and twin boundaries are respectively black and grey.

$\varepsilon_{SUP} = 0.1/985$	continuous	discontinuous
$\bar{D}_N(\bar{D}_A)$ [µm]	11(37)	24(84)
$\overline{GOS}_A$ [°]	0.7	0.45
T_G	1.3	5.5
T_A	96	120

Table 4.11: Average microstructural properties of two microstructures hardened at δ super-solvus temperatures after annealing at 985°C for two hours.

this trend is consistent with microstructures of Figure 4.30 where grain coarsening is more important if the average GOS value before annealing is higher. A final remark can be made on the twin density (T_A) of the sample deformed by continuous torsion after annealing ($120mm^{-1}$) that is almost two times lower compared to the twin density of sample B/985 that has a similar grain size ($\overline{D}_A$=97 µm). Such low twin density could be due both to the lower initial δ phase fraction or initial coarser grain size with respect to sample B. In fact, these parameters could increase the probability of the occurrence of "growth faults", as a migrating grain boundary would cross a higher number of particles or other grain boundaries.

Finally, these results confirm once again that critical hardening is responsible for abnormal grain growth occurring during δ sub-solvus annealing. Moreover, they prove that a small strain (ε=0.1) at δ super-solvus temperatures can also induce critical hardening in microstructures: the level of hardening (as indicated by the GOS parameter) decreases as straining temperature increases.

4.3 Room temperature hardening without δ phase

As discussed in section 1.3, one processing route of grain boundary engineering involves applying very low strains ($\varepsilon < 0.1$) at room temperature and annealing at high temperature for short times (few minutes), avoiding to trigger primary recrystallization. For this reason, it is worth discussing here some of the results that were obtained in a recent study of Inconel 718 grain boundary engineering [72]. Notably, the effect of room temperature low strains on microstructure evolution during short annealing (10 minutes) will be discussed.

4.3.1 Hardened microstructures

In the grain boundary engineering study, a reference strain-free and δ phase-free microstructure is hardened at room temperature. For this purpose, the same thermomechanical cycle of Figure 4.17(b) is employed with the only difference that the final small strain at high temperature (ε_{SUB}) is replaced with a room temperature strain (ε_{RT}). Two samples are hardened by applying $\varepsilon_{RT} = 0.1$ and $\varepsilon_{RT} = 0.05$. GOS distributions of the deformed microstructures are shown in Figure 4.31. It is

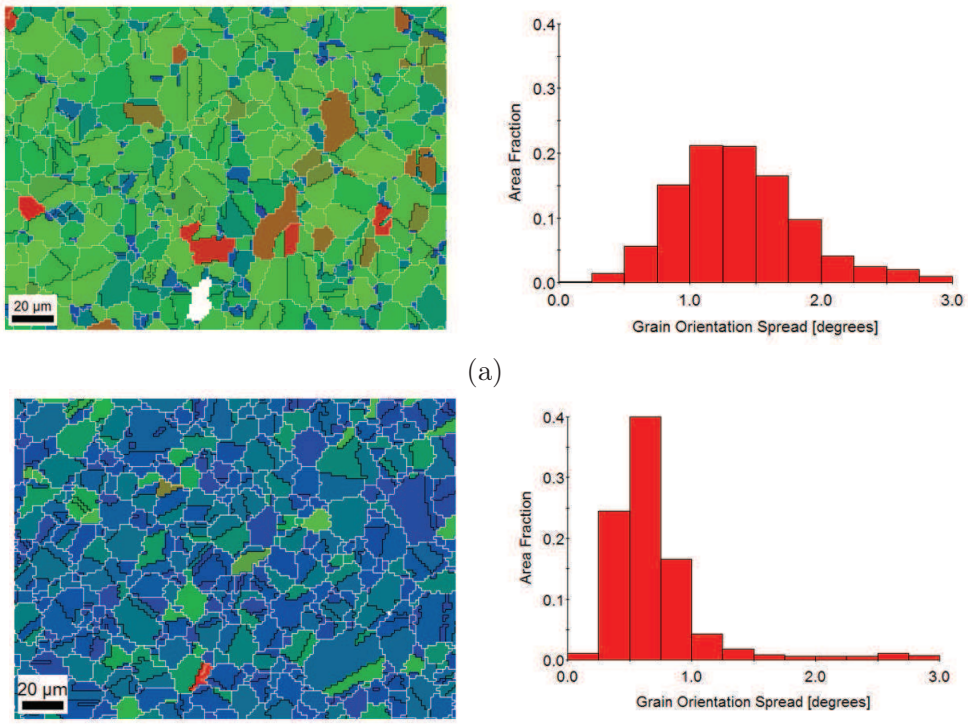

Figure 4.31: Grain orientation spread (GOS) distribution in samples hardened at room temperature with $\varepsilon_{RT} = 0.1$ (a) and $\varepsilon_{RT} = 0.05$ (b).

interesting to compare these GOS distributions with those of Figure 4.5 that were obtained after straining at sub-solvus temperatures. Indeed, for the same level of strain, the GOS distributions are very similar. Table 4.12 shows that average GOS

values of samples $\varepsilon_{RT} = 0.1$ and $\varepsilon_{RT} = 0.05$ are respectively higher and lower compared to those of samples $\varepsilon_{SUB} = 0.1$ and $\varepsilon_{SUB} = 0.05$ of Table 4.2. Hence, it is not possible to clearly assess the effect of strain temperature on intragranular misorientation. Moreover, the GOS parameter (like any other intragranular misorientation parameter) is influenced only by the presence of geometrically necessary dislocations. Then, it is not possible to exclude that room temperature straining stores in the microstructure a higher dislocations density due to the lack of thermally activated mechanisms like recovery or reduced dislocation mobility.

Concerning this last aspect, it is worth considering the stress-strain curve of the sample deformed at room temperature (see Figure 4.32). The curve exhibits a sharp peak that marks the transition from the elastic to the plastic regime. The offset yield stress (measured at $\varepsilon = 0.002$) is 430MPa. In the plastic regime, the stress increases as dislocations are generated in the material.

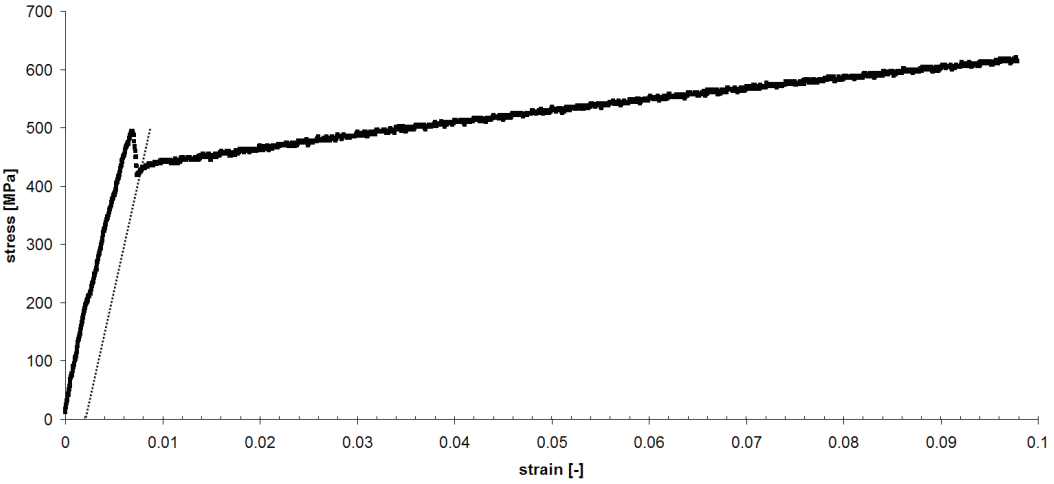

Figure 4.32: Stress-strain curve of the sample deformed by torsion at room temperature up to $\varepsilon_{RT} = 0.1$.

Now, as shown in Figure 4.18, before straining at room temperature the microstructure is completely recrystallized or strain free. Then, Eq.(2.18) should allow to roughly estimate the dislocation density as a function of strain in sample $\varepsilon_{RT} = 0.1$, by setting $\sigma_0 = 430MPa$ and assuming $\alpha = 0.2$. For $\varepsilon = 0.1$, Eq.(2.18) yields a dislocation density of about $2.3 \cdot 10^{14} m^{-2}$.

On the other end, the density of geometrically necessary dislocations (GNDs) can be estimated by EBSD using Eq.(2.17) and the grain average misorientation distribution of sample $\varepsilon_{RT} = 0.1$ (see Figure 4.33). The mean value of the distribution is $0.8°/1.2$ μm, which corresponds to a GND density of $0.9 \cdot 10^{14} m^{-2}$. As expected, this value is lower compared to the one obtained by the Taylor equation which should take into account the presence of both GNDs and SSDs.

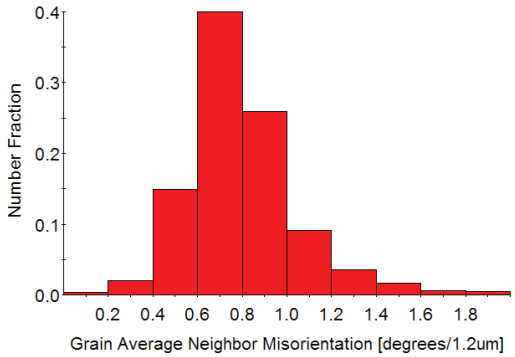

Figure 4.33: Grain average misorientation of sample $\varepsilon_{RT} = 0.1$.

4.3.2 Microstructure stability during annealing

Microstructures hardened at room temperature were annealed at 985°C for only ten minutes (during which δ phase particles are not supposed to precipitate), unlike all samples discussed in the previous section where annealing lasted for two hours. Figure 4.34 and Table 4.12 show that after annealing grain size coarsens in both samples. n sample $\varepsilon_{RT} = 0.05$ grain growth is limited and it does not involve a GOS reduction, suggesting that capillarity is the main driving force. Such result is consistent with the lack of δ phase particles. In sample $\varepsilon_{RT} = 0.1$ heterogeneous coarsening occurs. The decrease of average GOS suggests that stored energy reduction is the driving force for microstructure evolution. Now, it is worth comparing the microstructure of Figure 4.34(b) with the top of Figure 4.20(b) that was annealed for only 15 minutes. Indeed, the comparison shows that microstructure evolution is very similar in both samples. IThen, two remarks can be made. Even without second phase particles,

ε_{RT}	0.05	0.1	0.05/985	0.1/985
$\bar{D}_N(\bar{D}_A)$ [μm]	10(16)	10(17)	13(23)	10(37)
$\overline{GOS}_A$ [°]	0.7	1.4	0.7	0.9

Table 4.12: Average microstructural properties of samples hardened at room temperature with $\varepsilon_{RT} = 0.1$ and $\varepsilon_{RT} = 0.05$ and after annealing at 985°C for ten minutes.

inhomogeneous grain growth can be triggered as the growth rate of grains driven by stored energy is significantly higher than the capillarity driven growth rate. Secondly, the influence of room temperature low strains on microstructure evolution during annealing is very similar to that of low strains at δ sub-solvus temperature. In other words, the stored energy driving force appears to be of the same magnitude.

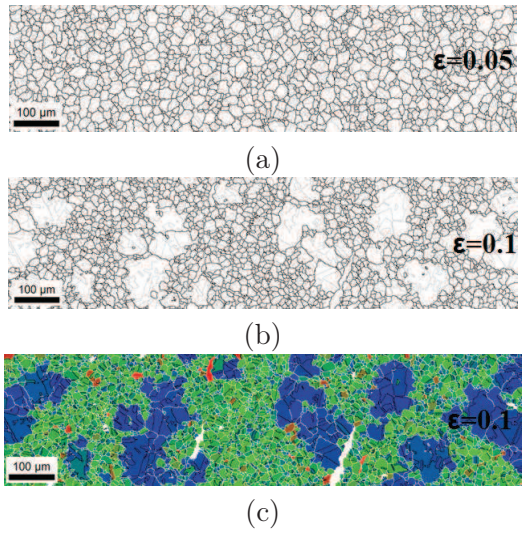

Figure 4.34: EBSD maps of two microstructures hardened at room temperature with $\varepsilon_{RT} = 0.05$ (a) and $\varepsilon_{RT} = 0.1$ (b,c). Grain and twin boundaries are respectively black and grey. In GOS map grain boundaries are white, twins are black and white grains have GOS values higher than 3°.

4.4 Summary

In this chapter, torsion tests are exploited to investigate the influence of small prior strains on the occurence of abnormal grain growth during δ sub-solvus annealing at 985°C for two hours. First of all, it is shown that a reference microstructure that is fine ($\overline{D}_N$=6 µm), recrystallized (strain stored energy-free) and containing δ phase particles (at least 1%) is stable during annealing thanks to Smith-Zener pinning. If the reference microstructure is strained at 985°C in the range $0.05 < \varepsilon < 0.1$, then inhomogeneous grain growth is triggered during annealing. If the strain is higher than $\varepsilon = 0.1$, then coarser but fairly homogeneous microstructures are formed. As for industrial pieces, the origin of the phenomenon is linked to a critical distribution of strain stored energy that triggers during annealing the growth of few low energy grains. Such low energy grains are probably already present in the microstructure before annealing but they can also form by nucleation. The final grain size after annealing could be related to the average intragranular misorientation, which itself is strongly linked to the level of strain applied before annealing.

It is also shown that the chemical heterogeneity of the initial billet from which torsion samples are machined affects the fraction of fine grains of the reference microstructure that remains after inhomogeneous grain growth. The fraction of δ phase particles of the reference microstructure has also a similar effect. However, in both cases inhomogeneous grain growth during annealing can not be avoided as it remains mainly governed by the critical stored energy distribution. If the reference microstructure is not strain-free, then the application of a small strain does not necessarily lead to inhomogeneous grain growth during annealing. Moreover, in this

case Figure 4.12 is no longer valid to predict the final grain size from the average intragranular misorientation before annealing. Finally, it is demonstrated that the thermomechanical cycle triggering inhomogeneous grain growth in torsion tests leads to equivalent results in compression experiments.

Concerning the role of temperature during straining, it is shown that small strains at δ super-solvus temperatures or even room temperature can also trigger inhomogeneous grain growth during annealing. In both cases the phenomenon leads to the formation of microstructures similar to those observed in δ sub-solvus torsion tests. Increasing the straining temperature leads to the formation of microstructures of lower average intragranular misorientation, but it does not prevent abnormal grain growth to occur.

Overall, torsion tests have allowed to confirm that a critical strain stored energy distribution can trigger inhomogeneous grain growth during annealing in microstructures with or without δ phase particles. Microstructure evolution involves the selective growth of few lower energy grains, while higher energy grains do not grow due to Smith-Zener pinning or the slower growth kinetics compared to the one of abnormal grains. It remains questionable if such lower energy grains already exist before annealing or they form by nucleation.

Then, in order to assess the validity of these mechanisms, microstructure evolution must be simulated taking into account in one single framework the principal driving forces for boundary migration: capillarity, stored energy and Smith-Zener pinning.

Résumé

Dans ce chapitre, des essais de torsion ont été réalisés pour étudier l'influence de petites déformations sur le déclenchement de la croissance anormale après un recuit de deux heures à 985°C (température inférieure à la température du solvus de la phase δ). Les résultats démontrent que une microstructure dite de référence, de taille de grains fine (D_N=6um), recristallisée (sans écrouissage) et qui contient des particules de phase δ (au moins 1%vol.) reste stable pendant le recuit à 985°C grâce à l'ancrage de Smith-Zener. Par contre, si la microstructure de référence est préalablement déformée ($0.05<\varepsilon<0.1$) à 985°C, la croissance anormale se produit au cours du recuit ; si la déformation appliquée est supérieure à $\varepsilon=0.1$, alors une microstructure grossière mais plutôt homogène apparaît. L'origine de la croissance anormale est liée, comme dans le cas des pièces industrielles, à une distribution critique d'énergie de déformation qui favorise la croissance d'un nombre réduit de grains de faible énergie par rapport aux grains voisins. Ces grains de faible énergie sont probablement présents dans la microstructure avant le recuit, mais ils pourraient aussi se former par un processus de germination. La taille de grains finale après le recuit a pu être reliée à la désorientation intragranulaire moyenne avant le recuit (Figure 4.12), qui elle-même dépend fortement du niveau de déformation appliqué. Cette relation est

identique à celle établie pour les microstructures issues de gammes de mise en forme industrielles. On a démontré également que l'hétérogénéité chimique de la billette initiale dont sont prélevées les éprouvettes de torsion influe sur la quantité de grains qui ne grossissent pas pendant la croissance anormale. La fraction de phase δ de la microstructure "de référence" produit un effet similaire sur l'évolution microstructurale. Cependant, dans tous les cas la croissance anormale ne peut pas être évitée, car le phénomène est principalement contrôlé par la distribution critique d'énergie de déformation. Si une microstructure écrouie est utilisée à la place de la microstructure de référence, l'application d'une petite déformation supplémentaire ne déclenche pas forcément la croissance anormale des grains. De plus, la courbe de la Figure 4.12 n'est plus valide pour prédire la taille de grain finale à partir de la désorientation intragranulaire moyenne avant recuit. Finalement, on a démontré que le même cycle thermomécanique qui déclenche la croissance anormale après déformation en torsion produit des résultats similaires avec une déformation par compression. Concernant l'effet de la température de déformation, les résultats ont démontré que de petites déformations appliquées à des températures au dessus de la température de solvus de la phase δ ou même à température ambiante peuvent également déclencher la croissance anormale pendant le recuit. Dans les deux cas, le phénomène provoque la formation de microstructures similaires à celles obtenues dans les essais de torsion réalisés à des températures en dessous de la température du solvus de la phase δ. L'augmentation de la température de déformation conduit à la formation de microstructures de plus faible désorientation intragranulaire moyenne pour un niveau de déformation donné, mais ne permet pas d'éviter la croissance anormale des grains. Les essais de torsion ont ainsi confirmé qu'une distribution critique d'énergie peut déclencher la croissance anormale des grains pendant le recuit à 985°C dans des microstructures avec ou même sans particules de phase δ. L'évolution microstructurale est caractérisée par la croissance préférentielle d'un nombre restreint de grains de faible énergie par rapport aux autres grains, qui eux ne grossissent pas à cause de l'ancrage de Smith-Zener ou ont une cinétique de croissance beaucoup plus lente que celle des grains anormaux. Ainsi, pour tester la validité de ce mécanisme de croissance anormale des grains, l'évolution microstructurale doit être simulée en prenant en compte dans un cadre unique les trois forces motrices principales pour la migration d'un joint de grains : la force capillaire, l'énergie de déformation et l'ancrage de Smith-Zener.

5 Simulation of Smith-Zener pinning and abnormal grain growth

Contents

In this chapter, a full field numerical simulation of microstructure evolution is exploited to test the physical mechanisms responsible for inhomogeneous grain growth that were identified by experimental characterization in prevoius chapters. Notably, microstructure evolution is simulated taking into account Smith-Zener pinning, capillarity and stored energy driven grain growth in a single framework. First of all, the numerical model based on a level set description of interfaces in a finite element context is presented. Then, the model is applied to simulate Smith-Zener pinning in a 2D polycrystal, showing its advantages compared to the existing models presented in the literature. Finally, inhomogeneous grain growth is simulated in a 2D polycrystal containing particles where strain stored stored energy distributions (previously estimated from experimental characterization) are taken into account.

5.1 Level set method

The numerical model of microstructure evolution is based on a level set description of interfaces in the context of a finite element formulation coupled with an anisotropic meshing and remeshing strategy. This approach was already used to simulate both 2D and 3D primary recrystallization [75] and grain growth [76] in polycrystals, but without second phase particles.

5.1.1 Formulation and algorithm

In the level set approach, the function ϕ is defined as the signed distance d from an interface Γ of a sub-domain G belonging to a domain Ω. The distance is evaluated on each interpolation point of the considered finite element mesh. The sign of ϕ is defined positive inside the sub-domain and negative outside. Then, the level 0 of the function allows to determine the interface:

$$\begin{cases} \phi(x) = (\chi_G(x) - \chi_{\overline{G}}(x))d(x,\Gamma), \quad x\epsilon\Omega \\ \Gamma = \{x\epsilon\Omega, \phi(x) = 0\}, \end{cases} \tag{5.1}$$

where χ_G and $\chi_{\overline{G}}$ are, respectively, the characteristic functions of G and the complement of G. A priori, if a microstructure contains N_G grains, then one level set function (ϕ_i) per grain G_i has to be considered.

If capillarity is considered as the only driving force for grain growth, assuming a constant mobility (M) and boundary energy (γ), the kinetic law for the grain boundary Γ_i of the grain G_i can be described as:

$$\vec{v}_i = -M\gamma\kappa_i\vec{n}_i, \tag{5.2}$$

where $\vec{n}_i = -\frac{\nabla\phi_i}{\|\nabla\phi_i\|}$ and $\kappa_i = \nabla\cdot\vec{n}_i$ correspond, respectively, to the outside unit normal and the mean curvature of Γ_i in the sense of fluid mechanics (i.e. equal to the sum of the two principal curvatures). Then, microstructure evolution is described by the following set of convection equations:

$$\begin{cases} \frac{\partial\phi_i}{\partial t} - M\gamma\kappa_i\vec{n_i}\cdot\nabla\phi_i = 0 \\ \phi_i(t=0,x) = \phi_i^0(x), \qquad \forall i\epsilon\{1,...,N_G\}, \end{cases} \tag{5.3}$$

where ϕ_i^0 is the imposed initial distance function of each grain. If all level set functions satisfy the metric property $\|\nabla\phi_i\| = 1$, then the problem of Eq.(5.3) can be reformulated as a set of diffusion equations, where the explicit calculation of the curvature and the normal of the grain boundaries can be avoided [76]:

$$\begin{cases} \frac{\partial\phi_i}{\partial t} - M\gamma\triangle\phi_i = 0 \\ \phi_i(t=0,x) = \phi_i^0(x), \quad \forall i\epsilon\{1,...,N_G\}. \end{cases} \tag{5.4}$$

As the resolution of Eq.(5.4) can result in values of $\|\nabla\phi_i\|$ different from unity, then it is necessary to reinitialize periodically all level set functions (so that $\|\nabla\phi_i\| = 1$), by solving this set of reinitialization equations:

$$\begin{cases} \frac{\partial\phi_i^*}{\partial\tau} + \lambda s_i(\|\nabla\phi_i^*\| - 1) = 0 \\ \phi_i^*(\tau=0,x) = \phi_i(t,x), \qquad \forall i\epsilon\{1,...,N_G\}, \end{cases} \tag{5.5}$$

where ϕ_i^* is the reinitialized function, τ is a fictional time, s_i is the sign of ϕ_i and λ is a numerical parameter linked to the mesh size and the simulation time step. Eq.(5.5) is solved for a total fictional time τ_{TOT}, which corresponds to the distance (from the zero level of the function) up to which the function is reinitialized. Finally, the simulation of capillarity driven grain growth involves all these steps at each time increment (details for each step are given in [75, 76, 77]):

1. Grain boundary migration is calculated by solving Eq.(5.4) for each active level set function.
2. All active level set functions are modified near the grain interfaces to remove vacuum regions appearing at multiple grain junctions [76]: $\phi_i^{**}(x,t) = \frac{1}{2}[(\phi_i(x,t) - \underset{j\neq i}{max}(\phi_j(x,t))]$.
3. All active level set functions are reinitialized (so that $\|\nabla\phi_i\| = 1$ near the grain interfaces), by solving Eq.(5.5), in a narrow zone around all interfaces which is defined by τ_{TOT}.
4. Negative level set functions all over the resolution domain are defined as non-active in the algorithm, as they correspond to disappeared grains.
5. Anisotropic remeshing is performed when at least one grain boundary leaves the anisotropically meshed layer (that is a narrow zone of anisotropic refined mesh around interfaces).

Stored energy driven grain boundary migration can be introduced in the level set framework by defining a constant energy value e_i for each grain G_i. Then, it is possible to build the velocity field $\vec{v}_E(x,t)$ associated with stored energy differences across grain boundaries as follows [77, 75]:

$$\vec{v}_E(t,x) = M\sum_{i=1}^{N_G}\sum_{\substack{j=1\\ j\neq i}}^{N_G}\chi_{G_i}(t,x)exp(-\alpha \mid \phi_j(t,x) \mid)(e_i - e_j)\vec{n_j}(t,x), \tag{5.6}$$

where α is a positive parameter calibrated to obtain a negligible exponential term outside the anisotropic mesh surrounding interfaces. The advantage of the velocity field defined by Eq.(5.6) is that it can be used for all grains and it does not require information concerning the microstructure topology (neighboring grains). Finally, the problem defined by Eq.(5.4) can be modified by adding a convection term that takes into account also stored energy driven grain growth:

$$\begin{cases} \frac{\partial\phi_i}{\partial t} - M\gamma\triangle\phi_i + \vec{v}_E(t,x)\cdot\nabla\phi_i = 0 \\ \phi_i(t=0,x) = \phi_i^0(x), \qquad\qquad \forall i\epsilon\,\{1,...,N_G\}\,. \end{cases} \tag{5.7}$$

The simulation of capillarity and stored energy driven grain growth involves the same steps that were previously defined for capillarity driven grain growth, except the first

one that is replaced by the following two steps:

- The velocity field associated with stored energy differences across grain boundaries is calculated using Eq.(5.6)
- Grain boundary migration is calculated by solving Eq.(5.7) for each active level set function.

It is to note that in order to reduce computation time, the level set functions of non-neighbouring grains in the initial microstructure (separated by a certain number of grains) are grouped to form global level set functions (families of grains) that are used to perfom the calculation steps described previously for the microstructure evolution. The grouping algorithm, based on graph coloration, is described in [78]. In practice, in Eq.(5.7) N_G is replaced by N_F, that is the number of grain families. Once again, a grain familiy is considered non-active in the algorithm when it is negative all over the domain, i.e. all family grains have disappeared. The above technique however presents the limitation that when grain growth proceeds, two grains belonging to the same family may become neighbors leading to a "numerical coalescence" of the two grains. This numerical weakness has been already discussed in the literature and solutions have been proposed for regular grids [79]. However, if the connected components (i.e. individual grains) of each global level set function can be easily extracted in regular grids, the problem is much complex when dealing with unstructured anisotropic finite element meshes as in this work. Finally, it was chosen to avoid (or delay) this numerical coalescence by fixing a sufficiently high number of grains that initially separate two grains belonging to the same global level set function.

5.1.2 Particle-grain boundary interaction

The main advantage of the level set approach compared to other numerical methods is the possibility to treat the particle-grain boundary interaction explicitely (through the direct effect on grain boundary curvature), taking into account both the particle morphology and the anisotropy of the interface energy.

The presence of particles is naturally taken into account via its effect on grain boundary curvature. Interestingly, in the level set formulation described in the previous section, the effect of particles can be introduced as a simple boundary condition:

$$\frac{\nabla\phi}{\|\nabla\phi\|} \cdot \overrightarrow{n} = \nabla\phi \cdot \overrightarrow{n} = \sin\alpha, \tag{5.8}$$

where $\overrightarrow{n}$ is the outside unit normal of the particle and α is the angle determined by the balance of surface tensions according to $\sin(\alpha) = (\gamma_{2P} - \gamma_{1P})/\gamma$ (see Figure 5.1). If a particle is incoherent, then the particle-grain interface energy can be considered isotropic: a 90° angle between the particle and the grain boundary is

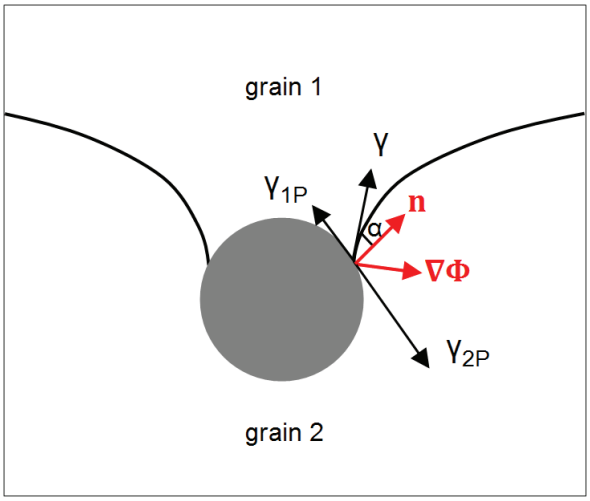

Figure 5.1: Scheme of the interaction of a grain boundary with a particle

imposed, corresponding to a null boundary condition in Eq.(5.8). In practice, the particles are treated as simple voids in the mesh and the boundary condition defined by Eq.(5.8) can be taken into account in the weak formulation of the microstructure evolution defined by Eq.(5.7):

$$\begin{gathered}\int_\Omega \frac{\partial \phi_i}{\partial t} v d\Omega + \int_\Omega \gamma M \nabla \phi_i \cdot \nabla v d\Omega + \int_\Omega \vec{v}_E \cdot \nabla \phi_i v d\Omega = \\ \int_\Gamma \gamma M \nabla \phi_i \cdot \vec{n} v d\Gamma, \quad \forall v \, \epsilon \, H^1(\Omega).\end{gathered} \tag{5.9}$$

Finally, the shape of particles is limited only by the complexity of the mesh. Moreover, if a particle is coherent (generally with respect to only one grain), then anisotropic interface energy can be handled. As an exemple, Figure 5.2 shows the shrinking of a circular grain in the presence of particles as a function of particle-grain interface energy. If particles are coherent (α=15° or α=30°), pinning pressure is higher so the distance swept by the migrating boundary before reaching the stable configuration is lower compared to the case of incoherent (α=0°) particles.

5.1.3 Microstructure generation

The initial grain structure is generated in a finite element mesh using the coupled "Advancing front packing/Voronoï-Laguerre tesselation" method developed in a level set context [78]. The initial grain structure is built in two steps: generation of a dense circle distribution thanks to an optimised advancing front packing algorithm, then calculation of level set functions of the Voronoï-Laguerre cells (the grains) from the circles using a Voronoï-Laguerre method. The main advantage of this approach is the possibility to generate grain structures obeying to specific grain size distribution laws. For exemple, Figure 5.3 shows that it is possible to generate a digital grain size distribution very close to the experimental distribution of an Inconel 718

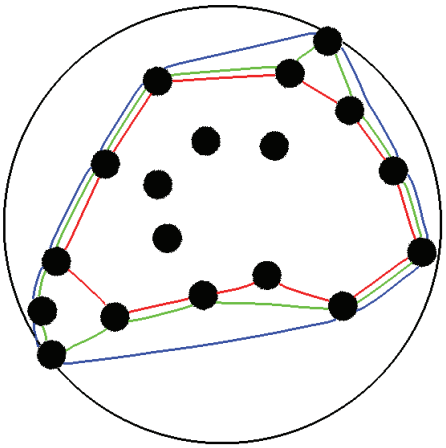

Figure 5.2: Shrinking of a circular grain of diameter=12 μm (black line) in the presence of secondary phase particles (radius=0.4 μm). If particles are incoherent (α=0°, red line) the circular grain shrinks the most before reaching the stable configuration. If particles are coherent (α=15°, green line or α=30°, blue line) shrinking stops earlier yielding different stable configurations.

microstructure. In fact, for that configuration (about 1450 grains in a 220x230 μm domain) the error of the surface-weighted grain size digital distribution with respect to the experimental one ($\sqrt{\frac{\sum(f_{EXP}-f_{NUM})^2}{\sum f_{EXP}^2}}$%, where f is the fraction of a certain grain size class) is only 3%.

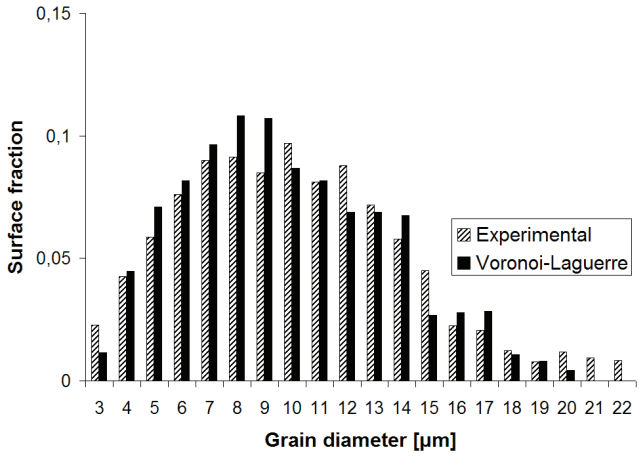

Figure 5.3: Comparison between an Inconel 718 experimental surface-weighted grain size distribution and a statistically equivalent digital distribution (about 1450 grains in a 220x230 μm domain): number-weighted grain size is 6.1 μm and surface-weighted grain size is 9.6 μm.

The generation of particles first involves the calculation of the level set function that describes the whole particle distribution. For randomly distributed monodisperse spherical particles, such level set function is calculated using the same tools

as those for generating grains [78]. Then, the particle level set function is used to remesh the simulation domain: anisotropic remeshing is performed around particles in order to obtain smooth interfaces [76]. Finally, all elements which are inside the particles are removed from the mesh.

Real particles morphology digitalization It is also possible to generate a particle population that reproduces the same morphology and distribution of particles as they appear on a backscattered electron (BSE) image of δ phase particles in Inconel 718. For this purpose, a marching squares method [80] is applied on a binary image of a microscopy image to calculate the global level set function of the particle distribution in the finite element mesh of the domain. Then, the same methodology used for spherical particles is applied to obtain the final mesh. Figure 5.4 illustrates the different steps required to generate the finite element mesh where particles appear as voids. It is to note that in the final simulation domain the population of particles closely resembles the experimental one. More precisely, only the smallest particles, hardly visible even on the binary image, are not taken into account.

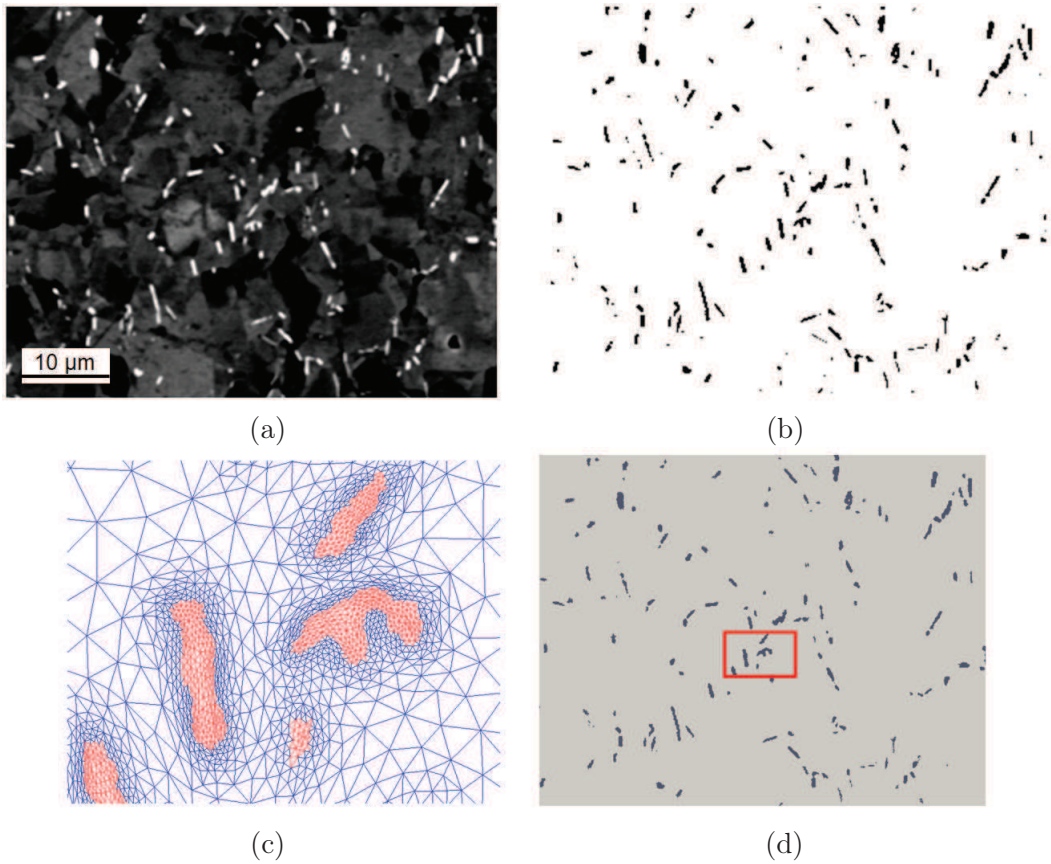

Figure 5.4: Digitalization process of a real distribution of δ phase particles in Inconel 718. Experimental BSE microscopy image (a), binary image of δ phase particles (b), detail of anisotropic meshing around particles before removing the internal red elements, final simulation domain where particles appear as voids.

5.1.4 Simulation parameters

All numerical calculations presented in this work are performed using the finite element C++ library "CimLib" developed at Cemef. Simulations are run on a computer cluster: on average 16 processors (2.3GHz, 2GB) are used to run numerical calculations, reaching a maximum of 64 processors for the most time-consuming ones. All simulations are performed on two-dimensional square domains and a stabilized P1 solver as SUPG or RFB method is used to solve Eq.(5.7).

The same values of grain boundary mobility (M) and energy (γ) that appear in Eq.(5.2) and Eq.(5.6) are used in all simulations. These values are chosen as close as possible to the grain boundary properties of Inconel 718 at a δ sub-solvus temperature (around 985°C). The value of grain boundary energy is set to $\gamma = 0.6J/m^2$, which corresponds to the energy of pure nickel at 1000°C [63]. The value of grain boundary is set to $M = 2,3 \cdot 10^{-13} m^4/(J \cdot s)$. Such value was calculated using an available experimental data set of Inconel 718 grain size evolution during annealing at different δ super-solvus temperatures [81]. Fitting Eq.(2.15) to experimental data allowed to determine mobility values at different δ super-solvus temperatures. Then, the following Arrhenius-type equation was calibrated to extrapolate the mobility value at 985°C:

$$M(T) = M_0 exp(\frac{-Q}{RT}), \tag{5.10}$$

where T is the temperature, $M_0 = 2981 m^4/(J \cdot s)$, $Q = 387 kJ/(mol \cdot K)$ and $R = 8.31 J/(mol \cdot K)$.

Particles are considered incoherent in all simulations, which undermines an isotropic particle-grain interface energy. Hence $\alpha = 90°$ is imposed in Eq.(5.8).

Grain sizes are measured automatically with the Visilog software using images of the grain structure at different time steps. It is to note that this methodology is imposed by the use of global level set functions that describe several grains belonging to the same family: the direct information on each individual grain (like its size) is lost in the finite element simulation.

5.2 Smith-Zener pinning

In this section, Smith-Zener pinning simulations are presented. The only driving force for boundary migration is capillarity (the curvature of grain boundaries). Then, Eq.(5.4) is solved to determine microstructure evolution. First of all, numerical parameters are calibrated and optimized in order to reduce computation time for all the considered numerical simulations. Notably, the influence of the simulation time step and the "roughness" of the interface of particles are tested in the simple case of a circular grain shrinking. Then, Smith-Zener pinning is simulated in polycrystals and the results are compared to those obtained by different numerical approaches in the literature.

5.2.1 Calibration of numerical parameters

A simple case of shrinking of a circular grain in the presence of circular particles is used to calibrate and optimize the simulation time step (taken in the range 0.075s-0.25s) and the "roughness" of the interface of particles (coarse, average, fine). All other simulation parameters are kept fixed. The initial diameter of the grain is 12 μm, the radius of particles is 0.4 μm and their surface fraction inside the grain is 8%. The average background mesh size is 2 μm, the full width of the anisotropic layer is 0.4 μm and the refined mesh size in the direction perpendicular to the grain interface is about 0.1 μm. The level set function is reinitialized only within the anisotropic layer, that is up to 0.2 μm from the zero isovalue. Anisotropic remeshing is performed every 10s. Figure 5.5 represents the evolution of grain shrinking with time step=0.1s

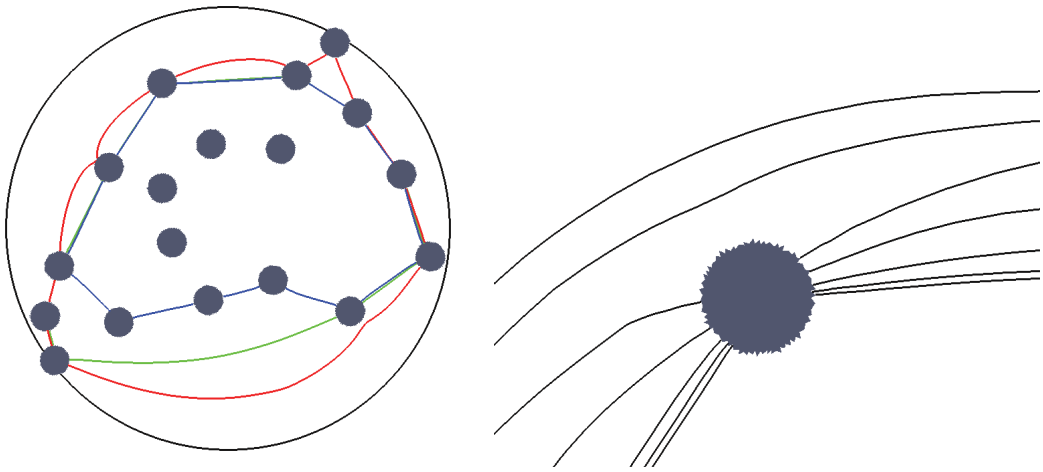

(a) (b)

Figure 5.5: Shrinking of a circular grain of diameter=12 μm in the presence of particles (radius=0.4 μm). The evolution from initial grain size (black line) to the stable grain size (blue line) is shown at intervals of 50s (a). Detail of the interaction grain boundary-particle is shown at intervals of 10s (b).

and average particle mesh size. It is interesting to note that as the grain boundary approaches a particle, boundary migration is locally accelerated. However, as the grain boundary crosses the particle it is slowed down and eventually pinned. After 200s the whole grain reaches a stable configuration and it stops to shrink. If the time step of the simulation is increased up to 0.25s, the evolution is similar but no stable configuration is reached, that is the grain continue to shrink until it disappears. On the contrary, if the time step is reduced to 0.075s, the same stable configuration is reached. These results show that the simulation time step must be lower than a critical value (in this case lower than about 0.1s) in order to properly take into account the pinning effect of particles. Indeed, if the time step is too high, with respect to the migration velocity of the grain boundary, the constraint imposed by Eq.(5.8) on grain boundary curvature is not properly applied. As a result, particles

only slow down migrating boundaries but they do not pin them.

Another important numerical parameter than can influence the pinnig effect is the "roughness" of the interface of particles. As shown in Figure 5.4 the roughness of the particles interface is determined by the mesh size on the normal direction of the particles interfaces before removal of the internal elements. Figure 5.6 shows that different levels of roughness can be obtained, going from coarse to fine interfaces. If the same case of circular grain shrinking (time step=0.1s) is run with each of these particles, then the same final stable configuration of Figure 5.5 is reached. Apparently, the particles roughness does not influence significantly the pinning phenomenon, then it is possible to limit the number of elements in the simulation by choosing particles with coarse or average roughness.

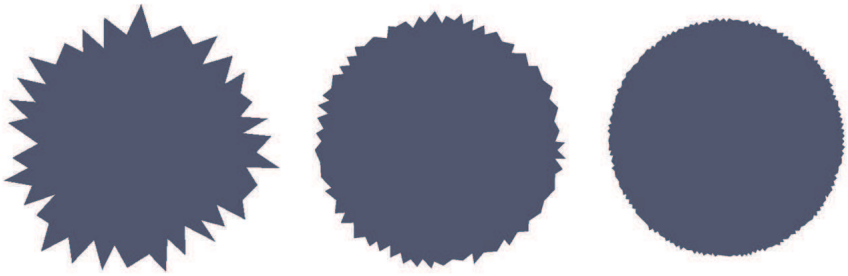

(a) (b) (c)

Figure 5.6: Different levels of particles (radius=0.4 μm) roughness: coarse (a), average (b), fine (c).

5.2.2 Simulation of Smith-Zener pinning

In the following, Smith-Zener pinning is simulated in a polycrystal with different populations of particles. The simulation domain is a square of dimensions [200x200 μm], containing about 1100 grains: the grain size distribution is generated using the experimental histogram of Figure 5.3. As considered in the calibration of numerical parameters, the average background mesh size is 2 μm, the full width of the anisotropic layer is 0.4 μm and the refined mesh size in the direction perpendicular to grain interfaces is about 0.1 μm. The number of elements in the mesh is about 500,000. Figure 5.7 illustrates an example of the anisotropic finite element mesh used in simulations. Level set functions are grouped in 26 families so that at least 3 different grains separate two grains belonging to the same family at the beginning of the simulation. Thus, no numerical coalescence occurs in all the considered simulations. Global level set functions are reinitialized only within the anisotropic layer, that is up to 0.2 μm from the zero isovalue. The simulation time step is 0.1s, while anisotropic remeshing is performed every 10s.

Figure 5.8 displays the number-weighted grain size evolution in the presence of increasing surface fractions of randomly distributed circular particles with radius=0.4

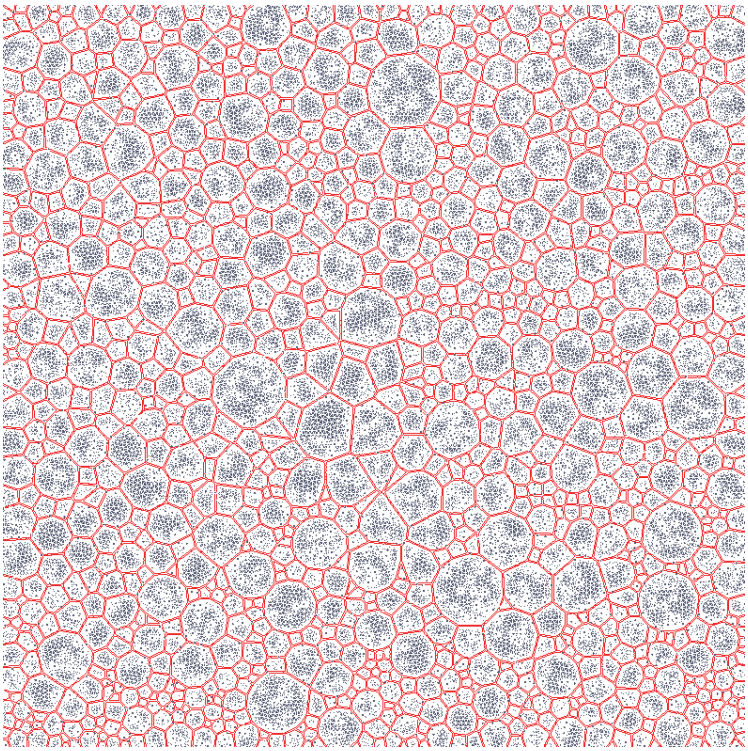

(a)

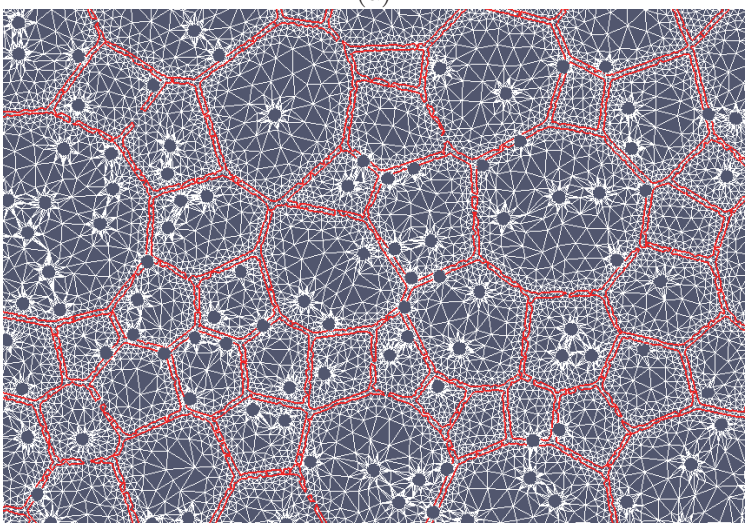

(b)

Figure 5.7: Mesh of the domain [200x200 μm] containing around 500,000 elements (a). Detail showing anisotropic meshing around grain boundaries (b) which are located in the region defined by the red lines. Particle radius is 0.4 μm and particle fraction is 4%.

μm. As expected, grain size reaches a limiting value that is linked to the fraction of particles. For the highest fraction (4%), the limit is reached after only 10 minutes, while for the lowest fraction (1%) it takes one hour.

The results concerning the limiting grain size that is reached after grain growth in the presence of several circular particles distributions are summarized in the plot of

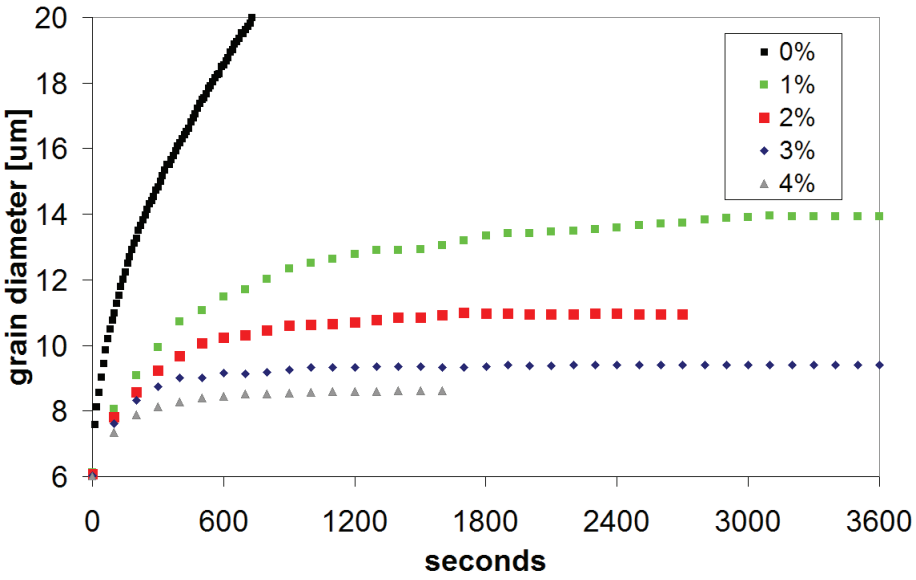

Figure 5.8: Number-weighted grain size evolution in the presence of increasing surface fractions of randomly distributed circular particles with radius=0.4 μm.

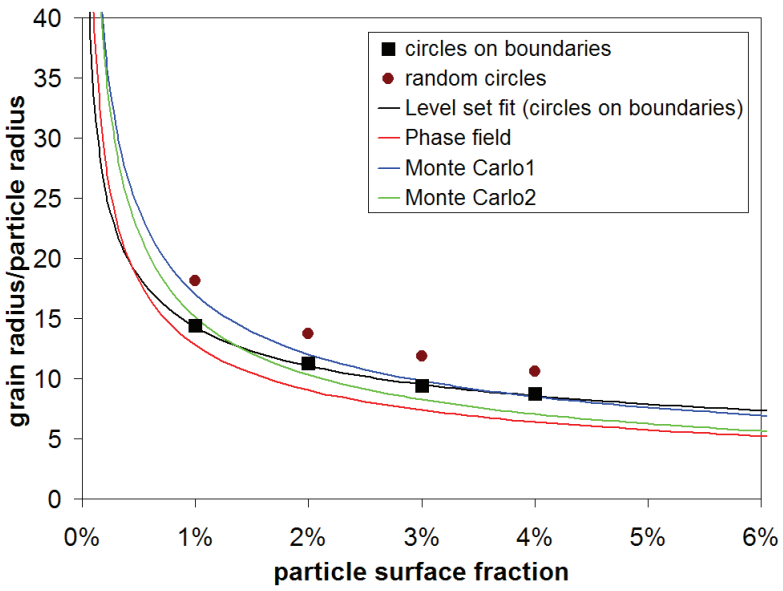

Figure 5.9: The level set results of the limiting grain radius normalized by the particle radius are plotted as a function of the total surface fraction of particles. Also Eq.(1.1) is plotted as determined by several numerical methods in literature [82]: Monte Carlo1 (m=0.5, K=1.7), Monte Carlo2 (m=0.55, K=1.2), phase field (m=0.5, K=1.3). The level set method yields m=0.37, K=2.6.

Figure 5.9. In this plot also Eq.(1.1) is plotted with different values of parameters K and m that were obtained by using other 2D numerical methods in literature [82]. In the case of randomly distributed circular particles (round points), the data obtained

in level set simulations fall above all curves. This is due to the fact that in level set simulations of this work, the imposed initial grain size structure is uncorrelated to the distribution of circular particles. Hence, all particles that fall inside the grains may not contribute to Smith-Zener pinning during grain growth. As reported in Table

f=1%	f=2%	f=3%	f=4%
initial fraction on boundaries [%]			
35	33	33	32
final fraction on boundaries [%]			
65	58	56	52

Table 5.1: Comparison of fraction of particles located at grain boundaries at the beginning or at the end of each simulation for random initial particle distributions.

5.1, the average final fraction of particles on boundaries is not higher than 65%. On the contrary, in the Monte Carlo or phase field simulations reported in the literature, the initial grain size is usually generated by nucleation of new grains in the presence of circular particles, then the fraction of particles on grain boundaries is higher from the beginning of the simulation. If in the level set simulation all circular particles are located on the initial grain boundaries, then the limiting grain size decreases as the final fraction of particles on grain boundaries is higher than 90% (see Table 5.2). Eq.(1.1) can be used to fit these data by setting m=0.37 and K=2.6, which are values consistent with those obtained in the literature. These results confirm that the degree of contact between particles and grain boundaries is a missing parameter in Eq.(1.1).

f=1%	f=2%	f=3%	f=4%
initial fraction on boundaries [%]			
100	100	100	100
final fraction on boundaries [%]			
90	94	96	98

Table 5.2: Comparison of fraction of particles located at grain boundaries at the beginning or at the end of each simulation for non random initial particle distributions.

In fact, in the literature it has been already proposed to modify Eq.(1.1) as [82]:

$$\frac{\overline{R}}{\overline{r}} = \frac{K}{f_{GB}^{m}}, \tag{5.11}$$

where f_{GB} is the surface fraction of particles located only on grain boudaries when grain growth stops.

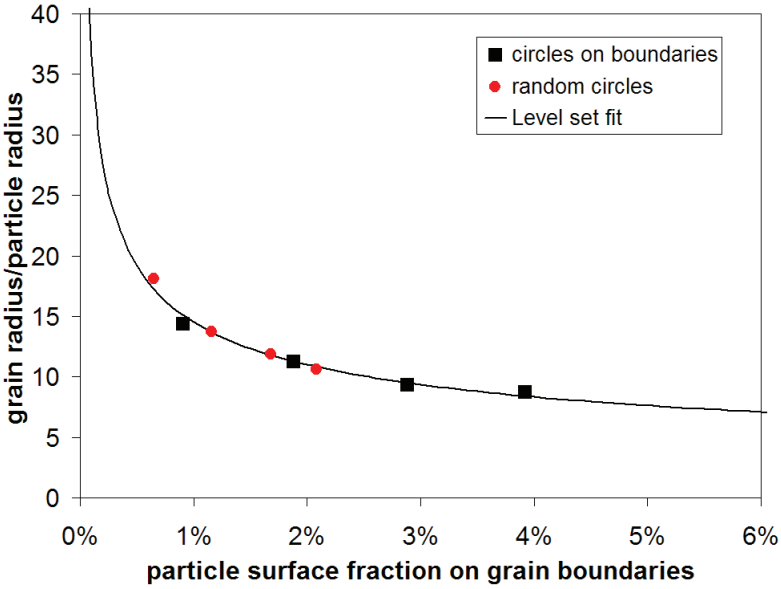

Figure 5.10: The level set results of the limiting grain radius normalized by the particle radius are plotted as a function of the final surface fraction of particles on grain boundaries. The level set method yields m=0.4, K=2.3.

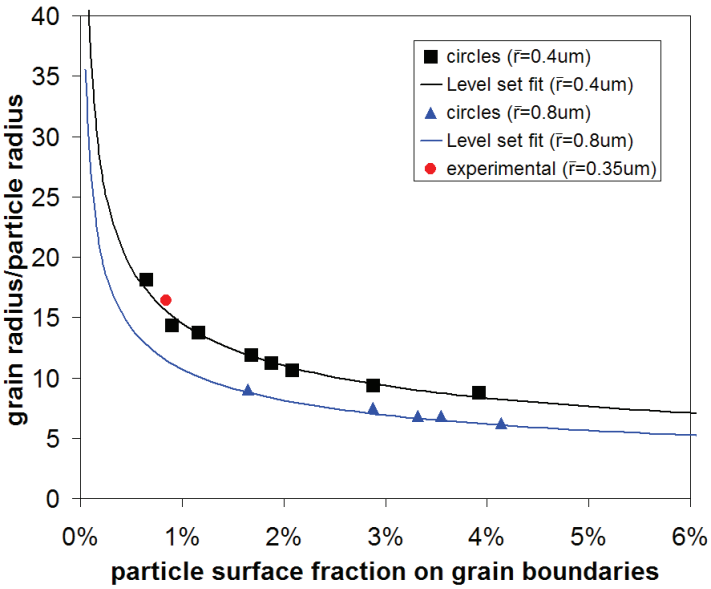

Figure 5.11: The level set results of the limiting grain radius normalized by the particle radius are plotted as a function of the final surface fraction of particles on grain boundaries. The level set method yields m=0.4, K=1.7 for particule radius=0.8 μm.

Interestingly, Figure 5.10 shows that if the total surface fraction of particles (on the x-axis) is replaced with the final surface fraction of particles on grain boundaries (when grain growth stops), then all data points fall on the same curve with parameters m=0.4 and K=2.3. However, the drawback of Eq.(5.11) is that it can not be

used to predict limiting grain sizes from initial particle distribution parameters, as it requires to know a priori the surface fraction of particles located only on grain boudaries when grain growth stops.

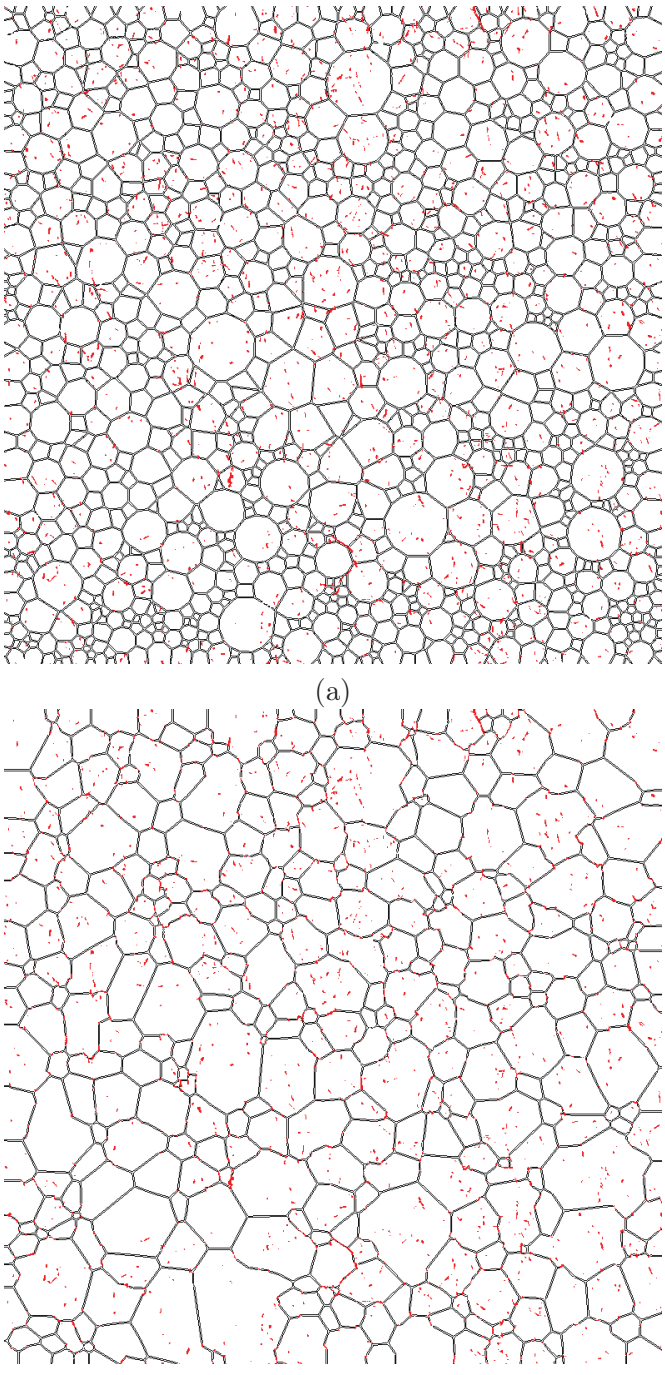

(a)

(b)

Figure 5.12: Simulation of grain growth with real particle morphology in a domain [200x200 μm]. Initial microstructure (a) and after 2400s (b) when grain growth has already stopped.

The plot of Figure 5.11 illustrates the influence of particle size on the limiting grain

size. If particle radius is increased up to 0.8 μm, then the value of m in Eq.(5.11) does not change compared to the one obtained by smaller particles (m=0.4). However, the value of k is lower (K=1.7). This result is quite interesting as it would suggest that Eq.(5.11) (or Eq.(1.1)) can not predict exactly the limiting grain size in microstructures characterized by different grain/particle size ratios, as it is generally found in the literature. In fact, this finding could be another reason of the scatter of k values reported in the literature. Interestingly, the higher pinning pressure of bigger particles, leading to a smaller limitin grain size, would be supported by Eq.(1.2): bigger particles are supposed to pin more strongly grain boundaries that can hardly overpass a particle once pinned.

The plot of Figure 5.11 shows also the influence on the limiting grain size of the experimental particle distribution generated as illustrated in Figure 5.4. The particle fraction of this distribution is 1.9%, while the average particle radius is 0.35 μm. It is interesting to note that, despite the very complex particle morphology (see Figure 5.12), the point related to the experimental distribution is very close to the curve of circular particles (radius=0.4 μm). This result would confirm that particle morphology has a little effect on Smith-Zener pinning in the considered conditions. Similar results can be found in the literature [17, 18], even if only the influence of spheroid and rod-like particles has been investigated.

5.3 Inhomogeneous grain growth

Experimental analysis has shown that inhomogeneous grain growth can occur in pinned microstructures due to critical distributions of strain stored energy. In the following, grain growth is simulated in a polycrystal using Eq.(5.7) which allows to take into account stored energy driven grain growth. First of all, the stability of an energy-free grain in a pinned microstructure is investigated. Finally, the influence of stored energy distributions (estimated from experimental characterization) on the occurence of inhomogeneous grain growth is discussed.

5.3.1 Strain energy and Smith-Zener pinning

The stability of an energy-free grain in a pinned microstructure is investigated in a domain [100x100 μm] containing circular particles of radius=0.4 μm and surface fraction equal to 4%. The same simulation parameters used for previous Smith-Zener pinning simulations are used: the only difference is that remeshing is performed more often (every 1s) to ensure that during migration the grain boundaries remain inside the anisotropic layer.

Several simulations are run by setting a constant positive value of energy for all grains but one (that is set to zero). Thus, the evolution of the strain-free grain is driven both by capillarity and the stored energy difference ($\triangle E$) with respect to all other grains. The energy difference is kept lower than $300kJ/m^3$, which corresponds

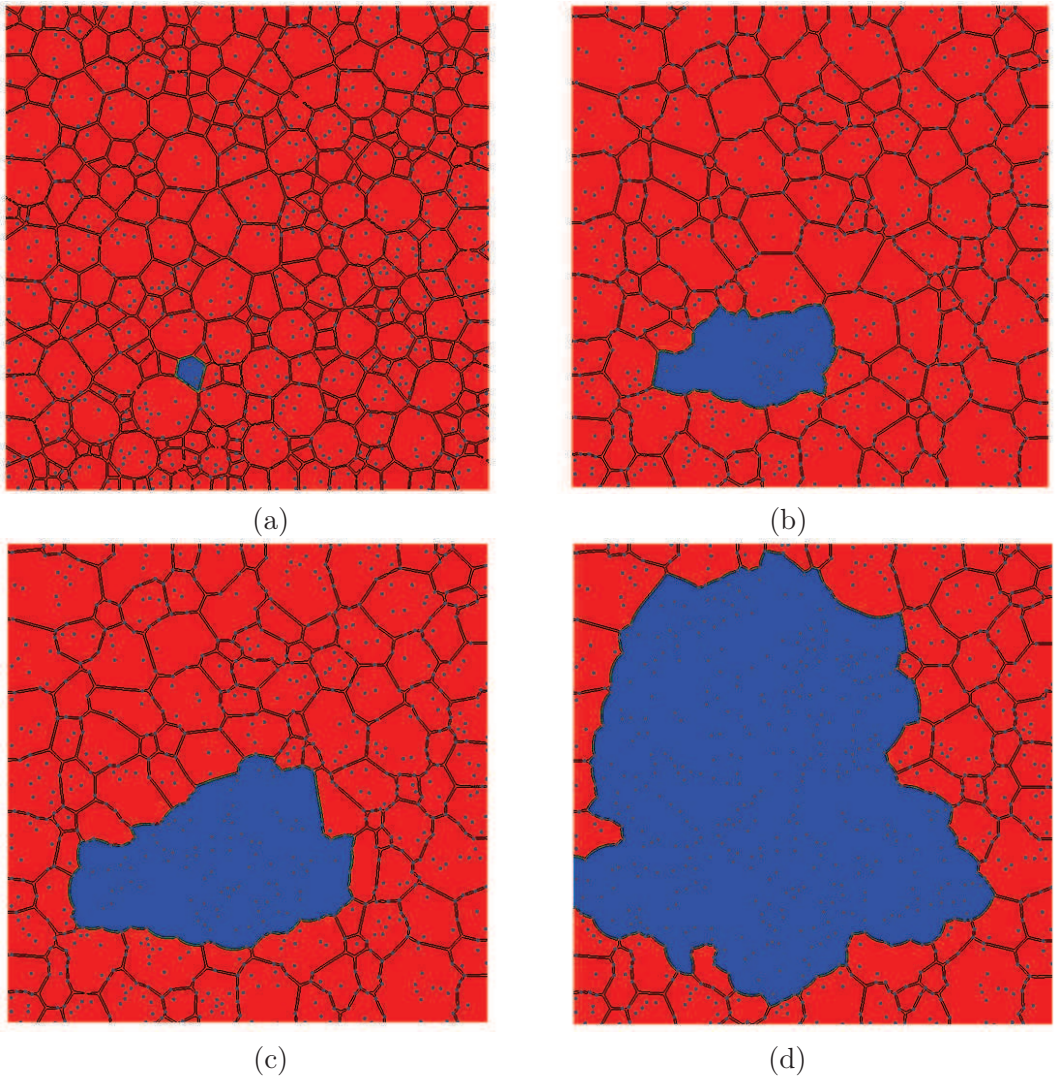

Figure 5.13: Evolution of an energy-free grain in a domain [100x100 μm] when the energy of all other grains is set to $E = 200kJ/m^3$: intial microstructure (a), after 600s (b), 1800s (c), 3600s (d).

to a driving pressure of $300kPa$. By comparison, the average capillarity driving pressure of a circular grain of the microstructure is $\frac{R}{\gamma} = 200kPa$, where $R = 3\mu m$ and $\gamma = 0.6J/m^2$.

Grain size evolution of the case with $\triangle E = 200kJ/m^3$ is illustrated in Figure 5.13. All grains, except the energy-free one, coarsen only up to 600s, but then grain growth stagnates due to particles pinning. On the contrary, the energy-free grain continue to grow and after one hour its grain size is more than ten times bigger compared to the initial one (about 7 μm). Eventually, the grain will cover the whole domain. Such grain evolution is interesting as it demonstrates that indeed small stored energy differences among grains can trigger inhomogeneous grain growth in pinned microstructures. Now, it seems worth to investigate what is the influence of the energy difference ($\triangle E$) on microstructure evolution. Figure 5.14 shows that

up to $\triangle E = 150kJ/m^3$, the energy-free grain grows faster initially, but then grain growth slows down and eventually the grain is pinned by particles like all other grains. Interestingly, a quite small increase of energy ($\triangle E = 175kJ/m^3$) leads to a metastable situation: the energy-free grain is almost pinned between 1200s and 2400s, but eventually it continues to grow. As expected, increasing further the energy difference up to $\triangle E = 300kJ/m^3$ accelerates significantly the growth of the energy-free grain that after only 600s is 8 times bigger than the average grain size.

Overall, these results show that the competition between the stored energy driven pressure for boundary migration and Smith-Zener pinning can lead to critical configurations where just a small variation of these pressures can trigger the abnormal growth of a grain.

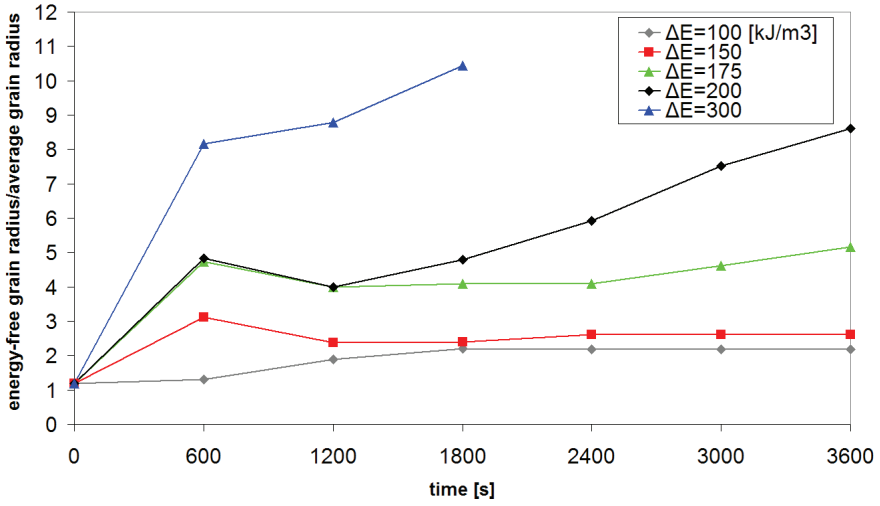

Figure 5.14: Evolution of the energy-free grain size during time as a function of the energy difference with surrounding grains.

5.3.2 Influence of strain energy distribution

In this section the influence of strain energy on the occurence of inhomogeneous grain growth is investigated. In particular, the objective is to assess if the critical strain energy distributions estimated from experimental data (notably EBSD) can trigger inhomogeneous grain growth in numerical simulations. For this reason, it seems worth to focus on the strain energy distribution induced by a δ sub-solvus strain of $\varepsilon_{SUB} = 0.1$. As already illustrated in Figure 4.20, such straining induces after annealing for only 15 minutes the growth of few grains, leading to inhomogeneous grain growth. In Figure 5.15 it is reported the GAM distribution of sample $\varepsilon_{SUB} = 0.1$ just after deformation (see Figure 4.5). Such distribution can be converted to the average density of geometrically necessary dislocations (GNDs) per grain using Eq.(2.17). Then, using Eq.(2.16) it is possible to estimate the average stored energy per grain. Indeed, such calculation doest not take into account the energy contribution from

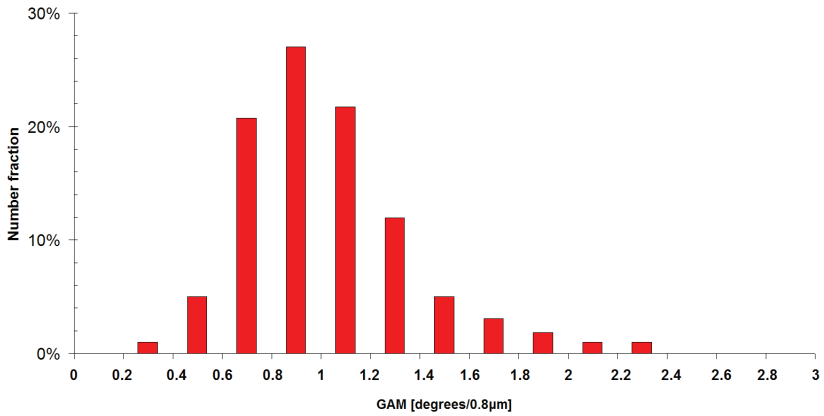

Figure 5.15: GAM distribution of sample $\varepsilon_{SUB} = 0.1$ before annealing.

statistically stored dislocations (SSDs) that can be hardly estimated. For this reason, it is proposed to multiply Eq.(2.17) by a positive constant parameter s, that would take into account the presence of additional statistically stored dislocations. This undermines that the SSDs density would increase linearly with the GNDs density. Finally, if s=1 only GNDs are considered. If s=2, then it supposed that 50% of dislocations are SSDs. If s=4, then 75% of dislocations are SSDs. Figure 5.16 reports the strain energy distribution of sample $\varepsilon_{SUB} = 0.1$ as a function of the parameter s. As expected, as s increases histograms widen and shift towards higher values.

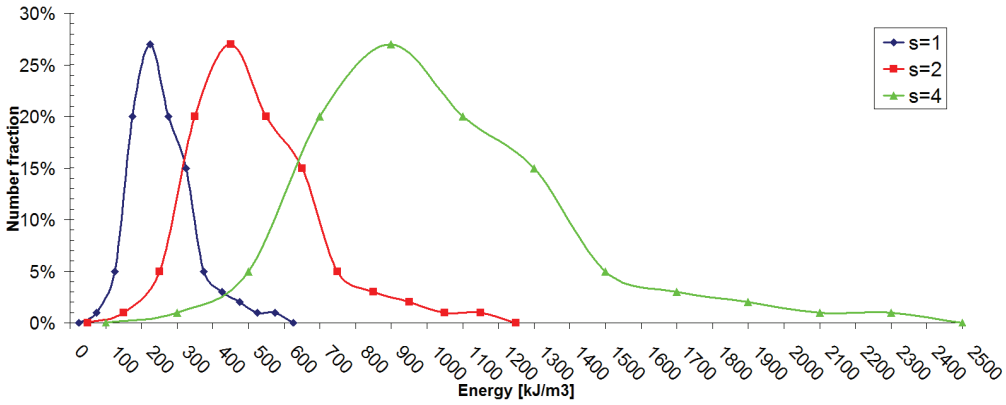

Figure 5.16: Strain stored energy distribution of sample $\varepsilon_{SUB} = 0.1$ before annealing. The parameter s is supposed to take into account the energy contribution of statistically stored dislocations.

The effect of strain stored energy on microstructure stability is investigated in a domain [200x200 µm] containing circular particles of radius=0.4 µm and surface fraction equal to 2% or 4%. The same simulation parameters used for previous Smith-Zener pinning simulations are used and remeshing is performed every 1s. Moreover, the grains level set functions are grouped in 91 global level set functions so that at least 6 different grains separate two grains belonging to the same family at the beginning of the simulation. This is necessary to avoid the "numerical coalescence" of

grains that is favoured by the introduction of strain stored energy which allows grains to grow overpassing the Smith-Zener limit. A different value of energy is initially assigned to each grain family so that the stored energy distribution of grains obeys one of the histograms of Figure 5.16. It is to note that, as microstructure evolves, each grain keeps its intial value of energy. Several simulations are performed using the same initial grain structure but changing the energy distribution ($s = 1$ or $s = 4$) or particle fraction (2% or 4%).

In the following, two simulations are presented where the same initial energy distribution of Figure 5.16 ($s = 1$) is imposed and particle fraction is equal to 2% or 4%. Figure 5.17 displays the evolution during annealing of the microstructure with particle fraction equal to 2%. The lowest energy grains (labeled by letters from A to N) reach the highest sizes, however some of them disappear or do not grow much. Overall, average grain size increases significantly due to stored energy differences among grains and the final microstructure contains mostly low energy grains.

Figure 5.18 illustrates the influence of the stored energy distribution ($s = 1$) on the limiting grain size with respect to previous Smith-Zener pinning simulations. As expected, the additional driving force due to stored energy differences leads to coarser microstructures with respect to those where capillarity is the only driving force. Nonetheless, a limiting grain size is reached even in the presence of a strain distribution as stored energy differences between grains decrease as grain growth proceeds. It is to note that the biggest grains in the final microstructure have not necessarily the lowest energy values, because the energy difference with respect to neighbor grains (i.e. the topology effect) controls energy driven grain growth. Now, it is interesting to measure the size evolution of three of the lowest energy grains (located at the centre of the simulation domain) in microstructures where particle fraction is either 2% or 4% (see Figure 5.19). If the particle fraction is 2%, then grains C and D stop to grow after only 600s due to Smith-Zener pinning, while grain B continues steadily but slowly to overgrow. Interestingly, if the particle fraction is 4%, then also grain D overgrow, because increasing the average pinning pressure, decreases the average growth rate of higher energy grains.

Overall, the stored energy distribution of Figure 5.16 with $s = 1$ does not trigger abnormal grain growth in simulations as it occurs experimentally (Figure 4.20). In fact, the size of the largest overgrown grain is only three times bigger than the average grain size and it takes about one hour of annealing to reach this size. The stored energy distribution only increases the limiting grain size of microstructures with respect to equivalent Smith-Zener pinning simulations where stored energy driven grain growth is not taken into account.

As already discussed, if $s = 1$ then strain stored energies are estimated taking into account only GNDs. Hence, it seems worth performing the same previous simulations by imposing the initial energy distribution of Figure 5.16 with $s = 4$. Figure 5.20 illustrates that after only 900s of annealing almost the same microstructures are

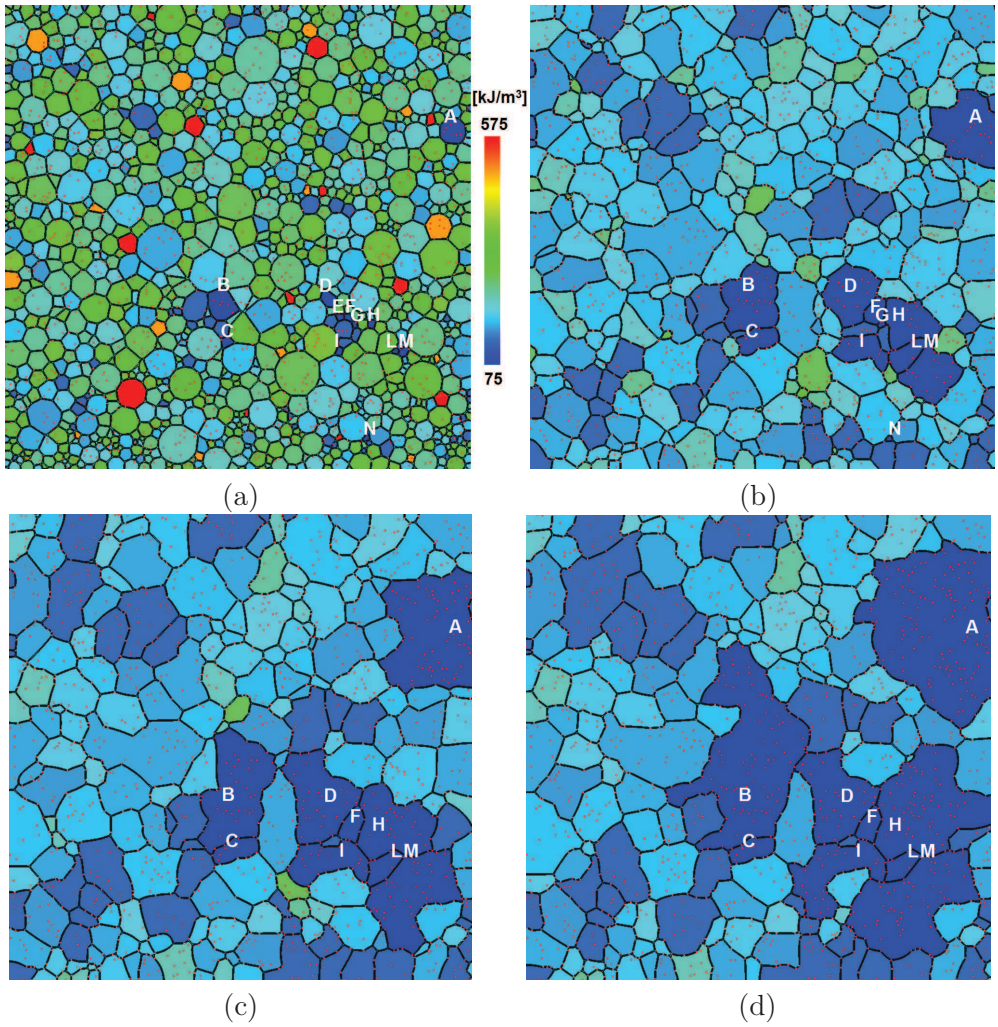

Figure 5.17: Evolution of a microstructure with particle fraction equal to 2% and energy distribution with $s = 1$: initial microstructure (a), after annealing at 985°C for 300s (b), 900s (c) and 3300s (d).

formed for particle fractions equal to 2% or 4%. Notably, the size reached by the lowest energy grains is the same, while the average size of all grains is smaller in the microstructure with the higher particle fraction. The evolution of individual grains (see Figure 5.21) reveals that in both microstructures grain B grows abnormally thanks to its initial grain advantage and its surrounding that is mainly composed by higher energy grains (see Figure 5.17). On the contrary, grains C and D start to grow abnormally but then they impinge on other low energy grains and so their growth is slowed down or stopped.

Indeed, the histogram of Figure 5.16 with $s = 4$ can trigger in simulations abnormal grain growth in a similar fashion to the evolution reported experimentally. Notably, abnormal grain size and growth kinetics are at least comparable. This result seems to confirm that the contribution of SSDs to strain stored energy is far from neglectable to describe correctly abnormal grain growth. However, it is necessary to recall that

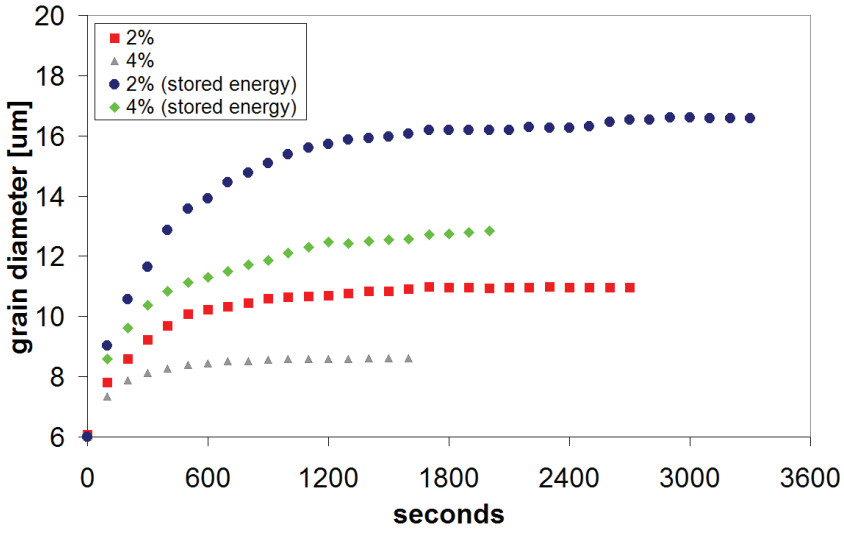

Figure 5.18: Grain size evolution in particle containing microstructures with or without stored energy distribution ($s = 1$).

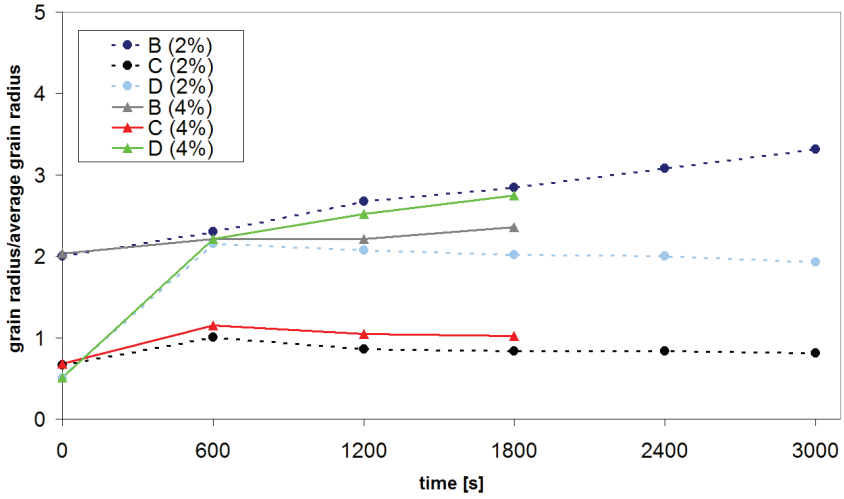

Figure 5.19: Grain size evolution of grains B, C and D in two microstructures with the stored energy distribution of Figure 5.16 ($s = 1$) and particle fraction equal to 2% or 4%.

in this work the numerical simulation of abnormal grain growth was limited to two dimensions, then the Smith-Zener pinning force is overestimated. It seems reasonable to suppose that the phenomenon would be triggered in a 3D simulation by using the same histogram of Figure 5.16 with $s < 4$.

Figure 5.20 suggests that particle fraction (2% or 4%) does not influence much the evolution of overgrown grains as it is mainly governed by stored energy reduction. On the contrary, the particle fraction governs the size and fraction of the grains that do not grow abnormally. Interestingly, similar results were obtained experimentally by comparing two microstructures with 5% or 0.3% of δ phase particles (see section

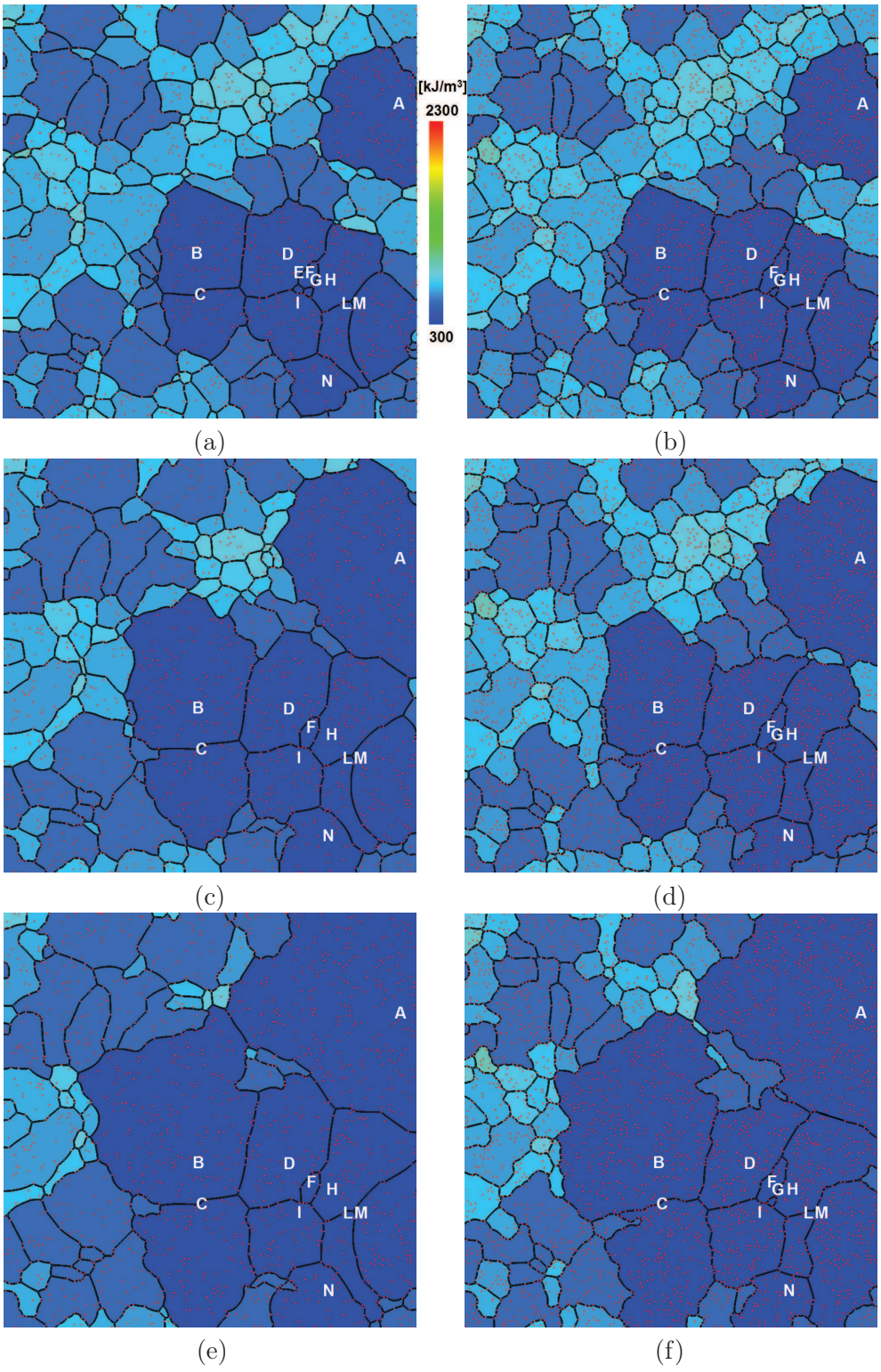

Figure 5.20: Evolution of the microstructures with the energy distribution of Figure 5.16 ($s = 4$) and a particle fraction equal to 2% (left) and 4% (right) after annealing at 985°C for different times: 300s (a,b), 600s (c,d) and 900s (e,f).

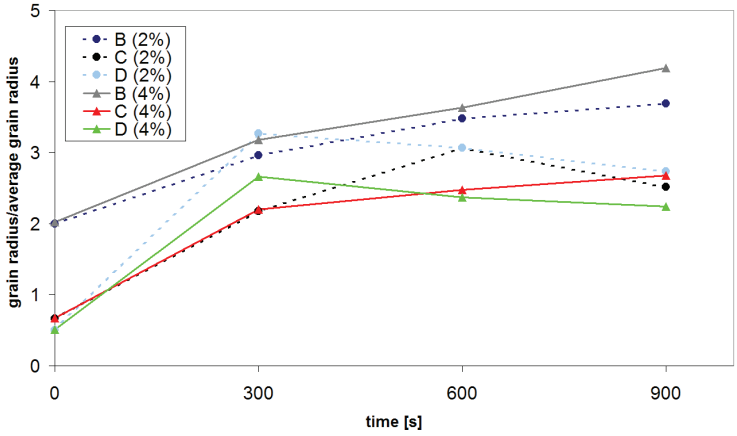

Figure 5.21: Grain size evolution of grains B, C and D in two microstructures with the stored energy distribution of Figure 5.16 ($s = 4$) and particle fraction equal to 2% or 4%.

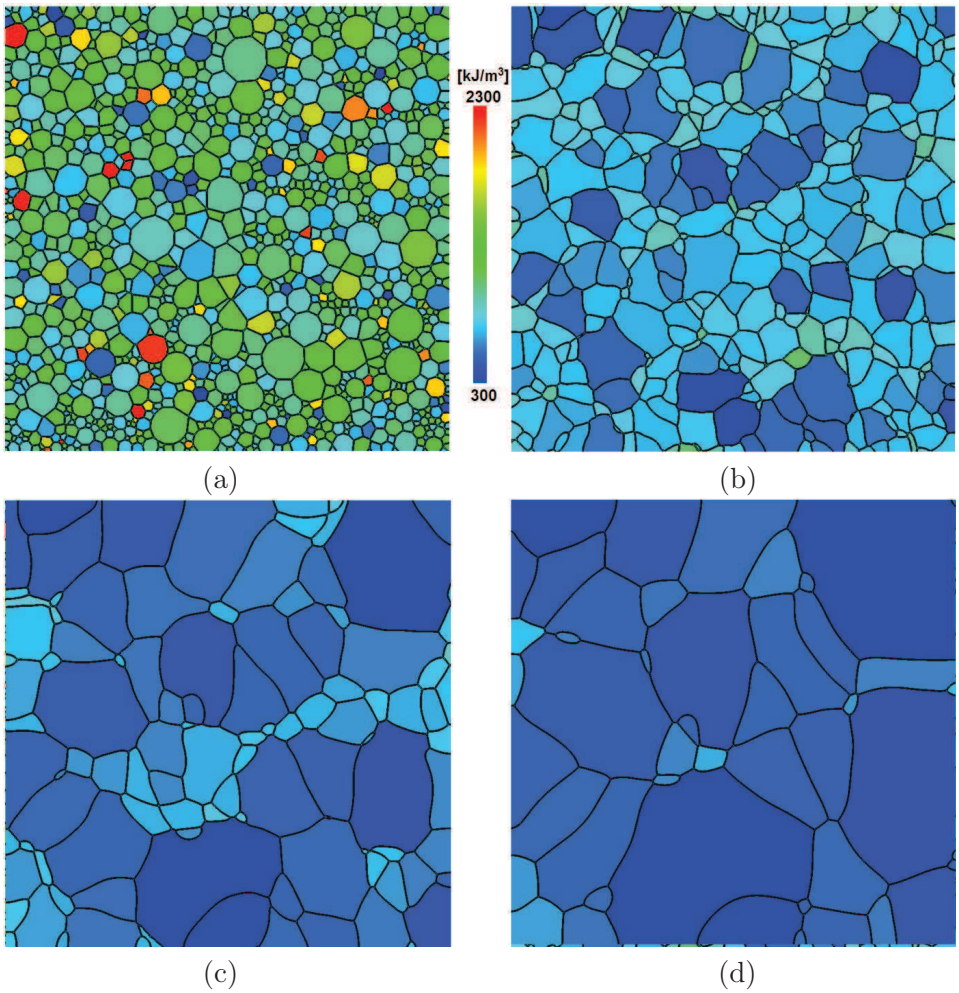

Figure 5.22: Evolution of a microstructure without second phase particles and the energy distribution of Figure 5.16 with $s = 4$: initial microstructure (a), after annealing at 985°C for 20s (b), 100s (c) and 300s (d).

4.1.3).

Now, it seems worth investigating if the histogram of Figure 5.16 with $s = 4$ can trigger abnormal grain growth also in the absence of second phase particles, as observed experimentally (see Figure 4.34). Figure 5.22 shows the evolution of microstructure during annealing: it is to note that the initial energy distribution is different from that of Figure 5.17. As expected, grain growth is faster without particles and after only 300s bigger grains reach the same size of overgrown grains of Figure 5.20 after 900s. However, microstructure evolution is fairly continuous: lower energy grains do not grow significantly faster than higher energy grains, leading to an inhomogeneous microstructure as that observed experimentally. Indeed, the validity of such result is limited by the small size of the simulation domain, thus it should be confirmed by performing simulations in bigger domains to increase its statistical relevance. However, if it could be confirmed, then it would suggest that the strain distribution of Figure 5.16 with $s = 4$ can trigger abnormal grain growth only if it is associated with a grain boundary pinning force of the same order of magnitude. Such pinning force is of course due to Zener pinning in particle containing microstructures. On the contrary, the origin of such pinning force in microstructures without particles is not clear and it should be investigated experimentally.

5.4 Summary

In this chapter, a 2D full field numerical simulation of microstructure evolution is exploited to investigate the validity of the postulated mechanism responsible for inhomogeneous grain growth that was identified by experimental characterization in prevoius chapters. The mechanism involves the selective growth of few low energy grains in a microstructure with or without particles. As the stored energy driving force is of the same order of magnitude as the capillarity or pinning force, it is necessary to model all three phenomena in a single framework.

First of all, it is shown that in the numerical model the interaction particle-grain boundary can be treated without any assumption (on particle shape or particle/grain energy), unlike all models proposed so far in the literature. In fact, particles are taken into account via their direct effect on grain boundary curvature, which leads to a physically consistent description of the interaction.

Several 2D simulations of capillarity driven grain growth (based on Inconel 718 at 985°C) with circular and coherent particles are performed. The results concerning the limiting grain size are consitent with those obtained in the literature using other numerical models. It is found that particle distribution has a great influence on the limiting grain size. All obtained results can be described with a Smith-Zener-like equation ($\overline{R} = K\frac{\bar{r}}{f^m}$) with the parameter K depending on the size of particles. The simulation of grain growth with a particle population having the same morphology of real δ phase particles has shown that morphology has not a great impact on the

limiting grain size in the considered conditions.

The introduction of stored energy in a pinned microstructure can trigger the abnormal growth of an energy-free grain driven by a stored energy force of the same order of magnitude as the pinning or capillarity force. A critical strain stored energy distribution measured experimentally from EBSD, taking into account only the contribution of geometrically necessary dislocations, does not trigger abnormal grain growth but only coarsening in simulations. However, if the same strain stored energy distribution is modified to take into account also the possible contribution of statistically stored dislocations, then abnormal grain growth occurs. The phenomenon involves the abnormal growth of few low energy grains, while higher energy grains are pinned by particles. Such mechanism would support the current explanation for inhomogeneous grain growth induced by small strains. Moreover, it is shown that the fraction of particles does not influence the occurrence of the phenomenon, but only the growth of the small higher energy grains.

Résumé

Dans ce chapitre, le mécanisme proposé dans les chapitres précédents comme responsable de la croissance anormale des grains est testé numériquement grâce à une simulation 2D en champ complet de l'évolution microstructurale. Le mécanisme est caractérisé par la croissance préférentielle d'un nombre restreint de grains de faible énergie par rapport aux grains voisins. La force motrice liée à l'énergie stockée pour la migration d'un joint de grains étant du même ordre de grandeur que la force capillaire et que la force d'ancrage de Smith-Zener. La simulation numérique développée s'appuie sur des fonctions level-set (LS) permettant de décrire le mouvement des interfaces dans un contexte éléments finis (EF) sur maillages non-structurés. Cette méthode permet de prendre en compte les trois forces précédemment évoquées, dans un cadre unique. Premièrement, on montre que dans le modèle numérique utilisé dans cette étude l'interaction particule-joint de grains peut être traitée sans aucune hypothèse concernant la forme de la particule ou l'énergie de l'interface particule/grain, à la différence de tous les modèles préexistants dans la littérature. En fait, les particules sont prises en compte à travers leur effet direct sur la courbure du joint de grains : l'interaction est donc décrite d'un point de vue physique et de manière très robuste. Plusieurs simulations 2D de croissance de grains sans énergie stockée, avec des propriétés de joints de grains correspondant à celles de l'Inconel 718 à 985°C, et avec des particules circulaires et incohérentes sont d'abord présentées. Les résultats en termes de taille limite de grains sont cohérents avec ceux obtenus avec d'autres modèles numériques dans la littérature. L'importance de la distribution spatiale des particules est notamment confirmée. Tous les résultats obtenus peuvent être décrits par une équation de type Smith-Zener ($\overline{R} = K\frac{\bar{r}}{f^m}$) avec le paramètre K qui dépend de la taille des particules. Une simulation de croissance de grains prenant en

compte la morphologie réelle des particules de phase δ de notre matériau a montré que la morphologie n'a qu'une faible influence sur la taille de grains limite, au moins dans les conditions testées. Par ailleurs, il est démontré que l'introduction d'énergie stocké dans une microstructure qui contient des particules peut déclencher la croissance anormale d'un grain d'énergie nulle : c'est le cas quand la force motrice liée à l'énergie stockée atteint une valeur du même ordre de grandeur que la force nette résultant de la capillarité et de l'ancrage de Smith-Zener. Une distribution d'énergie de déformation moyenne par grain (évaluée à partir de cartographies EBSD) ne prenant en compte que les dislocations géométriquement nécessaires, n'est pas suffisante pour déclencher la croissance anormale dans les simulations. Par contre, si la même distribution est modifiée pour considérer aussi la contribution potentielle de dislocations statistiquement stockées, alors la croissance anormale apparaît dans les simulations. Le phénomène, comme dans le cas expérimental, est caractérisé par la croissance préférentielle d'un nombre restreint de grains de faible énergie par rapport aux autres grains qui ne grossissent pas à cause de l'ancrage de Smith-Zener. De plus, si la fraction volumique de particules augmente de 2% à 4%, le phénomène constaté expérimentalement se produit : la seule différence entre les simulations porte sur la taille et la fraction des grains qui ne grossissent pas anormalement dans les microstructures.

Conclusion

Synthesis

The objectives of this PhD work were to understand, model and simulate numerically the phenomenon of inhomogeneous grain growth that can occur in Inconel 718 turbine disks during the annealing steps of hot forging sequences.

The experimental characterization (EBSD, SEM) of several microstructures taken from industrial pieces has allowed to propose a possible explanation for the origin of inhomogeneous grain growth occuring at different δ sub-solvus temperatures.

During annealing at 985°C, abnormal grain growth is triggered in those microstructures where a critical distribution of strain stored energy is present. It is shown that abnormal grain growth occurs when the stored energy driving pressure for boundary migration is of the same order of magnitude as the net force resulting from the capillarity and Smith-Zener pinning pressures (about 100kPa). The mechanism involves the selective growth of few lower energy grains at the expanse of neighboring higher energy grains. Such mechanism assumes that low energy grains are already present before annealing or that they could also be generated by nucleation. The proposed mechanism is consistent with the grain boundaries of overgrown grains, being high angle grain boundaries without any special property. It is shown that the average intragranular misorientation (via the GOS parameter) of a microstructure before annealing can be related to the grain size reached after annealing at 985°C (that is determined by the number of growing grains). Below a critical stored energy level, no grain growth occurs due to Smith-Zener pinning.

During annealing at 1010°C, abnormal grain growth is also triggered by strain stored energy reduction, with the same mechanism as the one occuring at 985°C. However, because 1010°C is close to the δ solvus temperature, the phenomenon can also be triggered by the dissolution of δ phase particles. In this case, few grains are supposed to gain a size advantage and grow faster than the others without an energy advantage.

Torsion tests have allowed to reproduce the phenomenon of inhomogeneous grain growth observed on industrial pieces during annealing at 985°C and to confirm its dependance from a critical distribution on strain stored energy. Moreover, a clear relation is established between small prior strains and the occurrence of the phenomenon during annealing. It is shown that a reference microstructure that is fine ($\overline{D}_N$=6 μm), recrystallized (strain stored energy-free) and containing δ phase particles (at least 1%) is stable during annealing thanks to Smith-Zener pinning. If the reference microstructure is strained at 985°C in the range $0.05 < \varepsilon < 0.1$, then inhomogeneous grain growth is triggered during annealing. The critical strain is about $\varepsilon = 0.07$ for a torsion test performed at 985°C and $\dot{\varepsilon} = 0.1s^{-1}$. As for industrial pieces, the origin of the phenomenon is linked to a critical distribution of strain

stored energy that triggers during annealing the growth of few existing lower energy grains or new grains formed by nucleation.

Concerning the role of δ phase particles, it is shown that they affect only the fraction of fine grains of the reference microstructure that remains after inhomogeneous grain growth at 985°C. If the initial microstructure is no longer strain-free, then the application of a small strain does not necessarily lead to inhomogeneous grain growth during annealing, as the cumulated amount of hardening is high enough to trigger the nucleation at many sites, thus reducing the final grain size. Finally, it is shown that small strains at δ super-solvus temperatures or even at room temperature can trigger inhomogeneous grain growth during annealing as well. In both cases the phenomenon leads to the formation of microstructures similar to those observed in δ sub-solvus torsion tests. The effect of increasing the straining temperature is to decrease the average intragranular misorientation of microstructures.

In conclusion, from a practical point of view, industrial forging cycles should not involve a hot deformation step (either below or above the δ solvus temperature) which ends by applying a small strain ($\varepsilon<0.1$) in some parts of the piece. Otherwise, abnormal grain growth is very likely to occur during the following annealing step.

2D numerical simulations of microstructure evolution using a full field numerical model have allowed to investigate the validity of the postulated mechanism responsible for inhomogeneous grain growth. First of all, it is shown that the numerical model can treat capillarity driven grain growth (based on Inconel 718 at 985°C) with circular and incoherent particles. The results concerning the limiting grain size are consitent with those obtained in the literature using other numerical models. It is confirmed that particle spatial distribution has a great influence on the limiting grain size. All obtained results can be described with a Smith-Zener-like equation ($\overline{R} = K\frac{\bar{r}}{f^m}$) with the parameter K depending on the size of particles. The simulation of grain growth with a particle population having the morphology of real δ phase particles has shown that morphology has not a great impact on the limiting grain size in the considered conditions.

Finally, it is shown that the introduction of stored energy in a pinned microstructure can trigger the abnormal growth of an energy-free grain driven by a stored energy force of the same order of magnitude as the net force resulting from the capillarity and Smith-Zener pinning pressures. If a critical strain stored energy distribution measured experimentally from EBSD is modified to also account for the possible contribution of statistically stored dislocations, then abnormal grain growth occurs. The phenomenon involves the abnormal growth of few low energy grains, while higher energy grains are pinned by particles. Such mechanism supports the current explanation for inhomogeneous grain growth induced by small strains. Moreover, it is demonstrated that the fraction of particles does not influence the occurrence of the phenomenon, but only the growth of the small higher energy grains.

Perspectives

In this work, the focus has been placed on the effect of small strains (ε<0.1, $\dot{\bar{\varepsilon}} = 0.05s^{-1}$) applied at δ sub-solvus temperatures on the occurrence of abnormal grain growth during annealing. It has been shown that similar results can also be obtained by straining (ε<0.1, $\dot{\bar{\varepsilon}} = 0.01s^{-1}$) at δ super-solvus temperatures in anisothermal conditions. Hence, it would be interesting to investigate the influence of higher δ super-solvus temperatures and the effect of strain rate on critical hardening. This analysis would allow to identify in a broader thermomechanical domain the conditions that trigger abnormal grain growth, in order to generalize the results of this work.

Geometrically necessary dislocation densities have been roughly estimated from intragranular misorientation data obtained by EBSD measurements in order to calculate strain stored energies. For the sake of a more precise quantification of the total density of dislocations, another experimental technique should be employed (for example electron channelling contrast imaging in a SEM) in order to estimate the fraction of geometrically necessary and statistically stored dislocations generated at low strains. Moreover, dislocation densities could also be investigated by performing precise finite element simulations of crystal plasticity, by using the numerical tools developed in Cemef [83, 84, 85].

The proposed mechanism of inhomogeneous grain growth assumes that abnormal grains already existed before annealing or that they also form by nucleation. However, it remains unclear if one origin is predominant with respect to the other. This aspect could be investigated by applying small strains on a strain strain-free coarse (100 μm) microstructure: if nucleation takes place, then several small strain-free nuclei should appear during the beginning of annealing. In this case the focus should be placed on the characterization of local intragranular misorientations (i.e. KAM) in order to investigate the possible sites of nucleation. Once again, experimental results may be compared to finite element simulations of crystal plasticity associated with a nucleation criterion.

If the growth of existing grains is predominant with respect to the growth of nuclei, then the occurence of inhomogeneous grain growth is mainly controlled by the initial distribution of stored energies in the microstructure, as it was demonstrated by numerical simulations. Hence, it would be interesting to try to predict the phenomenon also by using a mean field model that may take into account the effect of a stored energy distribution on grain boundary migration. Such mean field model could then be used to link the thermomecanical parameters of a forming process with the occurence of abnormal grain growth.

Concerning the full field numerical simulations of inhomogeneous grain growth, the maximum size of the simulation domain in this work was limited (due to computational time) only to 200x200 μm which contains about 1100 grains of average grain size 6 μm. Indeed, the results obtained should also be validated in bigger domain, at

least 400x400 μm (about 4500 grains) in order to increase the statistical relevance of the results.

High computational time is mainly due to the use of adaptive meshing associated with small time steps in order to precisely describe the grain/particle interaction. This could be overcome by considering an implicit introduction of Smith-Zener pinning in the level set formalism. For example, an average pinning force could be calibrated using the results of this work obtained by the explicit description of the grain/particle interaction.

All numerical simulations in this work were also limited to two dimensions. This aspect is an important limitation concerning the simulation of Smith-Zener pinning, as in 2D systems the phenomenon is "stronger" than in equivalent 3D systems. Hence, 3D simulations of Smith-Zener pinning and inhomogeneous grain growth should also be carried out. It is to note that, thanks to the considered level set approach, no further developments are necessary to deal with 3D configurations, but the simulations would be more time consuming.

Another significant improvement of the simulation of Smith-Zener pinning would be also to include the possibility for the particle population to evolve during the simulation. This would allow, for example, to investigate abnormal grain growth phenomena triggered by the dissolution of particles during annealing. However, this improvement would require to introduce differently in the considered level set formalism the effect of particles. Particles should be introduced as new objects described by level set functions, which could then evolve during the simulation.

Finally, the results in this work have shown that abnormal grain growth is always associated with high twin densities (with respect to microstructures obtained by capillarity driven grain growth). From the grain boundary engineering point of view, it would be interesting to employ the thermomecanical conditions leading to abnormal grain growth in order to maximize the twin density. The main advantage of using the thermomecanical conditions presented in this work is that all deformations are applied at high temperature. In fact, as straining at room temperature increases significantly the stress, it may be an issue when dealing with the size of industrial pieces.

References

[1] M. L. Brogdon, A. H. Rosenberger, A. Force, and M. Directorate, "Evaluation of the Influence of Grain Structure on the Fatigue Variability of Waspaloy," in *Superalloys 2008*, pp. 583–588, 2008.

[2] B. Flageolet, O. Yousfi, Y. Dahan, P. Villechaise, and J. Cormier, "Characterization of microstructures containing abnormal grain growth zones in Alloy 718," in *7th International Symposium on superalloy 718 and derivatives*, pp. 595–606, 2010.

[3] J. Uginet and B. Pieraggi, "Study of Secondary Grain Growth on 718 Alloy," in *Superalloys 718, 625, 706 and Various Derivatives*, pp. 343–352, 1997.

[4] G. D. Smith and H. L. Flower, "Super plastic forming of Inconel alloy 718SPF," in *Superalloys 718, 625, 706 and Various Derivatives*, pp. 355–364, 1994.

[5] P. A. Manohar, M. Ferry, and T. Chandra, "Five Decades of the Zener Equation," *ISIJ International*, vol. 38, pp. 913–924, 1998.

[6] T. Nishizawa, I. Ohnuma, and K. Ishida, "Examination of the zener relationship between grain size and particle dispersion," *Materials transaction*, vol. 38, pp. 950–956, 1997.

[7] C. S. Smith, "Introduction to Grains, Phases, and Interfaces-an Interpretation of Microstructure," *Trans Metall Soc AIME*, vol. 175, pp. 15–51, 1948.

[8] N. Moelans, B. Blanpain, and P. Wollants, "A phase field model for the simulation of grain growth in materials containing finely dispersed incoherent second-phase particles," *Acta Materialia*, vol. 53, pp. 1771–1781, 2005.

[9] F. Humphreys and M. Hatherly, *Recrystallization and related annealing phenomena*. Oxford: Elsevier, second ed., 2004.

[10] M. Miodownik, "Modeling and Simulation : Processing of Metallic Materials Monte Carlo Models for Grain Growth and Recrystallization," *ASM Handbook*, vol. 22, p. 3J, 2008.

[11] G. Jinhua, G. Raymond, and G. Thompson, "Computer simulation of grain growth with second phase particle pinning," *Acta Materialia*, vol. 45, pp. 3653–3658, 1997.

[12] D. Srolovitz, M. Anderson, G. Grest, and P. Sahni, "Computer simulation of grain growth-iii. influence of a particle dispersion," *Acta Metallurgica*, vol. 32, pp. 1429 – 1438, 1984.

[13] M. Miodownik, J. W. Martin, and a. Cerezo, "Mesoscale simulations of particle pinning," *Philosophical Magazine A*, vol. 79, pp. 203–222, 1999.

[14] M. Miodownik, "Highly parallel computer simulations of particle pinning: zener vindicated," *Scripta Materialia*, vol. 42, pp. 1173–1177, 2000.

[15] D. Fan, "Computer simulation of grain growth using a continuum field model," *Acta Materialia*, vol. 45, pp. 611–622, 1997.

[16] Y. Suwa, Y. Saito, and H. Onodera, "Phase field simulation of grain growth in three dimensional system containing finely dispersed second-phase particles," *Scripta Materialia*, vol. 55, pp. 407–410, 2006.

[17] L. Vanherpe, N. Moelans, B. Blanpain, and S. Vandewalle, "Pinning effect of spheroid second-phase particles on grain growth studied by three-dimensional phase-field simulations," *Computational Materials Science*, vol. 49, pp. 340–350, 2010.

[18] K. Chang, W. Feng, and L.-Q. Chen, "Effect of second-phase particle morphology on grain growth kinetics," *Acta Materialia*, vol. 57, pp. 5229–5236, 2009.

[19] J. Lépinoux, D. Weygand, and M. Verdier, "Modeling grain growth and related phenomena with vertex dynamics," *Comptes Rendus Physique*, vol. 11, pp. 265–273, 2010.

[20] D. Weygand, "Zener pinning and grain growth: a two-dimensional vertex computer simulation," *Acta Materialia*, vol. 47, pp. 961–970, 1999.

[21] G. Couturier, C. Maurice, and R. Fortunier, "Three-dimensional finite-element simulation of Zener pinning dynamics," *Philosophical Magazine*, vol. 83, pp. 3387–3405, 2003.

[22] G. Couturier, R. Doherty, C. Maurice, and R. Fortunier, "3D finite element simulation of the inhibition of normal grain growth by particles," *Acta Materialia*, vol. 53, pp. 977–989, 2005.

[23] M. Hillert, "On the theory of normal and abnormal grain growth," *Acta Metallurgica*, vol. 13, pp. 227 – 238, 1965.

[24] M. Mujahid, C. A. Gater, and J. W. Martin, "Microstructural Study of a Mechanically Alloyed ODS Superalloy," *Journal of Materials Engineering and Performance*, vol. 7, pp. 524–532, 1998.

[25] M. Mujahid and M. Martin, "The effect of oxide particle coherency on Zener pinning in ODS superalloys," *Journal of Materials Science letters*, vol. 13, pp. 153–155, 1994.

[26] S. J. Dillon, M. Tang, W. C. Carter, and M. P. Harmer, "Complexion: A new concept for kinetic engineering in materials science," *Acta Materialia*, vol. 55, pp. 6208–6218, 2007.

[27] D.-K. Lee, B.-J. Lee, K.-J. Ko, and N.-M. Hwang, "Comparison of the Advantages Conferred by Mobility and Energy of the Grain Boundary in Inducing Abnormal Grain Growth Using Monte Carlo Simulations," *Materials Transactions*, vol. 50, pp. 2521–2525, 2009.

[28] J. B. Koo, D. Y. Yoon, and M. F. Henry, "The effect of small deformation on abnormal grain growth in bulk Cu," *Metallurgical and Materials Transactions A*, vol. 33, pp. 3803–3815, 2002.

[29] V. Randle, "Strain-Induced Secondary Recrystallization," *Materials Science Forum*, vol. 113-115, pp. 189–194, 1993.

[30] G. Riontino, C. Antonione, L. Battezzati, F. Marino, and M. C. Tabasso, "Kinetics of abnormal grain growth in pure iron," *Journal of Materials Science*, vol. 14, pp. 86–90, 1979.

[31] T. A. Bennett, P. N. Kalu, and A. D. Rollett, "Strain-Induced Selective Growth in 1 . 5 % temper-rolled Fe1%Si," *Microsc.Microanal.*, vol. 17, pp. 1–6, 2011.

[32] Q. Li, B. Guyot, and N. Richards, "Effect of processing parameters on grain boundary modifications to alloy Inconel 718," *Materials Science and Engineering: A*, vol. 458, pp. 58–66, 2007.

[33] Q. Li, J. Cahoon, and N. Richards, "Effects of thermo-mechanical processing parameters on the special boundary configurations of commercially pure nickel," *Materials Science and Engineering: A*, vol. 527, pp. 263–271, 2009.

[34] V. Randle, "Mechanism of twinning-induced grain boundary engineering in low stacking-fault energy materials," *Acta Materialia*, vol. 47, pp. 4187–4196, 1999.

[35] M. Kumar, A. J. Schwartz, and W. E. King, "Microstructural evolution during grain boundary engineering of low to medium stacking fault energy fcc materials," *Acta Materialia*, vol. 50, pp. 2599–2612, 2002.

[36] C. P. Blankenship, M. F. Henry, E. S. Huron, and J. M. Hyzac, "Method for controlling grain size in Ni-base Superalloys," 1997 (Patent).

[37] D. D. Krueger, R. Kissinger, R. Menzies, and C. Wukusick, "Fatigue crack growth resistant nickel-base article and alloy and method for making," 1990 (Patent).

[38] M. Soucail, M. Marty, and H. Octor, "The Effect of High Temperature Deformation on Grain Growth in a PM Nickel Base Superalloy," in *Superalloys 1996*, pp. 663–666, 1996.

[39] E. Huron, S. Srivatsa, and E. Raymond, "Control of Grain Size Via Forging Strain Rate Limits for R'88DT," in *Superalloys 2000*, pp. 49–58, 2000.

[40] E. Raymond, R. Kissinger, A. Paxson, and E. S. Huron, "Nickel-base superalloy having improved resistance to abnormal grain growth," 1999 (Patent).

[41] R. F. Decker, A. I. Rush, A. G. Dano, and J. W. Freeman, "Abnormal Grain Growth in Nickel-base Heat-resistant alloys," tech. rep., University of Michigan, 1956.

[42] Y. K. Cho, D. K. Yoon, and M. F. Henry, "The Effects of Deformation and Pre Heat Treatment on Abnormal Grain Growth in RENE 88 Superalloy," *Metallurgical and Materials Transactions A*, vol. 32, pp. 3077–3090, 2001.

[43] D. A. DeMania, *Recovery and Recrystallization in Nickel-based Superalloy René 88 DT*. PhD thesis, University of Virginia, 2002.

[44] N. Bozzolo, N. Souaï, and R. Logé, "Evolution of microstructure and twin density during thermomechanical processing in a γ-γ' nickel-based superalloy," *Acta Materialia*, vol. 60, pp. 5056–5066, 2012.

[45] M. A. Miodownik, A. J. Wilkinson, and J. W. Martin, "On the secondary recrystallization of MA754," *Acta Materialia*, vol. 46, pp. 2809–2821, 1998.

[46] K. Kusunoki, K. Sumino, Y. Kawasaki, and M. Yamazaki, "Effects of the Amount of y ' and Oxide Content on the Secondary Recrystallization Temperature of Nickel-Base Superalloys," *Metallurgical Transactions A*, vol. 21, pp. 547–555, 1990.

[47] "Iconel alloy 718," tech. rep., Special Metals, 2007.

[48] X. Xie, C. Xu, G. Wang, J. Dong, W.-d. Cao, and R. Kennedy, "TTT diagram of a newly developed nickel-base superalloy-Allvac 718Plus," in *Superalloys 718, 625, 706 and Derivatives 2005*, pp. 193–202, 2005.

[49] A. Strondl, R. Fischer, G. Frommeyer, and A. Schneider, "Investigations of MX and γ'/γ " precipitates in the nickel-based superalloy 718 produced by electron beam melting," *Materials Science and Engineering: A*, vol. 480, pp. 138–147, 2008.

[50] S. Azadian, L. Wei, and R. Warren, "Delta phase precipitation in Inconel 718," *Materials Characterization*, vol. 53, pp. 7–16, 2004.

[51] A. Niang, B. Viguier, and J. Lacaze, "Some features of anisothermal solid-state transformations in alloy 718," *Materials Characterization*, vol. 61, pp. 525–534, 2010.

[52] D. Y. Cai, W. H. Zhang, and P. L. Nie, "Dissolution kinetics and behaviour of δ phase in Inconel 718," *Trans. Nonferrous Met. Soc. China*, vol. 13, pp. 1338–1341, 2003.

[53] H. Zhang, S. Zhang, M. Cheng, and Z. Li, "Deformation characteristics of δ phase in the delta-processed Inconel 718 alloy," *Materials Characterization*, vol. 61, pp. 49–53, 2010.

[54] Y. Wang, W. Z. Shao, L. Zhen, L. Lin, and Y. X. Cui, "Investigation on Dynamic Recrystallization Behavior in Hot Deformed Superalloy Inconel 718," *Materials Science Forum*, vol. 549, pp. 1297–1300, 2007.

[55] Y. Wang, W. Shao, L. Zhen, and X. Zhang, "Microstructure evolution during dynamic recrystallization of hot deformed superalloy 718," *Materials Science and Engineering: A*, vol. 486, pp. 321–332, 2008.

[56] J. Thomas, E. Bauchet, C. Dumont, and F. Montheillet, "EBSD investigation and modeling of the microstructural evolutions of superalloy 718 during hot deformation," in *Superalloys 2004*, pp. 959–968, 2004.

[57] H. Yuan and W. Liu, "Effect of the δ phase on the hot deformation behavior of Inconel 718," *Materials Science and Engineering: A*, vol. 408, pp. 281–289, 2005.

[58] L. Zhou and T. Baker, "Effects on dynamic and metadynamic recrystallization on microstructures of wrought IN-718 due to hot deformation," *Materials Science and Engineering: A*, vol. 196, pp. 89–95, 1995.

[59] K. Huang, *Towards the modeling of recrystallization phenomena in multi-pass conditions - Application to 304L steel.* PhD thesis, École nationale supérieure des mines de Paris, 2011.

[60] G. E. Dieter, H. A. Kuhn, and S. L. Semiatin, *Handbook of Workability and Process Design.* Ohio: ASM International, 2003.

[61] N. Souai, *Contrôle du maclage thermique et de la taille de grains par traitements thermomécaniques dans un superalliage base Ni.* PhD thesis, École nationale supérieure des mines de Paris, 2011.

[62] "TSL OIM analysis 5.3 guide," tech. rep., TSL, 2007.

[63] S. M. Foiles, "Temperature dependence of grain boundary free energy and elastic constants," *Scripta Materialia*, vol. 62, pp. 231–234, 2010.

[64] M. Hillert, "Influence of solute segregation on grain-boundary energy and self-diffusion," *Metallurgical Transactions A*, vol. 8A, pp. 1431–1438, 1977.

[65] B. R. Patterson and Y. Liu, "Relationship between Grain Boundary Curvature and Grain Size," *Metallurgical and Materials Transactions A*, vol. 23, pp. 2481–2482, 1992.

[66] M. Calcagnotto, D. Ponge, E. Demir, and D. Raabe, "Orientation gradients and geometrically necessary dislocations in ultrafine grained dual-phase steels studied by 2D and 3D EBSD," *Materials Science and Engineering: A*, vol. 527, pp. 2738–2746, 2010.

[67] H. Gao, "Geometrically necessary dislocation and size-dependent plasticity," *Scripta Materialia*, vol. 48, pp. 113–118, 2003.

[68] L. Kubin, "Geometrically necessary dislocations and strain-gradient plasticity: a few critical issues," *Scripta Materialia*, vol. 48, pp. 119–125, 2003.

[69] U. Kocks and H. Mecking, "Physics and phenomenology of strain hardening: the {FCC} case," *Progress in Materials Science*, vol. 48, pp. 171 – 273, 2003.

[70] M. Kassner, "Taylor hardening in five-power-law creep of metals and Class M alloys," *Acta Materialia*, vol. 52, pp. 1–9, 2004.

[71] B. Viguier, "Dislocation densities and strain hardening rate in some intermetallic compounds," *Materials Science and Engineering: A*, vol. 349, pp. 132 – 135, 2003.

[72] T. Mongis, "Ingénierie des joints de grains dans l'Inconel 718," tech. rep., Ecole nationale supérieure des mines de Paris, 2012.

[73] N. Bozzolo, S. Jacomet, and R. Logé, "Fast in-situ annealing stage coupled with EBSD: A suitable tool to observe quick recrystallization mechanisms," *Materials Characterization*, vol. 70, pp. 28–32, 2012.

[74] A. A. Guimaraes and J. J. Jonas, "Recrystallization and Aging Effects Associated with the High Temperature Deformation of Waspaloy and Inconel 718," vol. 12, pp. 1655–1666, 1981.

[75] M. Bernacki, H. Resk, T. Coupez, and R. E. Logé, "Finite element model of primary recrystallization in polycrystalline aggregates using a level set framework," *Modelling and Simulation in Materials Science and Engineering*, vol. 17, p. 064006, 2009.

[76] M. Bernacki, R. Logé, and T. Coupez, "Level set framework for the finite-element modelling of recrystallization and grain growth in polycrystalline materials," *Scripta Materialia*, vol. 64, pp. 525–528, 2011.

[77] M. Bernacki, Y. Chastel, T. Coupez, and R. Logé, "Level set framework for the numerical modelling of primary recrystallization in polycrystalline materials," *Scripta Materialia*, vol. 58, pp. 1129–1132, 2008.

[78] K. Hitti, P. Laure, T. Coupez, L. Silva, and M. Bernacki, "Precise generation of complex statistical Representative Volume Elements (RVEs) in a finite element context," *Computational Materials Science*, vol. 61, pp. 224–238, 2012.

[79] M. Elsey, S. Esedoglu, and P. Smereka, "Diffusion generated motion for grain growth in two and three dimensions," *Journal of Computational Physics*, vol. 228, pp. 8015–8033, 2009.

[80] J. F. Zaragoci, *Simulation numérique directe multiphasique de la déformation d'un alliage Al-Cu à l'état pâteux - Comparaison avec des observations par tomographie aux rayons X in situ en temps réel.* PhD thesis, École nationale supérieure des mines de Paris, 2012.

[81] A. Gamiette, "Adapting Inconel Metallurgical Post-Processor," tech. rep., École nationale supérieure des mines de Paris, 2009.

[82] N. Moelans, B. Blanpain, and P. Wollants, "Phase field simulations of grain growth in two-dimensional systems containing finely dispersed second-phase particles," *Acta Materialia*, vol. 54, pp. 1175–1184, 2006.

[83] R. Loge, M. Bernacki, H. Resk, L. Delannay, H. Digonnet, Y. Chastel, and T. Coupez, "Linking plastic deformation to recrystallization in metals using digital microstructures," *Philosophical Magazine*, vol. 88, pp. 3691–3712, 2008.

[84] H. Resk, L. Delannay, M. Bernacki, T. Coupez, and R. Logé, "Adaptive mesh refinement and automatic remeshing in crystal plasticity finite element simulations," *Modelling and Simulation in Materials Science and Engineering*, vol. 17, p. 075012, 2009.

[85] A. L. Fabiano, *Modelling of crystal plasticity and grain boundary motion of 304L steel at the mesoscopic scale.* PhD thesis, École nationale supérieure des mines de Paris, 2013.

Origine de l'éclatement de grain sur des pièces forgées en Inconel 718

RESUME : L'Inconel 718 est un superalliage base nickel très utilisé pour produire les disques de turboréacteurs. Typiquement, une gamme de forgeage à chaud se compose de plusieurs étapes de déformation et de recuit. La présence des particules de seconde phase (particules de phase δ dans l'Inconel 718) permet en principe de limiter la croissance de grains pendant les étapes de recuit grâce au phénomène d'ancrage de Smith-Zener. Néanmoins, l'hétérogénéité microstructurale (distribution des particules, écrouissage, composition chimique) peut favoriser une croissance anormale des grains pendant le recuit. Ce phénomène est connu industriellement sous la terminologie d'"éclatement de grains". Les objectifs de la thèse étaient d'identifier les mécanismes responsables de l'éclatement des grains qui peut survenir durant les étapes de recuit sur les pièces forgées en Inconel 718, de les modéliser, et de simuler numériquement le phénomène. Les mécanismes physiques à l'origine du phénomène sont d'abord étudiés expérimentalement grâce à la caractérisation (par MEB et EBSD) des pièces forgées. L'influence des particules de seconde phase et de l'énergie stockée (estimée par des mesures de désorientations intragranulaires) est notamment étudiée. A partir des observations réalisées, une explication est proposée : le phénomène apparaît lorsque les forces motrices pour la migration des joints de grains dépassent la force de freinage de Smith-Zener ; ceci peut se produire lorsque la microstructure contient de l'énergie stockée, distribuée de manière hétérogène. Des essais de torsion à chaud sont mis en place pour reproduire, en laboratoire le même phénomène, pour étudier la sensibilité aux paramètres thermomécaniques et pour tester les hypothèses émises concernant les mécanismes. Les mécanismes ainsi identifiés comme responsables de l'éclatement de grains sont corroborés au moyen d'un modèle numérique en 2D. Le modèle numérique en champ complet est basé sur la méthode des éléments finis, et utilise le formalisme level-set pour décrire les joints de grains. La simulation de l'évolution microstructurale prend en compte à la fois les forces motrices des joints de grains liées à la capillarité, à l'énergie stockée et à l'interaction des joints de grains avec des particules. Ainsi, l'effet de la distribution de l'énergie stockée (estimée à partir de données expérimentales) a pu être étudié numériquement dans des microstructures avec particules.

Mots clés : Ancrage de Zener, Croissance anormale des grains, Simulation en champ complet, Inconel 718, Energie de déformation.

Origin of inhomogeneous grain growth in Inconel 718 forgings

ABSTRACT: Inconel 718 is a nickel base superalloy commonly used to manufacture the rotating disks of turbojet engines. Such disks are generally produced by hot forging, which involves a sequence of different deformation and annealing steps. The presence of second phase particles (δ phase in Inconel 718) is commonly exploited to limit grain growth during annealing via the Smith-Zener pinning phenomenon. Nonetheless, microstructure heterogeneity (with regards to second phase particles, hardening, texture and chemical composition) can lead to inhomogeneous grain growth during annealing. The objectives of this PhD work were to understand, model and simulate numerically the phenomenon of inhomogeneous grain growth that can occur in Inconel 718 turbine disks during the annealing steps of hot forging sequences. The physical mechanisms which may explain the occurrence of the phenomenon are investigated experimentally by performing SEM and EBSD analyses of Inconel 718 industrial pieces. The focus is placed on the influence of second phase particles and strain energy (estimated from intragranular misorientations) on the occurrence of the phenomenon. From those observations, it is inferred that the phenomenon occurs when the grain boundary driving forces overcome the Smith-Zener pinning forces; this is achieved when stored energy is present and heterogeneously distributed. Moreover, hot torsion tests are carried out to reproduce the phenomenon in laboratory, to evaluate its sensibility to thermomechanical parameters and to test the previously postulated mechanism. The validity of this mechanism is finally demonstrated by modelling numerically the phenomenon in 2D. The full field numerical model is based on a level set description of the grain boundaries in a finite element context. Microstructure evolution is simulated explicitly taking into account Smith-Zener pinning, capillarity and stored energy driven grain growth in a single framework. The effect of strain stored energy distributions (estimated from experimental data) in pinned microstructures is investigated focusing on the conditions leading to inhomogeneous grain growth.

Keywords: Zener pinning, Abnormal grain growth, Full-field simulation, Inconel 718, Strain energy.

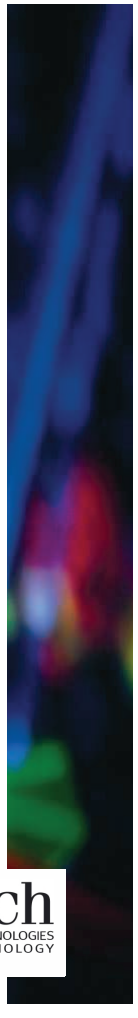

MINES ParisTech

ParisTech
INSTITUT DES SCIENCES ET TECHNOLOGIES
PARIS INSTITUTE OF TECHNOLOGY